THÈSE

En vue de l'obtention du

DOCTORAT DE L'UNIVERSITÉ DE TOULOUSE

Délivré par : *l'Institut Supérieur de l'Aéronautique et de l'Espace (ISAE)*

Présentée et soutenue le *18/11/2014* par :
Lokman BENNANI

Modélisation bidimensionnelle de systèmes électrothermiques de protection contre le givre

JURY

Jean-Jacques MARIGO	Ecole Polytechnique	Président du Jury
Pierre-Henri MAIRE	CEA/CESTA	Rapporteur
Cameron TROPEA	TU Darmstadt	Rapporteur
Patrick LABORDE	Université Paul Sabatier	Membre
Philippe VILLEDIEU	ONERA	Directeur de Thèse
Michel SALAUN	ISAE	Co-Directeur de Thèse

École doctorale et spécialité :
EDAA : Aéronautique et Astronautique
Unité de Recherche :
ONERA - DMAE - MH | Multiphasique Hétérogène
Directeur(s) de Thèse :
Philippe VILLEDIEU et Michel SALAUN
Rapporteurs :
Pierre-Henri MAIRE et Cameron TROPEA

Abstract

Icing has since long been identified as a serious issue in the aeronautical world. Ice build up, due to the presence of supercooled water droplets in clouds, leads to degradation of aerodynamic and/or air intake performances, among other undesirable consequences. Hence aircraft manufacturers must comply with certifications and regulations regarding flight safety in icing conditions. In order to do so, ice protection systems are used. Due to the multi-physical context within which these systems operate, numerical simulation can be a valuable asset.

The present work deals with the numerical modelling of electro-thermal ice protection systems. It is built around the development of three modules. Two of them are dedicated to modelling heat transfer in the system and in the ice block. The other one models the mechanical behaviour of ice and fracture.

Hence, the mechanical properties of atmospheric ice are reviewed in order to identify some mechanical parameters relevant to the fracture model. The fracture mechanics numerical method is used to investigate possible ice shedding mechanisms, that is to say the mechanisms leading to the detachement of ice, which are not yet well understood.

The final goal of this work is to propose a completely coupled 2nd generation simulation methodology for electro-thermal ice protection systems. Hence the feasibility of a coupled thermal computation with ice shedding prediction based on the developed modules is shown.

Keywords: Icing, ice shedding, ice protection, electro-thermal, de-icing, heat transfer, phase change, fracture mechanics, damage mechanics, numerical modelling

Résumé

Le givrage a depuis longtemps été identifié comme une problématique sérieuse dans le monde aéronautique. L'accrétion de givre, due à la présence de gouttelettes d'eau surfondue dans les nuages, dégrade les performances aérodynamiques et le rendement des entrées d'air parmi d'autres conséquences néfastes. Ainsi, les avionneurs sont sujets à des règles de certifications concernant la capacité à voler en conditions givrantes. Pour se faire, des systèmes de protection contre le givre sont utilisés. En raison de la complexité des phénomènes physiques mis en jeux, la simulation numérique constitue un atout lors de la phase de conception.

Ce travail de thèse porte sur la modélisation et la simulation numérique des systèmes électrothermiques de protection contre le givre. Il s'articule autour de trois approches de modélisation, qui ont donné lieu au développement de trois modules. Deux d'entre eux sont dédiés à la simulation du transfert de chaleur dans le système et dans la glace (changement de phase). Le troisième est lié à la modélisation du comportement mécanique du givre atmosphérique avec fissuration.

Ainsi, les propriétés mécaniques du givre atmosphérique sont revues de façon à pouvoir identifier les paramètres intervenant dans le modèle de fissuration. Ce modèle est ensuite utilisé pour étudier les mécanismes possibles de détachement du givre, qui ne sont à l'heure actuelle pas encore bien compris.

Le but final de ce travail est de proposer une méthodologie de simulation couplée pour les systèmes électrothermiques de protection contre le givre. Ainsi, la faisabilité d'un calcul couplé thermique-fissuration avec prédiction de détachement de givre est présentée.

Mots Clé: Givrage, protection contre le givre, électrothermique, dégivrage, thermique, changement de phase, fissuration, endommagement, modélisation numérique

Acknowledgements

CONTENTS

Roman

c, c_p	Specific heat $(J.kg^{-1}.K^{-1})$
L	Latent heat $(J.kg^{-1})$
h	Enthalpy per unit mass $(J.kg^{-1})$
T	Temperature $(K, °C)$
L_f	Melted length of ice (m)
L_t	Total contact length of ice (m)
$\boldsymbol{q}$	Heat flux per unit area $(J.m{-}2)$
$\boldsymbol{n}$	Outward unit normal vector
$\mathcal{D}$	Arbitrary domain
K	Cell
E	Edge OR Young's modulus
U	Generic scalar variable
Q_{src}	Volumetric heat source
t	Time (s)
d	Damage variable
g_c	Crack energy release rate $(J.m^2)$
l	Crack spreading length (m)

Greek

ϕ_L	Liquid fraction
α	Thermal diffusivity $(m^2.s^{-1})$
λ	Thermal conductivity $(W.m^{-1}.K^{-1})$ OR first Lamé coefficient(Pa)
Λ	Thermal conductivity matrix
χ	Solution of the transcendental equation for the academic Stefan problem
β	Catch efficiency
ρ	Density $(kg.m^{-3})$
ξ, η	Curvilinear coordinate system
θ	Kirchhoff variable
$\boldsymbol{\sigma}$	Stress tensor
$\boldsymbol{\epsilon}$	Strain Tensor
$\boldsymbol{u}$	Displacement field (m)
ϵ_i	ith eigen value of the strain tensor
μ	Second Lamé coefficient in Pa OR dynamic viscosity $(Pa.s^{-1})$
ν	Poisson's coefficient OR kinematic viscosity $(m^2.s^{-1})$

Subscripts

s	Solid phase
l	Liquid phase
m	Melting
rec	Recovery
K	Cell
bnd	Boundary

Superscripts

n	Time step

Operators and Functions

$\tilde{.}$	Cell average
$\lvert . \rvert$	Lengthor surface of condisered object
∇	Gradient differential operator
Δ	Laplacian
$tr(.)$	Trace

Abbreviation

ETIPS	Electro-Thermal Ice Protection System
PIIP	Pneumatic Impulse Ice Protection system
EEDI	Electro-Expulse De-Icing
EIDI	Electro-Impulse De-Icing
SLD	Supercooled Large Droplets
LWC	Liquid Water Content $(kg.m^{-3})$
MVD	Median Volumetric droplet Diameter (m)
htc	Heat Transfer Coefficient $(J.K^{-1}.m^{-2})$

Since the beginning of powered flight, icing has been identified as a serious issue in the aeronautical world. In early reports, it is referred to as "the ice problem". In typical icing flight conditions, the water droplets contained in clouds are in a supercooled state. When an aircraft encounters such conditions, those droplets freeze upon impacting its surface, therefore leading to ice build-up. In the aeronautical world, icing is one of the most serious hazards that can be encountered. Not only does it increase mass but it may also lead to a degradation of aerodynamic performances and blocked air intakes (among other undesirable consequences).

Aircraft manufacturers must therefore comply with certifications and regulations regarding flight safety in icing conditions. In order to achieve that goal, several ice protection technologies may be used. Over the decades, many concepts have been proposed, improved, analysed and tested. During the design of an aircraft, engineers have a very large choice of systems. However, each system has its pro's and con's, and will usually be best suited for a specific type of aircraft. For example, small commuter aircrafts very often use the pneumatic boots system. This type of system is refered to as a de-icing system. It allows ice to bluid up on the accreted surface before applying its method to free the surface from it. Larger aircraft such as those manufactured by Airbus or Boeing generally use the "bleed-air" system: hot air is taken from the engines and blown internally onto the protected surface, as shown figure 1. This type of system is refered to as an anti-icing system. Enough heat is provided to the surface so as to prevent the formation of ice upon it.
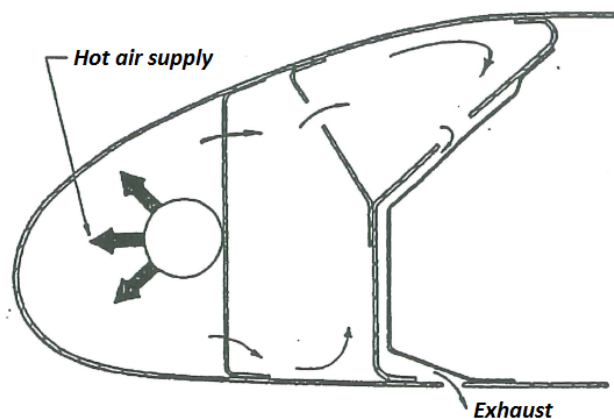
Figure 1: Illustration of a bleed air system [127]

However, although very efficient in protecting from icing, this system is energy-greedy. In the context of "more electric" aircraft and reduction of fuel consumption, alternative systems are being investigated for large airliners. One of these systems is the electrothermal ice protection system (ETIPS). The concept of this system dates back to the 30's [25] but only found a wide application much later for helicopter rotorblade de-icing. This system is composed of heater mats installed within

a multi-layered material as illustrated in figure 2. It can be used in anti-icing or deicing configurations [110, 149]. However, considering the previous discussion on energy, advantages are sought mainly through the use of the de-icing mode.
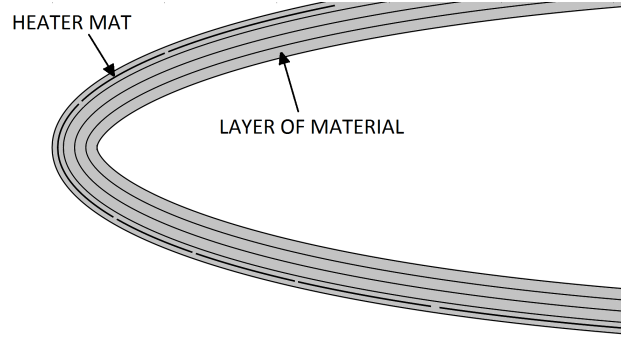
Figure 2: Illustration of an electro-thermal ice protection system

In de-icing mode, in order to protect the surface from ice build up, the electrical heaters are activated according to a defined power cycle. The heat provided by these heaters acts to melt the interface between the ice and the protected surface. The ice hence has less ability to remain attached to the surface and is eventually shed under the effect of aerodynamic forces.
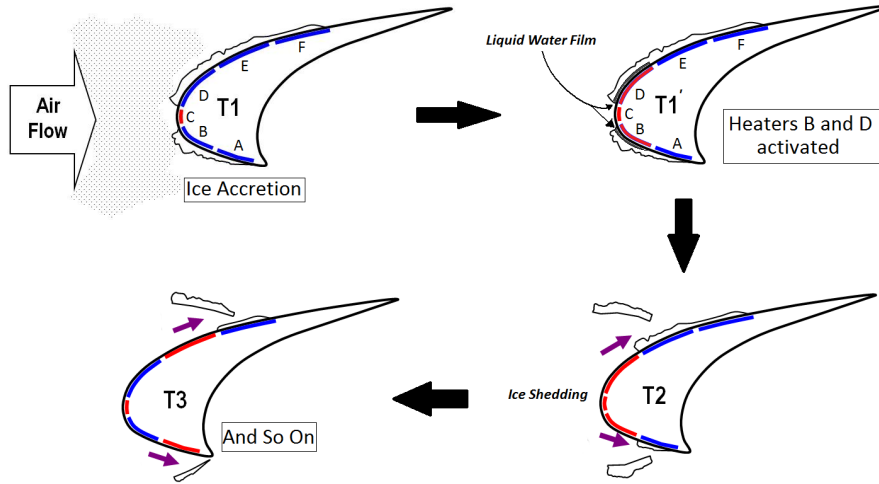
Figure 3: Illustration of the operating of an electro-thermal ice protection system

There are three main questions one seeks to answer when designing an ice protection system. The goal being to free the surface from ice as efficiently as possible, how much power should be applied? Where should it be applied? And for how long? These questions define the position of the heaters and the assigned power cycles. The choice of materials also has an impact on the design but has to be defined in concordance with structural and aerodyamic loads.

As it involves many physical processes, the industrial design of such a system is very complex. To this day it relies heavily on costly experimental testing. However, numerical simulation could be a great asset during the design phase. Beyond the financial argument, numerical simulation gives access and control over many parameters and variables. It enables to investigate mechanisms possibly out of reach of experimentation. It can also be used to test many configurations before building a prototype and performing wind tunnel tests.

Computer simulation of icing is an area of active research and many research groups have developed numerical methodologies to investigate ice accretion and ice protection. Actual standards include for instance ONICE2D developed at ONERA and LEWICE developed at NASA Glen [147]. Nevertheless, due to the highly multidisciplinar nature of icing, state of the art codes do not include all the physical

processes. Indeed, one major blocking point is the prediction of ice shedding, that is to say the moment when the electro-thermal system manages to enable ice detachment. The modelling of this phenomena is at the moment highly empirical. It is however a key point in evaluating the performance of an ice protection system. Questions that demand answering are when does the ice break? How much detaches? What is the residual ice shape? The question of what is the trajectory of the ice block after it sheds is another one, and has received more attention due to certification issues.

There is therefore a strong need for a modular and flexible numerical simulation strategy for electro-thermal ice protection systems. The goal of this thesis is to set up and investigate the feasability of an eletro-thermal ice protection system simulation methodology which incorporates and couples heat transfer with phase change and mechanical modelling to predict ice shedding. In order to build such a tool several modules are developed.

The first chapter of the thesis presents the icing issue in its generality. Several technological aspects such as various ice protection systems, icing condition detection or flight testing are discussed. State of the art numerical simulation methods for icing are then presented. Based on this state of the art, the industrial context, goals and scope of the thesis are defined.

In the second chapter the thermal models and associated numerical methods are discussed. In this work, heat transfer is treated with the finite volume method. Heat transfer in the ice and in the system are treated seperately. Concerning the system, an automatic structured mesh generation tool is developed. The nature of the mesh enables to use a simple flux scheme to solve the heat conduction equation. Changes in material constants are naturally taken into account and a simple extension to incorporate imperfect contact between layers is also exposed. The heaters are taken into account by defining a mean density and specific heat in their neighbourhood. The applied power is translated into a local heat source equally distributed on each side of the heater. Concerning heat transfer in the ice the enthalpy method is exposed. This method is able to robustly capture the melting front in the ice. Given the fact that the ice block may have an arbitrary shape an unstructured mesh is used. Therefore in this case the numerical fluxes are formulated using a reconstructed gradient scheme. These two modules are then coupled using an explicit procedure. Both modules and their coupled functionning are validated against analytical solutions.

The third chapter deals with the modelling of fracture to predict ice shedding. The approach is quite general and based on recent modelling techniques. After a short state of the art, the model is presented and derived. The main idea is to spread the fracture on a given length scale l by introducing an additional variable d. The model is then formulated in a quasi-static frame thanks to three equations defining a history funtion, the variable d and the displacement field. For this module, a finite element procedure is chosen as implementation framework. Methods specific to the problem of constitutive modelling of fractured media are discussed. The model is then assessed on simple test cases.

The fourth chapter starts with a general literature review on the mechanical properties of ice. Although the problem is treated in the framework of continuum mechanics, a short discussion on the crystalline structure of ice can be found in the appendix. The presentation then moves on to more macroscopic features such as porosity and grain size, effect of wind speed and accumulation temperature. Aspects specific to the adhesion of ice on surfaces are also discussed. Very few laws exist to characterise the mechanical behaviour of ice. However, the experimental data gathered in this literature review provides empirical laws which will be used as a first approach. The parameters defining these laws are then identified using the mechanical model and recent measurements for atmospheric ice.

The fifth chapter aims at identifying and investigating possible ice shedding mechanisms. The hypothesised process is based on external aerodynamic pressure being redistributed inside the liquid water film formed under the action of the ice protection system. This can induce an uplifiting force on the ice block leading to its detachement. Four possible detachement modes are then presented: purely adhesive, purely cohesive, bulk failure or a combination of all four. An investigation of the bulk failure mode is then performed on two numerical test cases. The results tend to show the relevance of the mechanism. A parametric analysis with respect to grain size and porosity is also performed. After what a simple adhesive debonding model, based on the comparison of the local tangential stress with measured maximum adhesive stress is formulated. This serves to give a first approach to investigate

the possibility of purely adhesive debonding. Finally, the possibility of a combined adhesive/bulk failure mode is investigated.

The sixth and final chapter is concerned with the coupling of the previous models to formulate a general methodology applicable to industrial cases. The coupled numerical framework is first presented. Then a dry air test case is performed and numerical results are compared to experimental data. Sources of error are investigated at this point so as to identify important parameters. After what a delayed activation de-icing case is formulated. It is a situation were the system is activated after having entered icing conditions. It is therefore representative of a non nominal operating mode of the system. This test case serves to prove the feasability of the numerical simulation methodology. However it also points out some difficulties and helps to draw a way forward towards a more quantitative study of electro-thermal ice protection systems.

This chapter aims at providing the global context of this study. Some historical aspects are included in order to show the evolution of some technologies. However, a full historical review of icing research is out of scope and hence the chapter is not exhaustive. First, generalities about icing phenomena are presented. Next, some experimental and flight test procedures are described. The fourth section is devoted to a few icing condition detection and measurment methods. Several ice protection technologies are then presented. To conlude, state of the art 2D modelling for icing simulation is exposed as well as the context and scope of the thesis.

Contents

The phenomenon of icing is due to the presence in clouds (usually cumuliform or stratiform) of supercooled water droplets. When these droplets impact the surface of an aircraft, their metastable state is broken and they freeze, leading to ice accretion.

Almost since the beginning of powered flight, icing has plagued the aeronautical world. Up until the mid-1920's, pilots were lacking on board instruments and could difficultly fly without visual reference. They hence did their best to avoid flying through clouds and therefore icing conditions were but very rarely encountered [158]. However, it did not take long before aircraft icing was identified as a serious threat.

By the mid-1920's airmail pilots were regularly flying through icing conditions in order to maintain schedule [158]. Reports on incidents and accidents, particularly on the New York-Chicago airway, started to come in: "The advent of winter brings us the ice problem, which is probably our greatest one" [155]. Indeed, the accumulation of ice leads to an increase in mass, a degradation of aerodynamic performances and obstructed visibility, which in those early days of aviation meant a big deal of problems. This marked the advent of aircraft icing research.

Since those pioneering days, enormous progress has been made in the aeronautical industry. The technology related to icing issues had its fair share of innovations, and systems are still being invented and perfected to this day. Aircraft are now much more efficient and airworthy, and the early days may seem to be well behind. However, needless to say that the economic and industrial context is always pushing aircraft manufacturers to search for more and more advanced technologies, and ice protection systems are no exception.

1.1 Icing

Depending on the atmospheric conditions, different types of ice may grow. When temperature is well below the freezing point, the water droplets freeze immediately upon impact. The solidification process is so fast that air bubbles can even be trapped. This has the effect of creating an opaque, white, porous ice, which is called rime ice. As freezing occurs immediately, rime ice has a tendency to follow the shape of the airfoil. On the other hand, if the temperature is closer to the freezing point, only a part of the droplet freezes on impact. The other part remains free to runback along the surface and freeze later. As the freezing process in this case is less abrupt, it is rarely accompanied by trapping of air bubbles. The ice that forms is transparent and is known as glaze ice. Because of liquid water runback, glaze ice shapes are often complex and accompanied by the formation of horns.

(a) Rime ice shape   (b) Glaze ice shape
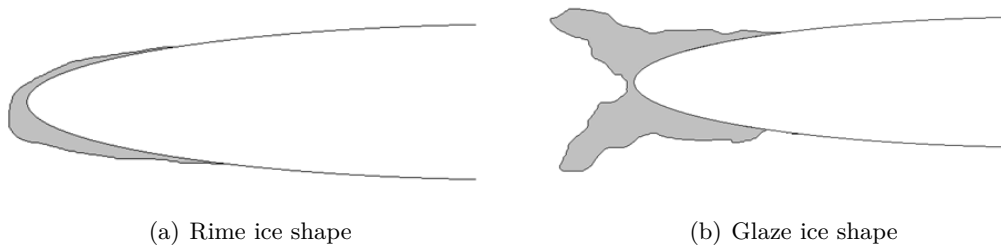
Figure 1.1: Rime and glaze ice growth

Icing conditions are usually defined by providing, in addition to the usual aerodynamic conditions (freestream Mach number, temperature and pressure), the MVD (Median Volumetric droplet Diameter) and LWC (Liquid Water Content). The LWC is the amount of water contained by unit volume in a cloud and has the unit $kg.m^{-3}$. The MVD is relative to a droplet size distribution. It is defined as the droplet diameter which divides the water volume in half, half the volume is in droplet sizes larger than the MVD and half the volume is in droplets sizes lower than the MVD.

It is interesting to note that a specific type of ice growth occurs under swept wing aerodynamics, due to three dimensional effects. In this case ice may grow to form a scallop shaped topology, as sketched figure 1.2.
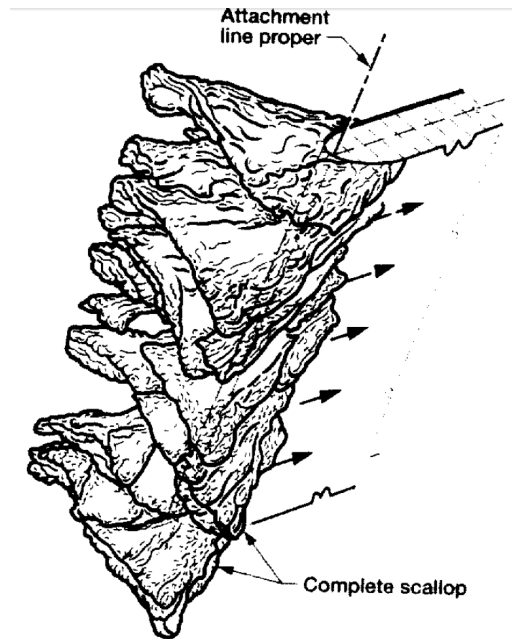
Figure 1.2: Scallop type ice shape formation on swept wings [97]

Icing has many undesirable effects. One immediate effect is the increase in mass due to the ice deposit. However, this effects is secondary in consequences compared to other effects. Indeed, ice accretion also has a very negative effect on aerodynamics, therefore imparing the performance and handling qualities of the aircraft. For example, as shown in figure 1.3, the presence of ice reduces lift and stall angle. Ice may also accumulate on air intakes causing loss of thrust and possible flameout by ingestion of ice blocks.
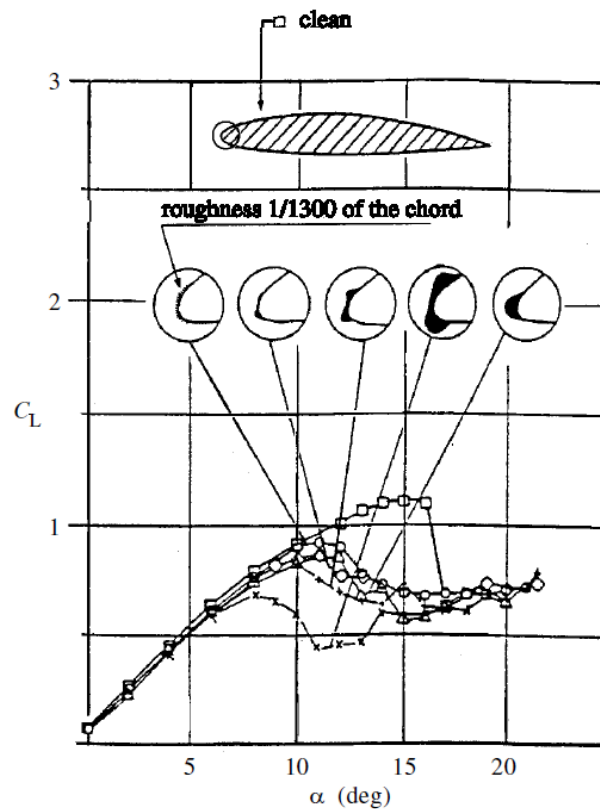
Figure 1.3: Effect of Various Ice Shapes on Lift [121]

Aircraft manufacturers must therefore comply with airworthiness standards relative to icing, which

are defined by appendix C of JAR/FAR 25 for large aircraft. Appendix C defines flight envelopes and icing conditions in which an aircraft must safely fly. The maximum continuous envelope is mostly relevant to stratiform clouds due to their large horizontal extent and lower liquid water content. On the other hand, the maximum intermittent envelope essentially concerns cumuliform clouds due to their large vertical extent and higher liquid water content.
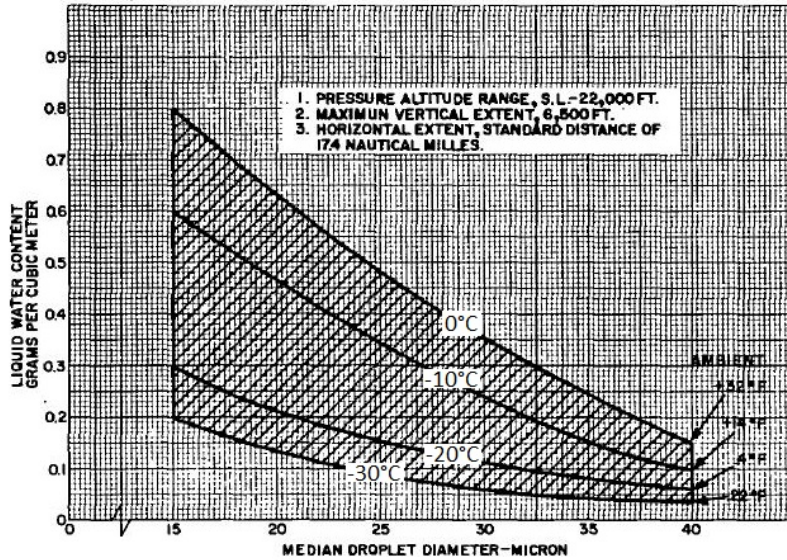
Figure 1.4: Flight envelope for maximum continuous icing certification
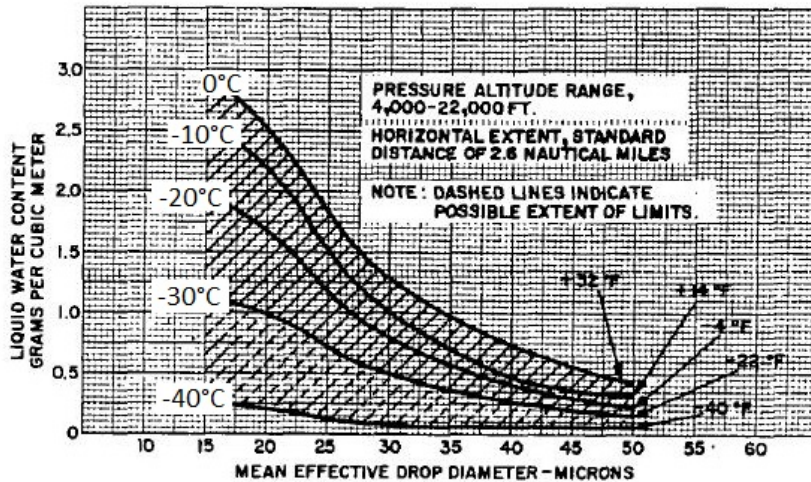
Figure 1.5: Flight envelope for maximum intermittent icing certification

One may note that the droplet size limit of appendix C is $50\mu m$. However, this limit can be exceeded due to the presence of SLD (Supercooled Large Droplets). These droplets present complicated physics with respect to impact such as splashing, deposition or bouncing (see figure 1.6). SLD also have a tendency towards more ballistic trajectories, and therefore may impact beyond the area protected by an ice protection system, making them particularly threatening to aircraft safety. An extention to appendix C flight envelopes is hence planned for the comming years.
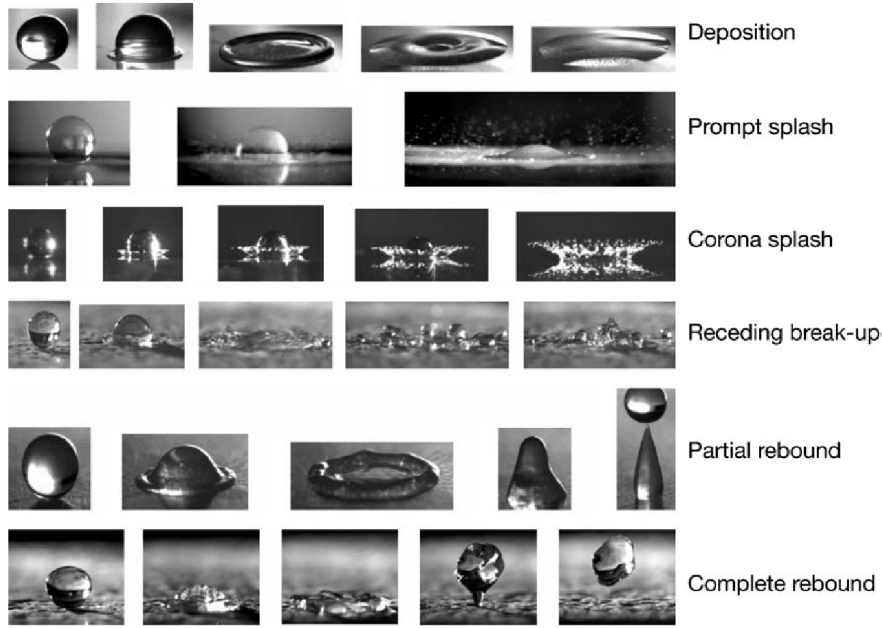
Figure 1.6: SLD impact regimes [54]

1.2 Experimental Procedures

1.2.1 Icing Wind Tunnels

In order to investigate icing phenomena and ice protection systems, wind tunnel tests are the intermediate step between computation and flight tests. The general architecture of an icing wind tunnel includes classical wind tunnel components, a water droplet spray generator and a heat exchanger to generate a supercooled state (see figure 1.7).
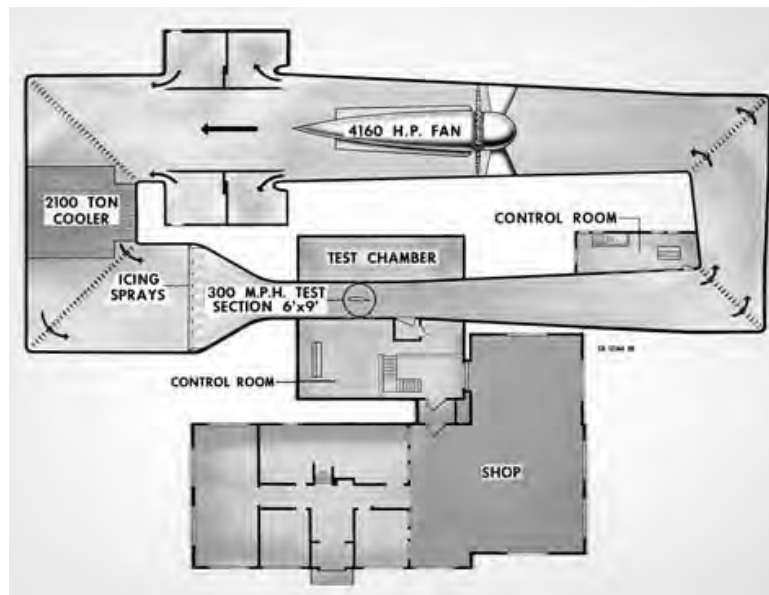
Figure 1.7: General Architecture of an Icing Wind Tunnel (NASA IRT)

Icing wind tunnels have been used over the decades for a vast number of studies, including ice accretion on various aeronautical objects, ice protection assessment, aerodynamic performance degradation, etc.

1.2.2 Articifial Ice shapes

The study of aerodynamic degradation may not only be conducted under icing conditions. In effect, some investigators have used simulated artificial ice shapes. This method enables better control over the ice shape, although sometimes very idealized. As early as the 30's, wind tunnel tests were conducted to study the aerodynamic effects of ice remaining on the wing in spite of de-icing boots activation [16]. To do so, a mixture of crushed slag and tar was applied to a strip of cloth and attached on the airfoil (see figure 1.8).
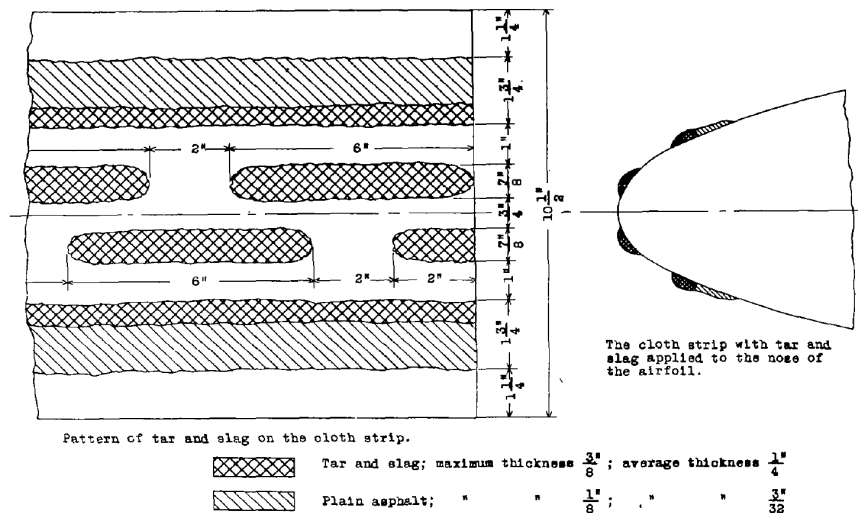
Figure 1.8: Simulated ice shape arrangement [16]

Other investigations involved a more controled and geometric approach [53]. Several generic idealized ice shapes were defined and placed on an airfoil according to several parameters (see figure 1.9).
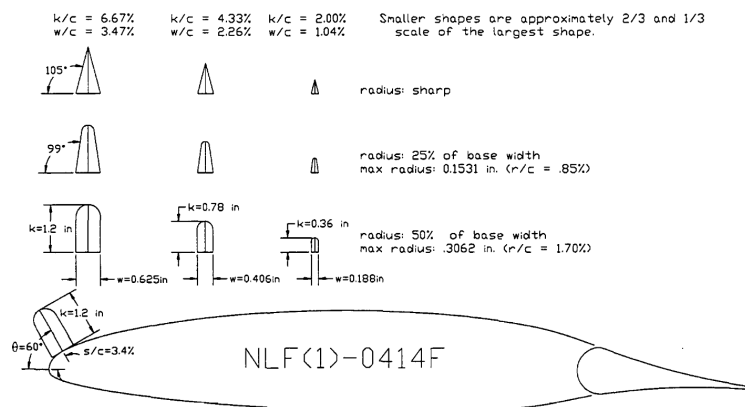
Figure 1.9: Generic idealized ice shape arrangements [53]

In more recent studies, realistic ice shapes were built and fit to a reduced scale aircraft in order to study the resulting aerodynamics. The ice shapes were placed on the wings and tail planes (example shown on figure 1.10) .
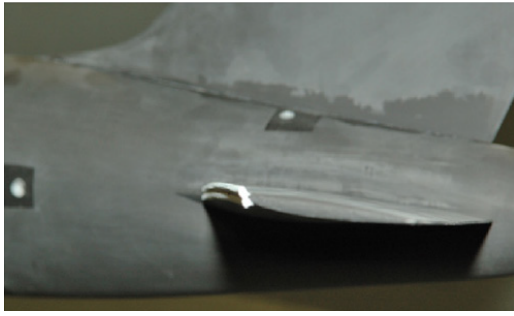
(a) Tail plane ice shape arrangement on reduced scale aircraft
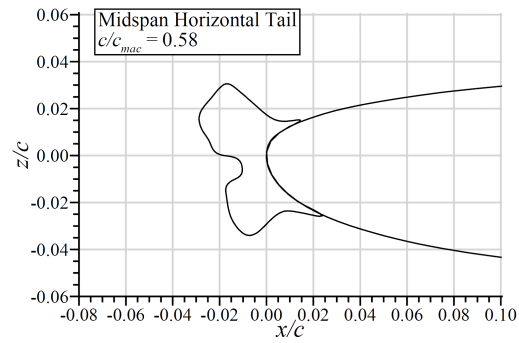
(b) Tail plane ice shape profile

Figure 1.10: Tail plane ice shape for aerodynamic study on reduced scale aircraft [6]

In a general way, the aerodynamic degradation usually presents itself in the form of increased drag, decrased lift slope and maximum lift and presence of separation. The amount of degradation may vary depending on the ice shape.

1.3 Flight Tests

The assessment of airworthiness and ice protection system performance in realistic icing conditions ultimately requires flight tests. In the early days this was achieved by either directly flying through icing conditions, or by integrating a prototype to a flight test aircraft. The latter possibility also included a water spray generator in order to simulate icing conditions (see figure 1.11).

Figure 1.11: Flight Test Apparatus for Vapor Heating Boiler System [138]

In a similar fashion as wind tunnel tests, one way of investigating in-flight icing is to attach artificial ice shapes to critical lifting and control surfaces. A recent example (see figure 1.12) used such a method to study the effects of different ice shapes on the aerodynamics of a business jet aircraft. The results were then used for flight simulation modeling [136].

(a) Lower runback ice shapes and horns

(b) Upper runback ice shapes and horns
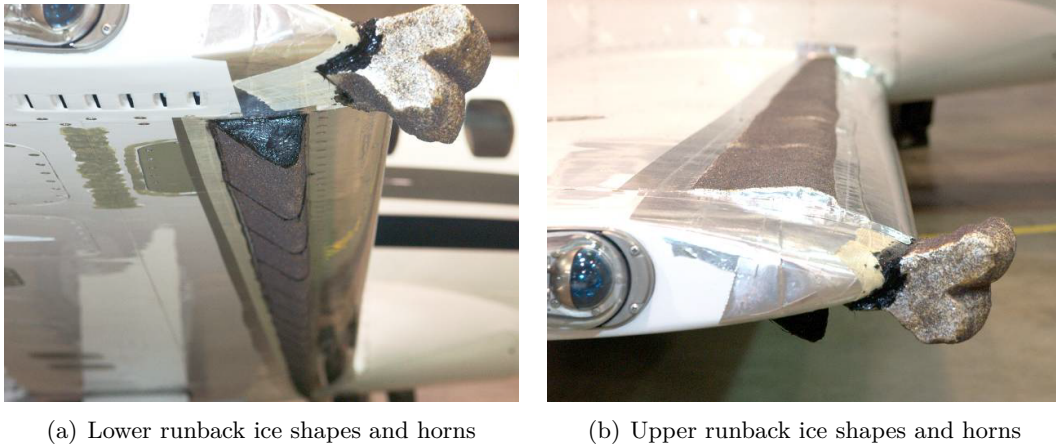
Figure 1.12: Simulated ice shapes for flight testing [136]

More modern methods involve the use of a spray rig, either placed on-ground (figure 1.13) or carried in-flight by an other aircraft (figure 1.14), to generate the icing conditions in which the aircraft is to be tested. These methods are the most costly and complex to perform.
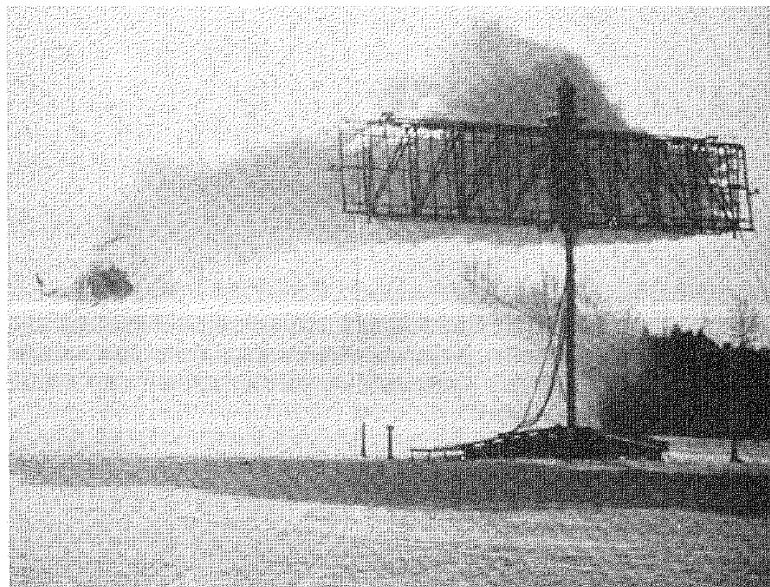
Figure 1.13: On-ground spray rig for helicopter icing studies [113]

Figure 1.14: USAF KC-135 tanker generating water spray for icing tests

1.4 Detecting/Measuring Icing Conditions

1.4.1 In-Flight Detection and Measurement

During flight, especially during night or in poor visibility conditions, it is important to provide the flight crew with information on possible icing conditions. To this end, several concepts have been proposed over time. One of the first ideas was to use a pressure differential probe, as sketched on figure 1.15. When icing conditions are encountered, the holes on the ice collecting elements clog and a pressure differential between the iced and ice-free probes is created. This activates an electric heater that de-ices the ice collecting probe which then re-equalizes pressures and cuts off the heater. This process then becomes cyclic and the activation times provide a measure of the severity of the icing conditions [108].
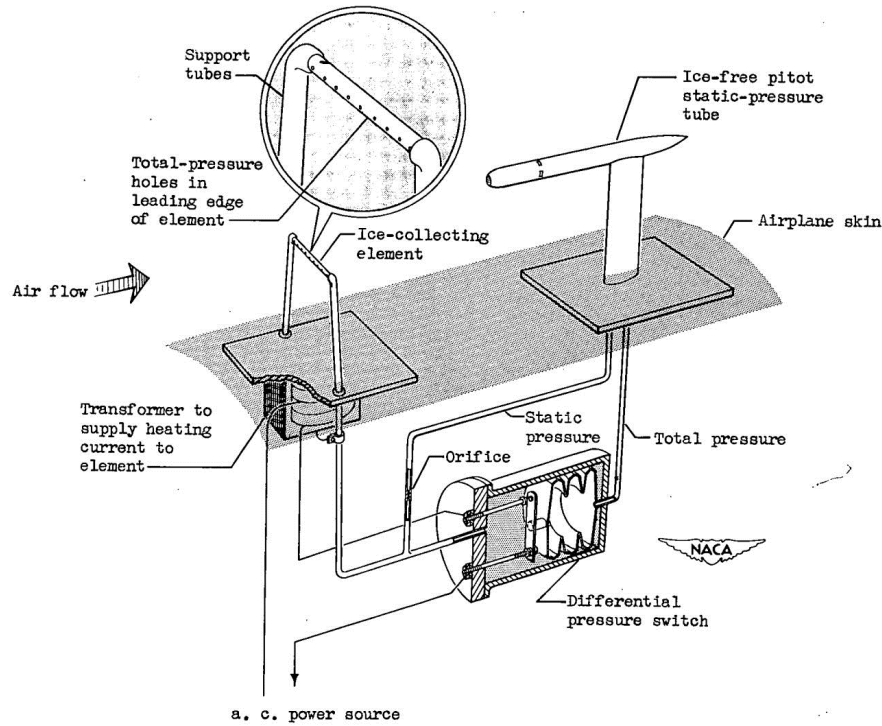
Figure 1.15: Architecture of a Pressure Differential Icing Condition Detector [108]

A more recent kind of system is the magnetostrictive ice detector. It consists of a high frequency vibrating probe and works in a cyclical fashion, similar to the pressure differential probe. When icing conditions are encountered ice starts to accumulate on the probe. This added mass changes the vibration frequency and enables icing condition detection. In the same way as the pressure probe system, a heater is then activated to shed the ice off the probe. Once the nominal frequency is attained the heaters are deactivated and a reassessment of icing conditions is possible [27].
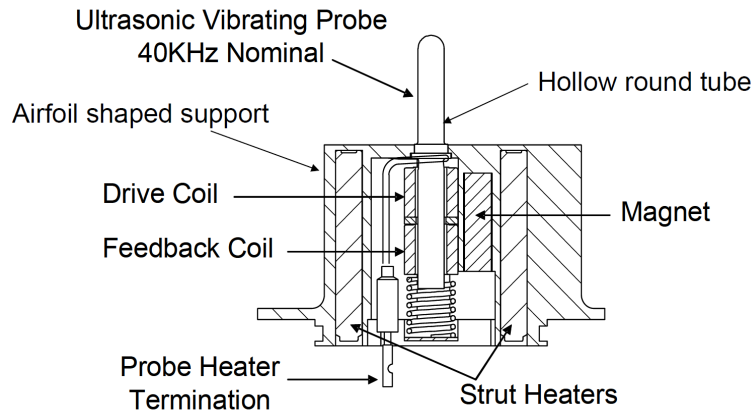
Figure 1.16: Magneto-Strictive Icing Condition Detector [27]

For in-flight icing investigations and analysis the knowledge of atmospheric conditions such as liquid water content or droplet size is essential. One of the early techniques for determining liquid water content, droplet size distribution and mean volumetric diameter was the rotating multicylinder method [112]. It is based on the idea that cylinders of different diameter will accumulate different quantities of ice. A theoretical analysis is first conducted to determine water droplet impingment characteristics on a cylinder of a given diameter D. The experimental method then consists of the following steps:

1. Expose a set of rotating cylinders to icing, in known aerodynamic and thermal conditions, for a given amount of time. An example of cylinder set is shown figure 1.16.

2. Disassemble the set and store the cylinders in individual containers. Deduce the amount of ice accumulated on each cylinder by weighing the containers.

3. Determine icing conditions by matching the measured data with theoretical computations.
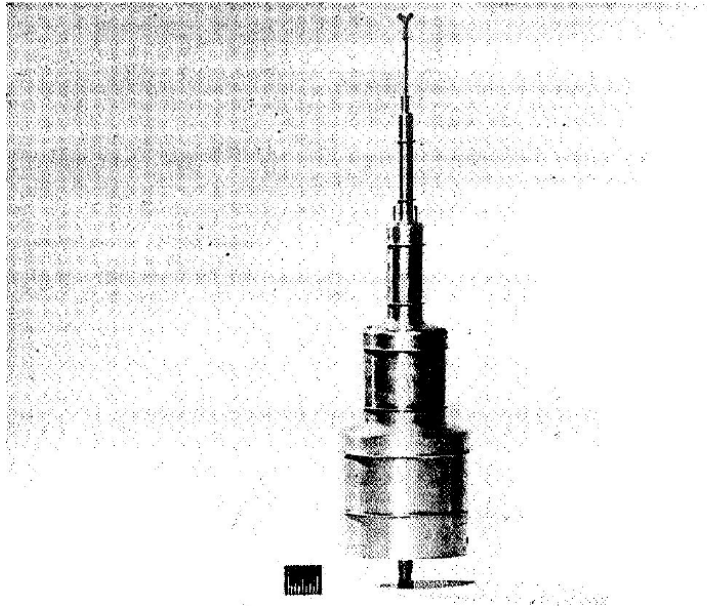
Figure 1.17: A multi-cylinder set [112]

This method had several known drawbacks, especially linked to droplet size determination, but it was considered as the most reliable at that time. As we shall see in the following section, newer, more elaborate methods are now being priviledged.

1.4.2 Remote Sensing

At present, active research is being conducted on remote sensing of icing conditions [21, 8]. As an example, recent work conducted by NASA investigates two systems. The first one is based on three subsystems:

1. A microwave radiometer, which measures integrated water content, atmospheric water vapour and temperature profile.

2. A laser ceilometer to detect the lower boundary of the cloud

3. A radar which captures cloud boundaries using reflectivity measurments in combination with the ceilometer data.

Liquid Water Content can then be deduced from the measurement of integrated water content and cloud geometry. Combined with reflectivity measurments, this information yields the droplet size distribution. Temperature, LWC and droplet size are then used to define the severity of the icing conditions.

1.5 Ice Protection Systems

At the end of the 1920's, icing had been identified as a serious threat that needed to be dealt with. Nevertheless, the rudimentary state of ice protection technology at the time left investigators to conclude that "safety, therefore, obviously lies in avoidance" [133]. Various ice protection concepts were rapidly thought up and perfected through the decades. Nowadays, as stated previously, aircraft manufacturers must comply with certifications and regulations regarding flight safety in icing conditions.

Over the years, many concepts have been proposed, improved, analysed and tested. During the design of an aircraft, engineers now have a very large choice of ice protection technologies. However, each system has its pros and cons, and will usually be best suited for a specific type of aircraft.

To sum up, ice protection systems come in three different categories :

- Chemical: systems based on chemical compounds may be either passive or active. In the passive case, an icephobic or water repelling coating is applyied to the critical surface. In the active case, anti-icing fluid is injected through a porous surface in order to prevent the formation of ice.

- Thermal: the system provides heat to the critical surface which either prevents the formation of ice (anti-icing) or removes ice by cyclic operating (de-icing).

- Mechanical: the system removes ice by surface deformation (only works in de-icing mode).

There are two operating modes for ice protection systems. Depending on the system, only one mode may be used or both.

- Anti-icing mode, which is fully evaporative or running wet, hence not allowing ice to form.

- De-icing mode, in which ice is allowed to form. The protected surface is then cleaned from ice by a cyclic activation of the system.

The following sections describe several examples of these systems starting with the original idea and then succinctely presenting its evolution.

1.5.1 Mechanical

1.5.1.1 De-Icing Boots

The pneumatic de-icing boots was probably the first fully operational ice protection system. The system has its origins in the early 30's. Tests were being conducted to study the effectivness of coated rubber sheets in preventing the formation of ice. Although ice accretion was reduced, ice eventually was able to accumulate. A means of removing this ice was necessary. To do so, B. F. Goodrich in cooperation with NACA, proposed to inflate the rubber sheet. The deformation would break the bonds at the ice/sheet interface and ice would subsequently be blown away by aerodynamic forces [151].

(a) Boots Deflated   (b) Boots Inflated
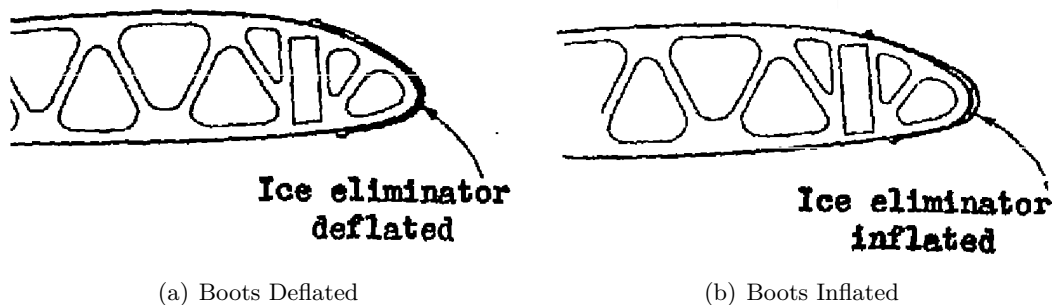
Figure 1.18: De-Icing Boots [151]

A former airmail pilot and an engineer were assigned the task to perform the first flight tests. While the pilot would fly through icing conditions, the engineer, sitting in the mail compartment, would inflate the boots using a bicycle pump [158]. These tests, although seemingly very rudimentary, proved the effectivness of the concept. So much that by 1932 the system was fully industrialised and adopted by many airline companies.

Clearly, the pneumatic de-icing boot system dominated the 30's. Nevertheless, this system was far from being fail-safe. There were reports of ice detaching from the propellers and cutting the rubber

sheet. Also, when approaching certain snow clouds, sparks caused by electric discharge had been observed to puncture the boots [25]. Finally, it was also reported that in some cases inflation of the de-icing boots would break the ice but fail to remove it [75, 25]. These drawbacks left the door open for other systems to develop.

A pulsating version of this system has also been developed [135]. The idea is to lay spanwise several inflatable tubes. By rapid pressurization, the system creates a longitudinally travelling shock wave inducing expansion of the tubes and shedding (see figure 1.19(b)). This device is called the Pneumatic Impulse Ice Protection system (PIIP).

(a) PIIP sketch
(b) PIIP operating principle
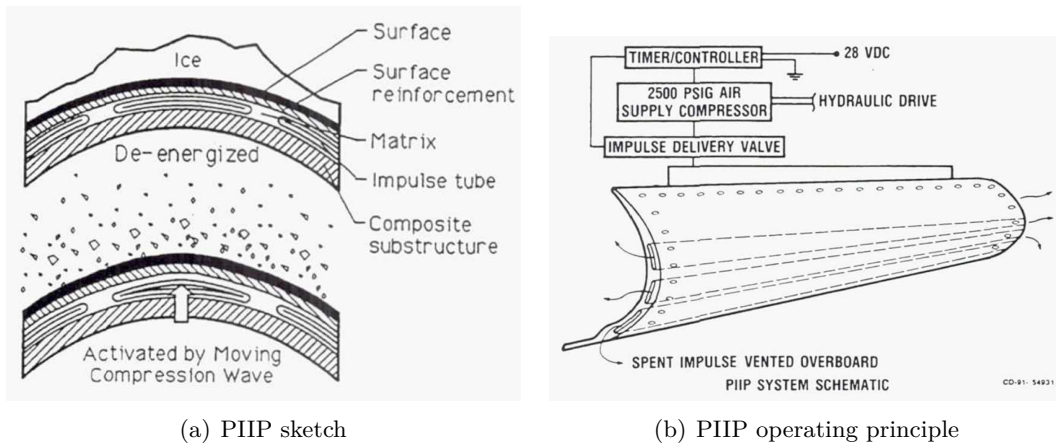
Figure 1.19: B. F. Goodrich Pneumatic Impulse Ice Protection system [135]

The pneumatic boot system has been perfected over the decades and is still in use at present times. Nowadays its main application may be found in small commuter aircrafts such as A.T.R.

1.5.1.2 Electro-Mechanical Systems

The basic strategy behind electro-mechanical systems is to feed a skin deforming device with high current pulses. There are two main architectures for this concept, electro-expulse and electro-impulse.

The Electro-Expluse De-Icing system consists in two layers of conductors, one being stationary while the other is allowed to move. It is embedded in an elastomere nylon composite matrix constituting the protected outer skin. When the system is activated, a high current pulse is delivered to the conductors in opposite directions, inducing a repulsive force. The mobile layer is then abruptly pushed up and the outer layer is deformed, hence breaking the ice that may have accumulated on it.
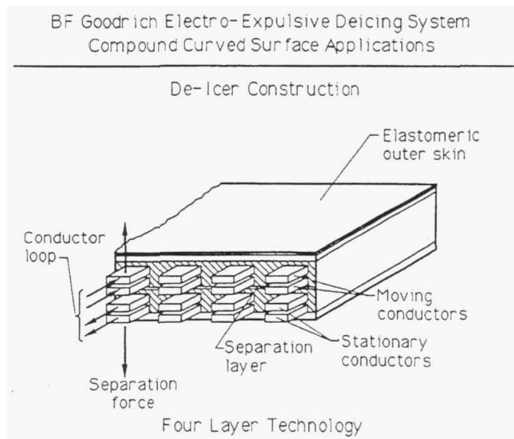
(a) B. F. Goodrich EEDI operation principle [45]   (b) Experimental operation example
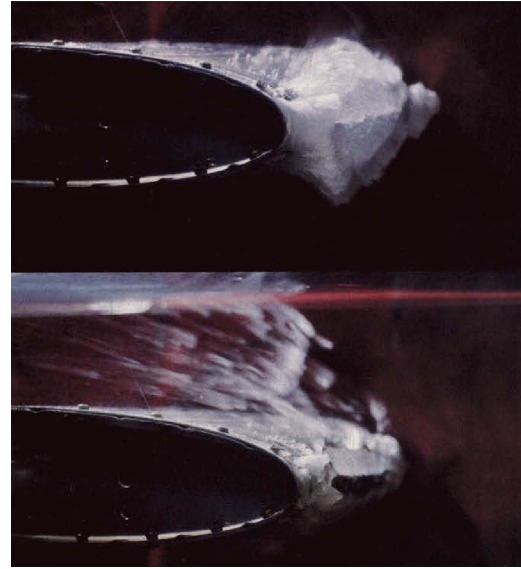
Figure 1.20: Electro-Expulse De-Icing mechanical system

The idea of Electro-Impulse De-Icing is to place coils made of copper ribbon wires beneath the protected surface. These coils are fixed and fed through a capacitor discharge. This creates, for an extremely short time lapse, a repulsive force between the surface and the coil. The small amplitutde and high acceleration deformation of the surface then acts to shed the ice [45].
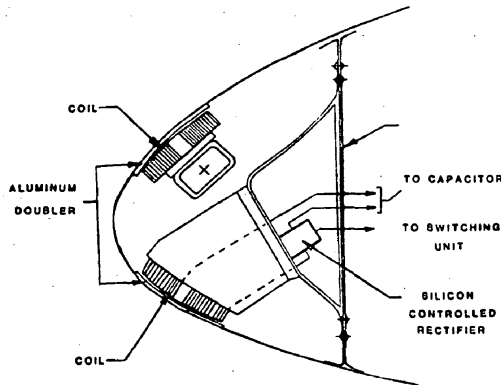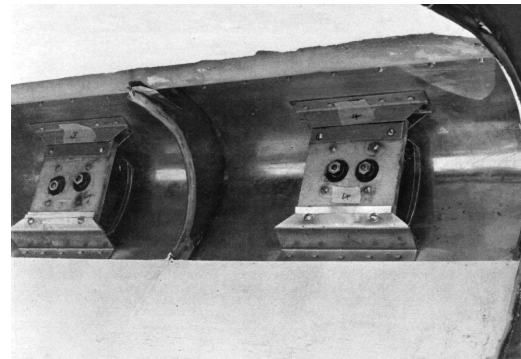
(a) EIDI sketch   (b) System placed inside leading edge for testing

Figure 1.21: Electro-Impusle De-Icing mechanical system [45]

Another system which may be included in the group of electro-mechanical functioning is the ultrasonic shear wave ice protection system. This system uses electromagnetic transducers to generate shear waves at the interface between ice and protected surface. The horizontal shear waves produced in this manner create sufficient interfacial stress to lead to ice shedding [105].

1.5.2 Thermal

The idea of thermal ice protection systems is to provide heat to the critical surface. This has the effect of either preventing ice formation by rendering the surface evaporative or running wet. Or, if ice accretion is allowed by the system, the heat then serves to melt some of the ice at the ice/critical surface interface. This will reduce the ability of ice to adhere to the surface and it will subsequentely be detached by the aerodynamic forces.

One problem that may arise with thermal systems, and which was observed as soon as they were first developed [132, 133], is the formation of runback ice in running wet mode. When such a system

is active, the water will indeed not freeze on the protected surface, but it may stream down beyond this region and then freeze, giving birth to ice formation such as that on figure 1.22. Such a situation may be accentuated in SLD icing conditions (that is to say involving Supercooled Large Droplets). Runback icing is therefore an important aspect of icing research and is taken into account during the system design phase to prevent it.
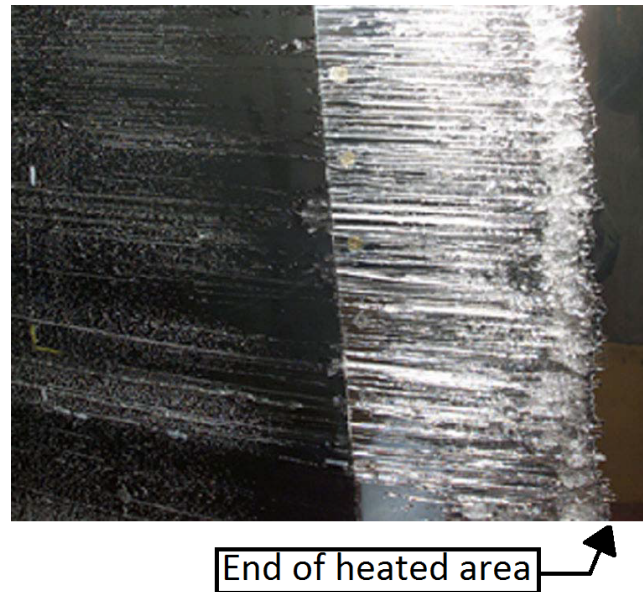
Figure 1.22: Example of runback ice formation due to thermal ice protection [141]

1.5.2.1 Hot Air Systems

The idea of using heat from the exhaust gases had originally been proposed since the late 1920's [132, 133]. Nevertheless this concept had several drawbacks. Firstly, it required knowledge about the heat effectively available and a better understanding of how it should be distributed to the various surfaces. Secondly, concerns about the corrosivness of the exhaust gases (later confirmed [41]) meant that they could not simply be circulated inside the wing. The industrialisation of the system at the time seemed complicated and doubts were at first emmited as to its ability to fully heat a whole wing and prevent runback icing [151]. In order to assess this concept, theoretical and experimental aspects of heat transfer on airfoils were investigated. This enabled the prediction of the amount of heat necessary to protect the airfoil from icing. The use of a vapor heating system using a boiler in the exhaust pipe was then proposed [138], as illustrated figure 1.23. Flight tests were conducted by placing a model wing and the boiler on a Fairchild monoplane. The main finding was that more than enough heat was available in the exhaust gases to prevent ice formation. It can be noted that the idea of using an electrical heating system was mentionned but was deemed as having too many drawbacks in terms of weight and efficiency.
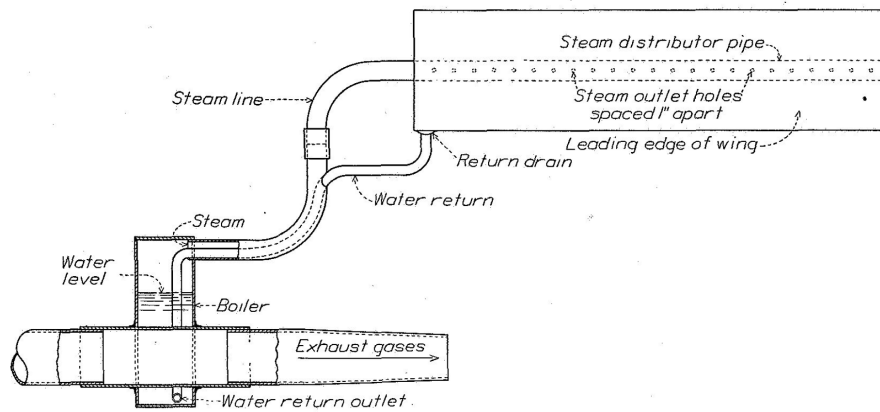
Figure 1.23: Vapor-Heating Boiler System [138]

Although these first results were promising, the full industrial application of the system required improvements and an integration at the construction stage. The remaining problem was to adequately distribute heat to the protected surface [75]. A preliminary study was conducted at the end of the 30's, but the full investigation of the potential of this system would be done during the 40's.

Improvement of exhaust thermal anti-icing systems essentially required better heat distribution architectures. Jurgen Ju-88 aircrafts were equipped with quite advanced hot air ice protection systems for the time. They were based on recovery of heat from exhaust gases through heat exchangers (such as the one illustrated figure 1.24). Hot air would then be circulated through the wing span to bring it to sufficient temperature [77].
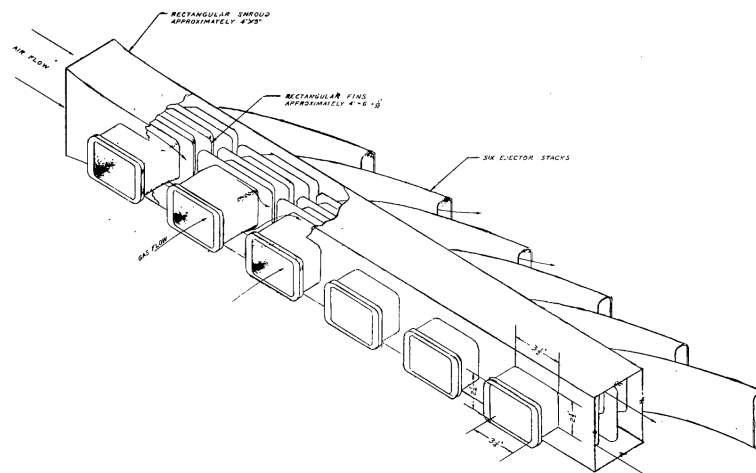
Figure 1.24: Jurgen Ju-88 Heat Exchanger [77]

Based on this design, the system was put through thourough testing by NACA. A first design analysis was held to define the architecture to be studied. It was then installed on a twin engine C-46 cargo airplane so as to investigate heat requirements, design, installation and performance in dry air and icing conditions. The goal was also to evaluate aerodynamic performance loss due to integration of the system in the airframe. Material fatigue due to thermal stress and corrosion effects were also investigated [7]. The ice prevention performance of the system was reported to be satisfactory, all protected surfaces conserving their function and no corrosion effects being observed. However, installation of the heat exchanger in the nacelle had to be considered at an early design stage in order to reduce the loss in cruise performance and effects of thermal stress due to temperature gradients were also noted.

The 40's also saw the advent of the turbojet engine. In severe icing conditions, ice could accrete at the compressor inlet, reducing thrust and even in some cases rendering the engine inoperative. The need for a means of ice prevention lead to the design of the bleed back hot gas system. In order to protect the compressor inlet from ice formation, hot air was bled from the turbine inlet and reinjected
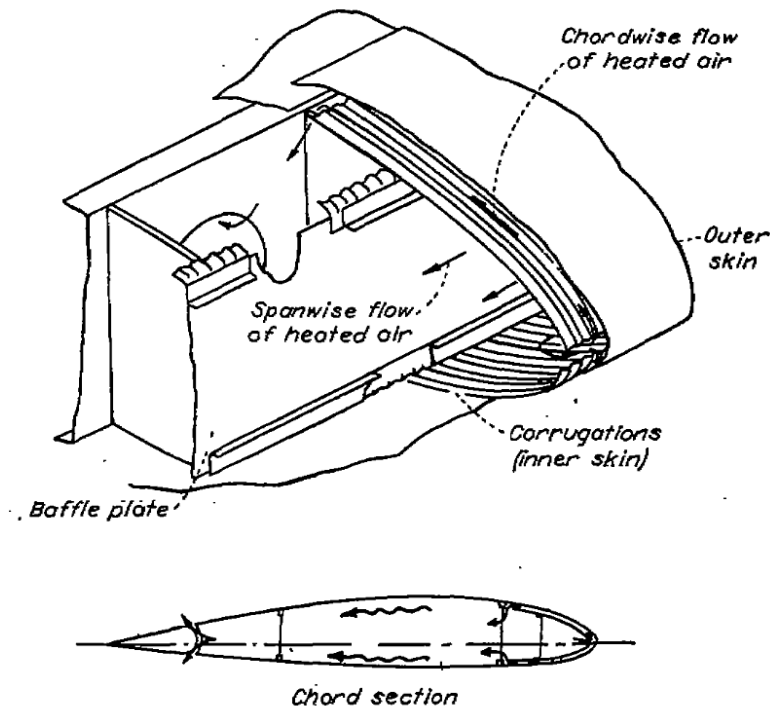
Figure 1.25: Structural integration of thermal ice protection system [7]

upstream of the compressor intake (see figure 1.26) [146]. Although resulting in a reduction of net thrust, the system successfully provided ice protection of the compressor inlet. However, one main drawback was ice shattering against the compressor inlet guide vanes subsequent to de-icing, which could lead to damage on first stage rotor blades or to combustion blow out.
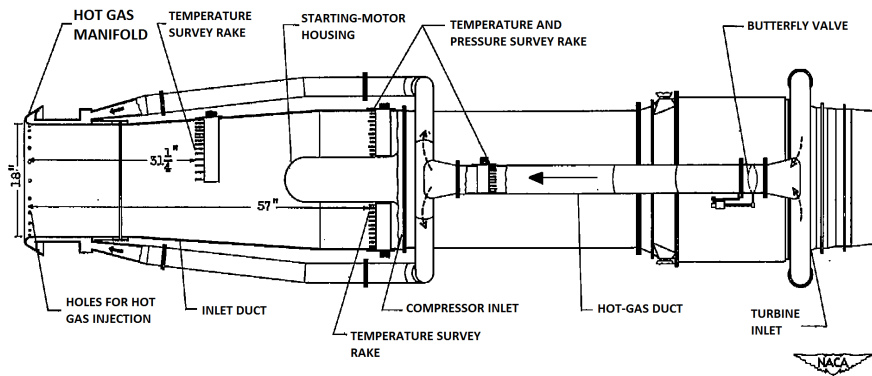
Figure 1.26: Hot air bleedback system [146]

With the turbojet engine also came high altitude and high speed flight. Studies showed that the heat required for continuous anti-icing of large critical surfaces could become very large, and even prohibitive, for such aircraft [134]. In order to reduce the energy penalty required by thermal systems, investigation began on cyclic de-icing. One concept was to use cyclically distributed heated gas. Preliminary investigation involved a three compartment wing section. Hot gas was distributed to each compartment intermittently. For this design, a parting strip (that is to say an area which is constantly protected from ice build up), produced by hot air, was found necessary for efficient ice removal [145].

In its present form (see figure 1.27), hot air ice protection is widely used in aeronautics in the form of the so called bleed-air anti-icing system. Hot air is extracted from a compressor stage and distributed to the critical surface by a picolo tube. It equips most of the large aircraft for wing and nacelle anti-icing.
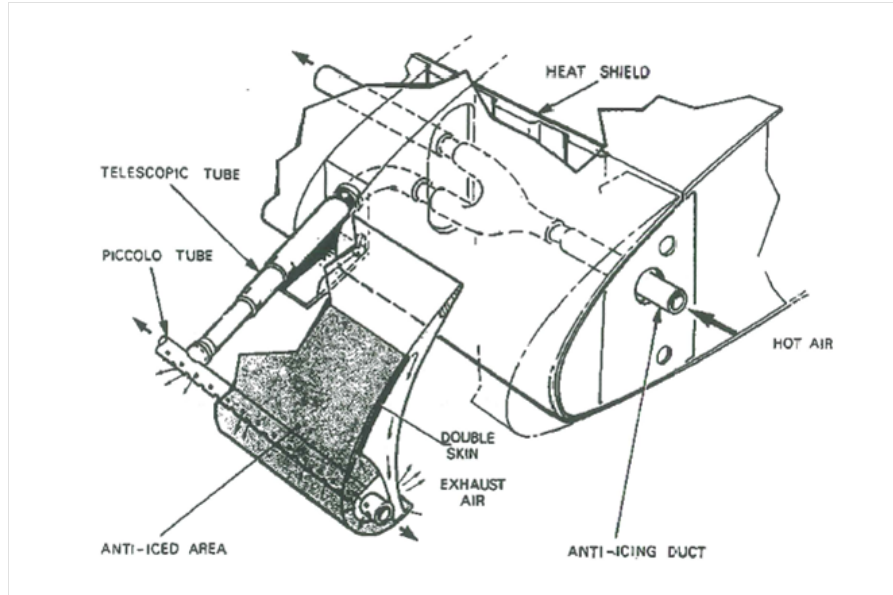
Figure 1.27: Architecture of a modern bleed air system

1.5.2.2 Electro-Thermal

The first investigation of an electro-thermal ice protection system goes back to the mid-30's [25]. The idea is to integrate electrical heating elements into or onto the surface that one wishes to protect. These heating elements then provide the energy to either operate in anti-icing or de-icing mode.

Early examples include two designs that were applied to propeller blade protection. The first one consisted in a neoprene shoe moulded with internal wires. The second design consisted in an outer layer of conducting material and an inner layer of isolating layer. Current was supplied to the outer conducting layer via two copper leads. The system provided an acceptable ice protection method. However, this concept had a major drawback. Alhtough being itself lighter in weight, the electro-thermal system required a heavy weight electrical generator [119, 120, 62].
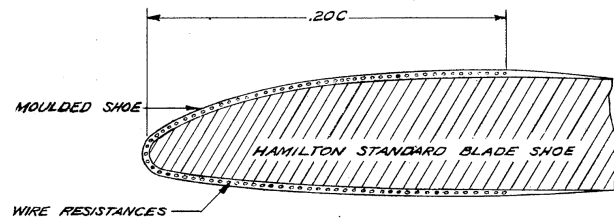
(a) Design based on wire resistances
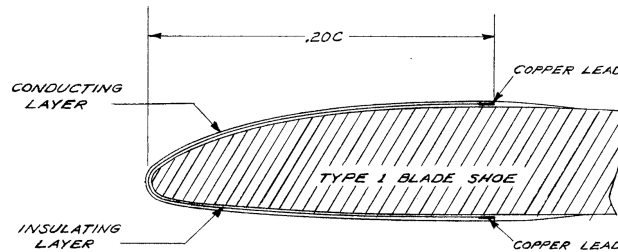
(b) Design based on conducting layer

Figure 1.28: Propeller electro-thermal ice protection shoes [120]

The arrival of turbojet engines also had its effect on electro-thermal technology. Due to the close spacing and motion between rotor and stator, mechanical abrasion would limit ice formation in the

initial compressor stages. Icing of this component was therefore deemed secondary. However, the inlet guide vanes were a more critical components. Icing of inlet guide vanes would seriously affect engine performance. An ice prevention method using electrical heaters was investigated. The heating element consisted of nichrome wires encased into glass cloth and having a hairpin shape [140]. It was shown experimentally that power requirements could be significantly reduced, while maintaining ice protection, by operating the heaters in a cyclical activation mode.

As stated in the previous section, cyclic de-icing presented significant advantages at the time regarding ice protection in high altitude and high speed flight. Therefore, in this context electro-thermal architectures were also investigated. The heating elements consisted of nichrome strips and were placed spanwise with very little spacing. The strips were integrated into a piling of glass cloth and neoprene. The use of a parting strip was found necessary for quick and complete ice removal. High local power densities and short cycles were also found to give best results. Moreover, attaining the melting temperature at the surface was insufficient to ensure ice removal. Peak temperatures of $10\text{-}35°C$ were found necessary for complete ice removal.
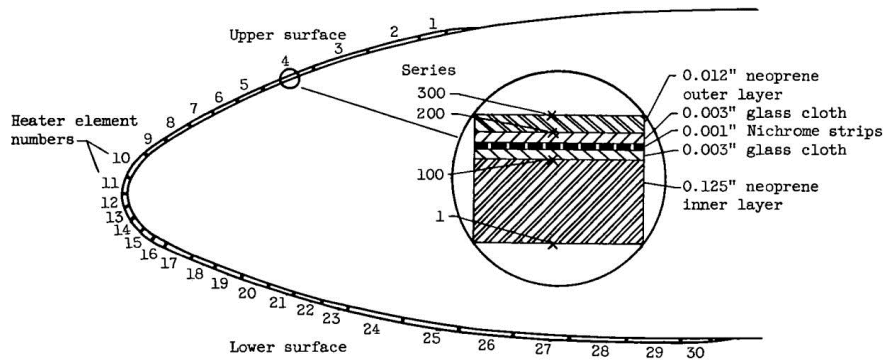
Figure 1.29: Electro-thermal system [65]

The architecture of an ETIPS usually involves a multi-layered stack of materials. Each stack may differ in material properties and thickness depending on the design and applications.

The operating of a modern electro-thermal ice protection system in de-icing mode is illustrated on figure 1.30. A parting strip (here heater C) is held active during the whole cycle. The remaining heaters are activated according to a defined cycle. This acts to create a liquid water film at the interface between ice and protected surface, hence reducing the ice's ability to adhere to the surface. Once a critical amount of water film is formed the ice block is shed under the effect of aerodynamic forces.
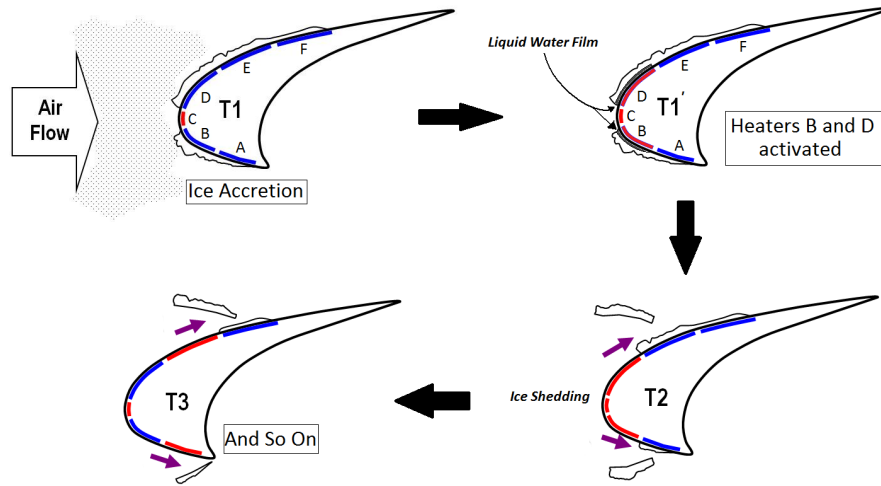
Figure 1.30: Operating of an electro-thermal system

1.5.3 Chemical

1.5.3.1 Passive Coatings

At the end of the 1920's, a refrigerated wind tunnel had been built by NACA. One of the first investigations to take place in this facility was the study of various coatings [92]. The tested substances were of two types: soluble in water and insoluble in water. It was believed that ice formation would be prevented by soluble compounds by lowering the freezing point of water and by insoluble compounds by repelling water. However, insoluble compounds proved to be totally uneffective. Soft soluble compounds were blown away from the leading edge and were therefore uneffective. Hard soluble compounds proved to be effective only within a certain temperature range [92]. This research marked the begining of a still very active branch of ice protection technology.

The fundamental idea is to cover the surface to be protected in order to prevent ice formation or to enhance the performance of the anti/de-icing system. There are two main categories of modern coatings for icing problems : icephobic and superhydrophobic. However these coating strategies cannot be standalone solutions to the icing problem and would have to be combined with other solutions [18].

On icephobic coatings ice adhesion strength is reduced making it easier for accreted ice to be shed. The two main qualities required for an icephobic coating are high ice adhesion reduction and high durability [22].

Investigations of ice adhesion reduction conducted in the 40's showed that although ice always adheres to a surface, its adhesion strength can be reduced by treating the surface with silicone. However every successive ice removal also tears a certain amount of silicone from the treated surface, thus decreasing the efficiency of the surface treatment [79]. Also it was found that there was a poor correlation between low ice adhesion and hydrophobicity. Further investigations were conducted during the 60's but it was found that, for durability reasons, coatings did not appear to have sufficient potential.

Later, NASA and BFGoodrich resumed these studies [12]. The conclusion was that the amount and shape of accreted ice was independent of the coatings tested. The surface properties had an effect on runback and water beading but as soon as a layer of ice was formed ice would subsequently grow on it making the coating ineffective. It was reported that although ice adhesion to greased surfaces was almost zero the ice block was held in place by aerodynamic forces and thus accreted normally. It was noted here also that hydrophobicity did not necessarily produce icephobicity.

Tests were also done at AMIL (Anti-icing Materials International Laboratory) in 2002 where seven different coatings were tested [22]. The ice was accumulated by simulating freezing drizzle conditions. None of the coatings reduced the amount of ice that accreted on the surface and best results were obtained with a compacted powder (adhesion reduced by 37%) but this performance was not enough

to enable natural ice shedding. Moreover, gradual degradation of the coated surface with successive ice removals was once again observed.

More recently icephobicity and durability of rough hydrophobic surfaces was tested [126]. The surfaces where either based on a fluoropolymer injected with TiO_2 nanopowder or an etched aluminium aloy substate that would be subsequently hydrophobised via treatment with an organosilane monolayer. Glaze ice was accreted on the surfaces in order to simulate atmospheric conditions. The results showed that although they have good ice releasing features, superhydrophobic fluoropolymer coatings have durability issues and their performances degrade with each de-icing cycle. As for the etched aluminium aloy, it maintained its ice-releasing performances throughout the tests but its adhesion strength was comparable to that of mirror polished aluminium.

As for superhydrophobic coatings, the idea is to prevent the ice formation by eliminating as much liquid water as possible before it freezes. The wettability of a surface is usually determined by the contact angle that forms at the interface between the surface and a water droplet. Moreover the droplet may have advancing and receding contact angles, thus defining the advancing-receding angle hysteresis $\Delta\theta = \theta_a - \theta_r$(angles defined as in figure 1.31). For contact angles $> 90°$ the surface is considered hydrophobic. Superhydrophobic coatings are defined by high contact angles ($> 150°$) and by a low advancing-receding angle hysteresis ($< 10°$) [123].
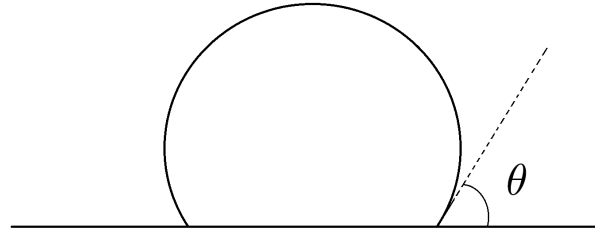
(a) Static contact angle
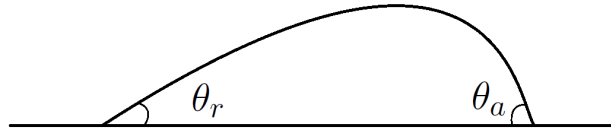
(b) Advancing receding contact angles

Figure 1.31: Contact angle definitions

While the classical Young and Dupré equation describes the wetting state of a perfectly smooth surface, extensions have been made by Cassie and Baxter [3] on one side and by Wenzel [116] on the other, to take into account the effects of surface roughness. The idea behind Wenzel's model is that the liquid penetrates the surface pores (caused by roughness), creating what is called a homogeneous wetting state (or also Wenzel state). As for Cassie and Baxter, they assume the contrary. The liquid will stay at the surface, leaving small pockets of air trapped in the asperities. This is called a heterogeneous wetting state (or Cassie-Baxter state). Superhydrophobic surfaces display micrometric to nanometric roughness arranged in a hierarchical way, as shown in figure 1.32. As predicted by the wetting models, for a hydrophobic surface, roughness will improve its hydrophobicity, while it will have the inverse effect on a hydrophilic surface [161].
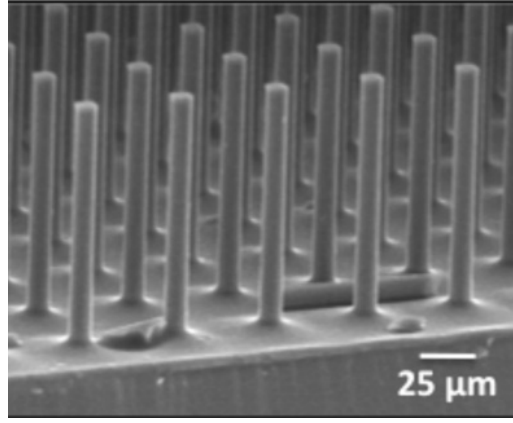
Figure 1.32: Example of a superhydrophobic surface microstructure [72]

The generation of superhydrophic coatings can be divided into two categories ([94, 114]) :

- creating a rough surface from a low surface energy material (such as fluorocarbons or silicones [94]).

- first creating a rough surface, then lowering its surface energy with a low surface energy coating.

Low surface energy materials are based on chemical groups such as $-CH_2-, -CH_3-$ or fluorocarbons for instance. The lotus leaf achieves a $> 160°C$ contact angle and nil sliding angle by means of a textured surface and by using paraffinic wax crystals (these crystals contain mainly $-CH_2-$ groups) [94].

Studies that evaluate the impact of wettability on freezing time of supercooled droplets have also been conducted [123]. Surprisingly, freezing time is most delayed for hydrophilic coatings. It is thus pointed out that the choice of the coating must be evaluated in accordance with the technology which is to be used and the desired performance.

As mentioned previously, some authors did not observe a clear correlation between hydrophobicity and icephobicity. Meuler *et al.* report that this may be caused by a wrong choice in the parameters used to investigate a possible correlation [5]. They conducted ice adhesion experiments on bare steel and steel coated with 21 different materials. They measured several parameters representative of the wettability of the surface and found strong correlation with the practical work of adhesion scaling factor $1 + \cos(\theta_{rec})$.

They also point out the fact that no known smooth surface material has a receding contact angle superior to that of 80/20 PEMA/fluorodecyl POSS : $118.2 \pm 2.4°$. Thus surface texture manipulation would be required so as to enable water to freeze in a Cassie-Baxter state.

1.5.3.2 Fluid Injection

In the mid-30's, Dunlop were developing anti-icing fluid systems. The idea was to inject a chemical (such as ethylene glycol), which would either reduce the freezing point of water or prevent the adhesion of ice, through a porous surface. This system was first fit on a De Havilland Leopard Moth [139]. It was reported to be successfull, but actually usefull in certain conditions only [150].
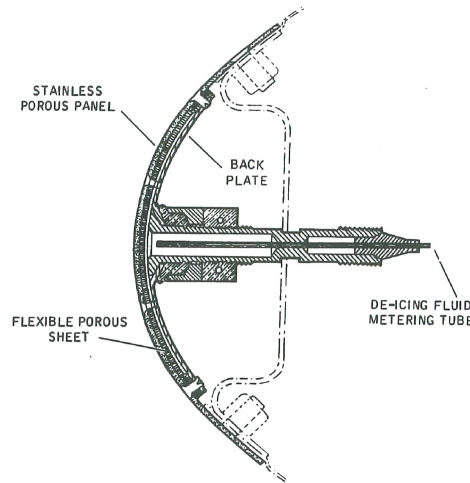
Figure 1.33: Illustration of a chemical injection ice protection system

1.5.4 Hybrid Systems

Given the wide variety of ice protection systems, it may be interesting to blend the best of several worlds. The driving idea being to compensate the cons of one design with the pros of another.

1.5.4.1 Pneumatic/Thermal Ice Protection

During the mid-1940's a hybrid electro-thermal/pneumatic de-icer prototype was built and studied [154]. The de-icer consisted of an electrically heated parting strip and pneumatic boots which would extend aft the parting strip. The inflatable boots consisted of a neoprene-covered nylon fabric. The electrical heating element consisted of chromel wire integrated into glass fabric and neoprene.
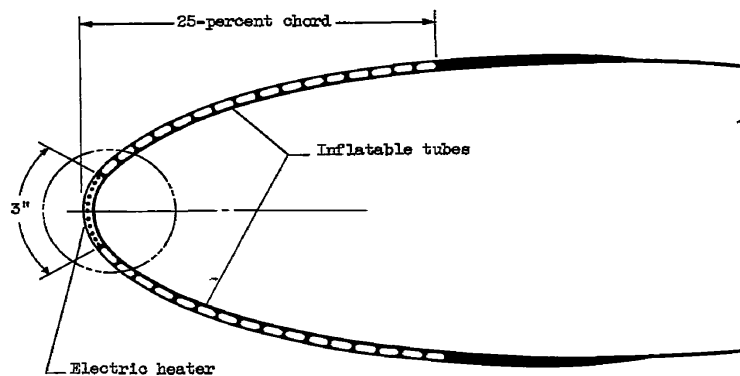
Figure 1.34: Hybrid electro-thermal/pneumatic de-icer [154]

1.5.4.2 Thermal/Electro-Mechanical Ice Protection

Another way of combining protection concepts may be found in the Thermo-Mechanical Expulsion Deicing System (TMEDS). The original idea was to continuously heat, by means of hot air or electrical power, the leading edge parting strip. Therefore this region would be in a running wet state. Runback ice is then allowed to form aft the parting strip. Electro-Expulse actuators are then placed in these regions and activated to remove the runback ice.
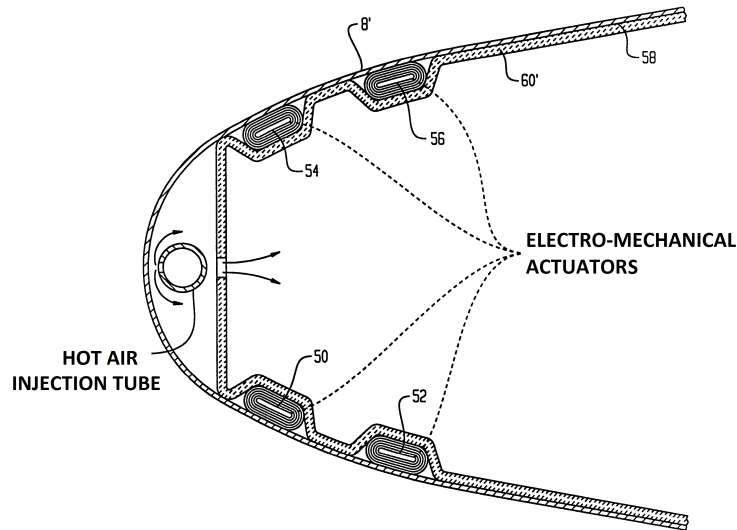
Figure 1.35: Hot Gas Hybrid Thermal/Electro-Mechanical de-icer [73]

1.5.4.3 Thermal/Coating Ice Protection

As a continuation of their 2002 experiments [22], researchers at AMIL have experimented combining thermoelectric anti-icing systems with hydrophobic coatings [40]. Three different coatings where tested (two hydrophobic and one superhydrophobic). Icing conditions where created using AMIL's icing wind tunnel. The superhydrophobic coating reduced the required power by 13% for rime ice and 33% for glaze ice while the hydrophobic coatings reduced power by 8% and 13% for rime and glaze ice respectively. However for hydrophobic coatings runback water froze on the unprotected areas. They were not able to repel the water up to the trailing edge. This was achieved with the superhydrophobic coating, leaving the surface mostly free of ice. This suggests that a superhydrophobic coating could significantly reduce the power requirement of anti-icing systems, although the question of durability still has to be investigated.

1.5.5 Currently Used Systems

Although many concepts for ice protection have been developed, only a few made it to industrial scale application. Many aspects have to be taken into account when chosing a specific system design, such as available power, certification, ease of integration and maintenance. At the present time we may sum up the situation in the following way:

- Small commuter aircraft: the most widely used system for this category of aircraft is the de-icing inflatable boots system.

- Large airliners: for this category of aircraft the bleed-air system is mostly used. Electro-thermal systems have been used in the past on the Transall and more recently on Boeing's 787 Dreamliner.

- Electrical heating is mostly used for helicopter rotorblade ice protection, probe and windshield de-icing.

The bleed air system is used by the vast majority of large airliners for nacelle and wing ice protection. This system, working in running wet or fully evaporative anti-icing mode, is highly effective. However, the heat required for such an operating mode also makes it an energy greedy system. The actual global context of reduction of fuel consumption is calling for alternative ice protection solutions. Moreover, the tendency towards more electrical aircraft architectures suggests that electrical solutions be the preferred way forward.

1.6 Numerical Modelling

The design of ice protection systems is a complex task. Even once a specific architecture has been chosen, the amount of power has to be chosen, as well as the way of distributing it. To this end ice accretion, water impingement and heat transfer with the ambiant atmosphere must also be evaluated. To perform this task, numerical simulation is a powerful tool. It provides a cheaper and complementary view to experimental investigation. Moreover, system parameters such as power or layout may be easily changed allowing more flexibility at the design level. For these reasons, icing codes have been developed for the last thirty years. Nevertheless, this is no easy task and the modelling of complex icing phenomena is an active field of research.

Due to the specific industrial context and development contraints of this work, the modelling and numerical simulation will be performed in two dimensions. It should be noted that numerical methods for icing simulation in three dimensions also exist. However, the main ideas remains the same as in two dimensions.

1.6.1 Typical Icing Code Architecture

There are two main aspects that one may wish to investigate regarding icing. In order to evaluate the performance of a particular wing or air intake design, it is interesting to perform a pure ice accretion simulation with a given exposition time to icing conditions. Therefore in this case the output of interest is the final ice shape. On the other hand, the assessment of ice protection technologies requires that a simulation of the system of interest be run simultaneously and coupled with one of ice accretion.

Accretion computation in state of the art codes is still based on Messinger's model, first proposed in 1953 [17]. Accretion modelling is one of the core components of icing simulation. However, in order to perform such a prediction, information about the aerodynamic flow field, particularly heat transfer, and water droplet impingment are needed.

Therefore, state of the art icing codes are usually split into several modules dedicated to specific tasks ranging from flow field computation to ice protection system simulation. Each of these building blocks is then integrated into a global computation loop according to simulation needs. A generic full state of the art simulation will typically go along the lines of figure 1.36. State of the art methodologies (with respect to icing simulation) for each of these steps are described in the following subsections.
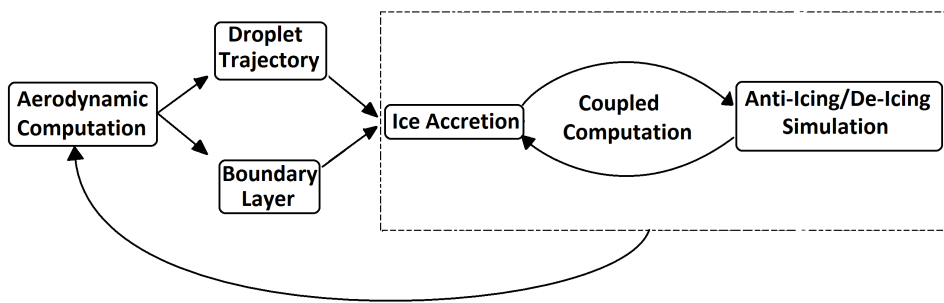
Figure 1.36: General Icing Code Architecture

1.6.2 Aerodynamics

The first step of the icing simulation is the computation of the aerodynamic flow field. This may be achieved in many ways, depending on computational time and precision contraints. Codes may be based on potential, Euler or Navier-Stokes equations. If the chosen equations are those of an inviscid flow (potential, Euler), then coupling with a boundary layer code is necessary. Indeed, it is essential to deduce from the aerodynamics the heat transfer characteristics of the flow at the surface of interest.

1.6.3 Droplet trajectory

Once the aerodynamic field is computed it may be used to predict droplet trajectories and catch efficiency. To do so two methods may be used: lagrangian or eulerian. In the lagrangian approach, one uses the knowledge of the aerodynamic field to follow the trajectory of individual particles.

The eulerian approach introduces the concept of water fraction field $\alpha(x,t)$, which is transported with the aerodynamic field. This approach translates into a conservation of mass equation and a transport equation.

Analysis of the droplet trajectories enable the evaluation of the catch efficiency β. It enables to link to the rate impacting mass of water per unit area to freestream parameters through the formula: $\dot{m}_{imp} = \beta V_\infty LWC$, where V_∞ is the freestream velocity and LWC is the liquid water content.

1.6.4 Ice Accretion: Messinger's Model

With knowledge of catch efficiency and convective heat transfer variables, it is possible to use Messinger's model. The shape is first discretized into control volumes. Each control volume is then treated as a thermodynamic open system.

(a) Heat transfer in icing conditions [17]   (b) Thermodynamic open system control volume
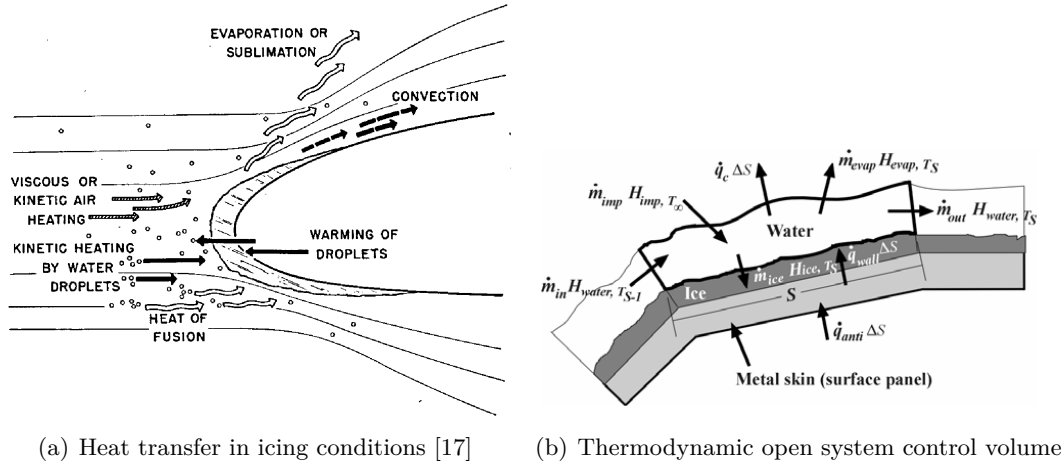
Figure 1.37: Illustration of Messinger's model

By using conservation of mass and energy and substituting enthalpies and heat fluxes by their expressions as functions of relevant temperatures, it is possible to express the problem as a function of two unknowns, the freezing fraction and the surface temperature T_s. The freezing fraction is defined by $f = \frac{\dot{m}_{ice}}{\dot{m}_{imp}+\dot{m}_{in}}$, where $\dot{m}_{ice}$ is the mass rate of formation of ice and $\dot{m}_{in}$ is the mass rate of water entering the control volume. The problem is then solved using an iterative algorithm [34].

Messinger's model is limited in its ability to treat runback icing and is formulated in a steady state setting. The model is therefore difficult to couple with unsteady ice protection system simulation. Moreover, it does not provide information about the temperature gradient through the thickness of the ice. Research is being conducted in order to propose new modeling strategies to overcome these drawbacks.

1.6.5 Electro-Thermal Ice Protection Modeling

Ice accretion prediction alone is already very useful for wing or air intake design. However, it is also necessary for the design of ice protection systems. M.A.D (Anti-icing De-icing Modelling) is a numerical tool, developed by ONERA and part of the 2D icing chain, that predicts the transient behaviour of such a system. Codes developed for this purpose at NASA, ONERA or DRA all used very similar modelling strategies [44]. The original methods and assumptions used in the code are the following [110] :

- The curved geometry is approximated by a flat plate.

- The domain is meshed as a cartesian grid.

- The ice shape is discretized in a staircase manner.

- Heat transfer is solved in the whole domain (ice block + structure) using the enthalpy method.

- Ice shedding is predicted by using an empirical criterion

- Energy and mass balances, similar to Messinger's model, are used at the ice/air interface to model ice formation.

- A second order finite different scheme is used for spatial discretization.

- The method of assumed states and the modified strongly implicit procedure are used for implicit time stepping [38, 87].
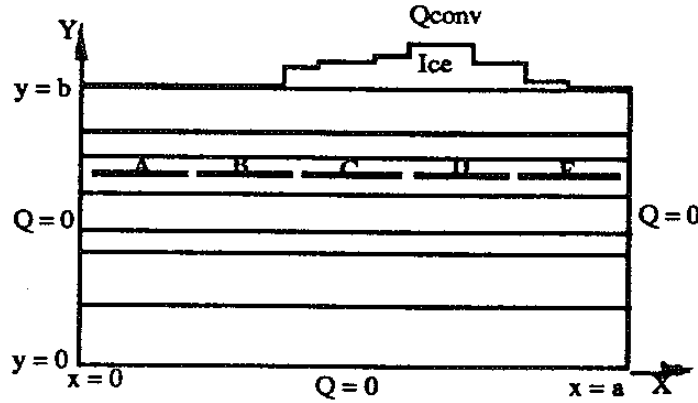
Figure 1.38: M.A.D geometry layout approximation [110]

One of the issues arising when studying electro-thermal systems (and de-icing systems in general) is ice shedding, that is to say the detachment process of ice and its subsequent evolution in the flowfield. At the time being, the main effort for ice shedding has been put on predicting were the ice will go once it detaches, usually using Monte-Carlo methods. This is an important aspect with regard to certification.

Concerning the actual detachement mechanism, very few studies exist. Scavuzzo *et al.* performed a finite element analysis of the stress distribution due to aerodynamic forces in an accreted ice block [118]. The focus of their study was to determine whether these forces were sufficient to lead to ice shedding. For low speeds (Mach < 0.45) the predicted effect of aerodynamic forces was found to be insignificant. However, for higher Mach numbers, it was found that the shear interfacial stress was approximately 20 % of the maximum debonding strength. Therefore they concluded that aerodynamic forces should be taken into account when performing stress analysis of ice accreted on aeronautical structures. More recently, Zhang *et al.* have used a crack propagation with re-meshing technique to study in-flight ice break up [1].

However, none of these studies took into account the effect of an electro-thermal ice protection system. Therefore a complete description has not yet been attained. To this day, ice shedding prediction in icing codes remains very empirical. Indeed, the approach consists in computing the ratio L_f/L_t, where L_f is the length of melted ice at the interface with the protected surface and L_t is the total contact lenght, as shown in figure . It then states that if this ratio is high enough (typically 80 %), then ice detaches from the surface. Hence, ice shedding modelling constitutes a major axis of improvement and is one of the main aims of this thesis.
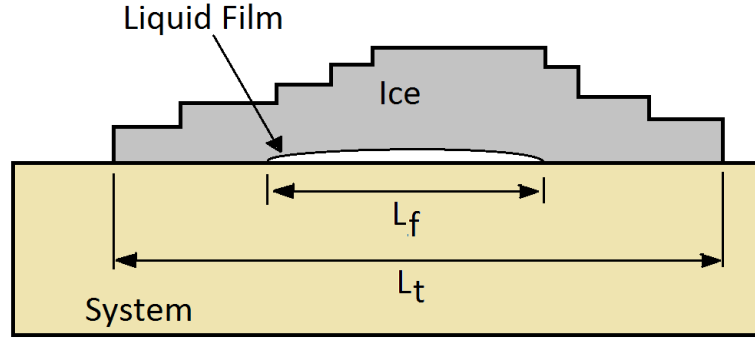
Figure 1.39: Liquid film and contact lengths in MAD

1.7 PhD Context, Scope and Goals

The context of more electrical aircraft and economic contraints in terms of fuel consumption are putting electrical ice protection systems back into consideration for large airliners. The design of such systems calls for numerical tools so as to investigate their operating.

Moreover, the context is also one of development of second generation icing codes at ONERA. Therefore, in order to ease coupling with newly developed modules, the architecture of the ETIPS simulation module has entirely been rethought. Due to industrial and development constraints modelling is done in two dimensions.

The objective of this thesis is to develop numerical models and methods in order to investigate the multiphysical operating of an electro-thermal ice protection system. A strong emphasis is put on atmospheric ice material modeling and prediction of ice shedding. The final goal is to propose a prototype code that is able to simulate a whole ETIPS de-icing cycle.

The upcoming chapters further describe this work in the following order:

- **Chapter 2: Thermal Modelling**: the thermal modelling method is presented and validated with analytical test cases. Although the techniques presented are not fundamentally new, they represent a significant part of the construction of the 2nd generation module, which is necessary for further study.

- **Chapter 3: Mechanical Modelling**: a mechanical modelling method relevant to fracture is exposed, assessed and validated against experimental data.

- **Chapter 4: Mechanical Properties of Atmospheric Ice**: the mechanical properties of ice are reviewed and empirical laws are formulated for atmospheric ice.

- **Chapter 5: Ice Shedding Mechanism**: an ice shedding mechanism based on brittle failure is proposed and investigated.

- **Chapter 6: ETIPS Performance Numerical Simulation**: a dry air simulation case of an electro-thermal ice protection system is described as well as a feasability of de-icing simulation with ice shedding.

The present section is devoted to presenting the thermal modelling approach related to ETIPS simulation. Two domains may be considered when modelling the operating of an ETIPS: the system itself and the ice accreted at the surface. The developed code is therefore separated into two blocks, each of them treating the heat transfer problems specific to each domain. These two modules are then coupled using an explicit procedure. In what follows, the equations are always solved in two dimensions. Moreover, as the chosen model to treat phase change in ice is based on a conservation of enthalpy scheme, the finite volume method is chosen for its conservative properties.

Contents

2.1 General Heat Transfer and Finite Volume Approach
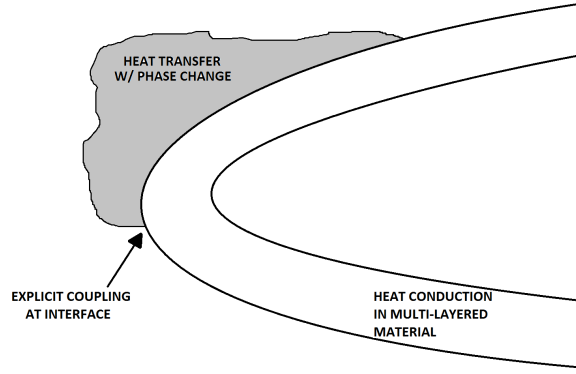
Figure 2.1: Heat transfer problems in two different domains

In order to model the thermal operating of an electro-thermal ice protection system, one must deal with two aspects (two domains, as shown in figure 2.1). Either heat conduction within the multi-layered structure is to be modelled, in which case changes in material constants have to be taken into account. Or heat transfer with phase change has to be simulated in an eventual ice block, in which case a specific treatment has to be perfomed to capture the melting front. So as to present these aspects in a unified way the following generic form of the energy conservation equation is considered:

$$\frac{\partial}{\partial t}\int_{\mathcal{D}}\rho h dV = \int_{\mathcal{D}}Q_{src}dV + \int_{\partial\mathcal{D}}-\boldsymbol{q}\cdot\boldsymbol{n}d\Gamma \tag{2.1}$$

where ρ is the density, h is the specific enthalpy, Q_{src} is a heat source term, $\boldsymbol{q}$ denotes the heat flux and $\boldsymbol{n}$ is the outward normal unit vector to domain $\mathcal{D}$ (where $\mathcal{D}$ is an arbitrary domain) .

To solve these equations, the finite volume numerical method is adopted. The domain $\mathcal{D}$ is partitioned into a set of cells which constitute the mesh. This equation holds for any domain $\mathcal{D}$ therefore on a particular cell K of the mesh we have:

$$\frac{\partial}{\partial t}\int_{K}\rho h dV = \int_{K}Q_{src}dV + \int_{\partial K}-\boldsymbol{q}\cdot\boldsymbol{n}d\Gamma \tag{2.2}$$

The integrals over K are evaluated by using the cell averaged value defined by:

$$\widetilde{U}_K = \frac{1}{|K|}\int_K U dV \tag{2.3}$$

Moreover ∂K being decomposed into an union of edges, the heat flux is approximated by a constant value q_f on each face which yields:

$$\frac{\partial}{\partial t}\widetilde{\rho h}_K|K| = \widetilde{Q}_{src,K}|K| + \sum_{E\in\partial K}-\boldsymbol{q_f}\cdot\boldsymbol{n_f}|E| \tag{2.4}$$

where $|K|$ is the area of cell K, $|E|$ is the length of edge E, $\boldsymbol{n_f}$ is the outward unit normal to edge E. The heat source term $Q_{src,K}$ will be used for taking into account the electrical heaters. The modelling relative to this aspect will be discussed later.

The transient term is discretized using an Euler scheme:

$$\frac{\partial}{\partial t}\widetilde{U}_K \simeq \frac{\widetilde{U}_K^{n+1} - \widetilde{U}_K^n}{\Delta t} \tag{2.5}$$

In order to close the problem, both the heat flux and specific enthalpy have to be linked to the temperature T. In a simple case of heat conduction, h takes the classical form $h = c_p T$. However, as both cases considered here involve melting fronts and/or changes in material parameters, the relation

$h(T)$ may not be that simple. On the other hand, in both cases the heat flux is modeled with Fourier's law:

$$\boldsymbol{q} = -\Lambda\boldsymbol{\nabla}T \tag{2.6}$$

where Λ is the heat conduction coefficient which may take either a scalar or tensorial form and will take different formulations depending on the case. Each specific treatment is described in the following sections.

2.2 Heat transfer in the (multi-layered) structure

A generic electro-thermal ice protection architecture may be seen as having two geometrical attributes and described as follows:

- An ETIPS is usually composed of several layers of different materials. Each layer has a specific thickness and material parameters. These layers therefore provide a natural geometrical attribute.

- Several zones, distributed chordwise, may also be identified on such a system. These zones are associated with the location of the heating elements.

Therefore, to sum up, the geometry of an ETIPS can be divided into several layers in thickness and several zones chordwise. This partition is illustrated on figure 2.2:

(a) Layer Distribution Example   (b) Zone Distribution Example
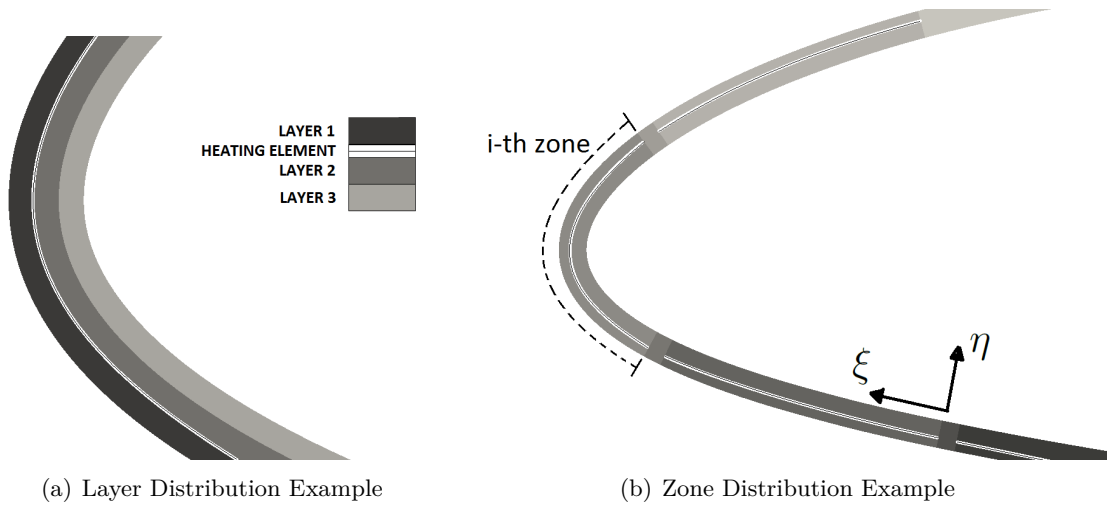
Figure 2.2: Layer and Zone distributions

2.2.1 Domain Discretization and Automatic Mesh Generation

The first step is the discretization of the multi-layered system. In order to do so, the external shape of the system (for example an airfoil or air intake) is specified. A line mesh is then defined to discretize the shape. The inner normals to this external shape are then computed at every node. After what the mesh is constructed by propagating the exterior shape along the normals according to layer discretization information (thickness and number of cells in each layer). This leads to the generation of a structured orthogonal mesh.
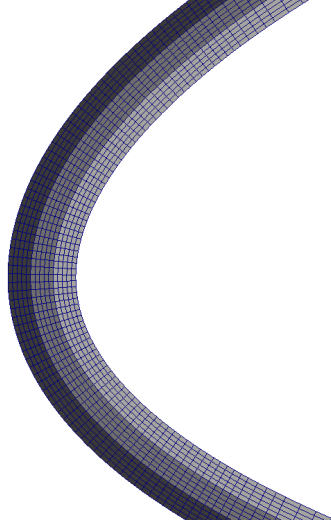
Figure 2.3: Multi-layered structure mesh example

2.2.2 Physical process and modelling

Here the problem of heat conduction in a structure composed of different materials and with localized heat sources provided by the heater mats must be solved. The mesh is constructed is such a way that every cell belongs to a well defined layer and zone of material. Thus the enthalpy derives directly for the classical relation: $\widetilde{\rho h}_K = \rho c_{p,K} \widetilde{T}_K$, which yields:

$$\rho c_{p,K} |K| \frac{\widetilde{T}_K^{n+1} - \widetilde{T}_K^n}{\Delta t} = \widetilde{Q}_{src,K} |K| + \sum_{E \in \partial K} (\Lambda \boldsymbol{\nabla} T) \cdot \boldsymbol{n_f} |E| \tag{2.7}$$

Due to the nature of the multi-layered stack of materials which constitutes the structure of the system, the thermal conductivity has two priviledged directions. They are shown in figure 2.2(b)) and are noted ξ and η. ξ corresponds to the transversal direction while η corresponds to the thickness direction. Therefore, in the (ξ, η) system of coordinates, the thermal conductivity matrix Λ has the form:

$$\begin{pmatrix} \lambda_\xi & 0 \\ 0 & \lambda_\eta \end{pmatrix}$$

Due to the way the mesh is constructed, the outward unit vector to a given edge will always be colinear to one of the eigen vectors of Λ. Hence the normal heat flux will either be :

$$q_{n,\xi} = \pm\lambda_\xi \partial_\xi T$$

or

$$q_{n,\eta} = \pm\lambda_\eta \partial_\eta T$$

The heater mats are considered to be located at the interface between two layers and are not explicitly meshed. So as to take into account their presence, they are assumed to be evenly shared, as shown in figure 2.4, between the adjacent cells j and $j+1$.
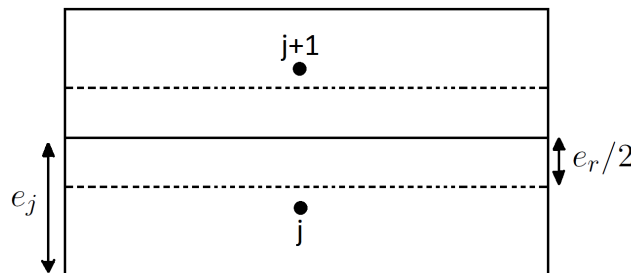
Figure 2.4: Heater evenly shared between adjacent cells

Therefore, the product ρc_p of each adjacent cell is modified according to the following formula, defining an equivalent mean value for ρc_p [110]:

$$(\rho c_p)_{eq} = \frac{(\rho c_p)_j \, e_j + (\rho c_p)_r \, e_r/2}{e_j + e_r/2} \tag{2.8}$$

where e_j and e_r are the thickness of the adjacent cell and the heating element respectively. If P is the power of the heating element, the heat provided is represented as a heat source $\widetilde{Q}_{src,j} = \frac{P}{2}$ in each adjacent cell.

2.2.3 Temperature Gradient Discretization

Due to the nature of the multi-layered structure, the heat flux must be discretized so as to account for discontinuities in material constants such as density or specific heat.
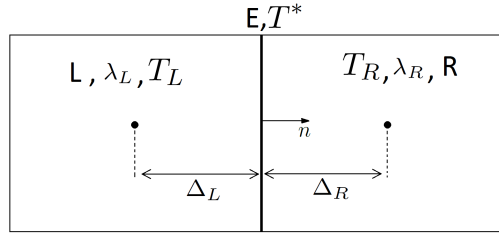
Figure 2.5: Illustration of structured mesh cell

Consider two adjacent cells R and L having a common edge E (see figure 2.5), as shown on figure 2.5. The normal heat fluxes at edge E with respect to cells R and L may be expressed as:

$$q_{n,L} = \lambda_L \frac{T_L - T^*}{\Delta_L} \tag{2.9}$$

$$q_{n,R} = -\lambda_R \frac{T_R - T^*}{\Delta_L} \tag{2.10}$$

Equating both normal fluxes yields:

$$T^* = \frac{\frac{\lambda_L}{\Delta_L} T_L + \frac{\lambda_R}{\Delta_R} T_R}{\frac{\lambda_L}{\Delta_L} + \frac{\lambda_R}{\Delta_R}} \tag{2.11}$$

Finally, the discretization of the heat flux at edge E is obtained by reinjecting this relation into one of equations (2.9) or (2.10):

$$q_{n,E} = \frac{\frac{\lambda_L}{\Delta_L} \frac{\lambda_R}{\Delta_R}}{\frac{\lambda_L}{\Delta_L} + \frac{\lambda_R}{\Delta_R}} (T_L - T_R) \tag{2.12}$$

This formulation naturally takes into account discontinuities in material constants. It is possible to extend the formulation to imperfect contact, as illustrated in figure 2.6.
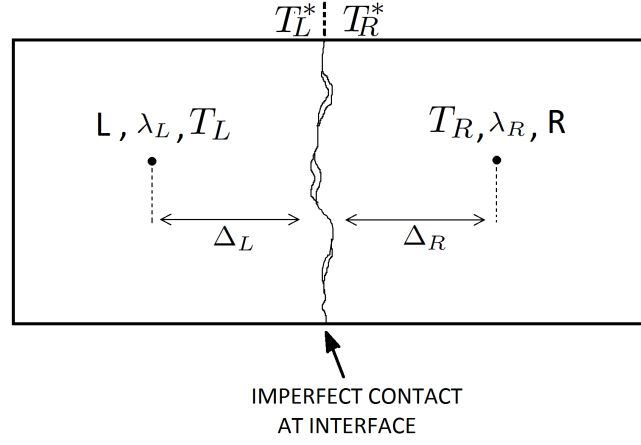
Figure 2.6: Imperfect contact

Such an interface can be modelled by considering that the normal heat flux is still conserved. However, due to the imperfections at the interface, there is a difference in wall temperature (no longer equal as previously for a perfect interface). This translates into equation 2.13 which introduces the thermal contact resistance RTC.

$$q_n = \frac{1}{RTC}(T_L^* - T_R^*) \tag{2.13}$$

where L and R represent each side of the contact interface. Using an approach analogous to that used for a perfect interface it can be shown that:

$$q_{n,E} = \frac{(T_L - T_R)}{RTC + \frac{\Delta L}{\lambda_L} + \frac{\Delta R}{\lambda_R}} \tag{2.14}$$

The issue with this approach is that the RTC is required and it is usually an unavailable datum.

2.2.4 Time Discretization

An implicit time marching algorithm is chosen due to the fact that some materials in the structure may be very good conductors. Indeed, this would put a harsh limit to the authorised value of the time step had we chosen an explicit formulation.

Combining both spatial and temporal discretizations, for a given cell i having neighbours $a1$, $a2$, $a3$ and $a4$, yields:

$$\rho c_{p,K}|K|\frac{\widetilde{T}_K^{n+1} - \widetilde{T}_K^n}{\Delta t} = \widetilde{Q}_{src,K}|K| + \sum_{a=a1,a2,a3,a4} C_a\left(\widetilde{T}_K^{n+1} - \widetilde{T}_a^{n+1}\right)|E| \tag{2.15}$$

which can be recast in matrix form:

$$(M + D)\widetilde{T}^{n+1} = M\widetilde{T}^n + Q \tag{2.16}$$

where M is a mass matrix (transient term) and D is a stiffness matrix (diffusion term). The coefficients C_a are of the form:

$$C_a = -\frac{\frac{\lambda_K}{\Delta_K}\frac{\lambda_a}{\Delta_a}}{\frac{\lambda_K}{\Delta_K} + \frac{\lambda_a}{\Delta_a}}$$

Note that in this case the coefficients C_a are always negative. This implies that the diagonal of $M + D$ is always positive and that the extradiagonal terms are always negative, which guarantees that the maximum principle is respected for any Δt. As a consequence the time marching is unconditionally stable. The linear system is solved using a conjugate gradient type iterative solver.

2.2.5 Boundary Conditions

Two types of boundary conditions are taken into account in the numerical method. The first one is a Dirichlet type imposed wall temperature boundary condition. In this case, the imposed wall temperaute T_w plays the role of the interface temperature T^*. Therefore the flux is simply written:

$$q_n = -\lambda_{bnd} \frac{T_{bnd} - T_w}{\Delta_{bnd}} \tag{2.17}$$

where the subscript *bnd* identifies values in the boundary cell. Using this formula, the associated coefficient C_a is easily identified. As T_w is imposed it remains on the right hand side when assembling the different terms of equation (2.16).
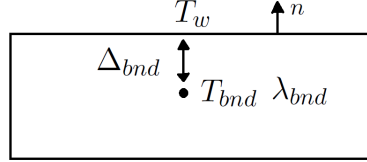
Figure 2.7: Dirichlet boundary condition

The second one is an imposed flux boundary condition. It includes both Fourier-Robin and Neumann boundary conditions. The Fourier-Robin part of the boundary condition serves to model convective heat transfer at the boundary whereas the Neumann part serves if only a boundary flux is imposed. It is written:

$$q_n = htc \left(T_{rec} - T^*\right) + \phi_0 \tag{2.18}$$

where htc is a convective heat transfer coefficient, T_{rec} is a recovery temperature and ϕ_0 is an imposed flux. Noting $\hat{\lambda} = \lambda / \Delta_{bnd}$, the flux may also be written:

$$q_n = \hat{\lambda} \left(T^* - T\right) \tag{2.19}$$

Equating both fluxes yields the formula used for the incorporation of this boundary condition:

$$q_n = \frac{\hat{\lambda} htc}{htc + \hat{\lambda}} \left(T_{rec} - T\right) + \frac{\hat{\lambda}}{htc + \hat{\lambda}} \phi_0 \tag{2.20}$$
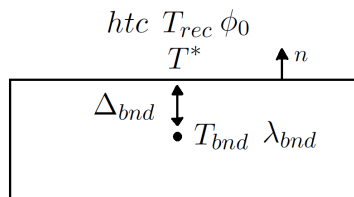
Figure 2.8: Fourier-Robin boundary condition

2.2.6 Academic Validation Case

In order to assess the performance of the developed tool, it is validated on an academic test case. As curved geometries will be most often considered in practical applications, a simple hollow cylinder geometry is considered. It is defined by an inner radius r_i and an outer radius r_o. It is made of a single material, which has a fixed uniformly distributed temperature on its inner and outer surfaces and a uniform initial temperature field (see figure 2.9). Here, the imposed boundary temperature is chosen to be 0 and the initial temperature is set to 1. Material paremeters are all set to a value of 1. r_i is set to $1.5m$ and r_o is set to $2.0m$.
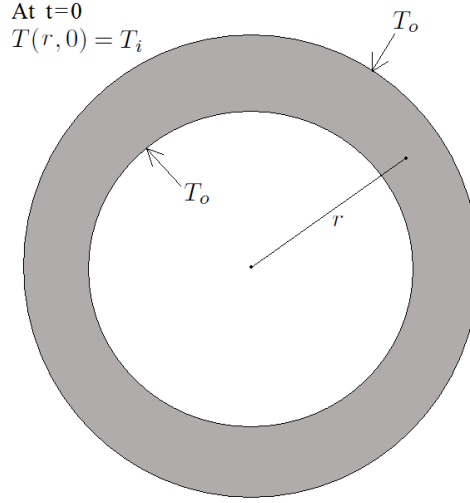
Figure 2.9: Illustration of the hollow cylinder academic case

Introducing the variables $R = r/r_o$ and $R_i = r_i/r_o$, the analytic solution, given in [60], is a temperature field that depends only of the radial coordinate r and time.

$$T = \pi \sum_{n=1}^{+\infty} f(R, \lambda_n) e^{-\lambda_n^2 \frac{\alpha t}{r_o^2}} \tag{2.21a}$$

$$f(R, \lambda_n) = \frac{J_0(\lambda_n R_i) \left[J_0(\lambda_n R) Y_0(\lambda_n) - J_0(\lambda_n) Y_0(\lambda_n R) \right]}{J_0(\lambda_n R) + J_0(\lambda_n)} \tag{2.21b}$$

where J_0 is the 0-th Bessel function of the first kind and Y_0 is the 0-th Bessel function of the second kind. λ_n are the solutions to equation 2.22. In order to perform numerical comparisons, the series defining the analytical solution is truncated at $n = 20$.

$$J_0(\lambda_n R_i) Y_0(\lambda_n) - J_0(\lambda_n) Y_0(\lambda_n R_i) = 0 \tag{2.22}$$

In order to assess the performance of the numerical method, the hollow cylinder is discretized using three different meshes. Their characteristics are given in table 2.1, where Δr is the mesh size in the thickness direction. It is also interesting to take a look at the transient behaviour of the numerical scheme. For such a setup, the characteristic conduction time may be evaluated as $t_c = \frac{(r_o - r_i)^2}{\lambda/(\rho c_p)}$ which in this case yields the value $t_c = 0.25s$. Hence for each mesh, three time steps will be chosen. Their non-dimensional values are given in table 2.2.

The analytical solution is compared to the numerical solution on figures 2.10, 2.11 and 2.12. For every mesh, the effect of the chosen time step is significant. For the higher time step, the numerical solution presents notable differences with the analytical one. For all meshes, the solution is much better when the time step is reduced. The improvement observed by taking more refined meshes is much slighter. Hence, even though the time marching scheme is unconditionally stable, the time step has to be chosen in accordance with the characteristic conduction time if the transient behaviour is to be correctly simulated.

Mesh	1	2	3
Nb Cells	900	3000	12000
$\Delta r(m)$	0.05	0.025	0.0125

Table 2.1: Mesh parameters

$\Delta t^* = \frac{\Delta t}{t_c}$	0.0004	0.004	0.02

Table 2.2: Non dimensional time steps
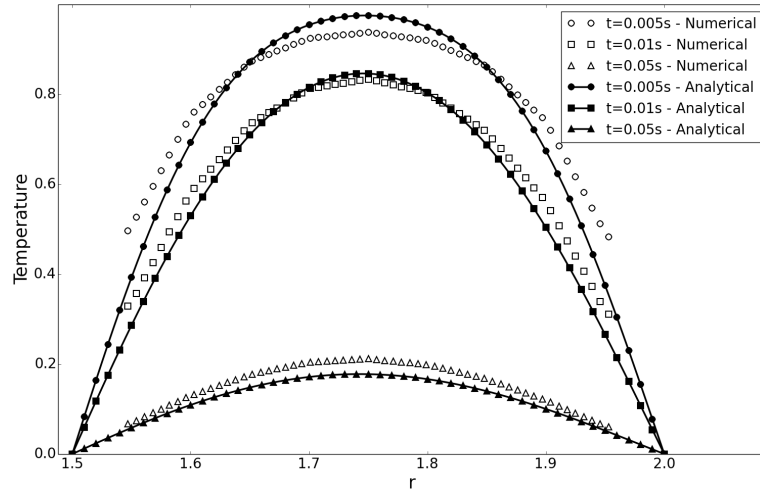
(a) Mesh nb 1 - $\Delta t^* = 0.02$
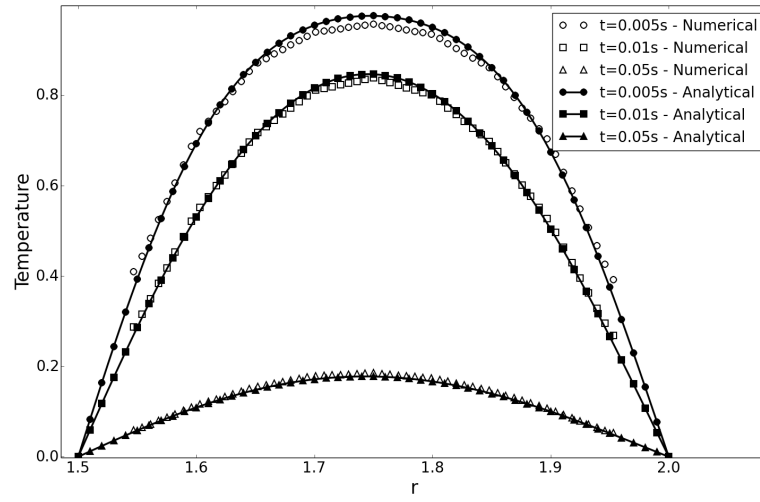
(b) Mesh nb 1 - $\Delta t^* = 0.004$
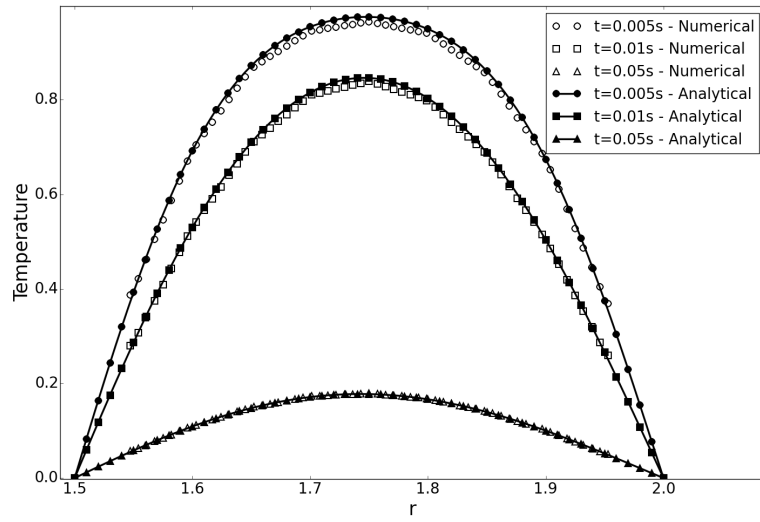
(c) Mesh nb 1 - $\Delta t^* = 0.0004$

Figure 2.10: Analytical and numerical solution on mesh no 1 for the different time steps
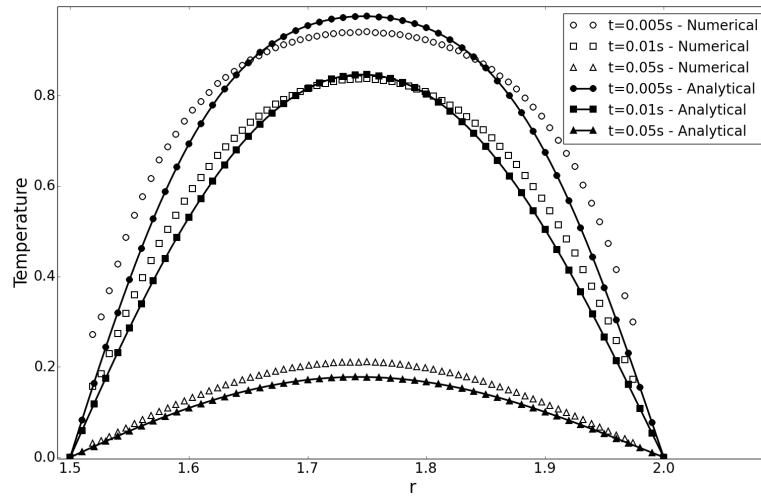
(a) Mesh nb 2 - $\Delta t^* = 0.02$
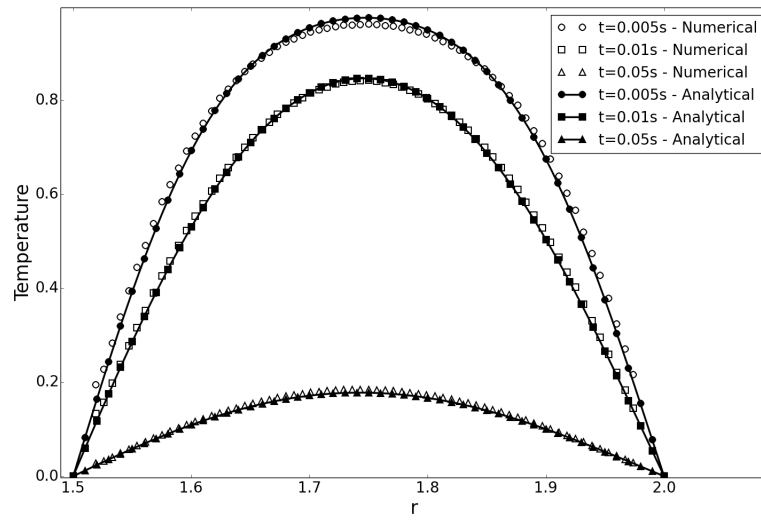
(b) Mesh nb 2 - $\Delta t^* = 0.004$
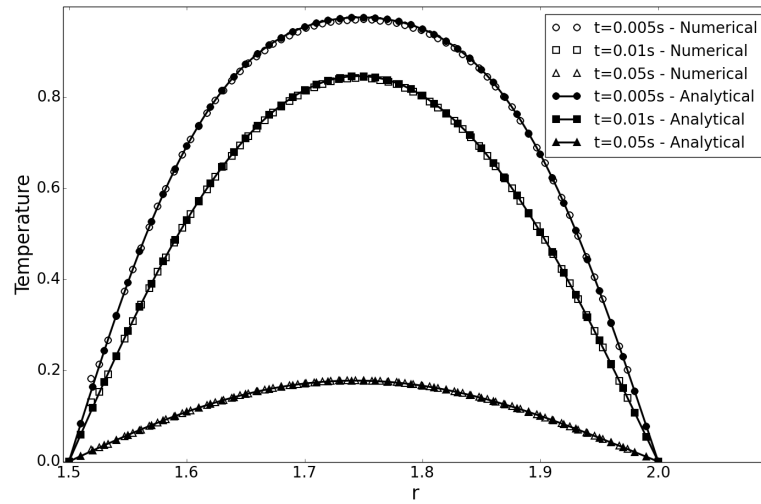
(c) Mesh nb 2 - $\Delta t^* = 0.0004$

Figure 2.11: Analytical and numerical solution on mesh no 2 for the different time steps
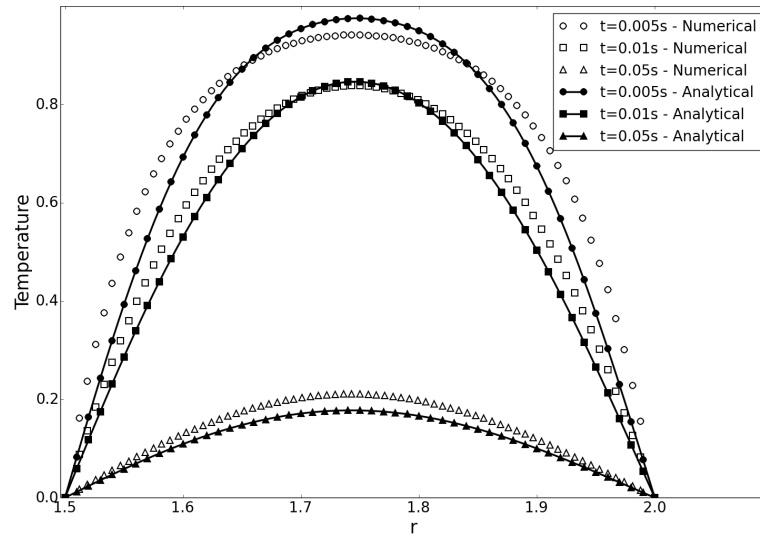
(a) Mesh nb 3 - $\Delta t^* = 0.02$
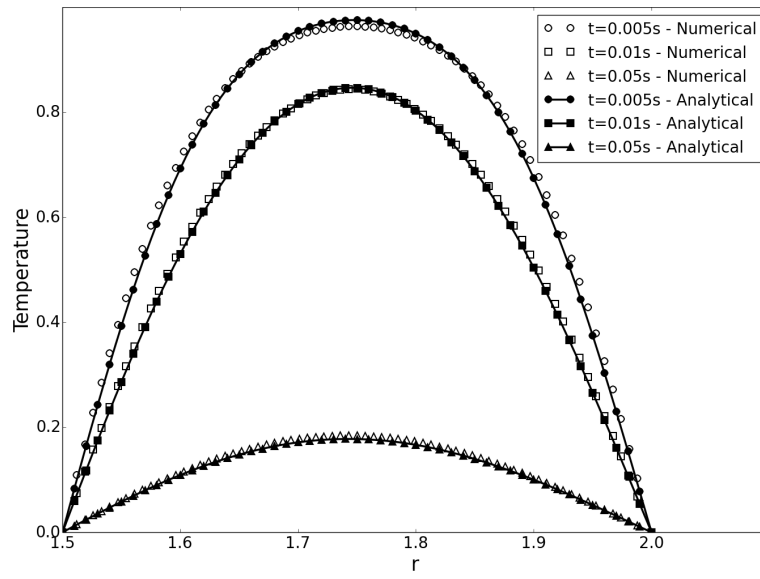
(b) Mesh nb 3 - $\Delta t^* = 0.004$
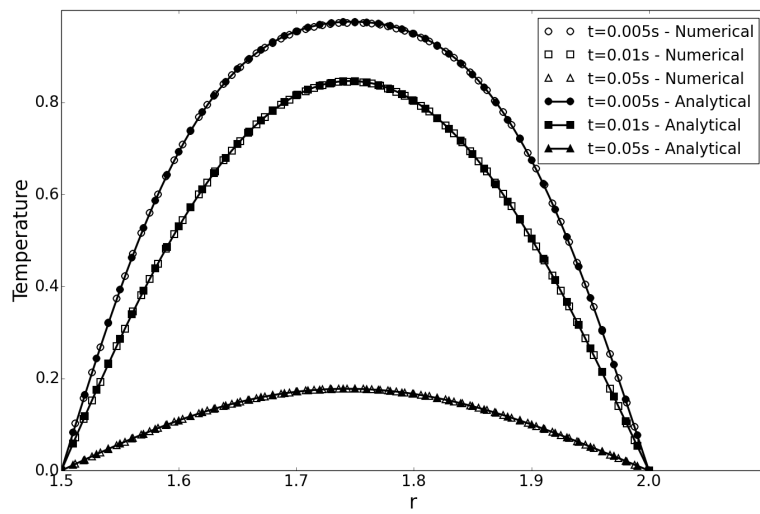
(c) Mesh nb 3 - $\Delta t^* = 0.0004$

Figure 2.12: Analytical and numerical solution on mesh no 3 for the different time steps

2.3 Heat transfer in the ice block

2.3.1 Domain Discretization and Mesh Generation

Due to the physical process of ice accretion, the ice block that builds up can have an arbitrary shape. Moreover, this shape can be quite complicated, presenting horns and other types of irregularities. Therefore, the ice block is discretized using an unstructured mesh. The open source meshing software GMSH is used [19].

2.3.2 Physical process and modelling

In the ice block the material remains the same over the whole domain, that is to say, water. The specific physical process that arises when dealing with this domain is phase change. This mechanism involves a discontinuous enthalpy-temperature relation. In order to capture the melting front arising from this discontinuity, many methods exist (eg : level set, phase field). In our case the so called enthalpy method is chosen. This method enables an efficient capturing of the melting front [129]. The main idea is to introduce a new variable, the liquid fraction, noted ϕ_L, and return to the general energy conservation equation (2.1), which may be recast in the following discretized form assuming no heat source:

$$\frac{\partial}{\partial t}\widetilde{\rho h}_K |K| = \sum_{E \in \partial K} \lambda \boldsymbol{\nabla_f} T \cdot \boldsymbol{n_f} |E| \tag{2.23}$$

Here the specific enthalpy h is not directly reexpressed in terms of temperature T. The time derivative is discretized using equation 2.5, yielding:

$$\frac{\widetilde{\rho h}_K^{n+1} - \widetilde{\rho h}_K^n}{\Delta t} |K| = \sum_{E \in \partial K} \lambda \boldsymbol{\nabla_f} T^n \cdot \boldsymbol{n_f} |E| \tag{2.24}$$

Formula 2.24 results in an explicit scheme. The right hand side is computed on each cell which then enables an update of the value of the enthalpy. Once the enthalpy at the next time step is known, the following relationship (2.25) is used to deduce the new value of the temperature field:

$$T = \begin{cases} T_m + \frac{h}{c_s} & h \le 0 \\ T_m & 0 \le h \le L \\ T_m + \frac{h-L}{c_l} & h \ge L \end{cases} \tag{2.25}$$

where L is the latent heat of fusion. Similarly, the liquid fraction is updated, which is a crucial element for computing the heat fluxes :

$$\phi_L = \begin{cases} 0 & h \le 0 \\ \frac{h}{L} & 0 \le h \le L \\ 1 & h \ge L \end{cases} \tag{2.26}$$

Note that for initialisation purposes, the following convention has been chosen for h :

$$h = \begin{cases} c_s (T - T_m) & T < T_m \text{ solid} \\ \phi_L L & T = T_m \text{ mixed state} \\ c_l (T - T_m) + L & T > T_m \text{ liquid} \end{cases} \tag{2.27}$$

In this approach the density ρ is assumed constant (and the same for water in both solid and liquid states).

2.3.3 "Kirchhoff" Flux

In order to correctly capture phase change, the heat flux, particularly the conductivity λ, have to be formulated carefully. Indeed, in a cell that is melting, the state is neither solid neither liquid, and therefore a mixture model has to be defined. Several choices are possible, however, according

to Solomon and Alexiades [129], the most convenient method is to define the conductivity λ by the following equation:

$$\frac{1}{\lambda} = \frac{\phi_L}{\lambda_l} + \frac{1 - \phi_L}{\lambda_s} \tag{2.28}$$

where λ_s is the conductivity of the solid phase and λ_l is the conductivity of the liquid phase, and use the "Kirchhoff" temperature, defined as:

$$\theta = \lambda \left(T - T_m \right) \tag{2.29}$$

The heat flux then reads:

$$\boldsymbol{q} = -\lambda \boldsymbol{\nabla} T = -\lambda \boldsymbol{\nabla} \frac{\theta}{\lambda} = -\boldsymbol{\nabla} \theta - \lambda \theta \boldsymbol{\nabla} \frac{1}{\lambda}$$

However, when $\boldsymbol{\nabla} \frac{1}{\lambda} \neq 0$ the cell is changing phase, hence $T = T_m$ which implies $\theta = 0$. Therefore, the "Kirchhoff" flux may simply be written as:

$$\boldsymbol{q} = -\boldsymbol{\nabla} \theta \tag{2.30}$$

As will be shown in the next subsection, using such a flux enables a natural separation between contributions of the two cells and two nodes linked to a given edge. Hence the problem of defining the value of k on a given edge is avoided.

2.3.4 Flux Discretization

In this case, the mesh being unstructured, $\boldsymbol{n}.\boldsymbol{e} \neq 1$ in general (see figure (2.13(a))). Therefore, using a flux of the form $\boldsymbol{q} = -\lambda \frac{T_A - T_B}{\Delta_{AB}} \boldsymbol{e}$ would not be, in general, a good approximation.

(a) Unit vectors on arbitrary adjacent cells (b) Neighbouring cells
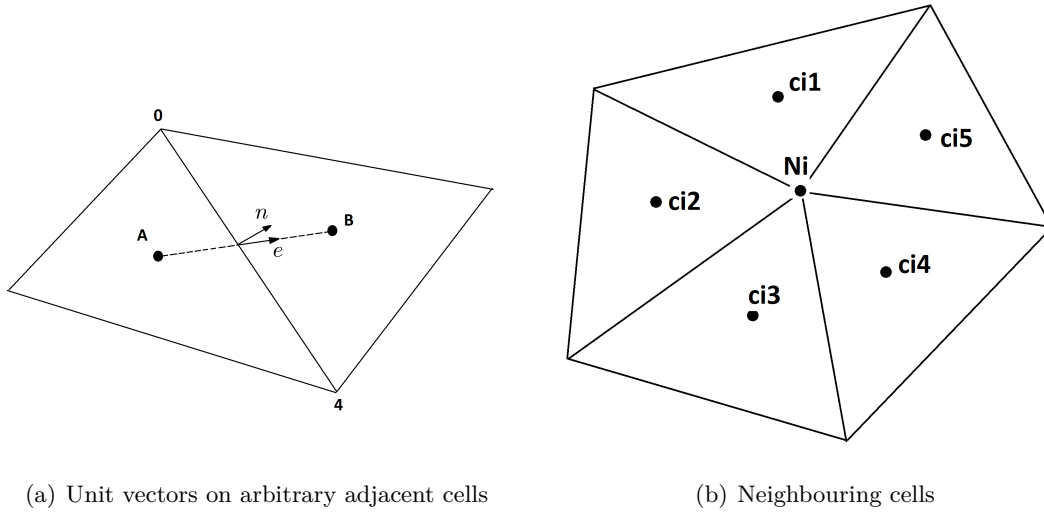
Figure 2.13: Cell and node geometrical definitions

Therefore, a gradient reconstruction scheme is used. The adopted approach follows the method described in references [15, 159]. The idea is to correct the edge gradient using a face gradient computed via linear field interpolation.

Suppose we wish to compute the "Kirchhoff" flux. The edge gradient is defined simply as:

$$\partial^{\boldsymbol{e}} \theta = \frac{\theta_B - \theta_A}{|X_B - X_A|} \tag{2.31}$$

where X_B and X_A are the positions of the centers of gravitiy of cells A and B and θ_B and θ_A are the cell centered values of θ.

Whereas the face gradient, that is to say the gradient in the direction tangent to the considered edge, is defined as:

$$\partial^{\boldsymbol{t}}\theta = \frac{\theta_0 - \theta_4}{|X_0 - X_4|} \tag{2.32}$$

where X_0 and X_4 are the positions of nodes 0 and 4 and θ_0 and θ_4 are nodal values of θ.

With these definitions in hand, the reconstructed gradient is given by the formula:

$$\boldsymbol{\nabla_r}\theta_{04} = \frac{1}{\boldsymbol{n.e}}\partial^{\boldsymbol{e}}\theta\boldsymbol{n} + \partial^{\boldsymbol{t}}\theta\left[\boldsymbol{t} - \frac{\boldsymbol{t.e}}{\boldsymbol{n.e}}\boldsymbol{.n}\right] \tag{2.33}$$

Thus the discretized normal heat flux takes the form :

$$q_n = \frac{1}{\boldsymbol{n.e}}\partial^{\boldsymbol{e}}\theta - \frac{\boldsymbol{t.e}}{\boldsymbol{n.e}}\partial^{\boldsymbol{t}}\theta$$

Noting $\Delta_{AB} = |X_B - X_A|$ and $\Delta_{04} = |X_0 - X_4|$, the terms $\partial^{\boldsymbol{e}}\theta$ and $\partial^{\boldsymbol{t}}\theta$ may be rewritten in terms of the temperature field:

$$\partial^{\boldsymbol{e}}\theta = \lambda_B\frac{T_B - T_m}{\Delta_{AB}} + \lambda_A\frac{T_m - T_A}{\Delta_{AB}} \tag{2.34}$$

$$\partial^{\boldsymbol{e}}\theta = \lambda_0\frac{T_0 - T_m}{\Delta_{04}} + \lambda_4\frac{T_m - T_4}{\Delta_{04}} \tag{2.35}$$

Therefore, the normal flux may be expressed in terms of temperature T:

$$q_n = \frac{1}{\boldsymbol{n.e}}\left[\frac{T_B - T_m}{R_B} + \frac{T_m - T_A}{R_A}\right] - \frac{\boldsymbol{t.e}}{\boldsymbol{n.e}}\left[\frac{T_0 - T_m}{R_0} + \frac{T_m - T_4}{R_4}\right] \tag{2.36}$$

where $R_j = \frac{\Delta_j}{\lambda_j}$ and Δ_j is either the distance between cell centers or the edge length (for example $R_B = \frac{\Delta_{AB}}{\lambda_B}$) . The flux therefore splits into the different contributions of each cell or node.

So as to compute this discretized flux, nodal values of T and λ are required (node 0 and node 4 in the previous derivation). They are obtained by linear interpolation from the cell centered values. To do so, the variable of interest V is approximated, in the neighbourhood defined by its adjacent cells, by a plane of equation:

$$V = a_{Ni}x + b_{Ni}y + c_{Ni} \tag{2.37}$$

At the cell center coordinates (x_{cj}, y_{cj}), the plane must fit at best the known values of V, yielding the linear system:

$$\begin{bmatrix} x_{c1} & y_{c1} & 1 \\ \vdots & \vdots & \vdots \\ x_{cn} & y_{cn} & 1 \end{bmatrix} \times \begin{bmatrix} a_{Ni} \\ b_{Ni} \\ c_{Ni} \end{bmatrix} = \begin{bmatrix} V_{c1} \\ \vdots \\ V_{cn} \end{bmatrix}$$

An interior node will have at least three non-degenerate neighbouring cells. In the case of a good quality mesh this leads to an overdetermined linear system. It is solved by a least squares algorithm, therefore determining coefficients a_{Ni}, b_{Ni}, c_{Ni} and hence the value of V_{Ni}. The least squares algorithm is based on a QR decomposition which is computed once and for all at the beginning of the simulation and stored for use in subsequent time steps.

A special treatment is required for boundary nodes as they may not have enough neighbouring cells. To overcome this problem the neighbouring cells of the two adjacent nodes are also used, resulting in a linear extrapolation procedure. For example, as shown in figure 2.14, if a point $P1$ only has two neighbouring cells $Cn1$ and $Cn2$, then the neighbouring cells of adjacent points $P2$, $P3$ and $P4$ are added to the set of neighbouring cells of $P1$.
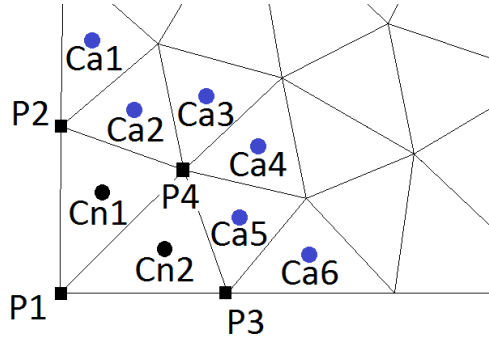
Figure 2.14: Treatment of boundary nodes

2.3.5 Time Marching Scheme and Stability Condition

The discretized equations are solved using an explicit time stepping method (see equation 2.24). Hence a stability condition has to be applied to the time marching numerical scheme. An upper bound time step can be provided by assuming that the domain is solid, which is the more limiting case due to its higher conductivity and lower specific heat. In this case the scheme may be written as:

$$\rho c_s |K| \frac{T_i^{n+1} - T_i^n}{\Delta t} = \sum_{E \in \partial K} \frac{\lambda_s}{d_{im}} \left(T_m^n - T_i^n\right) |E| + R_{nodal}$$

where the subscript m denotes the neighbouring cells of K, R_{nodal} is the sum of the nodal fluxes and d_{im} is the distance between cell centers. Separating instants $n+1$ and n on each side of the equation reads:

$$T_i^{n+1} = \left(1 - \frac{\Delta t}{\rho c_s |K|} \sum_{E \in \partial K} \frac{\lambda_s}{d_{im}} |E|\right) T_i^n + \frac{\Delta t}{\rho c_s |K|} \sum_{E \in \partial K} \frac{\lambda_s}{d_{im}} T_m^n |E| + \frac{\Delta t}{\rho c_s |K|} R_{nodal}$$

For the scheme to be monotonic, the temperature T_i^{n+1} has to be a linear combination of temperatures at time step n with positive coefficients. However, due to the presence of the nodal flux such a condition is difficult to exhibit. Thus, an approached value of the stability condition is obtained by neglecting the contribution of the nodal flux. In this case, the only coefficient which may be negative is the first one, hence the approached stability condition then reads:

$$\Delta t \leq \frac{\rho c_s |K|}{\sum\limits_{E \in \partial K} \frac{\lambda_s}{d_{im}} |E|}$$

This would return the exact stability requirement on Δt if the mesh was orthogonal. A "safety" factor of 0.8 is appied to the time step in order to account for its approached nature.

In this case the explicit formulation is justified by the fact that ice and water are not very good heat conductors. Therefore the time step is not too limited by the stability condition.

Nevertheless, it should be noted that the time step is homogeneous to h^2/α_s. Hence a too fine mesh may quickly lead to small time steps. As a first approach the explicit scheme is sufficient, but in order to speed up the computation in future work it will be necessary to use an implicit formulation. Such a formulation is not trivial due to the non linearity of the relationship between h and T.

2.3.6 Boundary Conditions

As in the case of the system heat condution module, two types of boundary conditions are considered: Dirichlet or Fourier-Robin. They are taken into account using the same method as for the system simulation module. As the time marching scheme is explicit, the flux is directly added to the right hand side in equation 2.24.

2.3.7 Gradient Reconstruction Validation

The gradient reconstruction scheme is validated by considering a linear temperature of the form : $T(x,y) = aX + bY + c$. Given the linearity of the interpolation method, the gradient reconstructed from such a linear field should be almost exact. This test is performed with the mesh shown on figure 2.15. The relative error may be defined as:

$$error = \max_K \left(\frac{\| \nabla_{num}T - \nabla_{exct}T \|_\infty}{\| \nabla_{exct}T \|_\infty} \right) \quad (2.38)$$
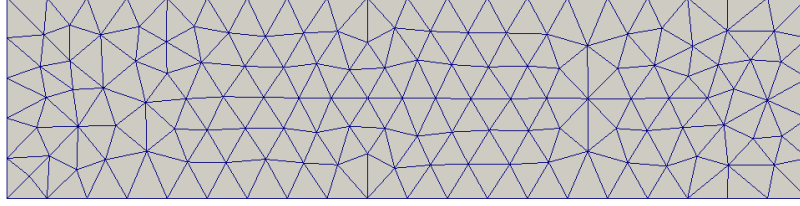
Figure 2.15: Mesh used for gradient reconstruction validation

As can be seen in figure 2.16, the gradient is computed with a relative error of 10^{-12}.
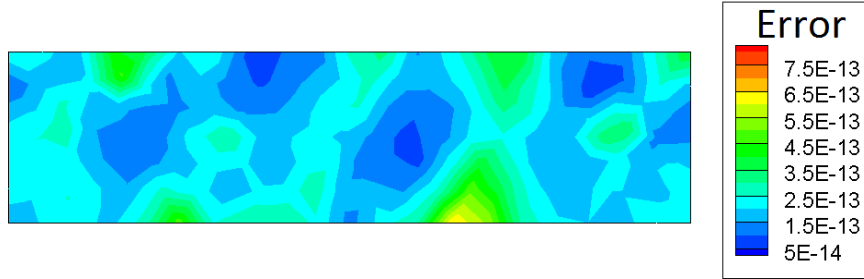
Figure 2.16: Gradient reconstruction error

2.3.8 Academic validation case

2.3.8.1 Pure Conduction: Rectangular Plate
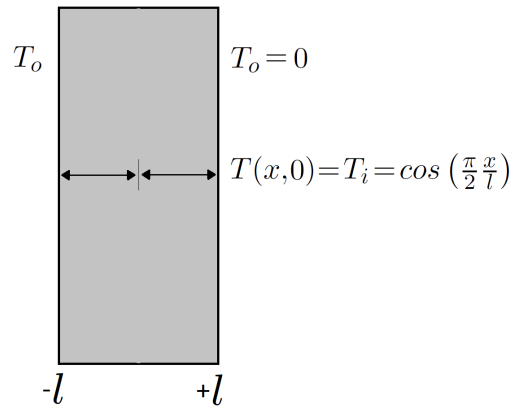
Figure 2.17: Illustration of the rectangular plate academic case

As a first step of validation a simple geometry is considered: A flat rectangular plate, made of a single material which has a fixed uniformly distributed temperature T_o on its inner and outer surfaces and a initial temperature field $T_i = cos\left(\frac{\pi}{2}\frac{x}{l}\right)$. The analytic solution then reads [60]:

$$T(x,t) = cos\left(\frac{\pi}{2}\frac{x}{l}\right) e^{-\frac{\pi^2}{4}\frac{\lambda}{\rho c_p}\frac{t}{l^2}} \tag{2.39}$$

In this academic case, ρ and λ were set to $1(SI)$ and c_p to $2(SI)$. The mesh that was used is shown in figure 2.18 and had a characteristic size of $h = 0.04m$. The time step was set to $0.0001s$ in accordance with the stability condition. An excelent match between analytical and numerical solutions is obtained.
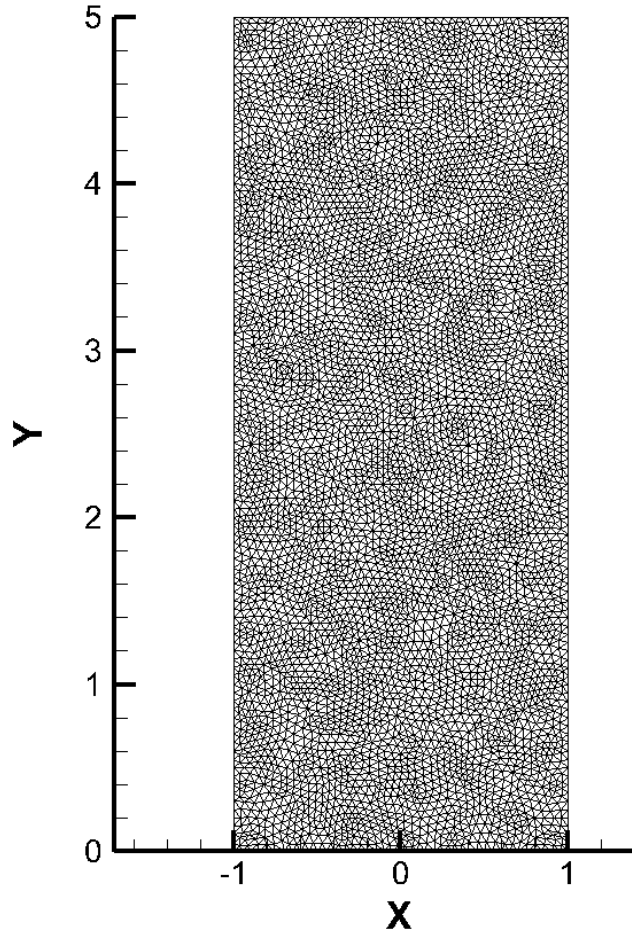
Figure 2.18: Mesh used for validation of the ice module in conduction
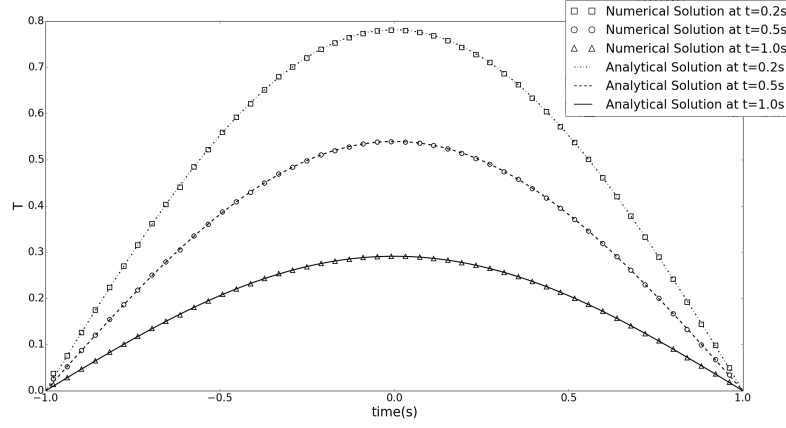
Figure 2.19: Comparison of analytical and numerical solutions

2.3.8.2 Phase Change: the Stefan Problem

As in the case of the heat transfer in the structure (section 2.2.6) it is important to assess if the numerical procedure correctly solves the mathematical equations used to model the problem. In this case a rectangular slab of ice uniformly heated at one of its surfaces is considered. The other boundaries are assumed adiabatic. The case is illustrated fig 2.20.
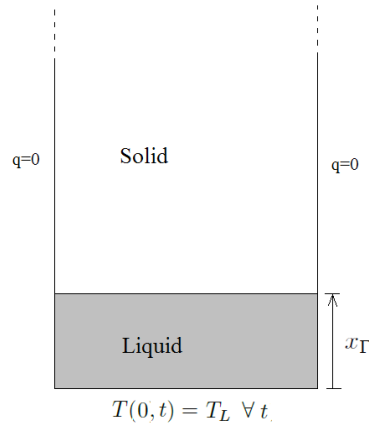
Figure 2.20: Phase change academic case

The problem reduces itself to a one dimensional one, for which analytical solutions are available [129]. In this case the position of the melting front is given by:

$$x_\Gamma(t) = 2\chi\sqrt{\alpha_l t} \tag{2.40}$$

Where α_l is the liquid thermal diffusivity and χ is the solution of the transcendental equation :

$$\frac{St_l}{e^{\chi^2} erf(\chi)} - \frac{St_s}{\nu e^{\nu^2 \chi^2} erfc(\nu\chi)} = \chi\sqrt{\pi} \tag{2.41}$$

Where the Stephan numbers St_l and St_s are defined as:

$$St_l = \frac{c_l(T_L - T_m)}{L} \qquad St_s = \frac{c_s(T_m - T(x,0))}{L} \qquad \nu = \sqrt{\frac{\alpha_l}{\alpha_s}} \tag{2.42}$$

The analytical temperature field is then given by:

$$
T(x,t) = \begin{cases} T_L - (T_L - T_m) \dfrac{erf\left(\frac{x}{2\sqrt{\alpha_l t}}\right)}{erf(\chi)} & 0 < x < x_\Gamma \\[4mm] T(x,0) + (T_m - T(x,0)) \dfrac{erfc\left(\frac{x}{2\sqrt{\alpha_s t}}\right)}{erfc\left(\chi\sqrt{\frac{\alpha_l}{\alpha_s}}\right)} & x > x_\Gamma \end{cases} \tag{2.43}
$$

In order to compare the analytical and numerical results concerning x_Γ, an integration of the numerical liquid fraction over the whole domain is performed. The result is then divided by the thickness of the slab. This yields the position x_Γ of the melting front. Moreover, so as to assess the effect of mesh size, two different meshes are considered for the computation. Their charactersitics and associated time steps are given in table 2.3.

Mesh	$h(m)$	Nb Cells	Time Step (s)
Coarse	10^{-4}	1000	$2\,10^{-3}$
Fine	10^{-5}	20000	$5\,10^{-5}$

Table 2.3: Mesh parameters for the Stephan problem

The results obtained with the coarse mesh are shown in figures 2.21 and 2.22. The numerical front position shows good agreement with the analytical one, although small deviations can be seen. Concerning the temperature field, the comparison is less good. The observed differences are due to the nature of the coarse mesh which has the effect of spreading the interface between solid and liquid phases, were in theory it should be a sharp front. This leads to a band of what is commonly called a "mushy" zone which is a mix of solid and liquid material, depending on the local value of the liquid fraction.
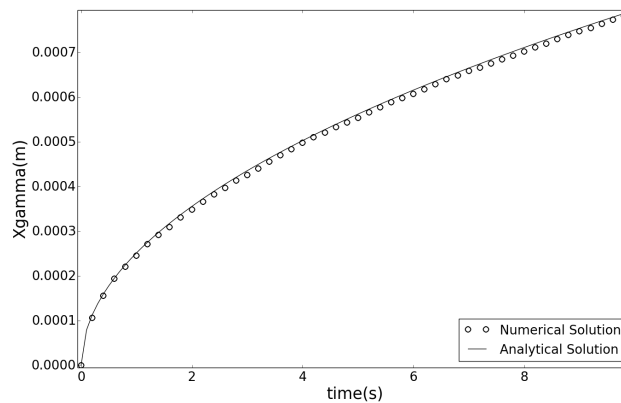
Figure 2.21: Comparison of analytical and numerical melting front positions for the coarse mesh
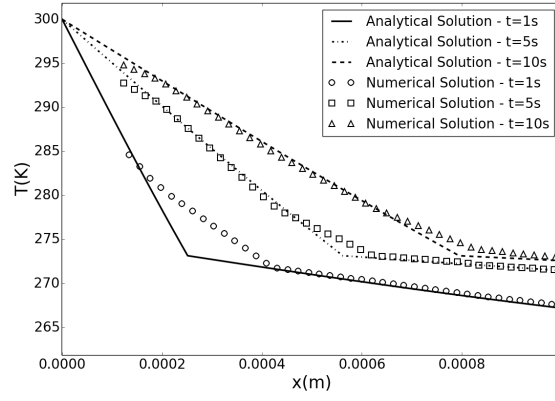
Figure 2.22: Comparison of analytical and numerical temperature profiles for the coarse mesh

On the other hand, the results obtained with the fine mesh are shown in figures 2.23 and 2.24. In this case, the front position shows improved matching with the analytical solution. Moreover, the numerical temperature field also compares very well with the analytical one. Indeed, due to the finer nature of the mesh, the melting front is much more localised, leading to a much smaller zone of mixed state material.
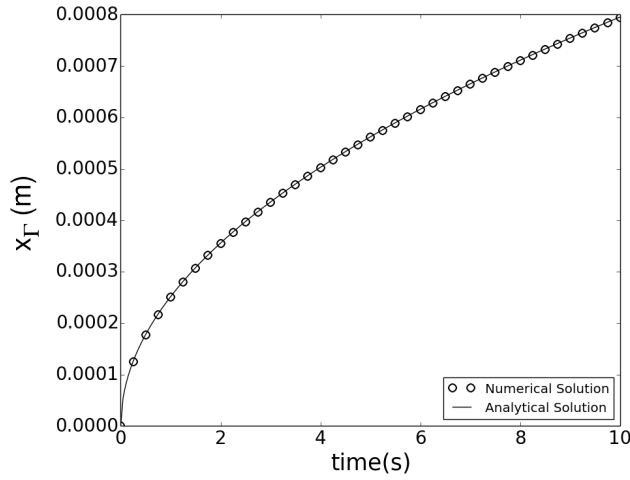
Figure 2.23: Comparison of analytical and numerical melting front positions for the fine mesh
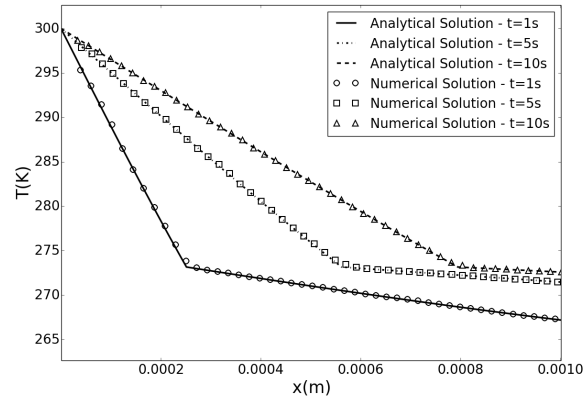
Figure 2.24: Comparison of analytical and numerical temperature profiles for the fine mesh

2.4   Coupling Procedure

So as to simulate phase change at the system/ice interface it is necessary to couple both modules. To do so an explicit coupling procedure is chosen. The meshes are built in such a way that their respective edges at the interface are matching, therefore becoming common to both domains (see figure 2.25). When either assembling the diffusion matrix in the case of the system solver, or the explicit flux in the case of the ice solver, those interfacial edges are hence no longer considered as boundary edges. They provide a connection to the corresponding cell of the adjacent domain.
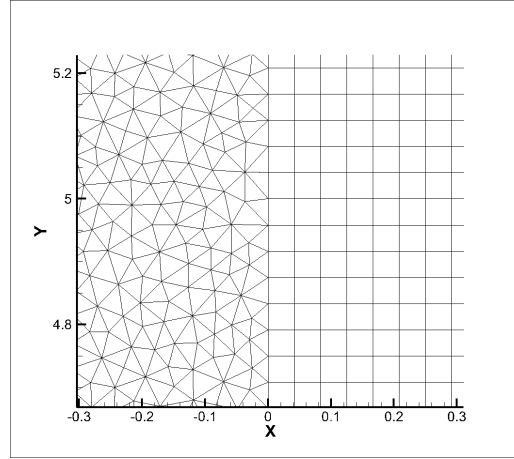
Figure 2.25: Mesh matching at the interface

The flux on an interfacial edge is computed using the method of the interfacial temperature T^*, as illustrated in figure 2.26. The interfacial flux on both sides can be written in terms of T^*. Equating both normal fluxes yields the interface temperature T^*. The flux is then computed in an analogous way to the procedure yielding formula (2.12).
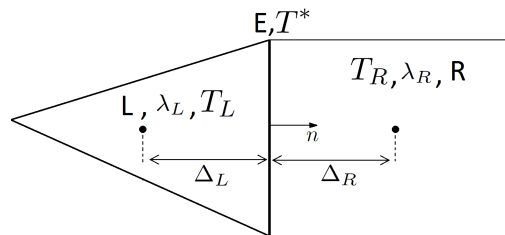
Figure 2.26: Adjacent cells at interface

The efficiency of this coupling procedure is validated with the hollow cylinder case (using the same physical parameters). A close up on the mesh is shown in figure 2.27. Each domain, ice and system, are meshed with 12000 elements, leading to a characteristic mesh size of $1.5\,10^{-2}m$. The time step is fixed by the stability condition in the ice domaine and therefore set to $5\,10^{-6}s$. With respect to the discussion of section 2.2.6, this corresponds to a non-dimensional time step of $2.4\,10^{-5}$, which means that the conduction time scale is correctly resolved. In this case as well, very good agreement is obtained (see figure 2.28).
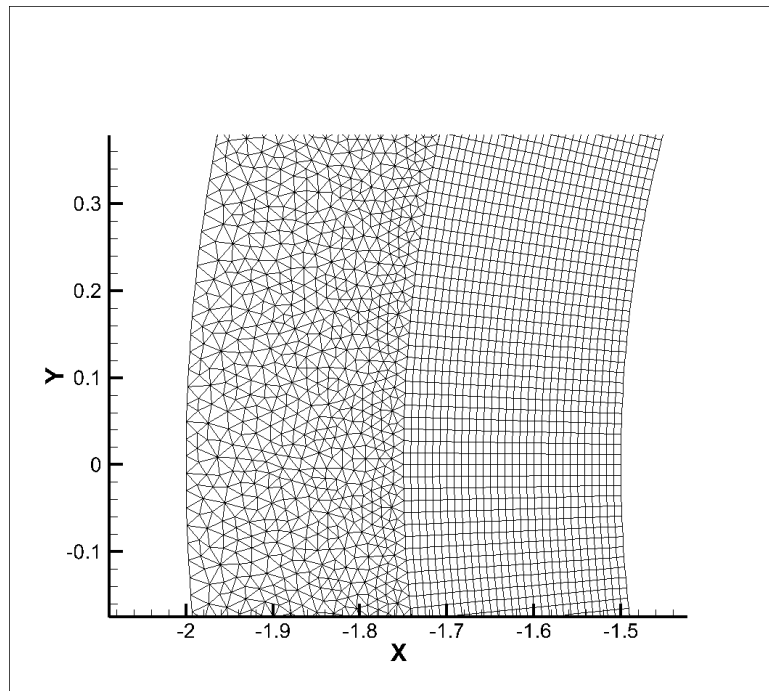
Figure 2.27: Mesh for coupling procedure validation
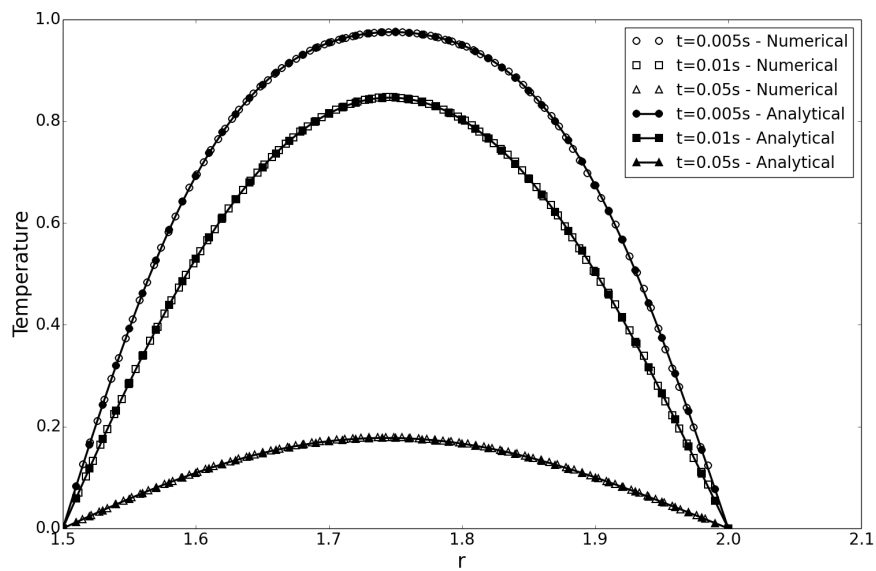
Figure 2.28: Comparison of analytical and numerical solutions

Figure 2.29 shows an illustrative application to a more practical problem. We can see the regions where the heater mats are active. The heat thus provided is transmitted to the interface and acts to melt the ice.
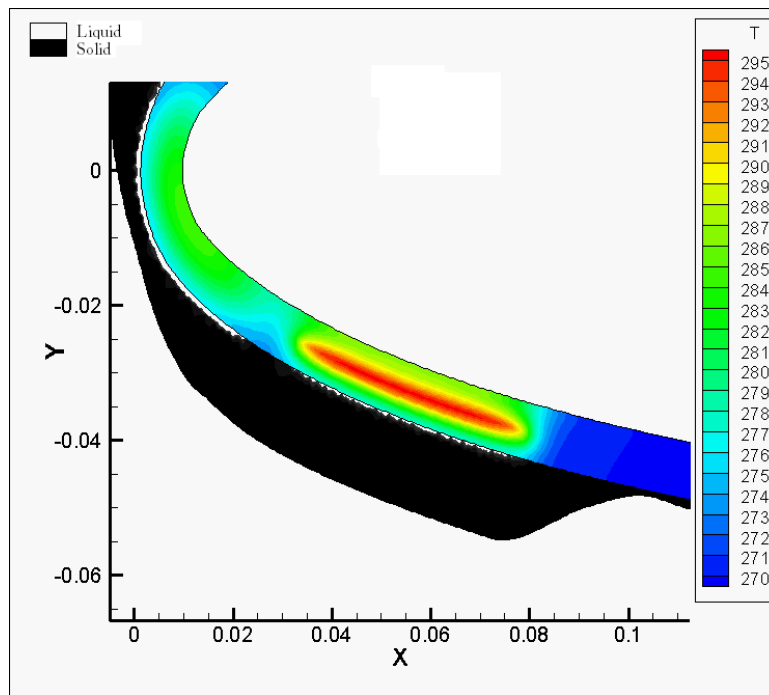
Figure 2.29: Simulation of ETIPS with ice block

The aim of this chapter is to present the modelling and numerical strategy adopted to simulate the cracking of the ice block. This method will subsequently be used to investigate ice shedding mechanisms. The first sections of this chapter give an overview of fracture mechanics. Then, the chosen model and numerical method are presented. After which a validation and model assessment analysis is performed.

Contents

3.1 Generalities

From a macroscopic point of view, the phenomenon of cracking occurs when a material is loaded above its critical yield strength. At the microscopic level, a material is never perfect. In fact, a certain number of defects are embedded into its structure. These imperfections may be point defects (vacancies, impurities), line defects (dislocations), planar defects (stacking faults, grain boundaries) or bulk defects (voids). Examples of point defects and grain boundaries will be given in section 4 and appendix C. The other types of defects will not be described in further detail. Suffice it to say that some of these defects move inside the material. Indeed under sufficient stress the atoms or molecules in the neighborhood of a defect rearrange their bonds creating a displacement of the defect. Due to their mobility these defects (especially dislocation) are known to pile up leading to high stress concentrations and which can act to break molecular bonds along crystal lattice planes [26].

Returning to a more macroscopic picture, there are two main behaviours a material can exhibit with respect to fracture: brittle or ductile. Brittle failure occurs when crack propagation is preceded by no (or very little) plastic deformation. On the other hand, ductile failure occurs after significant plastic deformation. In both cases, crack propagation is usually accompanied by plastic deformation at the crack tip. As will be seen in section 4, the behaviour of ice is predominantly brittle and therefore the chosen methodology will be one adapted to brittle failure.

3.2 Modelling of Fracture: Literature Review

In this section, classical aspects of fracture mechanics are briefly reviewed. Following this, several numerical methods and models are presented. However it should be noted that the list is not exhaustive and serves to give an overview of existing methods.

It is considered that there are three main failure modes which depend on the way the external loads are applied to a structure. As shown in figure 3.1 mode I is a purely tensile crack opening mode, mode II is a pure shear tearing mode and finally mode III is an out of plane shear tearing mode [137].
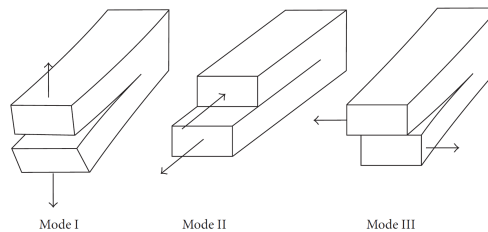
Figure 3.1: The various failure modes [137]

One of the first attempts to describe crack propagation goes back to the works of Griffith [2]. At that time, discrepancies were observed between theoretically predicted material strength and experimental measurments. To overcome this issue Griffith chose to attack the problem from the point of view of minimal potential energy. He considered that if a cracked equilibrium state is possible, then that state minimizes the potential energy of the whole system. In order to apply this principle, Griffith used elastic strain energies but also surface energies in order to account for the new surfaces appearing due to the fracture process. From this analysis he deduced an energetic failure criterion introducing the concept of strain energy release rate, usually noted g, which represents the dissipated energy per unit of newly created fractured area.

Griffith's approach also showed that some of the most essential features of crack propagation are concentrated near the crack tip [63]. A linear elastic analysis of the high stress concentration at the crack tip yields a singular stress distribution in that region. This analysis led Irwin, during the 50's, to introduce the concept of stress intensity factor, usually noted K (also K_I, K_{II} or K_{III} depending on the failure mode). They represent the intensity of the singularity at the crack tip. For example, for a plane stress elastic formulation, K_I may be defined as:

$$K_I = \lim_{r \to 0} \left(\frac{E}{8} \sqrt{\frac{2\pi}{r}} [\![u_2]\!] \right)$$

where $[\![u_2]\!]$ represents the jump of the displacement component u_2 across the crack. The singular stress field may then be written as:

$$\sigma_{ij} = \frac{K}{\sqrt{2\pi r}} f_{ij}(r, \theta)$$

where (r, θ) is a polar coordinate system whose origine is at the crack tip (see figure 3.2) and f_{ij} are functions which take various forms depending on the failure mode [63]. This analysis is at the basis of Linear Elastic Fracture Mechanics (LEFM).
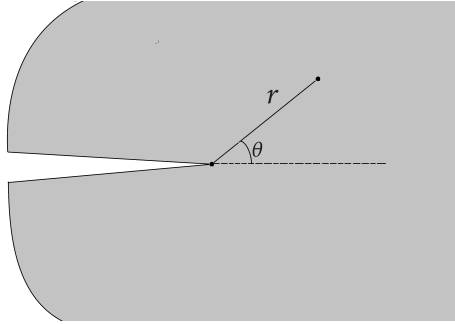
Figure 3.2: Polar coordinate development at crack tip

Fracture mechanics is a rich and complex domaine and many additional theoretical contributions were made over the years, such as the J-integral concept introduced by Rice [66]. However these aspects will not be presented in further detail.

3.2.1 Remeshing

One of the simplest ways of predicting crack propagation through a material is to use a crack propagation law and remesh the domain accordingly at each step. Cracking criteria deduced from LEFM include [137]:

1. Maximum principal stress: when the maximal principal stress $\sigma_{\theta\theta}$ exceeds a critical value σ_c then the crack is propagated in the direction perpendicular to the corresponding principal direction. The maximal principal stress is given by:

$$\sigma_{\theta\theta} = \frac{K_I}{\sqrt{2\pi r}} f_{ij}^I(r, \theta) + \frac{K_{II}}{\sqrt{2\pi r}} f_{ij}^{II}(r, \theta)$$

In other words, the crack will propagate according to the angle θ which maximizes $\sigma_{\theta\theta}$.

2. Maximum energy release rate: the crack is propagated in the direction which maximizes the energy release rate g.

3. $K_{II} = 0$: this criterion is based on the fact that in an isotropic medium, cracks propagate so as to maintain mode I failure at the crack tip [63].

It should be noted that criteria based on other concepts, such as configurational forces [81, 30], also exist.

3.2.2 XFEM

The eXtended Finite Element Method was originally developed by Belytschko [130] based on ideas of Melenk and Babuska [64]. The main idea is to use the concept of partition of unity to build enriched finite elements [131]. The displacement field is decomposed into a continuous and discontinuous part. The continous part is treated through standard finite element procedure. On the other hand the discontinuous part is treated through the use of an enrichment function and concepts of local partition of unity. An XFEM displacement field may therefore be written as:

$$\boldsymbol{u}^{XFEM} = \boldsymbol{u}^{cont} + \boldsymbol{u}^{enr}$$

The continuous displacement field is described with standard FEM shape functions λ_i:

$$\boldsymbol{u}^{cont} = \sum_i \lambda_i \boldsymbol{u}_i$$

As for the discontinuous displacement it is constituted of two parts, one to treat the part completely cut by the crack (noted S_c) and another to treat the specific behaviour around the crack tips (S_{ct} denotes the set of nodes around the crack tips):

$$\boldsymbol{u}^{enr} = \sum_{i \in Sc} b_i H \lambda_i + \sum_{i \in Sct} \sum_{j=1}^{4} c_{ij} F_j \lambda_i$$

where H is a Heaviside-like step function, F_j is a set of functions which characterize near tip behaviour and b_i and c_{ij} are additional enrichment degrees of freedom [109]. Figure 3.3 illustrates a possible repartition of crack tip nodes and crack nodes.
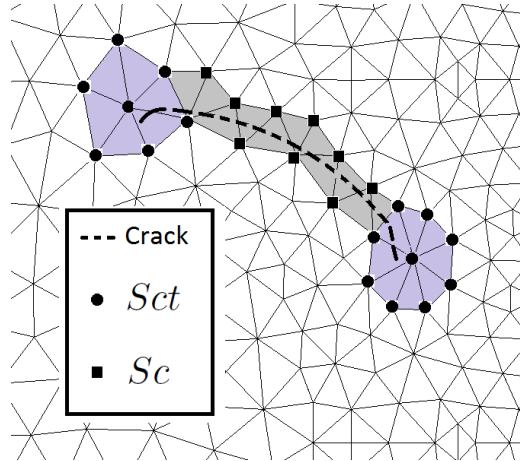
Figure 3.3: Illustration of crack tip and crack nodes

It should be noted that XFEM is a numerical framework to simulate crack propagation with minimal remeshing at every iteration. But it does not naturally incorporate crack nucleation and propagation. Therefore, formulation of crack nucleation and propagation laws is still required.

The XFEM method being quite general, it may also be applied to problems of dislocation or phase boundary evolution and also problems involving grain boundaries [131].

3.2.3 Cohesive Zone Model

Cohesive zone models originate in the 60's with the works of Dugdale [28] and Barenblatt [42]. The main idea is to concentrate the non-linear fracture phenomena into a cohesive or process zone located in the neighborhood of the crack tip [137]. The debonding process is then characterized thanks to a cohesive law relating traction T to crack tip opening displacement Δ. In its most simple setting the bulk of the material may follow a linear elastic constitutive law. A cohesive surface constitutive law is added to treat the cohesive surfaces enabling spontaneous crack nucleation and growth. The general process may be described in the following way [80]:

1. The bulk is governed by a linear elastic constitutive law (Zone 1 in figure 3.5).

2. Once the traction T reaches a critical value σ_c a crack will nucleate (Zone 2 in figure 3.5).

3. The crack then grows following the cohesive constitutive law (Zone 3 in figure 3.5).

4. The process ends when complete failure is reached ($\Delta = \Delta_c$), leading to the creation of two traction free surfaces (Zone 4 in figure 3.5).
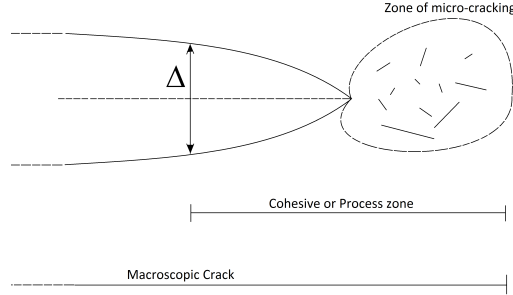
Figure 3.4: Illustration of cohesive process zone and crack tip opening displacement [137]
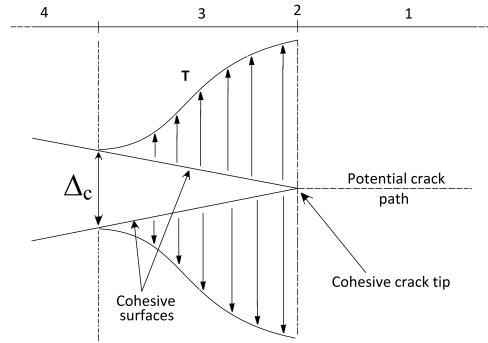
Figure 3.5: Illustration of cohesive zone modelling [80]

3.2.4 Variational Approach

The variational approach to fracture is mainly due to the work of Francfort and Marigo [36]. The method is based on an energy minimisation principle by defining the surface energy (in n-D) associated to a crack Γ:

$$E_c = \int_\Gamma g(x) d\mathcal{H}^{n-1}$$

where $\mathcal{H}^{n-1}$ is the $(n-1) - D$ Hausdorff measure and $g(x)$ is the energy density associated to the formation of an infinitesimal crack at x. For a smooth enough crack topology $\mathcal{H}^{n-1}(\Gamma)$ corresponds to the length of the crack in $2 - D$ and to its surface in $3 - D$.

The potential energy is then defined as:

$$E_p = \int_{\Omega \setminus \Gamma} W(\boldsymbol{\epsilon}) dV + \int_\Gamma g(x) d\mathcal{H}^{n-1}$$

where $W(\boldsymbol{\epsilon})$ is the bulk energy density. The resulting crack topology is that which minimizes E_p. This method is defined in a quasi-static framework. A way of imposing the irreversible behaviour of crack propagation is to consider that if s is a given step of the quasi-static process, then $\Gamma(s)$ contains all the previous crack topologies.

It is interesting to note that this kind of method incorporates crack propagation as well as crack nucleation. Due to this fact and to its flexibility, a model based on this method is adapted so as to construct the modelling and numerical strategy used in this work.

3.3 Modelling and Numerical Method

Modelling techniques based on continuum mechanics have already been applied to ice. Scavuzzo *et al.* performed a finite element analysis of the stress distribution due to aerodynamic forces in an accreted ice block [118]. More recently, Zhang *et al.* have used a crack propagation and re-meshing technique (based on the maximum principal stress criterion) to study ice break up [1]. However these studies did not take into account the effect of an ice protection system.

The equations which will be presented further will be solved in two dimensions. In elasticity, there are two possible formulations in two dimensions: plane stress or plane strain. Plane stress corresponds to the case of a medium which is very thin in the out of plane direction. Plane strain corresponds to the case where the dimension of the medium in the out of plane direction is very big compared to the other dimensions. In these formulations, the Lamé coefficient μ remains unchanged and λ takes the following expression:

$$\lambda = \begin{cases} \frac{E\nu}{(1-2\nu)(1+\nu)} & \text{plane strain} \\ \frac{E\nu}{(1-\nu^2)} & \text{plane stress} \end{cases}$$

Here we choose to use a method close to those of continuum damage mechanics. In the following paragraph we construct our model by adapting the approach adopted by Miehe *et al* [24], which is based on the variational approach of Francfort and Marigo [36]. The idea is to introduce a parameter d that characterises the local state of damage/fracture [63] in the ice block. The starting point is a principle of conservation of energy [2] whose physical motivation is the following: When a solid is deformed by action of external forces, it internally stores elastic deformation energy. If, locally, this energy exceeds a certain critical energy then it will cause an increase in crack surface. Therefore, if a crack nucleates and/or propagates, a possible mechanism (from a macroscopic point of view) is a process of energy transfer from the applied forces to elastic deformation energy, which in turn may be transformed into crack surface energy. Figure 3.6 illustrates this transfer from elastic to crack energy.
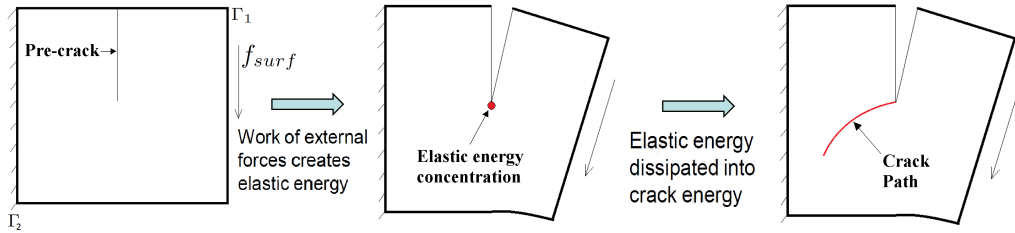
Figure 3.6: Energy transfer in crack opening mode

The main input parameters required for the model are a crack surface energy (3.2) and an elastic energy (3.8). Let $\psi(\boldsymbol{\epsilon}, d)$ be the elastic strain energy per unit volume, and $\phi(d, \boldsymbol{\nabla} d)$ be the fracture energy per unit volume. $\boldsymbol{\epsilon} = \frac{1}{2}(\nabla \boldsymbol{u} + (\nabla \boldsymbol{u})^T)$ is the strain and $\boldsymbol{u}$ the displacement field. Therefore the total elastic energy will be $E_{el} = \int_\Omega \psi(\boldsymbol{\epsilon}, d) dV$ and the total crack energy will be $E_{crack} = \int_\Omega \phi(d, \boldsymbol{\nabla} d) dV$. When external forces are applied, the change in energy is equal to the work produced by those forces. Thus we have:

$$\delta E_{crack} + \delta E_{el} = \int_\Omega \boldsymbol{f}_{vol}.\delta \boldsymbol{u} \, dV + \int_{\Gamma_1} \boldsymbol{f}_{surf}.\delta \boldsymbol{u} \, d\Gamma \tag{3.1}$$

where $\boldsymbol{f}_{vol}$ is a volume force, Γ_1 is a part of the boundary $\partial\Omega = \Gamma_1 \cup \Gamma_2$ where a surface force $\boldsymbol{f}_{surf}$ is applied. Γ_2 is the part of the boundary where a displacement $\boldsymbol{u}_d$ is imposed.

The crack energy is obtained by using a regularized crack energy functional given by Bourdin *et al.* [14].

$$E_{crack} = \int_\Omega \phi(d, \boldsymbol{\nabla} d) dV = \int_\Omega g_c [\frac{1}{2l} d^2 + \frac{l}{2} \boldsymbol{\nabla} d.\boldsymbol{\nabla} d] dV \tag{3.2}$$

where g_c is the crack energy release rate, the damage variable d lies between 0 and 1 ($d(x) = 0$ corresponding to an undamaged state and $d(x) = 1$ to a fractured state).

The term $\frac{1}{2l} d^2 + \frac{l}{2} \boldsymbol{\nabla} d.\boldsymbol{\nabla} d$ can be interpreted as a regularized approximation of the Dirac δ-function related to the crack surface. l is an adjustable parameter that controls the width of the regularized crack. From a minimization of surface energy view point, the regularization involves an interplay between $\frac{1}{2l} d^2$ which tends to localize and $\frac{l}{2} \boldsymbol{\nabla} d.\boldsymbol{\nabla} d$ which tends to spread. The elastic energy density will be defined in more detail further.

Using relation (3.2) and integrating by parts yields :

$$\delta E_{crack} = \int_\Omega \left[\frac{g_c}{l} d - g_c l \triangle d \right] \delta d \, dV + \int_{\partial\Omega} g_c l \boldsymbol{\nabla} d.\boldsymbol{n} \delta d \, d\Gamma \tag{3.3}$$

where n is the outward normal unit vector.

Using (3.3) and $\delta E_{el} = \int_\Omega \left[\frac{\partial \psi}{\partial \boldsymbol{\epsilon}} : \delta \boldsymbol{\epsilon} + \frac{\partial \psi}{\partial d} \delta d \right] dV$ we find:

$$\int_\Omega \left[\frac{\partial \psi}{\partial \boldsymbol{\epsilon}} : \delta \boldsymbol{\epsilon} + \left[\frac{\partial \psi}{\partial d} + \frac{g_c}{l} d - g_c l \triangle d \right] \delta d \right] dV + \int_{\partial\Omega} g_c l \boldsymbol{\nabla} d.n \delta d \, d\Gamma = \int_\Omega \boldsymbol{f}_{vol}.\delta \boldsymbol{u} \, dV + \int_{\Gamma_1} \boldsymbol{f}_{surf}.\delta \boldsymbol{u} \, d\Gamma$$

Moreover, the mechanical boundary condition gives us :

$$\int_{\partial\Omega} \boldsymbol{f}_{surf}.\delta \boldsymbol{u} \, d\Gamma = \int_{\partial\Omega} \boldsymbol{\sigma}.\boldsymbol{n} \delta \boldsymbol{u} \, d\Gamma = \int_\Omega div(\boldsymbol{\sigma}) \delta \boldsymbol{u} \, dV + \int_\Omega \boldsymbol{\sigma} : \nabla \delta \boldsymbol{u} \, dV \tag{3.4}$$

As the Cauchy stress tensor is symmetric, we also have $\boldsymbol{\sigma} : \nabla \delta \boldsymbol{u} = \boldsymbol{\sigma} : \delta \boldsymbol{\epsilon}$. Therefore:

$$\int_\Omega \boldsymbol{f}_{vol} \delta \boldsymbol{u} \, dV + \int_{\partial\Omega} \boldsymbol{f}_{surf} \delta \boldsymbol{u} \, d\Gamma = \int_\Omega [div(\boldsymbol{\sigma}) + \boldsymbol{f}_{vol}] \delta \boldsymbol{u} \, dV + \int_\Omega \boldsymbol{\sigma} : \delta \boldsymbol{\epsilon} \, dV$$

Given the mechanical equilibrium relation $div(\boldsymbol{\sigma}) + \boldsymbol{f}_{vol} = 0$, relation (3.1) reduces to :

$$\int_\Omega \left[\frac{\partial \psi}{\partial \boldsymbol{\epsilon}} - \boldsymbol{\sigma} \right] : \delta \boldsymbol{\epsilon} \, dV + \int_\Omega \left[\frac{\partial \psi}{\partial d} + \left[\frac{g_c}{l} d - g_c l \triangle d \right] \right] \delta d \, dV + \int_{\partial\Omega} g_c l \boldsymbol{\nabla} d.n \delta d \, d\Gamma = 0$$

This relation has to hold for every δd and $\delta \boldsymbol{\epsilon}$. Hence (3.5) :

$$\begin{array}{ll} \boldsymbol{\sigma} = \frac{\partial \psi}{\partial \boldsymbol{\epsilon}} & \text{in } \Omega \\ \frac{g_c}{l} d - g_c l \triangle d = -\frac{\partial \psi}{\partial d} & \text{in } \Omega \\ \boldsymbol{\nabla} d.n = 0 & \text{on } \partial\Omega \end{array} \tag{3.5}$$

The stress tensor $\boldsymbol{\sigma}$ is deduced from the choice of ψ. In the case of a linear homogeneous isotropic elastic material, the elastic energy is given by: $\psi(\boldsymbol{\epsilon}) = \frac{\lambda}{2} tr(\boldsymbol{\epsilon})^2 + \mu tr(\boldsymbol{\epsilon}^2)$. However, considering $-\frac{\partial \psi}{\partial d}$ is the source term, the driving force of the fracture process, ψ must also be chosen according to what part of the elastic deformation energy creates or propagates a crack. It is considered that in the case of brittle fracture, only the tensile energy interacts with crack propagation. Thus the elastic energy is split into purely tensile and compressive parts defined by using the eigenvalues of $\boldsymbol{\epsilon}$ (ϵ_1 and ϵ_2 in two dimension) and a positive/negative part function noted $< . >_\pm$:

$$\psi_0^+(\boldsymbol{\epsilon}) = \frac{\lambda}{2} < \epsilon_1 + \epsilon_2 >_+^2 + \mu(< \epsilon_1 >_+^2 + < \epsilon_2 >_+^2) \tag{3.6}$$

$$\psi_0^-(\boldsymbol{\epsilon}) = \frac{\lambda}{2} < \epsilon_1 + \epsilon_2 >_-^2 + \mu(< \epsilon_1 >_-^2 + < \epsilon_2 >_-^2) \tag{3.7}$$

ψ_0^+ and ψ_0^- represent respectively the undamaged tensile and compressive elastic energies. As stated before, only tensile energy interacts with crack propagation. Thus only $\psi_0^+(\boldsymbol{\epsilon})$, the tensile part, is multiplied by a function of d, say $f(d)$. The function $f(d)$ represents the degradation of tensile energy due to crack formation and is chosen accordingly:

$$E_{el} = \int_\Omega [f(d)\psi_0^+(\boldsymbol{\epsilon}) + \psi_0^-(\boldsymbol{\epsilon})]dV \tag{3.8}$$

Therefore f is a non increasing function, $f(0) = 1$ and $f(1) = 0$. Moreover, when $d = 1$ it is asked that the driving force $-\frac{\partial \psi}{\partial d} = -f'(d)\psi_0^+(\boldsymbol{\epsilon})$ be equal to 0. To do so the additional condition $f'(1) = 0$ is imposed. Under these conditions Miehe *et al* [24] proposed the function $f(d) = (1 - d)^2$. Using these new relations the complete set of equations becomes :

$$\begin{aligned}
-div(\boldsymbol{\sigma}(\boldsymbol{u}, d)) &= \boldsymbol{f}_{vol} & \text{in } \Omega \\
\boldsymbol{\sigma}.n &= \boldsymbol{f}_{surf} & \text{on } \Gamma_1 \\
\boldsymbol{u} &= \boldsymbol{u}_d & \text{on } \Gamma_2 \\
\frac{g_c}{l}d - g_c l \triangle d &= 2(1-d)\psi_0^+(\epsilon) & \text{in } \Omega \\
\boldsymbol{\nabla} d.n &= 0 & \text{on } \partial\Omega
\end{aligned} \tag{3.9}$$

Equations (3.9) are nonlinear and describe a stationary damaged equilibrium state compatible with the external constraints. They translate conservation of energy. In order to incorporate the irreversible aspect of crack propagation, Miehe *et al* [24] introduce a history function $\mathcal{H}$. They propose the following kind of iterative algorithm, which we have implemented using a finite element method:

- Compute the history field:
$$\mathcal{H}^i = max(\mathcal{H}^{i-1}, \psi_0^+(\boldsymbol{\epsilon}^{i-1})) \tag{3.10}$$

- Compute the damage field:

$$\frac{g_c}{l}d^i - g_c l \triangle d^i = 2(1 - d^i)\mathcal{H}^i \qquad\qquad \text{in } \Omega \tag{3.11}$$

$$\nabla d^i.n = 0 \qquad\qquad \text{on } \partial\Omega \tag{3.12}$$

- Compute the displacement field:

$$-div(\boldsymbol{\sigma}^i(\boldsymbol{\epsilon}^i, d^i)) = \boldsymbol{f}_{vol} \qquad\qquad \text{in } \Omega \tag{3.13}$$

$$\boldsymbol{\sigma}^i.n = \boldsymbol{f}_{surf} \qquad\qquad \text{on } \Gamma_1 \tag{3.14}$$

$$\boldsymbol{u}^i = \boldsymbol{u}_d \qquad\qquad \text{on } \Gamma_2 \tag{3.15}$$

The algorithm is initialised by performing a first purely linear elastic computation.

This algorithm can be interpreted as follows. Let's assume a first purely elastic computation has been realized as an initialisation. The locally available tensile energy may then be computed. This energy then becomes a source term for the damage equation. The evolution of damage then changes the way the material deforms. The new deformed state is obtained by solving the equilibrium equation, which in turn gives us a new tensile energy, and so on.

However, it is not exactly the tensile energy that is used to define the source term for the damage equation. Rather, it is a history function noted $\mathcal{H}$. If we consider the iterative process as pseudo-unsteady, the use of the history function can be interpreted in the following manner: At a given iteration i the tensile energy could locally be inferior to its value at iteration $i - 1$. Thus if, at a given iteration $d = 1$, nothing is preventing it from decreasing at any following iteration. But, clearly in our case, the problem of crack propagation is irreversible: d should not be allowed to decrease. Thus the history function $\mathcal{H}$ aims at taking into account the irreversibility of the crack propagation process. It records, locally, the maximum of the tensile energy over all iterations. This history function then becomes a source term for the equation that governs the evolution of damage. Intuitively, if at a given iteration there was enough tensile energy to increase the damage variable d, then this information will be contained in $\mathcal{H}$ for the following iteration. Nevertheless further investigation remains to be done in order to determine the relevance of this pseudo-unsteady interpretation.

The main advantage of this method is that it does not require an initial crack. On the other hand it should be noted that the main drawback is the need of a refined mesh. Especially in the case of imposed boundary load, the crack tends to spread if the mesh is not refined enough.

3.4 Numerical Method

In order to solve the previously presented problem a finite element procedure is implemented using Lagrange P1 shape functions (noted λ_i). The elements are always triangles and their nodes are noted a_i (see figure 3.7). Thanks to the shape functions, a function of interest can be represented locally over a given cell with te relation: $d_K = \sum_i d(a_i)\lambda_i$. Specific aspects relevant to each subproblem (history function, damage equation and equilibrium equation) are presented in the following subsections.
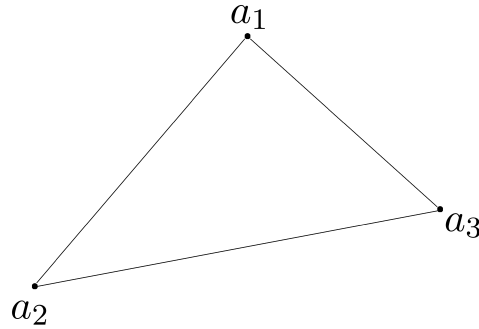
Figure 3.7: Finite element triangle

3.4.1 History Function

By definition, the history function $\mathcal{H}$ is locally equal to the maximum of tensile strain energy ψ_0^+. Its evaluation therefore requires computing the strain tensor first. As the chosen shape function are Lagrange P1, the strain tensor is constant on each cell of the mesh. On a given cell K, the characteristic polynomial of the two dimensional strain tensor has the well known form:

$$\chi = X^2 - tr(\boldsymbol{\epsilon}_K)X + det(\boldsymbol{\epsilon}_K) \tag{3.16}$$

The discriminant of this polynomial, $\Delta = tr(\boldsymbol{\epsilon}_K)^2 - 4det(\boldsymbol{\epsilon}_K) = (\epsilon_{11,K} - \epsilon_{22,K})^2 + 4\epsilon_{12,K}^2$, is always positive. The eigen values needed to define the tensile strain energy are therefore real and given by:

$$\epsilon_{1/2,K} = \frac{1}{2}\left(tr(\boldsymbol{\epsilon}_K) \pm \sqrt{\Delta}\right) \tag{3.17}$$

The tensile strain energy is then computed using (3.6):

$$\psi_{0,K}^+(\boldsymbol{\epsilon}) = \frac{\lambda}{2} < \epsilon_{1,K} + \epsilon_{2,K} >_+^2 + \mu(< \epsilon_{1,K} >_+^2 + < \epsilon_{2,K} >_+^2) \tag{3.18}$$

The associated eigen vectors may also be computed using standard methods of linear algebra. They are required to compute the projection operators defining the stress tensor (see section 3.4.3 and appendix A). The eigen vectors read:

$$\boldsymbol{V_1} = \begin{bmatrix} \frac{\epsilon_{12}}{\epsilon_1 - \epsilon_{11}} \\ 1 \end{bmatrix} \quad \boldsymbol{V_2} = \begin{bmatrix} \frac{\epsilon_{12}}{\epsilon_2 - \epsilon_{11}} \\ 1 \end{bmatrix} \quad \text{if } \epsilon_{12} \neq 0 \tag{3.19}$$

$$\boldsymbol{V_1} = \begin{bmatrix} 1 \\ 0 \end{bmatrix} \quad \boldsymbol{V_2} = \begin{bmatrix} 0 \\ 1 \end{bmatrix} \quad \text{if } \epsilon_{12} = 0 \tag{3.20}$$

3.4.2   Damage Equation

The weak formulation associated to (3.11) is:

$$\int_\Omega \left[\frac{g_c}{l} + 2\mathcal{H}\right] dv\, dV + \int_\Omega g_c l \boldsymbol{\nabla} d.\boldsymbol{\nabla} v\, dV = \int_\Omega 2\mathcal{H}v\, dV \tag{3.21}$$

As the he domain Ω is partitioned into cells K, the integrals over Ω are split into sums:

$$\sum_K \int_K \left[\frac{g_c}{l} + 2\mathcal{H}\right] dv\, dV + \sum_K \int_K g_c l \boldsymbol{\nabla} d.\boldsymbol{\nabla} v\, dV = \sum_K \int_K 2\mathcal{H}v\, dV \tag{3.22}$$

This equation does not present any specific discretization difficulties. Using classical finite element assembly procedures, equation 3.22 yields the global linear system:

$$A_d[d] = L_d \tag{3.23}$$

Solving this linear system provides the value of d at each node of the mesh. A direct solver based on the LU decomposition is used to solve the linear system.

3.4.3   Equilibrium Equation

The weak formulation associated to (3.13) is:

$$\int_\Omega \boldsymbol{\sigma}(\boldsymbol{u}) : \boldsymbol{\epsilon}(\boldsymbol{v})\, dV = \int_\Omega \boldsymbol{f}_{vol}.\boldsymbol{v}\, dV + \int_{\Gamma_1} \boldsymbol{\sigma}.\boldsymbol{n}.\boldsymbol{v}\, d\Gamma \tag{3.24}$$

Considering the stress tensor $\boldsymbol{\sigma}$ and the strain tensor $\boldsymbol{\epsilon}$ are symmetric, the contracted product $\boldsymbol{\sigma}(\boldsymbol{u}) : \boldsymbol{\epsilon}(\boldsymbol{v})$ may be expressed as:

$$\boldsymbol{\sigma}(\boldsymbol{u}) : \boldsymbol{\epsilon}(\boldsymbol{v}) = [\epsilon]^T [\sigma]$$

where $[\epsilon]^T = [\epsilon_{11}\ \ \epsilon_{22}\ \ 2\epsilon_{12}]$ and $[\sigma]^T = [\sigma_{11}\ \ \sigma_{22}\ \ \sigma_{12}]$

Therefore equation (3.24) is rewritten as:

$$\sum_K \int_K [\epsilon]_K^T [\sigma]_K\ dV = \sum_K \int_K v^T f_{vol}\, dV + \sum_K \int_{K\cap\Gamma_1} v^T f_{surf}\, d\Gamma$$

The stress tensor $\boldsymbol{\sigma}$ derives from the definition of the elastic energy and takes the form:

$$\boldsymbol{\sigma} = \frac{\partial \psi}{\partial \boldsymbol{\epsilon}} = f(d)\left[\lambda < tr(\boldsymbol{\epsilon}) >_+ \mathbb{1} + 2\mu\boldsymbol{\epsilon}_+\right] + \left[\lambda < tr(\boldsymbol{\epsilon}) >_- \mathbb{1} + 2\mu\boldsymbol{\epsilon}_-\right]$$

The problem here is that stress and strain are no longer linked by a linear constitutive law. The definition above involves non linear functions such as the positive part $< . >_+$ and is based on the following splitting of strain into tensile and compressive parts:

$$\epsilon = \boldsymbol{\epsilon}_+ + \boldsymbol{\epsilon}_-$$

Differentiating this relation with respect to $\boldsymbol{\epsilon}$ yields:

$$\mathbb{1} = \frac{\partial \boldsymbol{\epsilon}_+}{\partial \boldsymbol{\epsilon}} + \frac{\partial \boldsymbol{\epsilon}_-}{\partial \boldsymbol{\epsilon}} = \mathbb{P}^+ + \mathbb{P}^-$$

And therefore the splitting of $\boldsymbol{\epsilon}$ may be rewritten as:

$$\boldsymbol{\epsilon} = \underbrace{\mathbb{P}^+}_{\partial_{\boldsymbol{\epsilon}}\boldsymbol{\epsilon}_+} : \boldsymbol{\epsilon} + \underbrace{\mathbb{P}^-}_{\partial_{\boldsymbol{\epsilon}}\boldsymbol{\epsilon}_-} : \boldsymbol{\epsilon}$$

Thus, the tensile and compressive components of strain are linked to the strain tensor itself by the use of projection operators, here noted $\mathbb{P}^+$ and $\mathbb{P}^-$, through relations (3.25) and (3.26).

$$\epsilon_+ = \mathbb{P}^+(\epsilon) : \epsilon \tag{3.25}$$

$$\epsilon_- = \mathbb{P}^-(\epsilon) : \epsilon \tag{3.26}$$

These projection operators are fourth order tensors whose computation, outlined in appendix A, requires the eigen values and eigen vectors of ϵ. Moreover, note that the volumetric deformation term $tr(\epsilon)$ is also split into disctinct contribution ($< tr(\epsilon) >_\pm$) to tensile and compressive energies. Hence, on the whole, the mechanical equilibrium problem remains strongly non-linear. In order to linearize this problem, a method which takes advantage of the iterative approach to solving the global problem is used. Indeed, at any given iteration i of the global problem, the strain tensor at iteration $i-1$ is known. Therefore, it is ϵ^{i-1} which is used in order to compute the projection operators. Following these considerations relations (3.25) and (3.26) may be written in developed form as:

$$\epsilon^i_{\pm,kl} = \mathbb{P}^\pm_{kl11}\epsilon^{i-1}_{11} + \mathbb{P}^\pm_{kl22}\epsilon^{i-1}_{22} + \frac{1}{2}\left(\mathbb{P}^\pm_{kl12} + \mathbb{P}^\pm_{kl21}\right)2\epsilon^{i-1}_{12}$$

which leads to the following relation in matrix notation:

$$\left[\epsilon^i_\pm\right] = \left[\mathbb{P}^\pm\right]\left[\epsilon^{i-1}\right]$$

The same idea is used for the volumetric deformation term and reads:

$$< tr(\epsilon^i) >_+ = \begin{cases} 0 & \text{if} \quad tr(\epsilon^{i-1}) < 0 \\ tr(\epsilon^i) & \text{if} \quad tr(\epsilon^{i-1}) \geq 0 \end{cases}$$

$$< tr(\epsilon^i) >_- = \begin{cases} tr(\epsilon^i) & \text{if} \quad tr(\epsilon^{i-1}) \leq 0 \\ 0 & \text{if} \quad tr(\epsilon^{i-1}) > 0 \end{cases}$$

The stress tensor may finally be expressed in matrix form as:

$$\left[\sigma^i\right] = \left[\lambda f(d)\left[\mathbb{T}^+\right] + 2\mu f(d)\left[\mathbb{P}^+\right]\right][\epsilon] + \left[\lambda\left[\mathbb{T}^-\right] + 2\mu\left[\mathbb{P}^-\right]\right][\epsilon] \tag{3.27}$$

where $\left[\mathbb{T}^\pm\right]$ is the term $< tr(\epsilon^i) >_\pm \mathbb{1}$ in matrix notation. For the sake of clarity, the previous equation is condensed by defining:

$$\left[\mathbb{C}^i\right] = \left[\lambda f(d)\left[\mathbb{T}^+\right] + 2\mu f(d)\left[\mathbb{P}^+\right]\right] + \left[\lambda\left[\mathbb{T}^-\right] + 2\mu\left[\mathbb{P}^-\right]\right]$$

and therefore relation (3.27) becomes:

$$\left[\sigma^i\right] = \left[\mathbb{C}^i\right]\left[\epsilon^i\right] \tag{3.28}$$

Returning to the discretized weak formulation, a classical finite element procedure can now be used to assemble the linear system:

$$A_u[u] = L_u \tag{3.29}$$

Here again, a direct solver based on the LU decomposition is used to solve the linear system.

3.5 Boundedness of d

The modelling strategy presented previously is based on the introduction of a damage variable d which is required to vary between 0 and 1. Therefore, one question that may be asked is the following: does the model guarantee the boundedness of d? Under what conditions? This aspect is considered in the two following sections from a continuous and discretized view point.

3.5.1 Continuous formulation

In order to study this matter from a continuous point of view, let's recall the weak form of the governing equation for d:

$$\int_\Omega \left[\frac{g_c}{l} + 2\mathcal{H} \right] dv \, dV + \int_\Omega g_c l \nabla d . \nabla v \, dV = \int_\Omega 2\mathcal{H} v \, dV$$

Due to the positivity of $\mathcal{H}$ (by contruction), g_c and l, the maximum principle (see appendix B) guarantees that $d \geq \inf_\Omega(2\mathcal{H})$. Therefore, as $\mathcal{H} \geq 0$, d is bounded below: $d \geq 0$.

Moreover, performing the change of variable $d^* = 1 - d$ yields the following weak form:

$$\int_\Omega \left[\frac{g_c}{l} + 2\mathcal{H} \right] d^* v \, dV + \int_\Omega g_c l \nabla d^* . \nabla v \, dV = \int_\Omega \frac{g_c}{l} v \, dV$$

Once again, the maximum principle guarantees that d^* is bounded below: $d^* \geq 0$. Hence, it follows that $d \leq 1$.

Therefore, from a continuous point of view, the boundedness of d is guaranteed and $0 \leq d \leq 1$.

3.5.2 Discretized formulation

From a discretized point of view d is the solution of the linear system:

$$A_d d = R_d$$

In order to solve this problem, one may use the Jacobi method (note that the Jacobi method is used for the proof only, and not the solve systems 3.29 and 3.23). It is based on the decomposition of A_d into the sum of a diagonal, lower and upper part: $A_d = D_d + L_d + U_d$. The solution is then obtained via the following iterative algorithm:

$$D_d d^{k+1} = R_d - U_d d^k - L_d d^k$$

The matrix A_d is the sum of a mass matrix M_d and a stiffness matrix S_d. Both these matrices are assembled from elementary matrices computed on each cell. For Lagrange P1 shape functions in two dimensions, they take the form [128]

$$M_{d,K} = \left(\frac{g_c}{l} + 2\mathcal{H} \right)_K |K| \begin{bmatrix} \frac{1}{6} & \frac{1}{12} & \frac{1}{12} \\ \frac{1}{12} & \frac{1}{6} & \frac{1}{12} \\ \frac{1}{12} & \frac{1}{12} & \frac{1}{6} \end{bmatrix}$$

$$S_{d,K} = \frac{g_c l}{4|K|} \begin{bmatrix} ||a_2 a_3||^2 & (a_2 a_3 | a_3 a_1) & (a_2 a_3 | a_1 a_2) \\ (a_2 a_3 | a_3 a_1) & ||a_3 a_1||^2 & (a_3 a_1 | a_1 a_2) \\ (a_2 a_3 | a_1 a_2) & (a_3 a_1 | a_1 a_2) & ||a_1 a_2||^2 \end{bmatrix}$$

Assuming the algorithm is initialized with $d^0 = 0$, the positivity of d at subsequent iterations is guaranteed if all components of the diagonal matrix D_d and right hand side R_d are positive and all components of L_d and U_d are negative.

The right hand side is positive by definition of $\mathcal{H}$. Moreover, given the positivity of the diagonal terms of the elementary mass and stiffness matrices, the diagonal matrix D_d will also be positive.

However, the fact that all components of L_d and U_d are negative is not guaranteed apriori. First, the non diagonal terms of $M_{d,K}$ are positive. This issue may be overcome by using mass lumping, a standard procedure in finite element computation, which consists in concentrating all terms of the mass matrix onto its diagonal. The lumped mass matrix then has the form:

$$M_{d,K}^{lumped} = \left(\frac{g_c}{l} + 2\mathcal{H} \right)_K |K| \begin{bmatrix} \frac{1}{3} & 0 & 0 \\ 0 & \frac{1}{3} & 0 \\ 0 & 0 & \frac{1}{3} \end{bmatrix}$$

Second, the non diagonal terms of $S_{d,K}$ are not necessarily negative. Indeed, in the case of an element as illustrated in figure 3.8, the scalar product $(a_2 a_3 | a_3 a_1)$ will be positive.
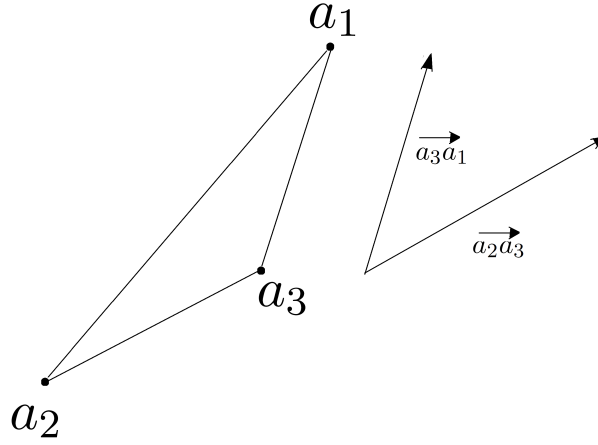
Figure 3.8: Case leading to a negative non-diagonal term of elementary stiffness matrix

Nevertheless, a good quality mesh will be composed of elements such as the one shown on figure 3.9, thus leading to negative non-diagonal components.
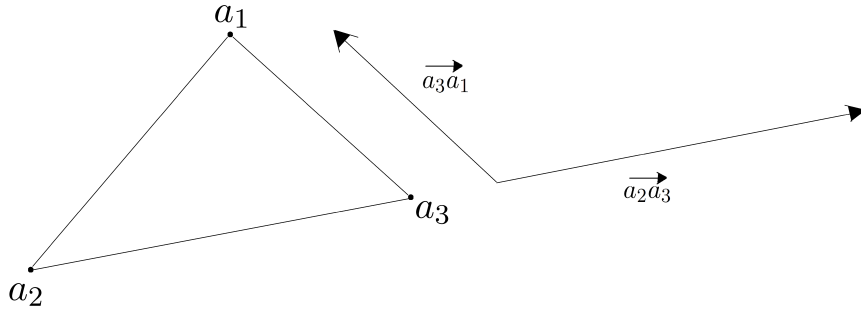
Figure 3.9: Case leading to a positive non-diagonal term of elementary stiffness matrix

Therefore, sufficient conditions to ensure the positivity of d are to use a lumped mass matrix and that the mesh elements do not present angles superior to 90°. A similar analysis can be performed for $d^* = 1 - d$ therefore leading to the boundedness of d between values of 0 and 1.

However, these conditions do not seem to be necessary for stability. In fact, tests were performed with a non-lumped mass matrix and bad quality elements (presenting one angle greater than 90°). Values of d were observed to go out of the bounds $[0, 1]$ only very slightly (effects to the third decimal). In addition, d remained bounded between 0 and 1 when tests with a lumped mass matrix and a bad quality mesh were performed. Additional properties must therefore come into play to ensure stability and boundedness in these cases.

3.6 Academic Validation

In order to validate the finite element procedure, simple test cases are considered. They are all based on a square domain, $\Omega = [0, L] \times [0, L]$, illustrated on figure 3.10.
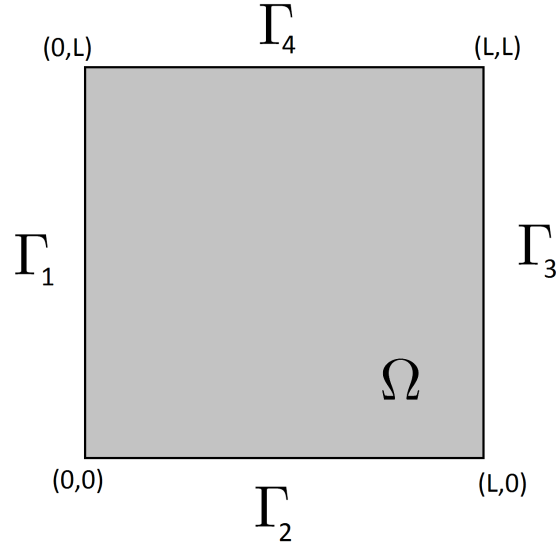
Figure 3.10: Square domain used for validation cases

3.6.1 Damage Module

So as to validate the damage module the following problem is considered on $\Omega = [0, L] \times [0, L]$:

$$d^i - \triangle d^i = f \qquad\qquad \text{in } \Omega \qquad\qquad (3.30)$$

$$\nabla d^i . n = 0 \qquad\qquad \text{on } \Gamma_1, \Gamma_2, \Gamma_4 \qquad\qquad (3.31)$$

$$d^i = 0 \qquad\qquad \text{on } \Gamma_3 \qquad\qquad (3.32)$$

Here f is taken constant and due to the homogeneity of the boundary conditions the problem reduces to a one dimensional one. The analytical solution is given by:

$$d_{analytical} = f \left(1 - \frac{ch(x)}{ch(L)} \right)$$

As shown in figure 3.11 excelent agreement is obtained between analytical and numerical solutions.
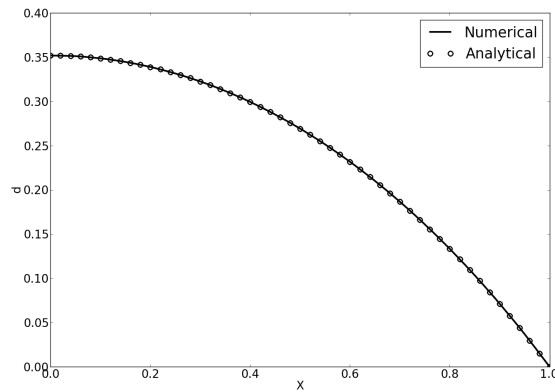
Figure 3.11: Comparison between numerical and analytical solutions

3.6.2 Elasticity and Elastic Energy

In order to validate the elasticity module the displacement field is given as:

$$u_x = ax \ , \ u_y = 0$$

where a is a positive constant. Thus the corresponding strain tensor and stress tensor are given by:

$$\epsilon = \begin{bmatrix} a & 0 \\ 0 & 0 \end{bmatrix}$$

$$\sigma = \begin{bmatrix} (\lambda + 2\mu)a & 0 \\ 0 & \lambda a \end{bmatrix}$$

Computing $\sigma.n$ on the various boundaries provides the loads to apply as Neumann boundary conditions:

$$T_3 = \begin{bmatrix} (\lambda + 2\mu)a \\ 0 \end{bmatrix}$$

$$T_{2,4} = \begin{bmatrix} 0 \\ \pm \lambda a \end{bmatrix}$$

On boundary Γ_1 a homogeneous Dirichlet condition is applied, which is compatible with the given displacement field and stress tensor. The given displacement field is linear and P1 elements are used. Hence, by applying the previous boundary conditions, the finite element procedure should yield $(u_x = ax, u_y = 0)$ alsmot exactly. Moreover, the eigen values of ϵ are simply $\epsilon_1 = a$ and $\epsilon_2 = 0$ and therefore the tensile elastic energy reads:

$$\mathcal{H} = \frac{\lambda}{2}a^2 + \mu a^2$$

In addition, the projection operator trivially decomposes ϵ into:

$$\epsilon_+ = \begin{bmatrix} a & 0 \\ 0 & 0 \end{bmatrix}$$

$$\epsilon_- = \begin{bmatrix} 0 & 0 \\ 0 & 0 \end{bmatrix}$$

As shown in figure 3.12 the numerical result agrees very well with the expected outcome. All the aforementioned variables, that is to say displacement, elastic energy, strain tensor and strain decomposition are retrieved with a relative error of 10^{-15}.
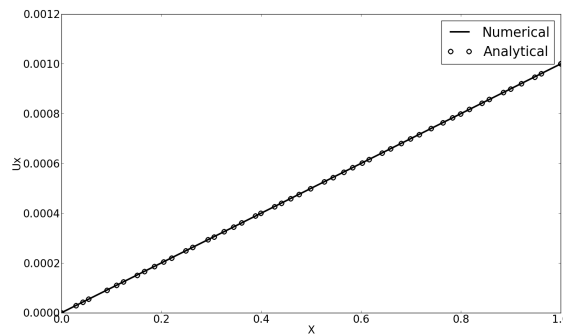
Figure 3.12: Comparison between numerical and analytical results

It is interesting to note that this test was also performed with a negative value for a and that the correct history function and strain decomposition was also obtained.

3.7   Model Assessment

Now that the modelling strategy is established, it is interesting to perform preliminary checks in order to assess its performance. To do so, the effects of mesh size and spreading length l will first be studied. Secondly, numerical predictions and experimental data will be compared to see how the model performs. Due to the lack of experimental data on atmospheric ice, an experimental test case performed on concrete is reproduced (Nooru-Mohamed [102]).

   All computations in this section will be based on the same generic test case (see figure 3.13). It consists of a square specimen ($200mm \times 200mm$) of plain concrete submitted to mixed mode loading, shear and axial at the same time. The specimen has a thickness of $50mm$ which is relatively small compared to the other dimensions, therefore a plane stress formulation is chosen. The material parameters are chosen to be $E = 30GPa$, $\nu = 0.2$ and $K_{IC} = 1MPa.m^{-1/2}$ [102, 124].
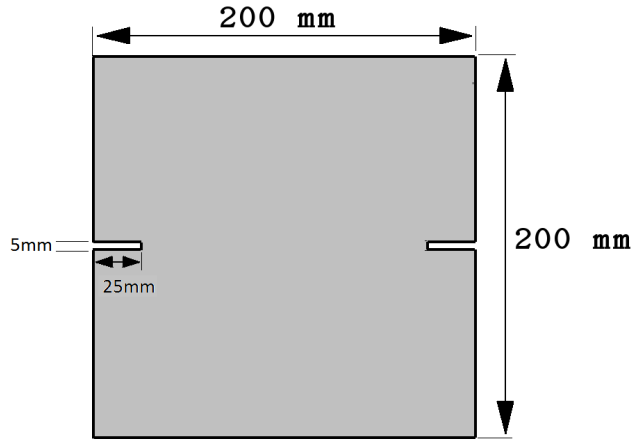
Figure 3.13: Generic double edged notch problem illustration

3.7.1   Size Effects

For the study of size effects two meshes ("coarse": 30,000 elements, and "fine": 65,000 elements) are considered. These meshes are designed to have an element characteristic size of respectively $h = 2mm$ and $h = 1mm$ in the region where the crack is expected to propagate. On each mesh two spreading lengths will be investigated, $l = 2mm$ and $l = 5mm$. A fixed displacement field is imposed at the upper left corner boundary (Γ_u on figure 3.14): $u_x = 20\mu m$, $u_y = 25\mu m$. A homogeneous Dirichlet boundary condition is applied on Γ_0: $u_x = 0m$, $u_y = 0m$.
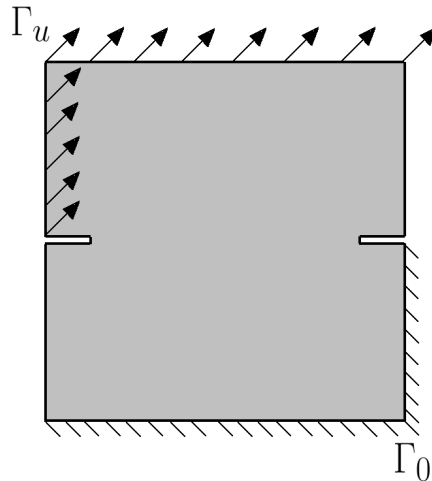
Figure 3.14: Double edged notch problem with fixed Dirichlet boundary conditions

As can be seen on figures 3.15 and 3.16, the crack topology for this problem consists of two curved symmetric branches that originate at the notch tips. This topology is typical of this type of double edged mixed mode setup, as presented in the next subsection.

Let's start by taking a look at the effect of the spreading length. Figure 3.15 shows the results of two computations made on the "fine" mesh with $l = 2mm$ and $l = 5mm$. The crack paths obtained with $l = 5mm$ are clearly more spread out than those obtained with $l = 2mm$. The crack paths change from one value of l to another, especially near the end of the paths, but this effect is very slight. The same effect is observed on the "coarse" mesh (see figure 3.16).

The effect of mesh size can be seen by comparing figures 3.15(a) and 3.16(a) for $l = 5mm$ as well as figures 3.15(b) and 3.16(b) for $l = 2mm$. For $l = 5mm$ the effect is extremely slight. The same comment can be made for $l = 2mm$.

(a) $l = 5h = 5mm$ (b) $l = 2h = 2mm$
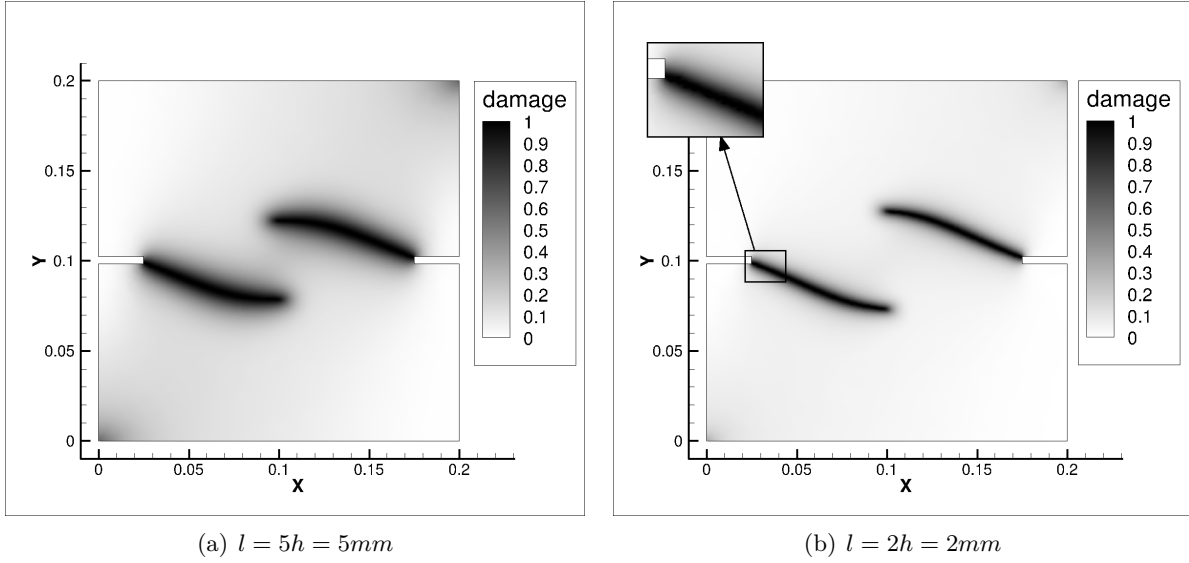
Figure 3.15: "Fine" mesh computation; $h = 1mm$

(a) $l = 2.5h = 5mm$ (b) $l = h = 2mm$
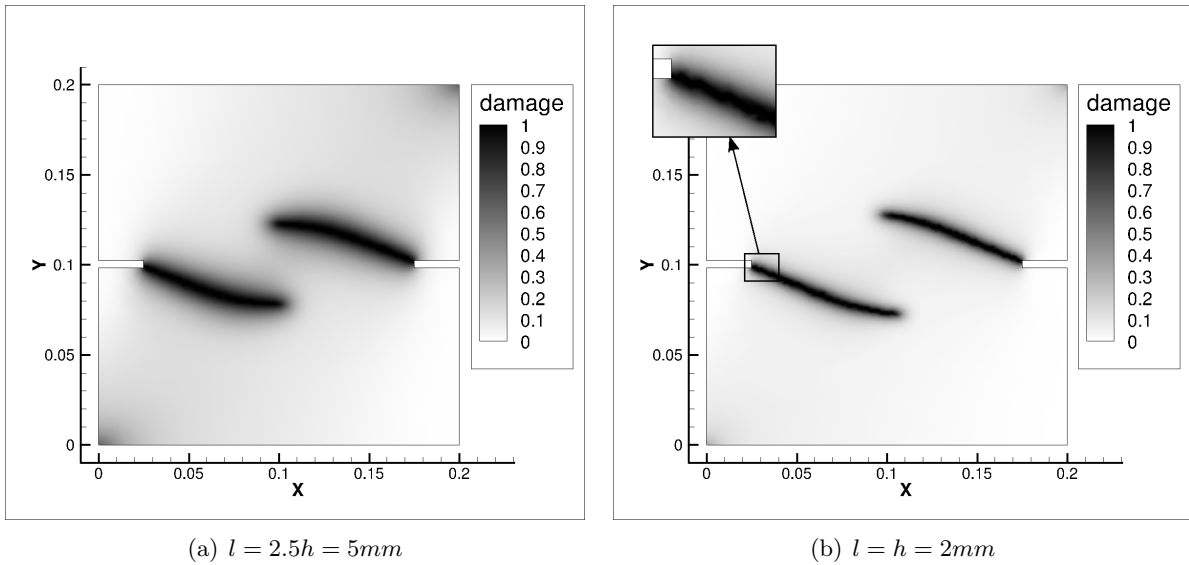
Figure 3.16: "Coarse" mesh computation; $h = 2mm$

The choice of l is not arbitrary, it can't be chosen too small. For example $l = 0.5h$ yields an irregular solution (see figure 3.17(a)). Choosing $l = 0.25h$, as shown on figure 3.17(b), completely kills the solution and the crack branches fail to propagate. Thus, this implies good knowledge of the

mesh so as to correctly set the spreading length. We join Miehe *et al* [24] and consider that a good compromise consists in choosing $l = 2h$.

(a) $l = 0.5h = 1mm$ (b) $l = 0.25h = 0.5mm$
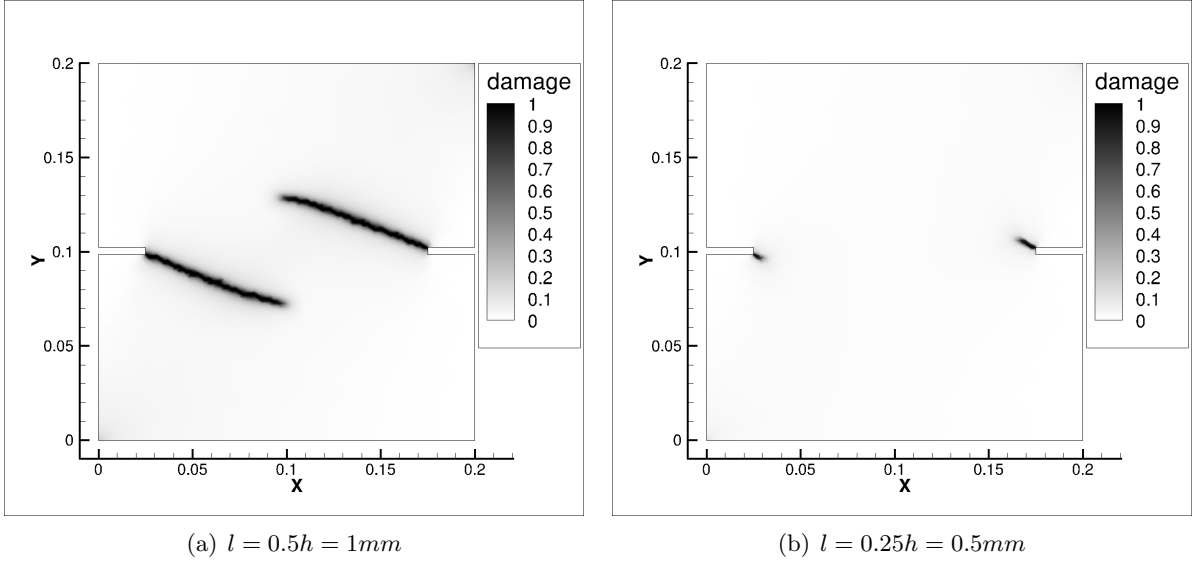
Figure 3.17: "Coarse" mesh computation with under-resolved l

To sum up this section on size effects:

- Reasonably increasing l will spread out the crack but will not significantly change the results. l should not be increased too much so as to maintain a good level of definition for the solution.

- Decreasing l to under-resolved values kills the solution and brings about misleading results.

- For $l \geq 2h$ the result will not be significantly mesh sensitive.

3.7.2   Comparison With Experiment

The experimental setup is sketched figure 3.18. To be more precise, the following load path is reproduced: first apply a shear load in displacement control until $Ps = 10kN$ (s axis). Then apply an axial displacement till failure, while maintaining $Ps = 10kN$ with lateral displacement control (t axis).

To the author's knowledge, comparison of this numerical fracture mechanics model with this kind of experiment has not yet been performed. Therefore it also serves as an assessment of the model itself. Numerically this was achieved by imposing displacements at boundaries Γ_u and Γ_0 in the following way:

- Apply displacement u_x and compute Ps.

- Adjust displacement u_x so as to obtain $Ps = 10kN$.

- Apply displacement u_y until failure.

- Adjust u_x at each iteration to maintain $Ps = 10kN$ while simultaneously enforcing failure with displacement u_y.
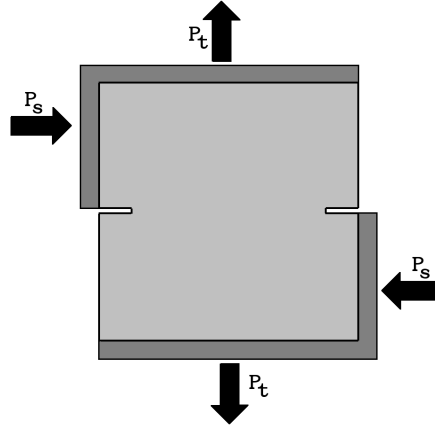
Figure 3.18: Double edged notch problem with axial and shear loads
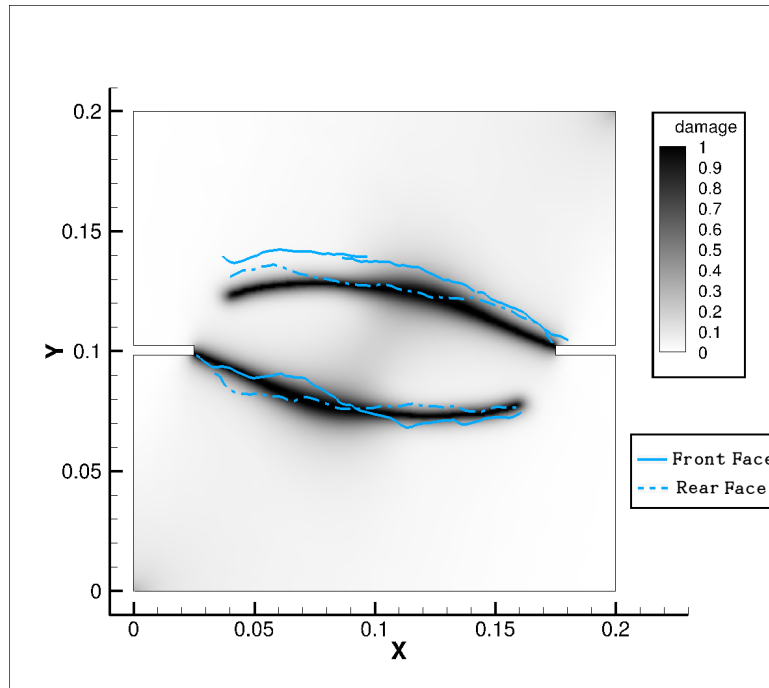
Figure 3.19: Comparison between experiment and numerical simulation

Figure 3.19 shows the crack paths obtained numerically and the experimental crack paths (respectively at the front and rear faces of the concrete specimen). The crack topology consists of two curved branches each taking their origin at one of the notches. The numerical results match the experimental paths quite well, with a very good agreement for the lower branch. As for the upper branch the model predicts a path that passes slightly lower than the experiment. The crack paths predicted by the model are symmetric with respect to one another. This comes as no surprise given the symmetry of the setup and the hypotheses on the material (linear homogeneous isotropic). This symmetry is not observed for the experimentally obtained crack paths. This very sligth difference can be explained by the fact that the concrete specimen is not really homogeneous and isotropic. It consists of a mixture of cement, river gravel and sand amongst other consituants [102]. Although the agregates formed by the mixture process are of small size compared to the dimensions of the specimen (ratio 100 [102]) the resulting material will not be perfectly homogeneous and isotropic. Given the highly nonlinear character of crack propagation it is not surprising to observe slightly unsymmetric crack paths.

In the present chapter the mechanical properties of atmospheric ice are reviewed. The chapter is concluded with the identification of empirical laws defining the mechanical properties of atmospheric ice.

Contents

4.1 Literature Review

4.1.1 Elastic Behaviour

In the case of fresh-water ice, according to Schulson and Duval [33], the most precise results for the elastic constants were obtained by Gammon *et al.* [107]. In the case of a homogeneous polycrystalline ice aggregate, it may be assumed that the grains (crystallites) are oriented randomly making it elastically isotropic. The parameters characterising homogeneous isotropic elastic behaviour of polycrystalline ice are given in the following table (4.1) [33][107]:

Young's modulus, E	$9.33\,10^9\ Pa$
Poisson's ratio, ν	0.325

Table 4.1: Elastic constants of interest for isotropic polycrystalline ice at $T = -16°C$

Young's modulus for atmospheric ice was recently estimated by Eskandarian using poroelasticity and Hill's averaging method. The reported values are around $9.5 MPa$ [83]. Kermani also attempted to measure Young's modulus by static loading using an extensometer but found values around $5 MPa$. He pointed out that these measurments were less accurate citing several sources of error [89].

4.1.2 Anelastic Behaviour

- Plastic behaviour : The plastic behaviour of ice is highly anisotropic and is dominated by basal slip [96, 31]. As an illustration, the critical resolved shear stress (that is the stress needed to initiate slip on a 45° plane [29]) is 60 times greater for non-basal slip than for basal slip. This basal slip is caused by dislocations in the basal plane [31].

- Ductile behaviour: Ductile behaviour appears at low strain rates (less than $10^{-7}s^{-1}$) and involves plastic deformation. At these low rates there is no formation of cracks. Deformation of ice is accompanied by creep inducing a wide range of phenomena such as grain reorientation by migration of grain boundaries or recrystallization [33].

- Brittle behaviour: Brittle behaviour appears at high strain rates (greater than $10^{-3}s^{-1}$) and involves fracture and crack propagation. These high rates initiate cracks making ice brittle independently of the stress state[31].

- Ductile-to-Brittle transition : For intermediate values of strain rate cracks will also develop. At those rates ice will be brittle under tension and ductile under compression.

4.1.3 Grains and Air Bubble Inclusions

As stated in chapter 1, the white and opaque external structure of rime ice is due to the rapid freezing of accumulating water droplets which acts to trap air bubbles. An example of such air bubble inclusion is shown in figure 4.1. Kermani *et al.* have recently studied the internal structure of atmospheric ice [91]. They show that the size of air bubbles inclusions increases with decreasing accumulation temperature.
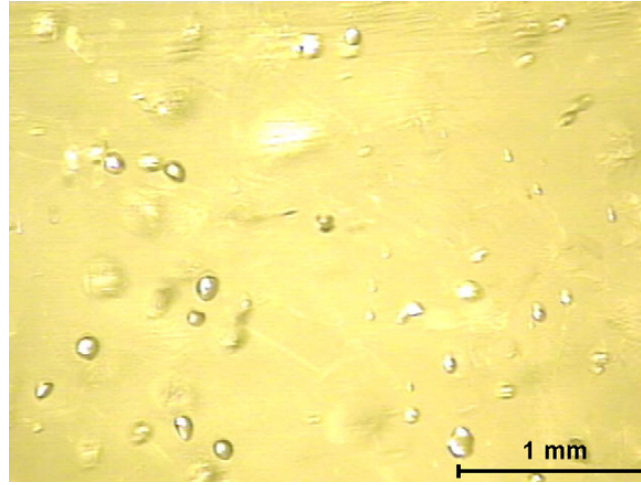
Figure 4.1: Air bubble inclusion in atmospheric ice accumulated at $-10°C$ [91]

Another important aspect of the structure of atmospheric ice is grain geometry. Indeed, as shown in figure 4.2, atmospheric ice forms from a polycristalline growth process resulting in a structure of many grains aggregated together. The size of the grains is of the order of magnitude of $1mm$ and their size seems to decrease with accumulation temperature [106, 90].

Figure 4.2: Grain boundaries in atmospheric ice accumulated at $-4.8°C$ [106]

It is also interesting to note that grains show preferential elongation in the direction of accumulation, as shown in figures 4.3 and 4.4. This indicates that atmospheric ice has a columnar-like polycristalline structure.
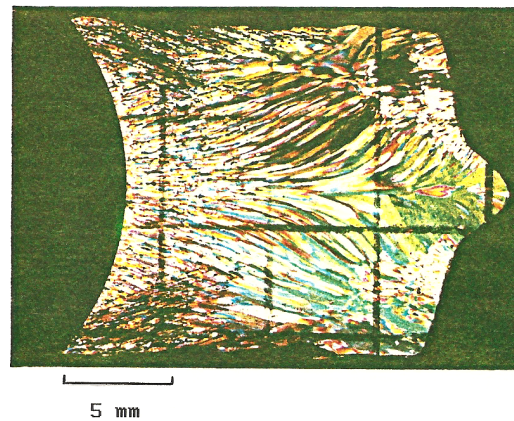
Figure 4.3: Grain elongation in atmospheric ice [106]
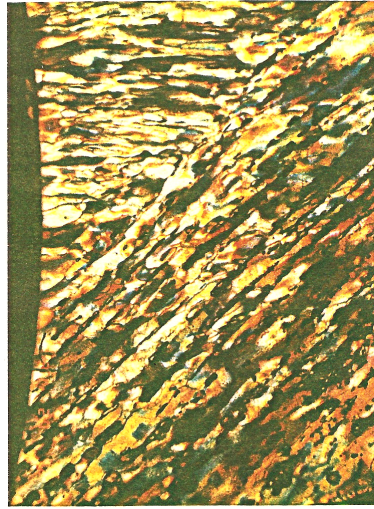
Figure 4.4: Zoom on grain elongation in atmospheric ice [106]

4.1.4 Fracture

As noted by Petrovic fracture of ice has not been intensively investigated [61]. The fracture toughness of ice as a function of temperature is shown figure 4.5. The results are scattered around the values of 80 to $140 kPa.m^{1/2}$ and no clear trend seems to be apparent.
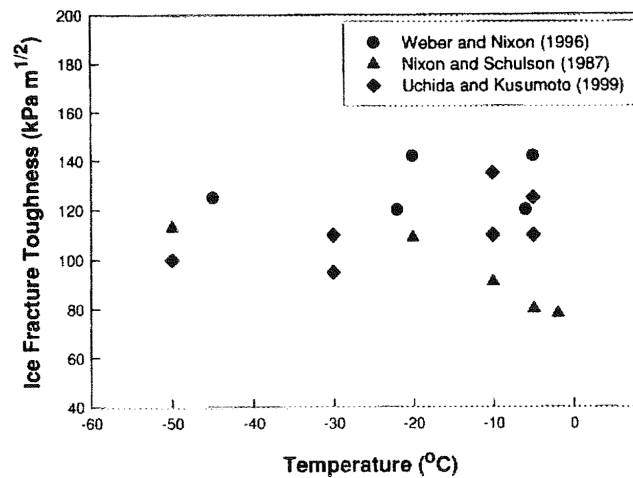
Figure 4.5: fracture toughness of ice as a function of temperature [61]

The process by which cracks appear in fresh-water ice has also been investigated. For example, in the light of high speed photography results, Schulson describes the brittle compressive failure of ice as a multistep process [31, 33]:

1. Crack nucleation at grain boundary for applied stresses of about one quarter to one third of the terminal failure stress. These first cracks are inclined by 45° to the direction of loading.

2. Increase of crack density as load rises. Out of plane or secondary cracks extend from the primary cracks oriented in a direction roughly parallel to the load axis. These extentions are termed wing cracks.

3. Terminates by sudden formation of macroscopic shear faults.
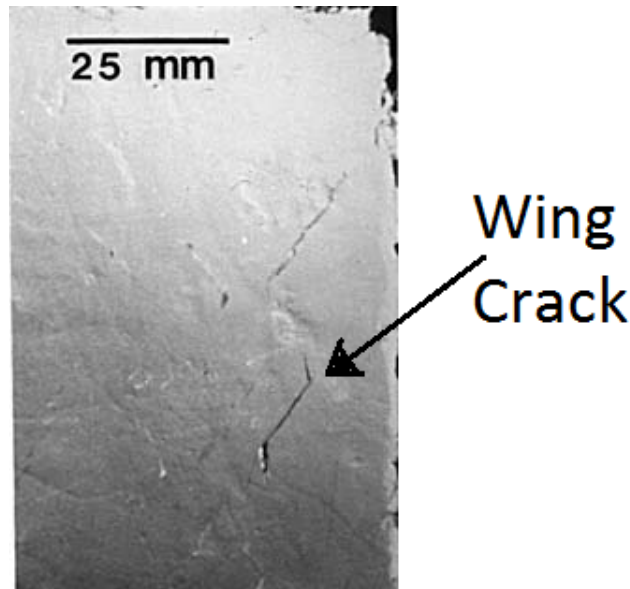
Figure 4.6: Wing crack in ice under compression [33]

A review by Frost also provides interesting information on possible crack nucleation mechanisms [52]. Frost points out that preexisting flaws, inclusions or voids are natural stress concentrators leading to fracture. However, he focuses his study on additional mechanisms relevant to polycrystalline ice. It is shown that for polycrystalline ice without any preexisting flaws, grain boundary sliding is probably the dominant crack nucleation mechanism. In the case of single crystals, or for grain geometries where grain boundary sliding is not active, then the tips of dislocation pile ups are likely to be the dominant crack nucleation sites.

Thermal shock effects have also been investigated, on a theoretical and experimental level, by King and Fletcher [152, 153]. In their experimental procedure they prepared ice spheres, cylindrical slabs and thin plates. For each of these geometries one of the surfaces was heated by bringing it into contact with liquid water. In the case of spheres (2 or $3cm$ in diameter and with presence of bubbles or clear), it was observed as shown in figure 4.7 that a temperature difference of $\approx 10°C$ is necessary in order to create cracks. The temperature dependence then increases in a more or less linear way up to 100% fracture probability for $20°C$. As pointed out by the authors, the presence of bubbles did not have an effect on the fracture probability despite the fact they are viewed as stress concentration centres.
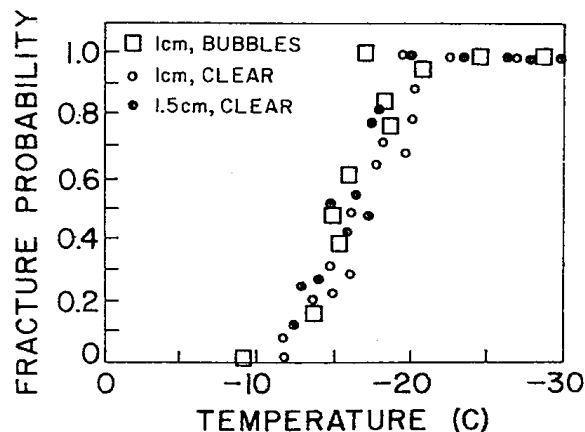
Figure 4.7: Effect of temperature on fracture probability for spheres [153]

4.1.4.1 Tensile Strength of Ice

The tensile strength of freshwater or sea ice has been studied by several authors due to the variety of engineering situation where failure under tension occurs (ice breaking by ships, bending of ice sheets

on marine structures) [33]. According to Schulson and Duval, tensile failure of ice often involves rapid crack propagation with no creep deformation. The reported values of tensile strength for fresh-water ice range from $0.8MPa$ to $1.2MPa$. However, as shown in figure 4.8, effects of grain size induce tensile strengths ranging from $0.6MPa$ to $2.3MPa$.
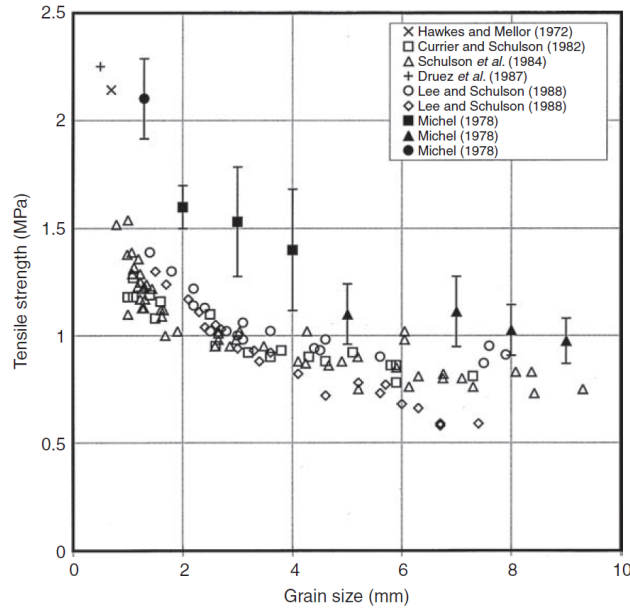
Figure 4.8: Tensile strength of fresh-water ice as a function of grain size [33]

Although atmospheric ice is also involved in many physical and engineering situations, tensile strength studies are much rarer. Recently Mohamed and Farzaneh prepared specimens of atmospheric ice accumulated at $-10°C$ and several wind speeds. The tensile strength of these specimens was measured at different testing temperatures. The results of their study are shown in figure 4.9.
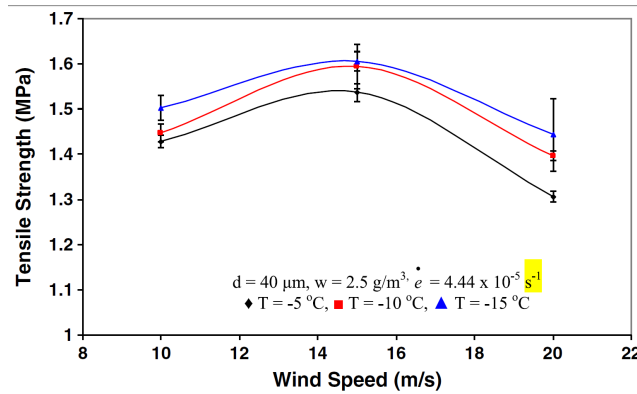
Figure 4.9: Tensile strength of atmospheric ice for different testing temperature and accumulation wind speeds [11]

4.1.4.2 Compressive Strength of Ice

The compressive strength of ice is usually much higher than its tensile strength. In his review on fresh-water ice, Petrovic reports values ranging from $5MPa$ to $20MPa$ and above [61].

As for atmospheric ice, recent measurments performed by Kermani *et al.* also exhibit a higher compressive strength, as shown in figure 4.10. However, in the case of these experiments the values of compressive strength are a little lower than those reported for fresh-water ice, remaining in the range of $2MPa$ to $6MPa$ [91].
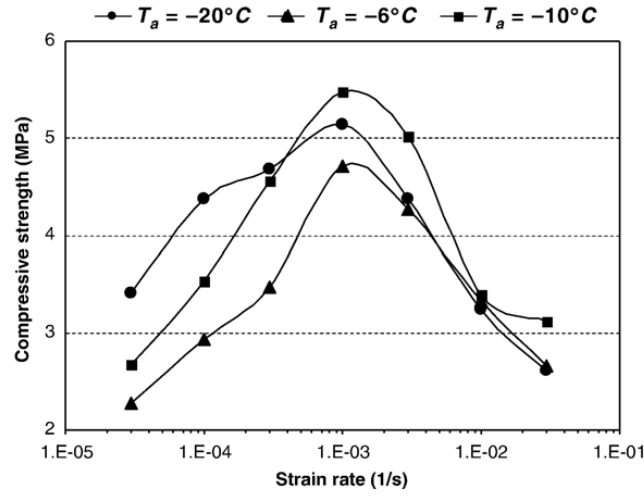
Figure 4.10: Compressive strength of atmospheric ice for different accumulation temperatures and strain rates [91]

4.1.4.3 Bending Strength of Atmospheric Ice

In addition to their study on the compressive strength of atmospheric ice, Kermani *et al.* have also studied its bending strength [90]. As can be seen in figure 4.11, the bending strength of atmospheric ice is higher than that reported by other authors for fresh-water ice. Its value seems to be almost unaffected by testing temperature. For an accumulation temperature of $-10°C$ the bending strength of atmospheric ice is about $2.8MPa$.
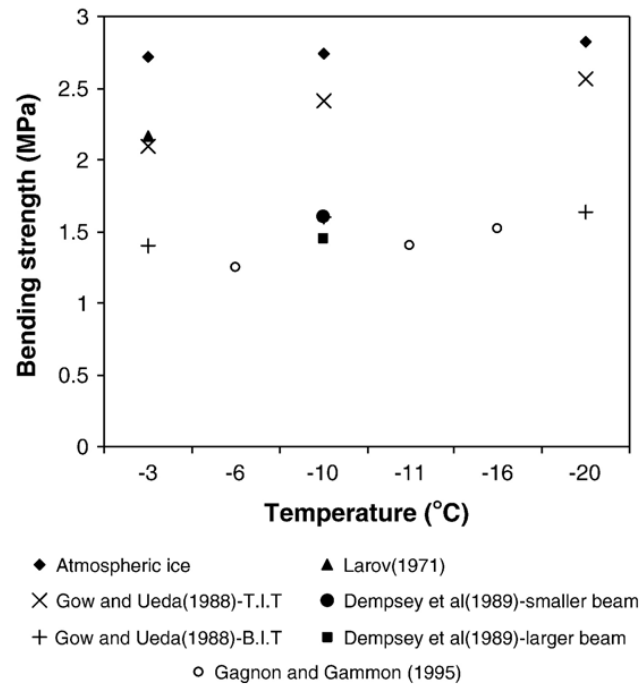
Figure 4.11: Bending strength as a function of temperature: atmospheric ice compared to freshwater ice (T.I.T = Top In Tension, B.I.T = Bottom In Tension) [90]

4.1.5 Ice Adhesion

There are several general theories of adhesion that describe the various mechanisms by which adhesion may occur [93, 82, 10] such as electrostatic charge transfer, mechanical interlocking, molecular diffusion or chemical bonding.

There are however some specific theories which have been proposed for ice adhesion which deserve to be mentioned. Weyl, and later Jellinek, investigated during the 50's and 60's the liquid-like layer theory of adhesion. The theory is based on ideas first proposed by Faraday during the 1850's [51, 84]. The idea is that water being a dipolar molecule, a water surface as well as an ice surface will lower its surface energy by changing its electronic charge distribution. This would have the effect of inducing an electrical double layer at the surface of water or ice, creating disturbances in the surface layers. The surface layers and the bulk would therefore have different properties [51, 50].

Based on this theory, Jellinek estimated the tensile and shear stress needed to separate an ice block from a solid surface [48]. However, quantitative estimates yield values well above the tensile strength of ice, thus predicting a cohesive break. He also formulated an estimation of the shear strength needed for separation, assuming the solid surface has velocity v_t and the liquid to be Newtonian. Jellinek pointed out the fact that discussions assuming a liquid-like layer should be semi-quantitative at best due to the lack of knowledge on such a layer. Nevertheless he considers the assumption of a liquid-like layer essential to understanding experimental results on the adhesive properties of ice[48].

Since then, further progress has been made. In the light of X-Ray diffraction, proton channelling, optical ellipsometry and nuclear magnetic resonance experiments it becomes evident that a special layer exists at the surface of ice. Petrenko [142] reports and describes these experiments, giving further insight on the nature, structure and thickness of the liquid-like layer. As predicted before, the thickness of the layer decreases with temperature. Atomic force microscopy experiments provided upper limit values of $12nm$ at $-24°C$ and $70nm$ at $-0.7°C$ [117].

Molecular dynamics simulations where also run by Girardet and Toubin [20]. Figure 4.12 clearly shows the apparition of a disordered layer at the surface of ice with increasing temperature, thus confirming the possibility of the existence of a liquid-like layer at the surface of ice.
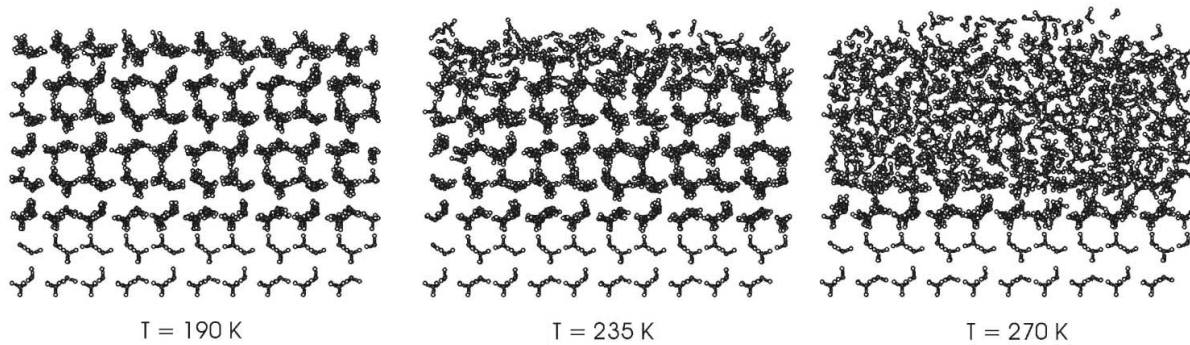
Figure 4.12: Molecular dynamics simulation showing the apparition of a liquid-like layer with increasing temperature [20]

Based on similar ideas, Petrenko and Ryzhkin proposed an electrostatic ice adhesion theory [56]. They evaluated the adhesion energy per unit area by numerically solving the problem of minimization of potential electrostatic energy. The adhesion energies range from $0.08 J.m^{-2}$ to $1.3 J.m^{-2}$. These results are comparable, at least in the proximity of the lower bound, to those obtained experimentally by Sonwalkar [101] using Raman spectroscopy (bearing in mind that they were obtained at different temperatures). Thus, as concluded by Petrenko and Ryzhkin, electrostatic interaction may play an essential role in ice adhesion.

4.1.6 Adhesion Experiments: Natural Ice

Many author's have studied the adhesion of ice to various substrates. However these experiments often dealt with the adhesion of natural ice. For example Landy and Freiberger [93] prepared their ice specimens by filling ice holders to about 3/4 with distilled purified water. They were not obtained by freezing on impact of supercooled water droplets. Nevertheless the adhesive behaviour of natural ice can give an idea of the orders of magnitude and phenomena likely to be observed in the case of atmospheric ice.

Jellinek provided some of the first studies and was one of the main contributors on natural ice adhesion in the 50's and 60's [51, 50, 48, 49]. More specifically he studied the shear and tensile adhesive strength of ice to polystyrene and PMMA (polymethylmethacrylate). His results for ice/polystryene are summed up by figures 4.13(a) and 4.13(b). These curves were obtained by averaging at least 12 runs.
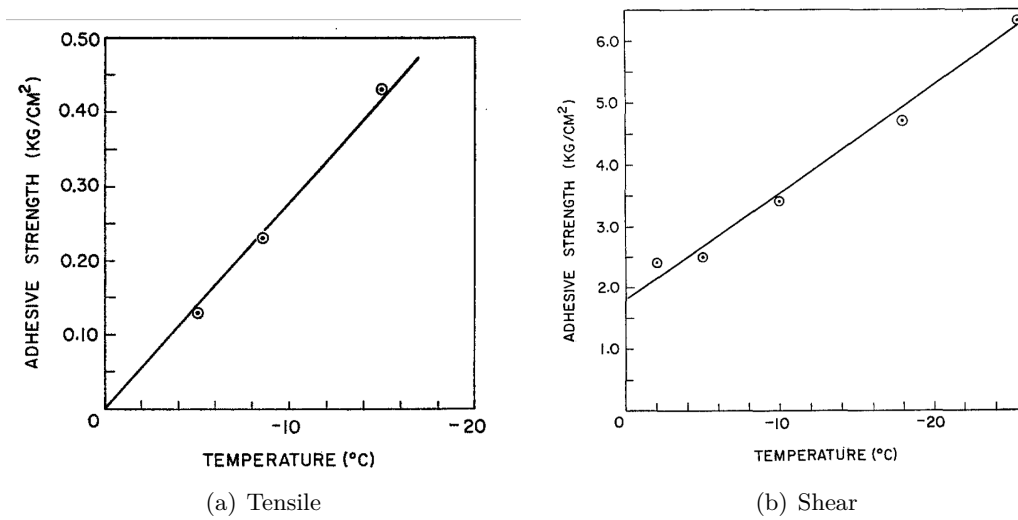
(a) Tensile

(b) Shear

Figure 4.13: Tensile and shear adhesive strength of ice to polystyrene[48]

Jellinek therefore observed a linear dependence with respect to temperature of ice adhesion to polystyrene. As for the ice/PMMA interface, the mean adhesive strength at $-5°C$ was found to be $4, 4kg.cm^{-2}$ (standard deviation ± 2.9). 19 adhesive breaks were observed and adhesive strength was found to be larger than that of ice/polystyrene. In a way analogous to his theory for tensile failure, Jellinek proposes a "weakest imperfection" theory of ice adhesion using a Weibull law. However he notes that this "weakest imperfection" theory fails to explain the difference in shear and tensile behaviours. He then turns to the liquid-like layer assumption to do so.

Landy and Freiberger on their side studied ice adhesion to different substrates[93]. As shown in figure 4.14, ice adhesion strength and behaviour greatly depends on the type of surface considered. Moreover some substrates lead to weaker adhesive strength, which also illustrates the idea behind the surface coating ice adhesion reduction strategy.
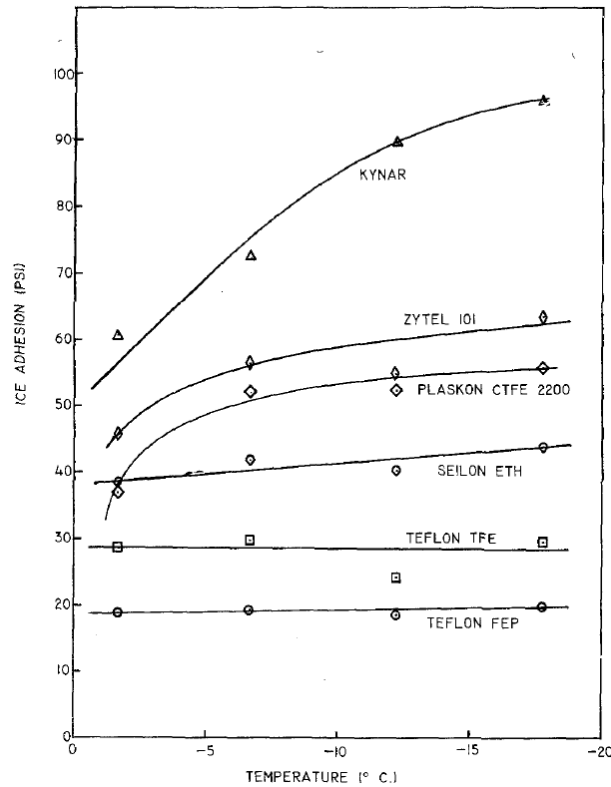
Figure 4.14: Temperature dependence of ice adhesion to various substrates [93]

As far as the order of magnitude are concerned, as compared to the values for atmospheric ice, they all remain in the same range: $\approx 0.2 MPa$ to $\approx 1.0 MPa$.

4.1.7 Adhesion Experiments: Atmospheric Ice

The experiments discussed previously dealt with natural ice. One of the first studies involving impact atmospheric ice can be found in the works of Druez *et al.* [59]. They studied the influence of surface roughness, airflow velocity and ambient temperature on the adhesion properties of ice formed by impact of supercooled droplets ($MVD = 20\mu m$, $LWC = 2.8 g/m^3$). Figures 4.15, 4.16 and 4.17 gather the main experimental results of this study.
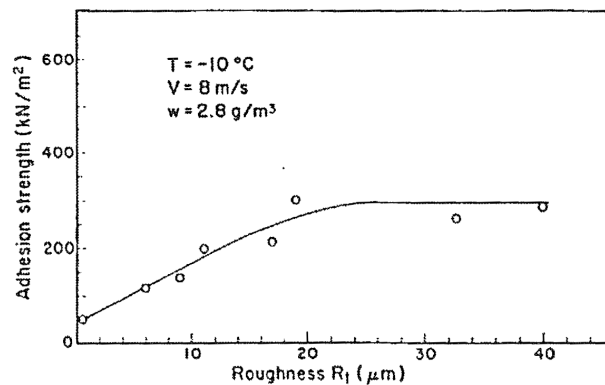
Figure 4.15: Roughness effect [59]
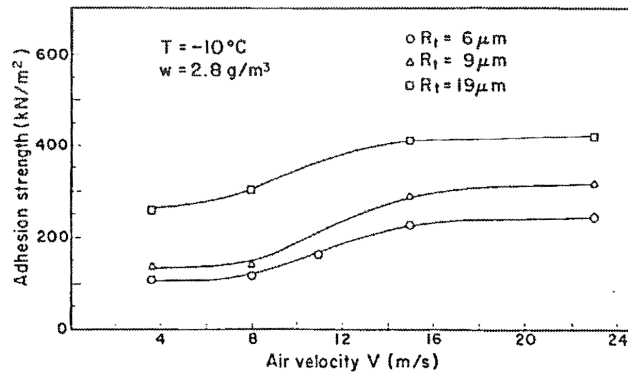
Figure 4.16: flow speed effect [59]
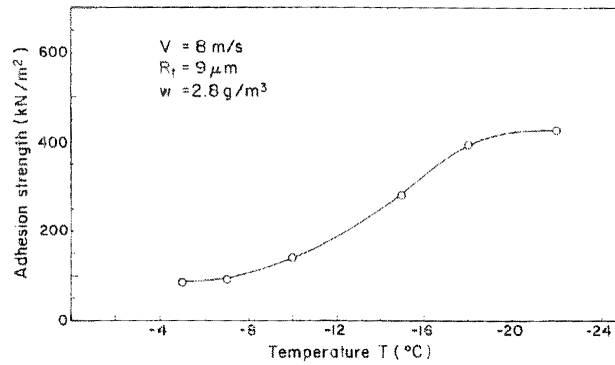
Figure 4.17: Temperature effect [59]

We see in figure 4.15 that the adhesion strength increases with the roughness of the surface until $R_t = 25\mu m$. Beyond this value the adhesion strength seems to stabilise. Figure 4.17 shows that decreasing temperature leads to higher ahdesion strength. Whereas figure 4.16 depicts the fact that increasing air velocity up to $\approx 16 m.s^{-1}$ also increases adhesion strength (above which adhesion strength stabilises). The adhesion strengths found range from $\approx 0.15 MPa$ to $0.4 MPa$. Moreover, Druez *et al.* also point out that the grain size of impact ice decreases with increasing air velocity. They also briefly discuss the nature of the observed adhesive ruptures (adhesive, cohesive or adhesive/cohesive), classifying them as adhesive.

Similar experiments were also conducted by Scavuzzo *et al* [122]. They mainly investigated the effects of surface temperature and droplet impact speed.
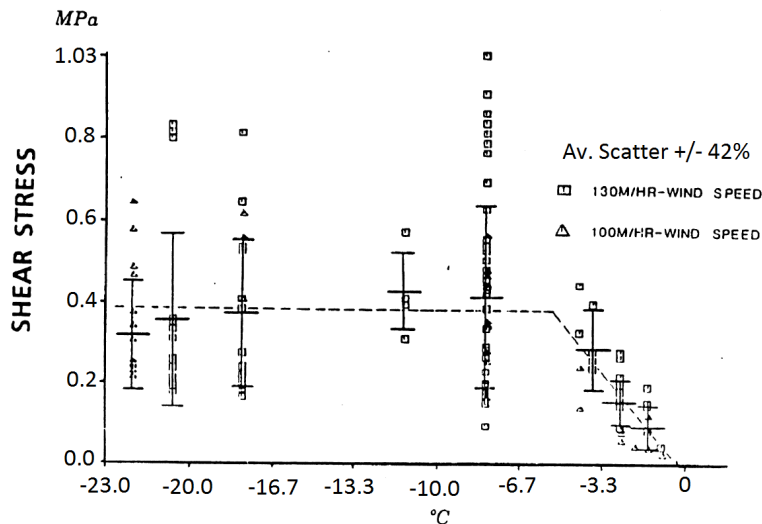
Figure 4.18: Effect of surface temperature [122]

These results are similar to those of Druez *et al.*. The adhesion strength increases with increasing impact speed and decreasing surface temperature. Both studies point out the fact that the results are highly scattered due reproducibility issues.

Another interesting study is that of Wei and coworkers [160]. In their study, they test a fracture mechanics approach to the ice/metal adhesion, a method they consider to be more suitable to the problem of interface failure. For this purpose they prepare three types of ice, one of which is granular ice formed by spraying fine water mist on the metal surface. Two different surfaces were used, aluminium and steel. It was observed that the fracture energy for those surfaces is very close ($\approx 1 J.m^{-2}$). In order to initiate crack propagation, an interfacial precrack was introduced. Figure 4.19 shows a fractography visualisation of the fracture process.
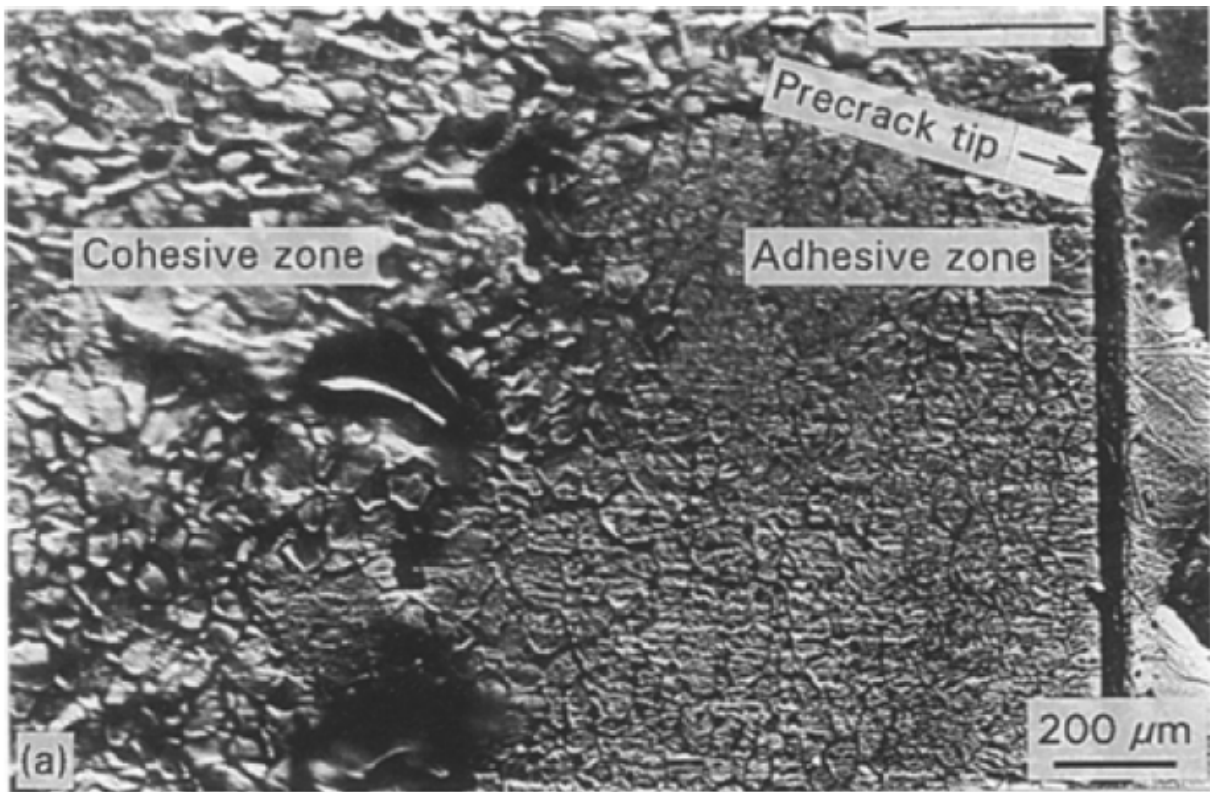
Figure 4.19: Fracture process for an ice/metal interface [160]

Wei *et al.* distinguish two domains. On the one hand, just beyond the precrack line is a flat zone implying that the crack was propagating on the interface leading to adhesive debonding. On the other hand, more to the left we can observe cleaved ice grains. This means that the crack then deviated into the bulk of the ice body leading to a cohesive fracture mechanism. Wei *et al.* then conclude, by investigation of the whole interface, that the fracture process was generally mixed (cohesive/adhesive) with a dominant adhesive part. They also point out the fact that the fracture processes were macroscopically brittle but that dislocation slip in the ice crystal suggest microplastic deformation processes.

Finally, it is interesting to take a quick look at the results obtained by Sonwalkar [101] via Raman spectroscopy which are briefly summed up table 4.2:

Material	W_a $mJ.m^{-2}$	σ kPa
Titanium	93.48	436.00
Copper	93.94	421.94
Aluminium	97.25	351.61
Stainless steel	103.72	416.31
PTFE (Polytétrafluoroéthylène)	63.60	175.80

Table 4.2: Work of adhesion and adhesion strength for various ice/surface interfaces at $T_0 = -20°C$ [101]

Their results are comparable in order of magnitude to those obtained by Scavuzzo [122], and as mentioned previously, to those obtained by Petrenko and Rhyzhkin using their theoretical electrostatic model.

4.2 Parameter Identification

4.2.1 Empirical Laws

One of the main problems that arises is to determine what mechanical properties are going to be used in order to characterise atmospheric ice. Unfortunately, very few studies on the subject exist. Most studies are interested in the tensile or compressive strength but do not provide many information on mechanical characteristics in the form of well defined laws [59, 90, 11]. These experiments are very difficult to conduct due to the vast number of parameters on which those properties depend, making the issue all the more complicated. Moreover, atmospheric ice can have a porous nature (in the case of rime ice for example), adding some more difficulties. Work in this direction can be found, for example, in [83], where Eskandarian reports a determination of Young's modulus and Poisson's ratio for porous ice.

Therefore, as a first approach, data and empirical laws given by experiments for natural ice are used as a starting point. These laws are more precise, and more widely studied. Nevertheless, they apply to different types of ice (natural, polycrystaline, sea water). As such, they do not apply to atmospheric ice. Therefore only the general form of the empirical laws is retained. In section 4.2.2 their parameters will be identified so as to fit experimental data for atmospheric ice.

The temperature dependence of Young's modulus is obtained using the formula (4.1), given in [33]:

$$E(T) = E(T_r) \left[1 - a(T - T_r) \right] \tag{4.1}$$

where $a = 1.42 \, 10^{-3} K^{-1}$ and T_r is the temperature at which the initial measurement was conducted.

Grain size (d_{grain}) and porosity (ϕ) take different values depending on the way the ice was formed. They also affect the material paremeters. Shulson and Duval report that the effect of porosity on Young's modulus can be taken into account with the following empirical law: $E = E_0 - b\phi$ [33]. In order to take into account both effects of temperature and porosity, we propose to combine this empirical law with relation 4.1 to form the following law:

$$E = E(T_r) \left[1 - a(T - T_r) \right] - b\phi \qquad \phi \leq 0.1 \text{ and E is in GPa} \tag{4.2}$$

In the same way, for fracture toughness, two empirical laws, $K_{I0}^* = \left[K_{I0} + \frac{\gamma}{\sqrt{d_{grain}}} 10^{-1.5} \right]$ and $K_{IC} = K_{I0}^*(1.0 - c\phi)$[33], are combined to give:

$$K_{IC} = \left[K_{I0} + \frac{\gamma}{\sqrt{d_{grain}}} 10^{-1.5} \right] (1.0 - c\phi) \qquad \text{with } d_{grain} \text{ in meters} \tag{4.3}$$

where $b = 35.1 \, GPa$, $c = 1.0$, $K_{I0} = 58.3 \, kPa.\sqrt{m}$ and $\gamma = 42.4 \, kPa.m$. K_{IC} is the fracture toughness (the critical stress intensity factor). It may be linked to the crack energy release rate with the relations:

$$g_c = (1 - \nu^2) \frac{K_{IC}^2}{E} \qquad \text{for plane strain} \tag{4.4}$$

$$g_c = \frac{K_{IC}^2}{E} \qquad \text{for plane stress} \tag{4.5}$$

Moreover, as shown in figure 4.5, ambient temperature also has an effect on fracture toughness. In order to formulate an empirical law, the experimental data of Liu *et Al.* are used. The results of their measurements are shown on figure 4.20.
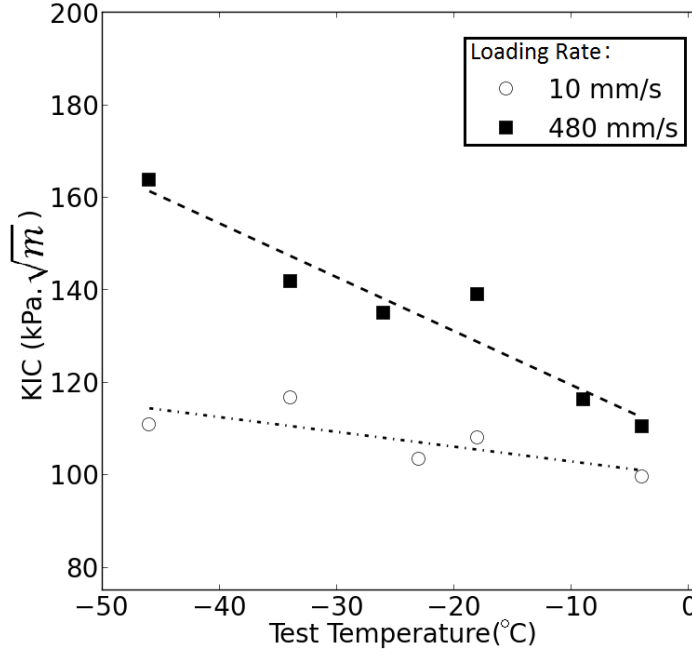
Figure 4.20: Effect of testing temperature on fracture toughness at different loading rates [55]

Hence, as a first approximation this effect can be taken into account with a relation such as: $K_{IC,T} = K_{IC,ref} - c_T(T - 273.15)$. We propose to integrate this relation into (4.3) in two ways:

$$\text{Law 1} : K_{IC} = \left[K_{I0} - c_T(T - 273.15) + \frac{\gamma}{\sqrt{d_{grain}}} 10^{-1.5} \right] (1.0 - c\phi) \tag{4.6a}$$

$$\text{Law 2} : K_{IC} = \left[K_{I0} + \frac{\gamma}{\sqrt{d_{grain}}} 10^{-1.5} \right] (1.0 - c\phi) - c_T(T - 273.15) \tag{4.6b}$$

where c_T is a parameter which will be identified, and $T < 273.15K$. Intuitively, Law 1 means that K_{I0} is the reference fracture toughness. On the other hand, Law 2 represents the case where the fracture toughness resulting from the accumulation thermal conditions is the reference to which the ambiant temperature conditions apply. However, as will be shown later, the difference between each law is slight.

4.2.2 Parameter Identification: Experimental Test Case

As stated section 4.2.1, the parameters defining the mechanical properties of ice have to be redefined. Mohamed *et al* have performed experiments in order to characterize the tensile strength of atmospheric ice [11]. We reproduce here these experiments and evaluate the tensile strength given by the damage mechanics model (introduced in chapter 3). This will serve to assess the applicability of this method to more complex situations and the suitability of the chosen mechanical properties. The goal here is not to provide extremely precise laws. They serve to give a good enough framework so as to confidently interpret the results that will come out of the numerical experiments.

The computational domain reproduces the shape of the experimental specimen (minus the region in contact with the elastic holder, via which stress in transmitted to the specimen during the test). It has a dumbell shape with dimensions as shown figure 4.21. All three experimental test temperatures are considered: $-5°C$, $-10°C$ and $-15°C$. The accumulation temperature was the same for all samples and set to $-10°C$. Mohamed *et al* report a grain size of $0.7mm$ and a porosity of 3%.
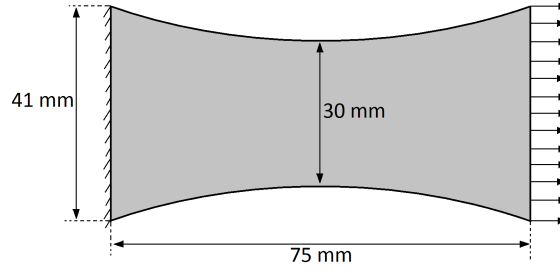
Figure 4.21: Dumbell shape

If we choose relations (4.2) and (4.3) in their initial form, the model gives a tensile strength of $1.1MPa$ for all temperatures. This means we are underestimating tensile strength and capturing no test temperature effect. Hence the choice to incorporate test temperature effect with relation (4.6). Therefore as stated before, the parameters defining the mechanical properties of ice have to be redefined. To sum up, we are going to start by using the following relations (law 1 for K_{IC}):

$$E = E(T_r)\left[1 - a(T - T_r)\right] - b\phi \qquad \phi \leq 0.1 \text{ and E is in GPa}$$

$$K_{IC} = \left[K_{I0} - c_T(T - 273.15) + \frac{\gamma}{\sqrt{d_{grain}}}10^{-1.5}\right](1.0 - c\phi)$$

with d_{grain} in meters and $T < 273.15$. According to Schulson and Duval [33], coefficients a and b have the values: $a = 1.42\,10^{-3}K^{-1}$ and $b = 35.1GPa$. With the law for Young's modulus now fixed, for each temperature, we apply the mean experimental tensile strength and search for the values of K_{IC} that lead to a fractured state. We are then left with the problem of defining a law which will yield these values. As c_T defines the effect of test temperature on K_{IC}, it needs to be redefined. Moreover, considering the initial relation (4.3) underestimates tensile strength, a good choice is to also redefine the parameter K_{I0}, which almost acts as an offset value. With all other parameters fixed we are led to the following set of 3 equations for 2 unknowns:

$$\begin{bmatrix} 1 & -(T1 - 273.15) \\ 1 & -(T2 - 273.15) \\ 1 & -(T3 - 273.15) \end{bmatrix} \begin{bmatrix} K_{I0} \\ c_T \end{bmatrix} = \begin{bmatrix} \frac{K_{IC}(T=T1)}{1.0-c\phi} - \frac{\gamma}{\sqrt{d_{grain}}}10^{-1.5} \\ \frac{K_{IC}(T=T2)}{1.0-c\phi} - \frac{\gamma}{\sqrt{d_{grain}}}10^{-1.5} \\ \frac{K_{IC}(T=T3)}{1.0-c\phi} - \frac{\gamma}{\sqrt{d_{grain}}}10^{-1.5} \end{bmatrix}$$

where $T1 = 268.15K$, $T2 = 263.15K$ and $T3 = 258.15K$. We solve this underdetermined linear system with a least squares method. We obtain: $K_{I0} = 72.0kPa.\sqrt{m}$ and $c_T = 1.0kPa.\sqrt{m}.K^{-1}$. Taking law 2 for K_{IC} yields the same values. Figure 4.22(a) is a plot of tensile strength with temperature, on which we compare our numerical results with those of Mohamed *et al*'s experiments. The identification process is successful in providing a good match between experiment and simulation. We can see on figure 4.22(b) that the crack topology consists of a straigth crack cutting through the ice at the location of minimal section. The computations were performed with a 40000 element mesh such that $l = 5.0\,10^{-4}$.
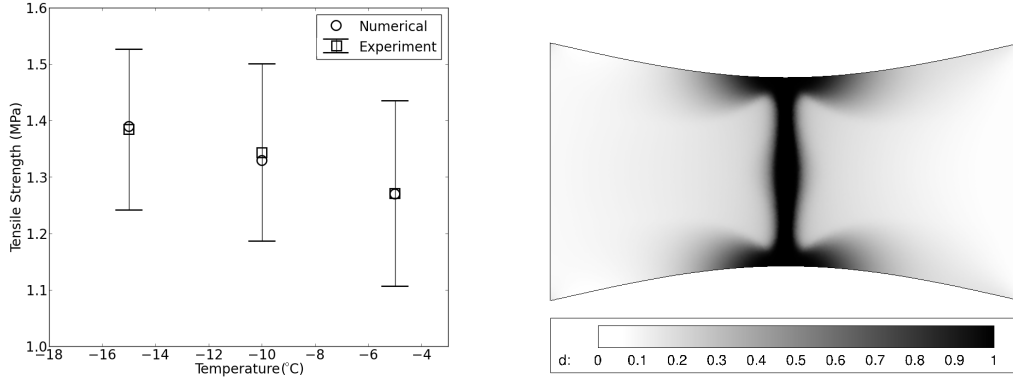
(a) Experimental and Numerical Tensile Strength. The error bars represent the standard deviation on Mohamed *et al*'s data

(b) Damage field: fractured state

Figure 4.22

On figure 4.23, we plot the critical stress intensity factor given by both laws as a function of grain size and porosity at fixed temperature. Both laws yield the same results when varying grain size. A slight effect is noted with increasing porosity. However this effect is small and switching laws did not produce any visible effect when performing the subsequent simulations.
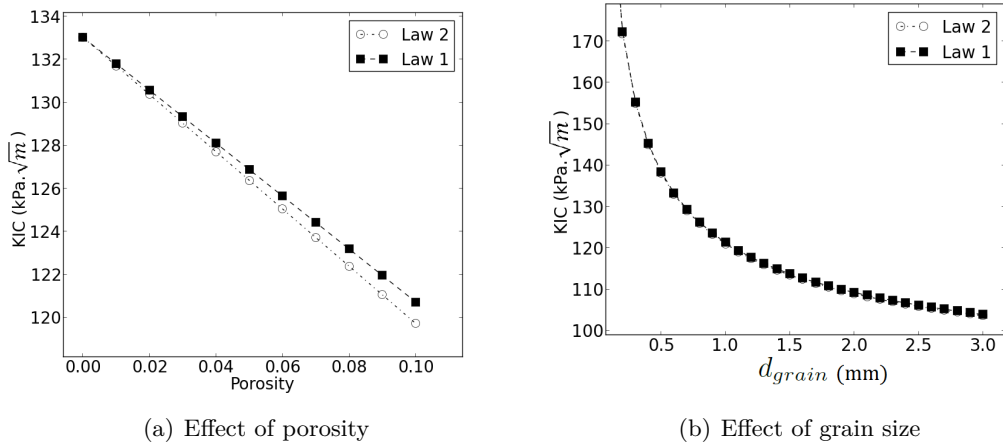
(a) Effect of porosity

(b) Effect of grain size

Figure 4.23: K_{IC} as a function of grain size and porosity: Comparison between law 1 and law 2

The subject of this chapter is the investigation of possible ice shedding mechanisms from aeronautical surfaces such as wings or air intakes. First the mechanisms are proposed from a phenomenological point of view. They are then investigated by defining several numerical experiments. The results are discussed as well as the limitations of the different approaches.

Contents

5.1 The Issue of Ice Shedding

First, let us recall how an Electro-Thermal Ice Protection System (ETIPS) operates:

- It may operate in anti-icing mode, in which case ice is not allowed to form on the protected surface.

- It may operate in de-icing mode. In this case, ice is allowed to form on the protected surface. It is removed by cyclically heating the surface thanks to electrical heaters. The heat provided acts to melt the corresponding part of the ice/surface interface. Once enough ice has melted, the ice no longer has enough ability to adhere to the surface and is shed under the effect of aerodynamic forces.

From an energy consumption perspective, the de-icing mode is prefered in order to fully take advantage of such a system. The operating in de-icing mode is illustrated in figure 5.1. The heater labeled C serves as what is called a parting strip: it remains activated during the whole cycle. It is usually positionned so as to prevent ice from accumulating at the leading edge or stagnation point. In this chapter, the mechanism by which the de-icing operation terminates, that is to say ice shedding, is investigated. The problem of its prediction is a key point in the evaluation of an electro-thermal ice protection system's performance. Moreover, predicting when and what amount of ice is shed is also important with regards to subsequent impact analysis.
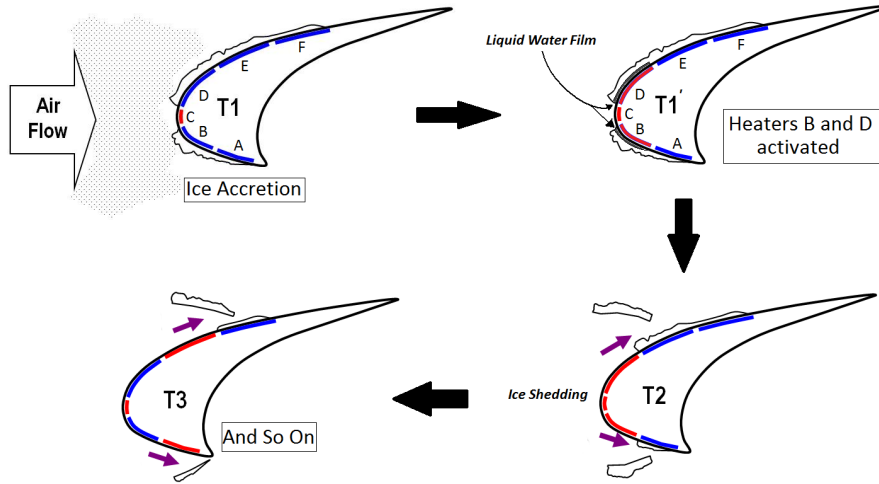
Figure 5.1: ETIPS operating illustration

5.2 Proposed Mechanism

Let us consider a situation as depicted figure 5.2, where ice has accreted just after the parting strip. The contact zone between the ice and the surface extends over a curvilinear distance, say L_t. The mechanism we propose is based on two observations. Firstly, the flow over such a shape will induce pressure variations over the lump. Figure 5.3 depicts a typical pressure distribution. Secondly, due to the ETIPS, a certain amount of ice in contact with the surface has melted. This leads to the creation of a thin film of liquid water extending over a distance L_f. A contact point, P_c, exists between the external flow and the film. The pressure at this point will be entirely redistributed by the film over the length L_f due to the absence of motion in the liquid water film[1] (hydrostatic pressure

---

[1]In fact, as liquid water takes up less volume than ice, a gap may form in the melted region. That is to say, the water film may not entirely occupy the volume formerly made out of ice and air may be allowed to fill in the gap. However, we would still be in a case of hydrostatic pressure equilibrium. Therefore we would still have pressure redistribution as described.

equilibrium). The presence of the ice shape will cause an acceleration of the flow when passing over it, which decreases pressure at the same time. This means the pressure recovered in the film will be higher than that acting on the external surface.
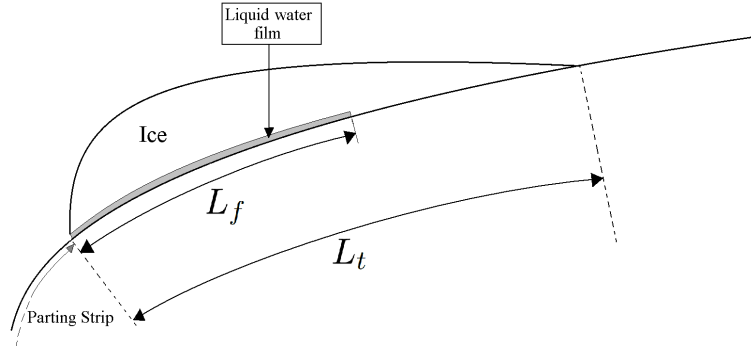
Figure 5.2: Geometrical Illustration
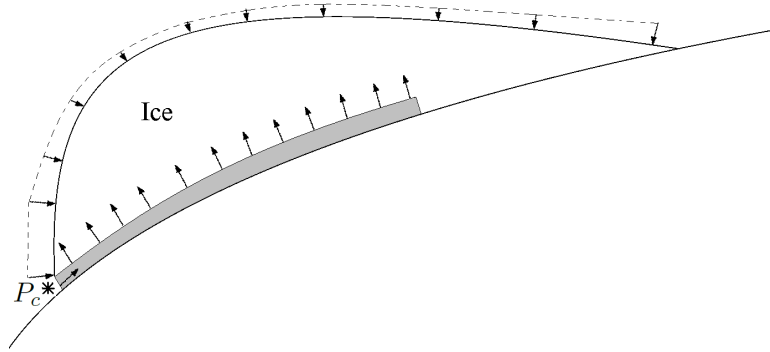
Figure 5.3: Schematic Pressure Distribution

This pressure distribution creates a lifting force. To this force, one has to add the viscous forces, which are tangential. Thanks to these forces several outcomes may be possible:

- The whole length is melted ($L_f = L_t$) in which case the ice no longer adheres to the surface (or only by means of surface tension effects).

- Adhesive interfacial debonding : part of the length $L_f = x\% L_t$ is melted and the adhesion forces that maintain ice on the surface are no longer strong enough.
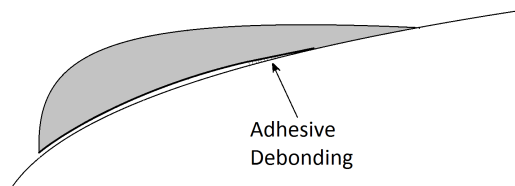
Figure 5.4: Adhesive debonding

- Cohesive interfacial debonding : part of the length $L_f = x\% L_t$ is melted, ice can still adhere, but a crack may nucleate due to stress concentration and propagate along the interface.
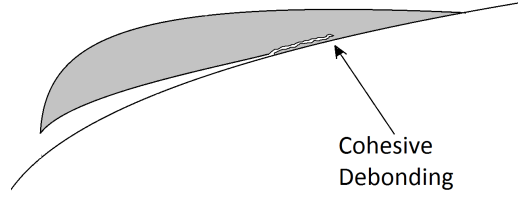
Figure 5.5: Cohesive debonding

- Bulk failure : part of the length $L_f = x\%L_t$ is melted, ice can still adhere, but a crack may nucleate due to stress concentration and propagate inside the bulk of the ice block, therefore tearing off a part of the ice.
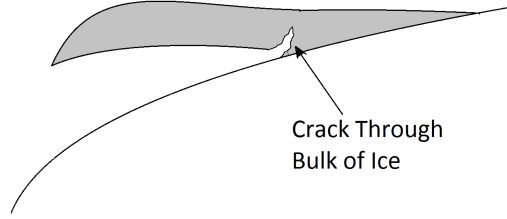
Figure 5.6: Bulk failure

- Ice shedding is due to an interplay of all or part of the previous mechanisms, as the experiments of Wei *et al.* seem to suggest [160].
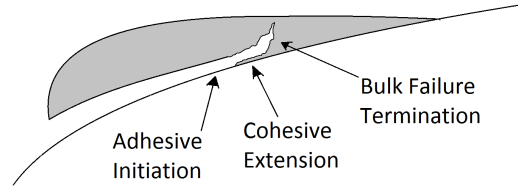
Figure 5.7: Adhesive initiation followed by cohesive extension. Process terminates with bulk failure

The mechanisms leading to ice shedding are to this day not well understood. No attempt has been made yet to explain how,when and under what conditions ice shedding will occur under the effect of a thermal de-icing system. Experimental observation shows that brittle failure plays a crucial role. Using numerical experimentation, three mechanisms are investigated: purely adhesive, bulk failure and adhesive mixed with bulk failure. An emphasis is put on the bulk failure mode.

5.3 Bulk Brittle Failure

Icing and ice protection are complex unsteady phenomena. Icing codes typically include several modules in order to determine water droplet catch efficiency, ice growth and heat and mass transfer. A true electrothermal de-icing numerical simulation requires going through all of these steps and adding a shedding criterion. But we will not use this whole panel of modules. What we are examining is a very specific mechanism. We therefore use the possibilities offered by numerical simulation to look into the effects of varying only some parameters, all others being fixed. We consider two cases (described below). In these cases time is frozen: the ice shape is constant, the flow field is constant, and we vary the length of the water film L_f, grain size d_{grain} and porosity ϕ.

The numerical experiments are defined by using two elements:

- An aerodynamic shape: here we consider a flat plate and a NACA0012 airfoil

- A generic ice shape: we choose it to be shaped as a teardrop. It represents a simple form of intercycle ice shape. Its characteristic thickness is noted h_{ice} and is set to $3.0mm$.

The ice shape is then placed on the aerodynamic shape. In the case of the airfoil, we choose a location that is coherent with the actual functionning of an ETIPS (not far from the parting strip). The ONERA Aero2D Euler solver is used to obtain the pressure distribution on the ice shape. This pressure distribution will define the Neumann boundary conditions for the crack propagation problem. Figure 5.8 is a generic sketch where we have illustrated the three different boundary conditions:

$$u = 0 \qquad\qquad \text{on } \Gamma_u \qquad\qquad (5.1)$$

$$\sigma.n = p_{exterior}.n \qquad\qquad \text{on } \Gamma_{exterior} \qquad\qquad (5.2)$$

$$\sigma.n = p_{redistributed}.n \qquad\qquad \text{on } \Gamma_p \qquad\qquad (5.3)$$
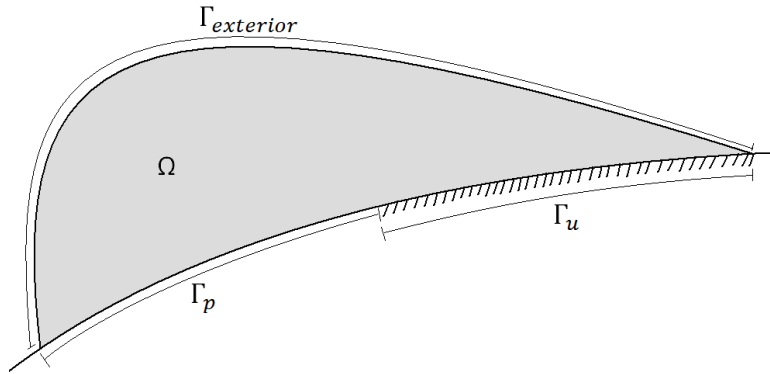
Figure 5.8: Boundary definitions

As explained previously, the only varying parameters will be L_f, d_{grain} and ϕ. Therefore the aerodynamic flow field is fixed once and for all for each case i.e. we do not consider any feedback process due to the eventual lifting of the ice shape, we discuss the implications of this simplification further on.

Before we proceed to the actual test cases, we simplify a little further our problem. First we do not substract from the ice shape the melted region that consitutes the water film as we consider it to be negligibly small. Moreover, at the time being, we do not take into account surface tension effects. Therefore what we are considering is an idealized situation whose only goal is to help us investigate and extract what phenomena may be relevant or not.

We choose to explore different values of porosity (0% to 10% with 1 point increment, at fixed grain size of $0.7mm$) and grain size ($0.1mm$, $0.3mm$, $0.5mm$, $0.7mm$, $1.0mm$, $1.5mm$, $2.0mm$, $2.5mm$, $3.0mm$, at fixed porosity of 3%) in order to evaluate their possible impact. Of course the impact that may or may not be observed numerically is directly linked to the empirical laws chosen and identified in sections 4.2.1 and 4.2.2.

In typical icing conditions, ice will build up along the whole wing span. Therefore, in this case, plane strain seems to be the better choice for the two dimensional formulation of elasticity, for it corresponds to the case of a body of infinite span. However we also chose to use plane stress in order to gauge the impact of the 2D elasticity formulation.

To summarize we define two numerical experiments, one which is defined by a flat plate, and the other by a NACA0012 airfoil. The experiment consists in varying L_f until fracture occurs, starting with $L_f = 0$.

The aerodynamic computations are done with an in-house compressible Euler solver (2nd order Roe scheme (MUSCL) and implicit time stepping). Meshes for both cases consisted of ~ 35000 triangular elements.

5.3.1 Flat Plate Configuration

This may be the simplest case we can consider, an ice shape attached to a flat plate, illustrated in figure 5.9 (not to scale). The total length of the flat plate, L_{fp} is set to $0.9m$. The length of the beveled region is $L_b = 0.05m$. The thickness of the plate is $h_{fp} = 2.2mm$. In this case $L_t = 31.225mm$. The aerodynamic conditions are the following:

Mach	P_∞ (Pa)	T_∞ (K)	α (°)
0.4	61640.0	263.15	0.0

Table 5.1: Aerodynamic conditions
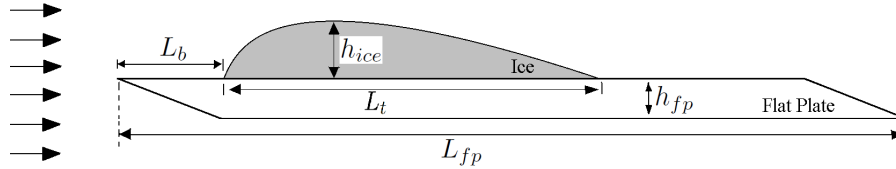
Figure 5.9: Flat Plate Test Case

The mesh for this test case consisted of 40000 triangular elements. Due to the bending nature of the uplifting force, it is expected that the stress concentration, leading to crack nucleation and propagation, will occur at the junction between melted and adhering ice. Hence mesh was refined in this area so as to set l to $4.0 \, 10^{-5}m$. A typical mesh is shown in figure 5.10.
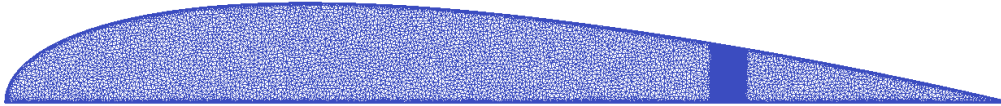
Figure 5.10: Flat plate mesh

On figure 5.11(a) we see the pressure distribution as given by the Euler solver, and the damage field for $\frac{L_f}{L_t} = 72\%$, $d_{grain} = 0.7mm$ and $\phi = 3\%$. As expected the pressure decreases when the flow goes over the bump. The uplifting force leads to a completely cracked state. If the ratio $\frac{L_f}{L_t}$ is too low, damage bearly accumulates and fracture does not occur, as shown in figure 5.11(b) ($\frac{L_f}{L_t} = 71\%$, $d_{grain} = 0.7mm$ and $\phi = 3\%$).

(a) Clear fractured state through the ice.

(b) No fracture if $\frac{L_f}{L_t}$ too low
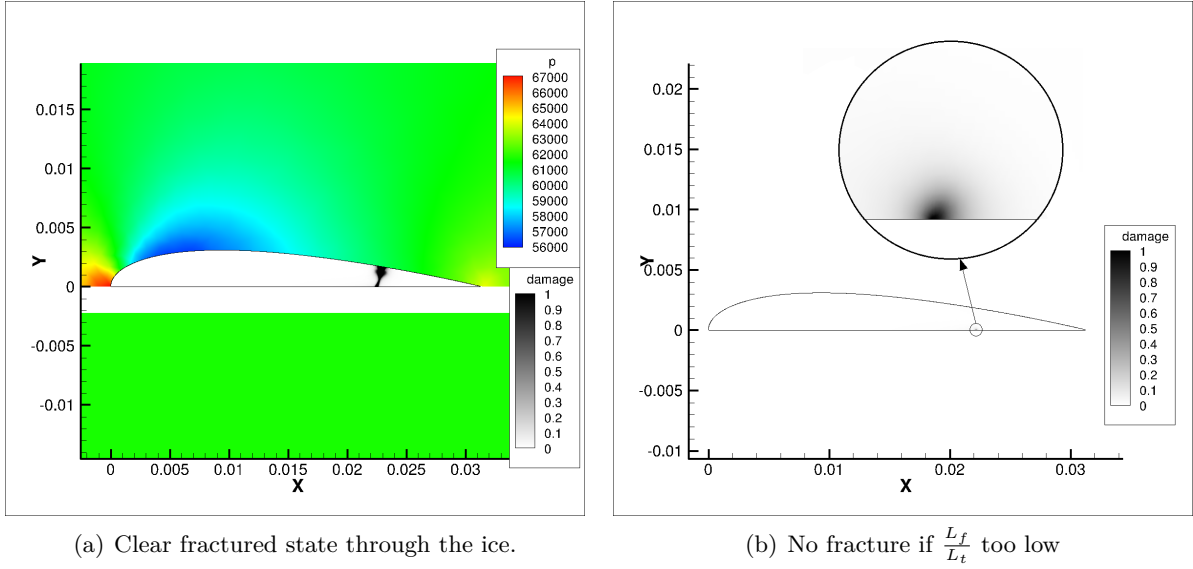
Figure 5.11: Pressure and Damage Fields

Figures 5.12 represent $\frac{L_f}{L_t}$ as a function of grain size and porosity. Increasing grain size clearly has the effect of lowering the critical melted length. This is in agreement with the fact that grain size reduces fracture toughness. Variation of porosity has a lower impact on $\frac{L_f}{L_t}$. Still, the effect is visible: increasing porosity decreases the critical value of $\frac{L_f}{L_t}$.

Switching from plane strain to plane stress has the effect of reducing $\frac{L_f}{L_t}$. However the trends and conclusions remain the same as in plane strain.

(a) Effect of grain size

(b) Effect of porosity
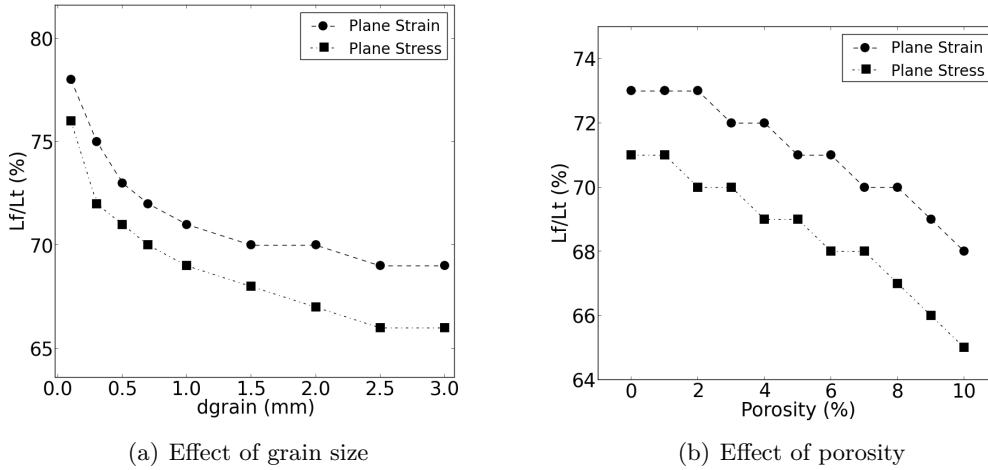
Figure 5.12: Critical value of $\frac{L_f}{L_t}$ as a function of porosity and grain size, for both plane strain and plane stress.

5.3.2 Airfoil Configuration

Here a more realistic case is considered: a NACA0012 airfoil on which we attach the ice shape. The aerodynamic conditions for this test case are almost the same as for the flat plate, except for the angle of attack which is set to 4°. The case is illustrated on figure 5.13(not to scale). The ice shape starts at $x = 0.02m$ and extends over a curvilinear distance of $L_t = 0.0337m$.

Mach	P_∞ (Pa)	T_∞ (K)	α (°)
0.4	61640.0	263.15	2.0

Table 5.2: Aerodynamic conditions
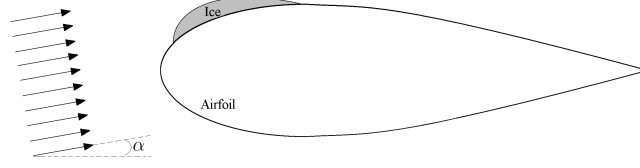
Figure 5.13: Airfoil Test Case

The mesh was built using the same characteristics as for the flat plate case and is shown in figure 5.14.
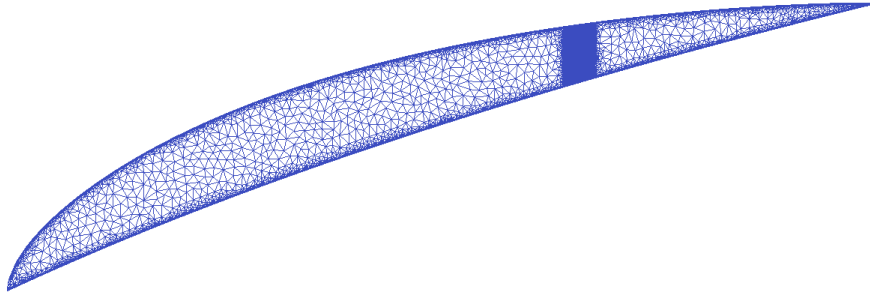
Figure 5.14: Airfoil mesh

As in the case of the flat plate, we see a pressure decrease over the bump. However the pressure decrease is more pronounced, due to the airfoil curvature. This leads to lower critical values of $\frac{L_f}{L_t}$. On figure 5.15 we see the pressure distribution as given by the Euler solver, and the damage field for $\frac{L_f}{L_t} = 62\%$, $d_{grain} = 0.7mm$ and $\phi = 3\%$.
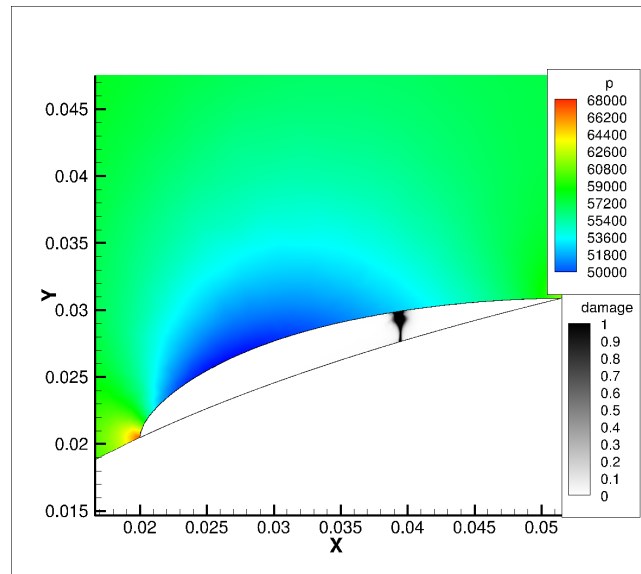
Figure 5.15: Clear fractured state through the ice

As in the case of the flat plate, increasing grain size decreases the critical value of $\frac{L_f}{L_t}$ (see figure 5.16(a)). This decrease is sharp in the range of small grain sizes and tends to stabilise for the higher

values of grain size. The effect of porosity is again much slighter but still visible and has the same effect, as can be seen on figure 5.16(b). Here again, switching to plane stress decreases the values of $\frac{L_f}{L_t}$.

(a) Effect of grain size   (b) Effect of porosity
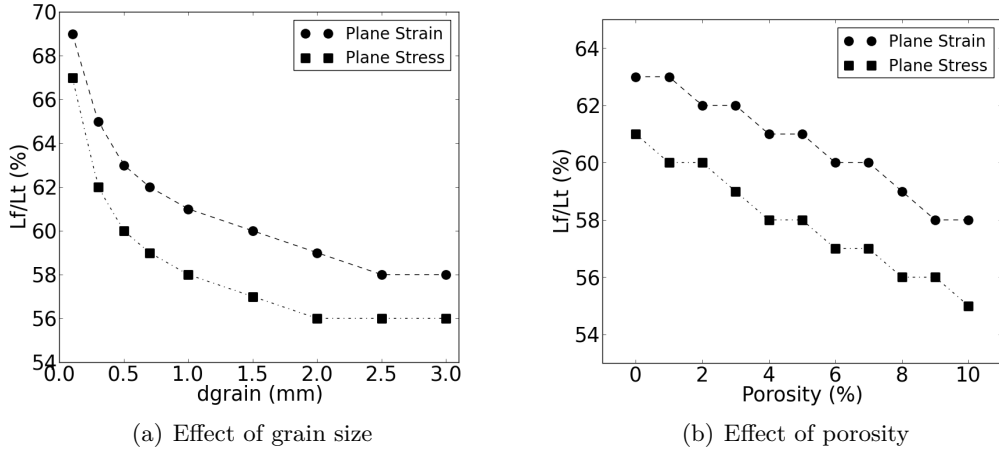
Figure 5.16: Critical value of $\frac{L_f}{L_t}$ as a function of porosity and grain size, for both plane strain and plane stress.

5.3.3   Discussion

The results of the numerical experiments show that, in both the flat plate and airfoil cases, a phenomenon of detachment before complete melting of the interface is possible. At a given critical value of $\frac{L_f}{L_t}$, the stress concentration is sufficient to enable crack nucleation and propagation over the whole thickness, therefore tearing off a certain amount of ice. The crack always nucleated from the inner tip of the melted region.

The effects of grain size and porosity on $\frac{L_f}{L_t}$ are visible. In both cases, grain size has a prominent effect for values ranging from $0.1mm$ to $1.5mm$, where the critical value of $\frac{L_f}{L_t}$ is abruptly decreased when grain size increases. For values ranging from $1.5mm$ to $3.0mm$ the effect of grain size tends to reach a limit. As for porosity, its effect is lower but more regular. Increasing porosity decreases $\frac{L_f}{L_t}$ and it does so in a steady manner.

In fact, if we look back at figures 4.23(b) and 4.23(a), and compare them to figures 5.12 and 5.16. We observe that they exhibit the same trends with respect to grain size and porosity. The mathematical model restitutes the effects of the empirical laws. One could argue that from this point of view the conclusions concerning the effect of porosity and grain size were predictable (qualitatively) and are somewhat artificial. But we should bear in mind that the problem is non-linear. The pressure distributions could have been such that the shedding would have always occured for the same value of $\frac{L_f}{L_t}$, leaving d_{grain} and ϕ to have insignificant effects. Or, it could have been that their effects on E and K_{IC} would have not been sufficient to change the outcome of the simulations. The fact that an effect is numerically predicted means that, for this specific kind of ice shedding situations, those two material parameters seem to be relevant.

Moreover, grain size and porosity can be linked to the atmospheric conditions. As stated earlier, the values of grain size and porosity depend on a vast number of parameters. The structure of atmospheric ice is the result of many droplets crystalizing one on top of each other or next to each other. It seems that the lower the accumulation temperature, the lower the grain size and the higher the porosity [90]. The fact that grain size decreases when decreasing the accumulation temperature would mean that, in severe icing conditions, the critical value of $\frac{L_f}{L_t}$ is higher. An ice protection system would need to melt more ice for shedding to occur. However, porosity goes in the opposite way: it increases with decreasing accumulation temperature. It would have the effect of reducing the value of $\frac{L_f}{L_t}$. Still, the effect of grain size should be prominent at those temperature, for Kermani *et al.* report an average value of less than $0.5mm$ at $-10°C$ [90]. Work remains to be done to clarify this conclusion.

5.4 Adhesive Debonding

The previous section was devoted to investigating the possibility of a bulk failure ice shedding mechanism. However, this may not be the only mechanism at play. Indeed, as stated in section 5.2, it may also be possible that a purely adhesive mechanism is involved.

So as to investigate such a possibility, a simple adhesion model is used. Within the finite element procedure it is possible to compute the stress in every interfacial element. Therefore, at every interfacial edge of the mesh, it is possible to compute the shear stress by projecting the stress tensor on the normal and tangential unit vectors. A simple procedure would therefore be to compare this shear stress to a maximum shear stress (such as that measured by Scavuzzo *et al* [122]) so as to determine if the edge remains in a bonded state or transitions to a debonded state. Numerically, this aspect may be treated through a Fourier-Robin boundary condition, defined by:

$$\sigma.n + \alpha u = \beta p_{redistributed}.n$$

where the parameter α and β define the bonded or debonded state. If the edge is in a debonded state then $\alpha = 0$ and $\beta = 1$. Conversely if the edge is in a bonded state then α is set to a large number and $\beta = 0$. Therefore, this boundary condition can be seen as switching between homogeneous Dirichlet boundary and Neumann boundary conditions. In the bulk of the ice, the damage model is not activated and therefore the mechanical behaviour in the bulk reduces to that of a classical linear elastic medium.

Given the various experimental results for atmospheric ice adhesion, the critical shear adhesive stress is set to $500kPa$ (see figure 4.18). With this simple model at hand, the airfoil case is performed with $d_{grain} = 0.7mm$ and $\phi = 3\%$. The mesh that is used is the same as for the following case and will be discussed in more detail in section 5.5. The critical length was found to be $L_f = 35\%L_t$, leading to a completely debonded state, as shown in figure 5.17.
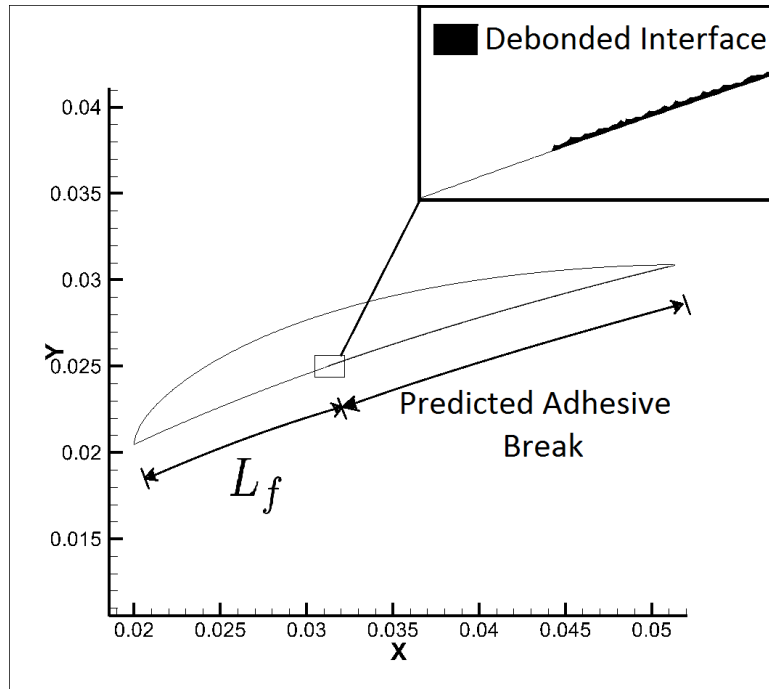
Figure 5.17: Fully debonded state

One of the most important points that is raised by this simulation is that, according to this model, adhesive debonding occurs before the possibility of bulk failure. Indeed, in the same conditions, bulk failure occurs for $L_f/L_t = 62\%$, as opposed to 35% in the case of purely adhesive debonding. Hence, this result opens the door to the possibility of a mixed adhesive/bulk failure mechanism.

However, it should be noted that such a simple adhesive debonding model can only provide a first approach. A way of extending this investigation would be to use other models, such as cohesive zone

modelling which seems adapted to such problems. Another solution, in the line of Fremond's adhesion model, would be to extend this modelling strategy by introducing an interface damage variable d_i which would control the switching parameters α and β. These parameters would then become function of d_i. The problem would then be to formulate a law governing the behaviour of d_i.

5.5   Adhesive Debonding Followed by Bulk Failure

In the light of the previous result, the final step is to investigate the possibility of a mixed debonding process. In order to do so, the fracture model and simple adhesion model are used together in the following way:

1. Compute shear stress at every interfacial edge due to uplifting force.

2. Apply adhesive debonding where predicted by the simple model.

3. Change interfacial boundary condition accordingly.

4. Apply fracture model to predict if crack nucleation/propagation occurs or not.

The previous steps are repeated in a loop until a final state is reached. It should be noted that, if adhesive debonding occurs at a given step, the following fracture computation has to be allowed to reach its equilibrium state in order to remain consistent with the quasi-static approach. A restriction to the amount of debonded edges at each iteration was imposed. In effect, the simple adhesion model may result in the debonding of many edges in one step. This could lead in predicting bulk failure much later. The restriction was imposed such that no more than a length of $10h$ could be debonded at every iteration.

This procedure is applied to the airfoil case with $d_{grain} = 0.7mm$ and $\phi = 3\%$. As the region of crack propagation in this case is not known apriori, the mesh is constituted of 110000 elements of same size with l set to 10^{-4}.
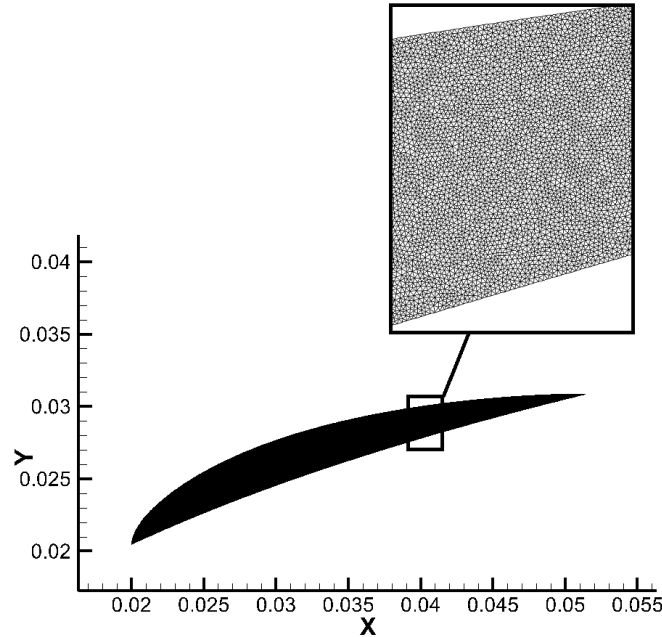
Figure 5.18: Mesh used for adhesive and adhesive/bulk failure simulations

As adhesive debonding is predicted for lower values of L_f/L_t, the critical length predicted is again $L_f = 35\%L_t$. The shedding process starts with purely adhesive debonding. Once a critical adhesive debonding length is reached, a crack nucleates and propagates through the bulk, as shown in figure

5.19. Hence, this simulation tends to show that an adhesive debonding process acting on its own is impossible.
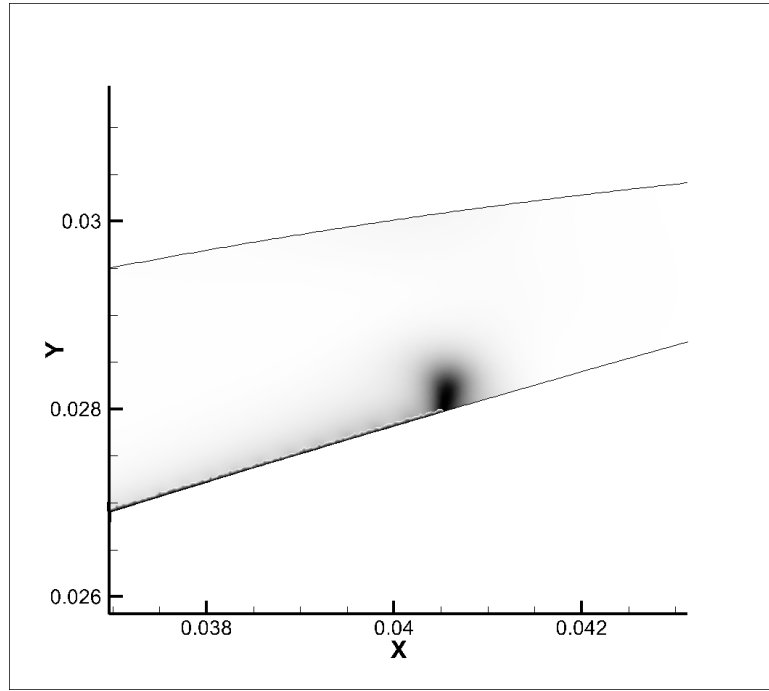
Figure 5.19: Adhesive debonding with crack initiation
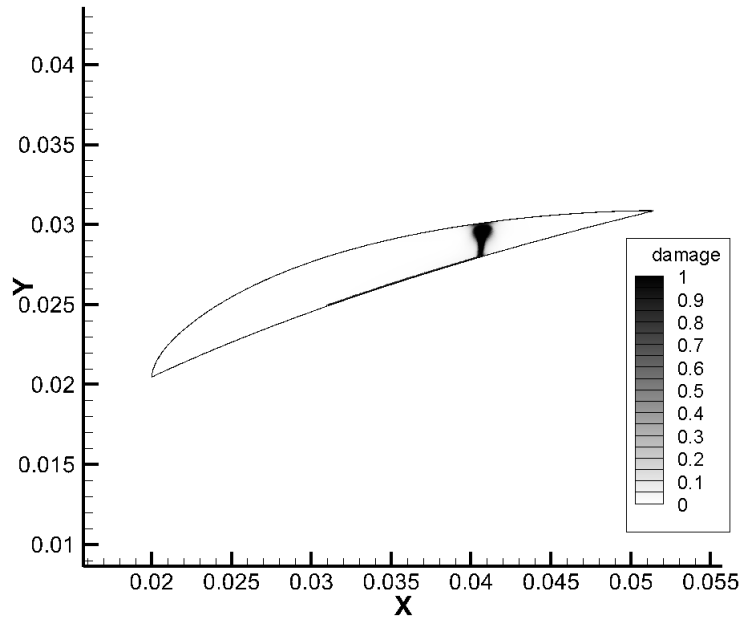
Figure 5.20: Fully debonded/fractured state

5.6 Remarks

In view of the lack of precise experimentation on this particular issue, it is difficult to determine which mechanism is dominant over the others. Hence the proposed ice shedding mechanisms remain to be investigated experimentally. If it were to be found that adhesive debonding occurs before bulk failure, then the mixed adhesive/bulk failure mechanism would be the most relevant one. Indeed, as shown by the computations, a purely adhesive debonding process seems impossible. At one point

the critical bulk failure would be reached, therefore ending the adhesive process. The possibility of cohesive interfacial debonding also remains to be added in the modelling strategy and investigated. That being said, the global process by which shedding is induced by pressure redistribution in the liquid water film remains relevant. Shedding is predicted even in the worse case scenario of having to wait until bulk failure occurs.

Some limitations should also be noted:

- Empirical laws were used in order to characterize the mechanical behaviour of atmospheric ice which have their limitations. It is very complicated to characterise the mechanical properties of atmospheric ice. Most of the time experimental results are highly scaterred and no precise laws are available.

- A simplified inter-cycle ice shape has been assumed.

- The ice shape may grow in time. This is not taken into account. However this should not have a large effect. The characteristic time of crack propagation is much lower than that of ice acccretion (as soon as the critical ice shedding conditions are reached).

- Surface tension was not taken into account. However, the surface tension of a water/air or water/ice interface is in the order of $10^{-2} J.m^{-2}$ whereas g_c for ice is in the order of $1 J.m^{-2}$. Hence, when fracture of ice occurs, the energy at play will be 100 times larger than the surface tension energy. Therefore surface tension is not expected to play a significant role.

- Viscous flow effects such as friction were not taken into account. However the contribution of friction is expected to be negligible compared to pressure.

- In reality, a feedback process between the lifting of the ice shape and the flow field occurs. The lifting of the ice shape occurs simultaneously with a corresponding change in the flow field. And this change in flow field immediately induces a new lifting force on the ice shape. This process is not taken into account. We consider the pressure distribution given by the first computation as fixed. Still, the change in presure distribution would lead to a higher uplifting force in this case. Therefore this should not impact the results significantly.

- Possible thermo-elastic effects, due to temperature gradients, are not taken into account. The thermal strain due to a temperature difference of ΔT will be of the order of $\epsilon_T = \alpha \Delta T$, where α is the thermal expansion coefficient in K^{-1}. Hence the thermal stress due to this temperature difference will be of the order of $\sigma_T = E\alpha\Delta T$. The thermal expansion of ice has a value of about $\alpha = 5\,10^{-5} K^{-1}$. Therefore a temperature difference of $\Delta T = 20K$ will yields a thermal stress of the order of $1\,MPa$. As the tensile strength of ice is of the same order of magnitude, thermo-elastic effects could play a role. This is consistent with the experiments of King and Fletcher [152, 153] (see figure 4.7).

Still, even though the modelling strategy has some limitations, the proposed mechanisms consitute an interesting way forward for future investigation and modelling of ice shedding. With an improved adhesion model, these mechanisms could provide quantitative and qualitative explanations to experimental observations made when testing de-icing systems in icing wind tunnels.

ETIPS PERFORMANCE: NUMERICAL SIMULATION

This final chapter is devoted to coupling and applying the previously presented methodologies to investigate the operating of electro-thermal ice protection systems in various situations. The main goal is to assess the feasability of a coupling methodology taking into account all the previously mentionned thermal and mechanical processes.

Contents

6.1 The INUIT Numerical Tool

During this thesis, several modules were developed in order to simulate the operating of electro-thermal ice protection systems. Put together, they form the building bricks of a numerical tool called I.N.U.I.T (Integrated NUmerical model of Ice protection sysTems). The tool was developed with a strong industrialisation constraint of being easily usable and interfaced with other modules. In time, it is planned to integrate the different bricks of this module in a global two dimensional icing tool developed at ONERA called IGLOO2D (IcinG tooL bOx Onera).

INUIT is built around three modules which were implemented based on the numerical models presented in chapters 2 and 3.

- ETIPS simulation module: simulates the thermal operating of an electro-thermal ice protection system.

- Thermal Ice: simulates heat transfer with phase change in an ice block.

- Mechanical Ice: predicts if the ice fractures under the effect of aerodynamic loads.

To ease the use of the ETIPS simulation module, an automatic structured mesh generator was also implemented and is part of a postprocessing module. It was built around previously defined user input contraints.

6.2 Dry Air Run

This test case deals with the ice protection of a helicopter main rotor blade airfoil section. The simulation settings reproduce the experimental setup of a run from an icing wing tunnel test campaign, performed at C.E.Pr (Centre d'Essai des Propulseurs) for Aerospatiale [111]. This case is what is called a dry air run. The run is performed at subzero flow conditions but without activating the water sprays. Therefore no ice accretion occurs during this kind of test. The goal of this procedure is to evaluate the temperature response of the system alone. Moreover, in combination with surface temperature measurements or temperature sensor data acquisition, this kind of test enables the assessment of the ETIPS numerical model.

6.2.1 Aerodynamic Setting

The airfoil that is used is a NACA23012 airfoil shape with a chord of $0.6m$. The aerodynamic conditions are summed up in the following table:

Mach	P_∞ (Pa)	T_∞ (K)	α (°)
0.5	79470.0	243.15	6.0

Table 6.1: Aerodynamic conditions for dry air run

So as to obtain the thermal boundary condition for the ETIPS simulation, a steady aerodynamic computation is performed in two steps. A first flow field (external to the boundary layer) is computed using the in-house Euler solver of the ONERA 2D icing tool. The computed pressure coefficient is shown in figure 6.1.
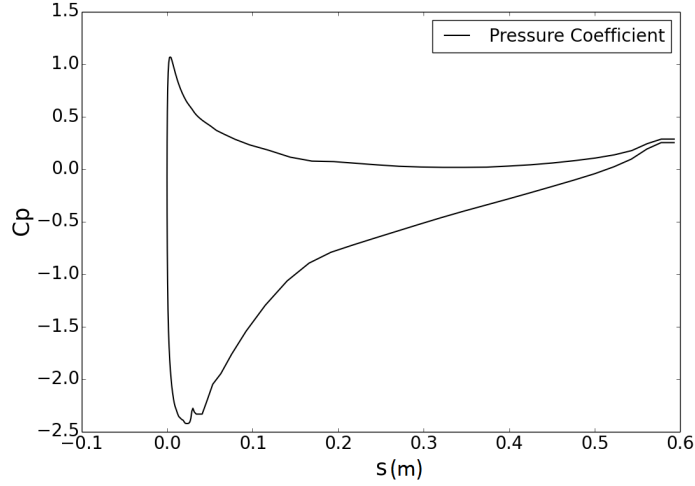
Figure 6.1: Pressure coefficient as a function of curvilinear abscissa s, obtained by the Euler solver

Using this flow field, an integral boundary layer module is run in order to compute the heat transfer coefficient (htc) and the recovery temperature (T_{rec}), which are shown in figures 6.2 and 6.3. More information on boundary layer computation can be found in appendix D. These two parameters serve to specify the Fourier-Robin thermal boundary condition $\phi = htc(T_w - T_{rec})$, where T_w is the surface temperature. It can be observed that the heat transfer coefficient starts at a value of about $450 W.m^{-2}.K^{-1}$ and decreases downstream until the laminar-turbulent transition is reached. At this point, due to the mixing features of turbulent flow, the heat transfer coefficient suddenly increases. As for the recovery temperature, it is defined as:

$$T_{rec} = T_e \left(1 + r \frac{\gamma - 1}{2} M_e^2 \right)$$

therefore it is directly linked to the external Mach number and external temperature. At the stagnation point, the external velocity is zero and hence at this point the recovery temperature is equal to the external flow temperature. At the stagnation point the external temperature is close to the total freestream temperature of $255K$, which corresponds to the observed peak in figure 6.2.
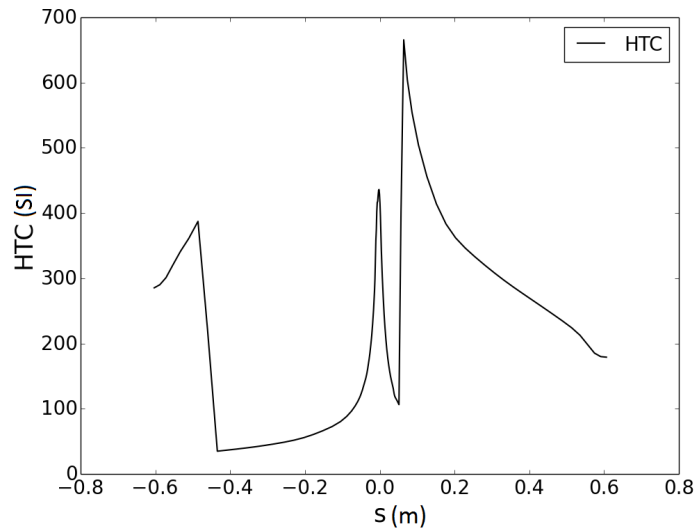
Figure 6.2: Heat transfer coefficient obtained by the integral boundary layer module

107
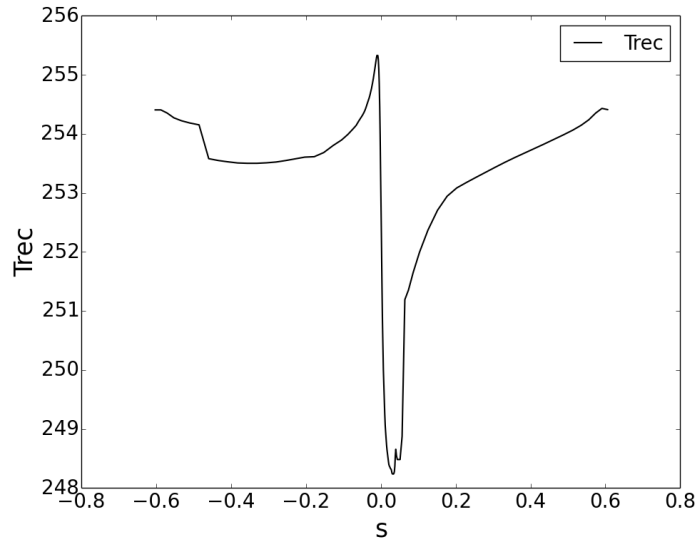
Figure 6.3: Recovery temperature obtained by the integral boundary layer module

6.2.2 ETIPS Setting

The system consists in 5 heater mats of length $3.125cm$, all separated from each other by a distance of $5mm$. The heaters are labeled from A to E as shown in figure 6.4. Heater D is centered with respect to the leading edge.
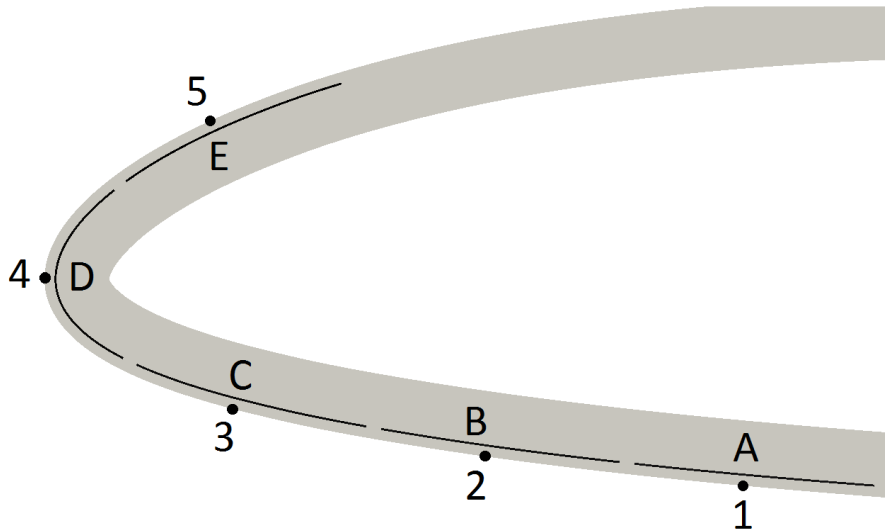
Figure 6.4: Illustration of the system

The heaters are embedded within a muli-layered stack of materials, whose characteristics are given in the following table:

Layer No	$\rho(kg.m^{-3})$	$c_p(J.kg^{-1}.K^{-1})$	$\lambda_\xi(W.m^{-1}.K^{-1})$	$\lambda_\eta(W.m^{-1}.K^{-1})$	thickness (m)
1	1000	2350	17.03	17.03	$8.e-04$
2	1250	2009.	0.293	0.293	$3.e-04$
3	1000	2381.	0.313	0.313	$1.e-04$
4	1250	2009.	0.293	0.293	$2.e-04$
5	1250	2009.	0.293	0.293	$5.e-04$
6	1000	1717	0.25	0.25	$2.52e-03$
7	1000	1717	0.25	0.25	$4.e-03$

Table 6.2: Multi-layered stack characteristics

The layers are numbered from the outer layer to the inner layer, that is to say layer no 1 is the layer in contact with the aerodynamic flow. The heaters are embedded between layers no 5 and 4. They have a density of $\rho = 1000.0 kg.m^{-3}$, a specific heat of $c_p = 3410.0 J.kg^{-1}.K^{-1}$ and a thickness of $1\,10^{-4}m$. Note that in order to remain consistent with formula (2.8), layer n° 4 may be meshed with at most 2 cells.

The heaters are all activated for $16s$ according to the cycle $D - E - C - B - D$. The end of the cycle is followed by a pause of $68s$. Heater A is never activated in this cycle and no heater serves as a parting strip (heater D is not activated permanently). The applied power is the same for all heaters and set to $27kW.m^{-2}$.

The mesh is defined using the curvilinear abscissa discretization (truncation abscissas set to $0.2m$ and $-0.2m$) defined in table 6.3 and layer discretization defined in table 6.4. The resulting mesh is shown in figure 6.5.

Zone No	$s_1(m)$	$s_2(m)$	nb of cells
1	-0.2	-0.115375	100
2	-0.115375	-0.084125	40
3	-0.084125	-0.082125	2
4	-0.082125	-0.050875	40
5	-0.050875	-0.048875	2
6	-0.048875	-0.017625	40
7	-0.017625	-0.015625	4
8	-0.015625	0.015625	80
9	0.015625	0.017625	4
10	0.017625	0.048875	40
11	0.048875	0.2	150

Table 6.3: Zone discretization

Layer No	thickness (m)	nb Cells
1	$8.e-04$	4
2	$3.e-04$	3
3	$1.e-04$	1
4	$2.e-04$	2
5	$5.e-04$	3
6	$2.52e-03$	20
7	$4.e-04$	20

Table 6.4: Layer discretization
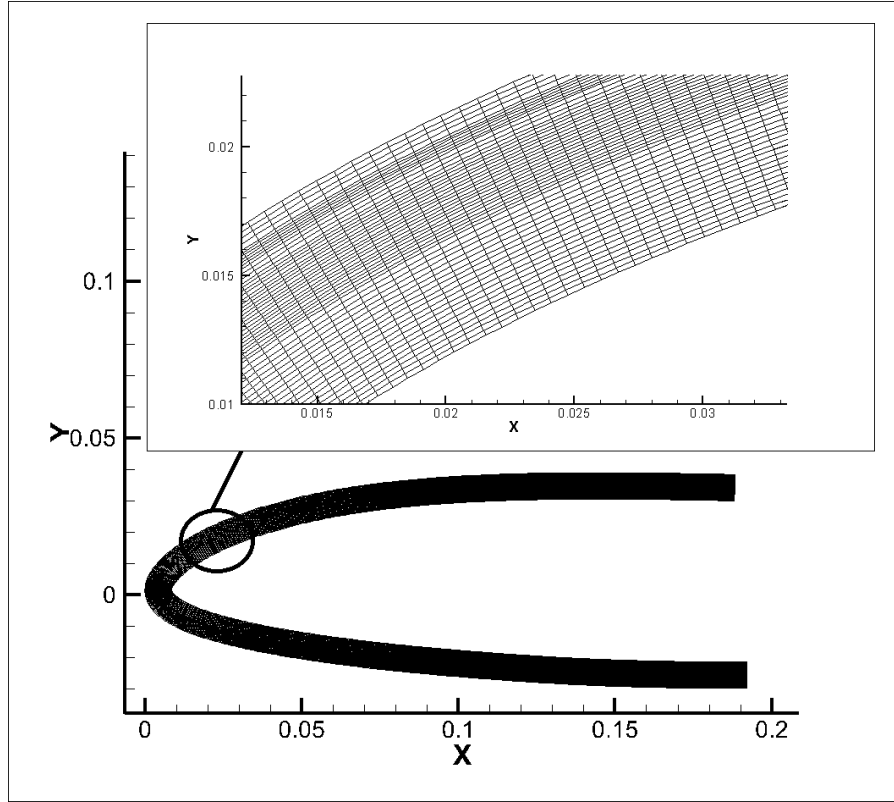
Figure 6.5: Mesh generated with data from tables 6.4 and 6.3

6.2.3 Results

In the experimental setup, surface temperatures were acquired using an infrared camera. According to Henry [111], the measured temperatures are at the middle of the surface zone corresponding to each heater (see location of points 1 to 5 in figure 6.4). However, only surface temperatures at points 2, 3 and 4 (corresponding to heaters B, C and D) are reported in reference [111]. The temperatures were extracted during the second cycle.

This experimental data is compared to the surface temperature computed by the ETIPS simulation module in figure 6.6. The predicted temperatures are of the same order of magnitude as those measured experimentally, except for heater B. The activation/deactivation cycles can clearly be identified. Experimentally, the peak temperature is attained on heater C and is of $30°C$. On the other hand, the numerical peak temperature is of $35°C$ and is attained on heater B.
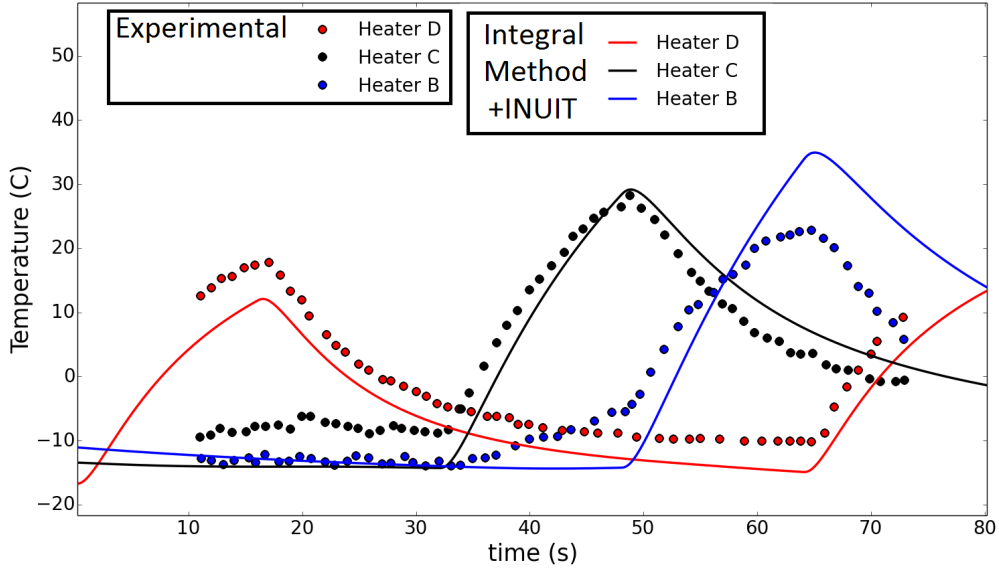
Figure 6.6: Comparison between experimental data and our numerical results for run 14 [111]

In order to perform further investigation, the boundary layer code CLICET [13] was also used to compute the convective heat transfer characteristics of the flow field. This code solves the full two dimensional boundary layer equations, as opposed to an integral formulation. The AHDC (Compressible Arnal-Habiballah-Delcourt) laminar/turbulent transition criterion and the Spalart-Allmaras turbulence model were used. The results in term of htc and T_{rec} are compared to those obtained by the integral boundary layer module and shown in figures 6.7 and 6.8. Although some differences may be noted with respect to T_{rec}, the main difference resides in the heat transfer coefficient. CLICET predicts that the laminar/turbulent transition (visible from the discontinuities) occurs much earlier than MIS2D. Although the heaters remains within the laminar region, even when predicted by CLICET, the fact that the transition occurs earlier is consistent with the lower temperature measurments on heater B.
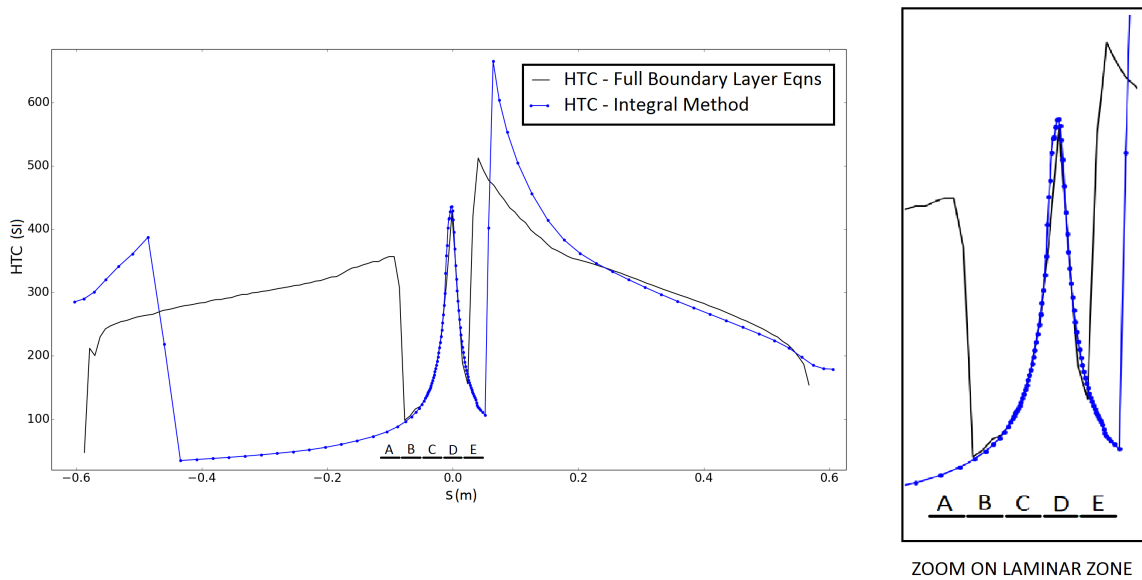
Figure 6.7: Comparison between the htc computed by CLICET and the integral boundary layer method
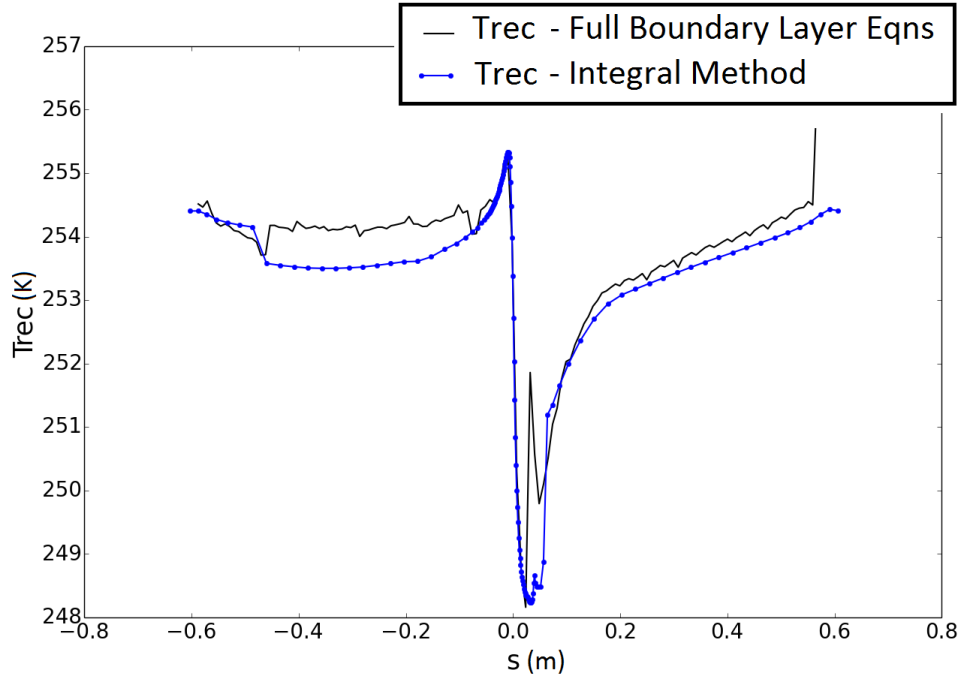
Figure 6.8: Comparison between the T_{rec} computed by CLICET and the integral boundary layer method

The predicted resulting surface termperatures are compared to those obtained previously and with the experimental data. However, the experimental data was measured for heaters that are within the predicted laminar zone. Given the fact that both boundary layer codes predict very similar convective variables in the laminar zones, the results at those probed locations differ but very slightly (see figure 6.9).
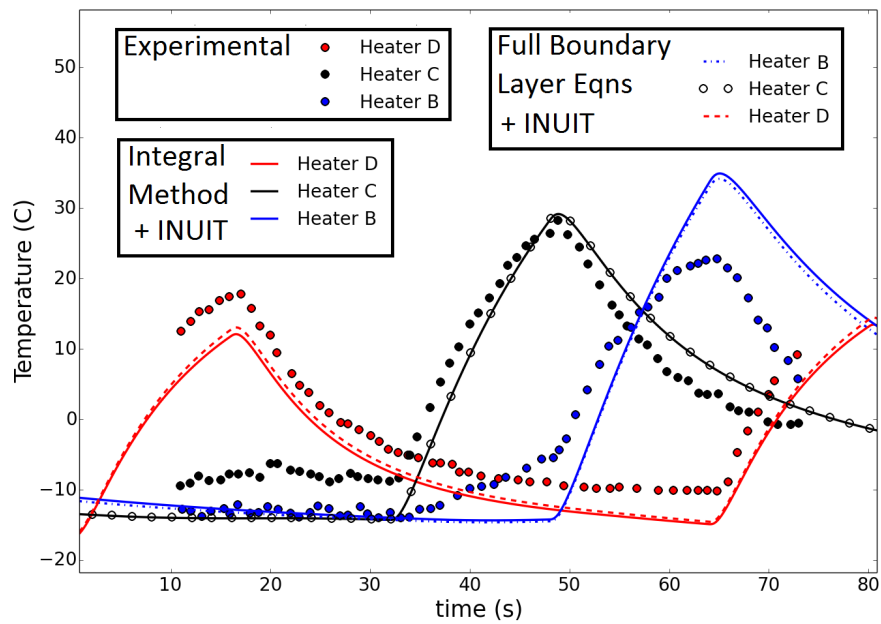
Figure 6.9: Comparison between experimental data and our numerical results (MIS2D and CLICET) for run 14 [111]

6.2.4 Sources of Error

Although the results presented in the previous section exhibit the correct orders of magnitude, they are not as good as they could be. It is interesting to try to identify the possible sources of error, their origins and impact on the predicted temperatures.

In order to analyse this issue, let us first solve a simplified problem from which analytical solutions may be extracted. Consider a rectangular domaine of dimension $L_x \times L_y$ as illustrated in figure 6.10. Let T be the temperature at the center of the domaine and ρ, c_p and λ denote respectively the density, specific heat and conductivity of the material. Assume the left boundary is subject to a convective boundary condition defined by a heat transfer coefficient *htc* and a recovery temperature T_{rec}. The right boundary is subject to a heat source Q which is active when time t is less than activation time t_a and deactivated after t_a (operating in the same manner as the heaters). The upper and lower boundaries are assumed adiabatic.
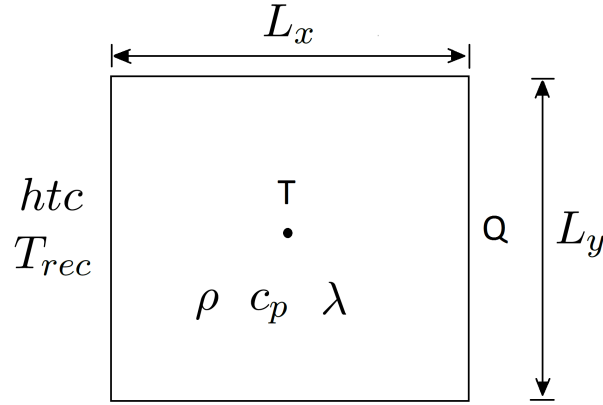
Figure 6.10: Simplified problem

Using the same methodology as in chapter 2 and defining:

$$H^* = \frac{1}{\frac{1}{\hat{\lambda}} + \frac{1}{h}}$$

with

$$\hat{\lambda} = \frac{\lambda}{0.5 L_x}$$

the flux on the left boundary is expressed as:

$$\phi_l = H^* \left(T_{rec} - T \right)$$

Conservation of energy yields the following governing equations for temperature T:

$$\dot{T} + \frac{H^*}{\rho c_p L_x} T = \frac{H^*}{\rho c_p L_x} T_{rec} + \frac{Q}{\rho c_p L_x} \qquad \text{for } 0 \leq t \leq t_a \tag{6.1}$$

$$\dot{T} + \frac{H^*}{\rho c_p L_x} T = \frac{H^*}{\rho c_p L_x} T_{rec} \qquad \text{for } t \geq t_a \tag{6.2}$$

$$T = T_0 \qquad \text{at } t = 0 \tag{6.3}$$

The solution to this E.D.O can be obtained analytically and reads:

$$T = \left[T_0 - T_{rec} - \frac{Q}{H^*} \right] e^{-\frac{H^*}{\rho c_p L_x} t} + T_{rec} + \frac{Q}{H^*} \qquad \text{for } 0 \leq t \leq t_a \tag{6.4}$$

$$T = \left[T(t_a) - T_{rec} \right] e^{-\frac{H^*}{\rho c_p L_x} (t - t_a)} + T_{rec} \qquad \text{for } t \geq t_a \tag{6.5}$$

The governing equation and corresponding solution is analogous to that of the charge and discharge of a capacitor in an RC circuit. The term $\frac{H^*}{\rho c_p L_x}$ defines the dynamic behaviour and may be reexpressed as:

$$\frac{H^*}{\rho c_p L_x} = \left[\frac{\rho c_p L_x}{\hat{\lambda}} + \frac{\rho c_p L_x}{htc}\right]^{-1} = \frac{1}{\tau_{cd} + \tau_{cv}}$$

where $\tau_{cd} = \frac{\rho c_p L_x^2}{\lambda}$ is the characteristic conduction time and $\tau_{cv} = \frac{\rho c_p L_x}{htc}$ is the characteristic convection time. These two time constants governe the dynamic behaviour of the thermal system and involve material parameters, geometric length scales and htc. From this simple approach it may also de deduced that when the source term Q is activated, the asymptotic temperature is $T_{rec} + \frac{Q}{H^*}$. When the source term is deactivated the asymptotic temperature is simply T_{rec} which is consistent with the restoring nature of such a boundary condition.

So as to perform a numerical application, the input parameters are chosen to be of the same order as those of run 14 and are summed up in table 6.5. For an activation time of $t_a = 60s$, the result is shown in figure 6.11, where we can also see the dynamics and asymptotic temperatures.

htc	300	$W.m^{-2}.K^{-1}$
T_{rec}	250	K
T_0	240	K
ρ	1000	$kg.m^{-3}$
c_p	2000	$J.kg^{-1}.K^{-1}$
Q	15	$kW.m^{-2}$
λ	20	$W.m^{-1}.K^{-1}$
L_x	0.001	m

Table 6.5: Parameters for simple model analysis
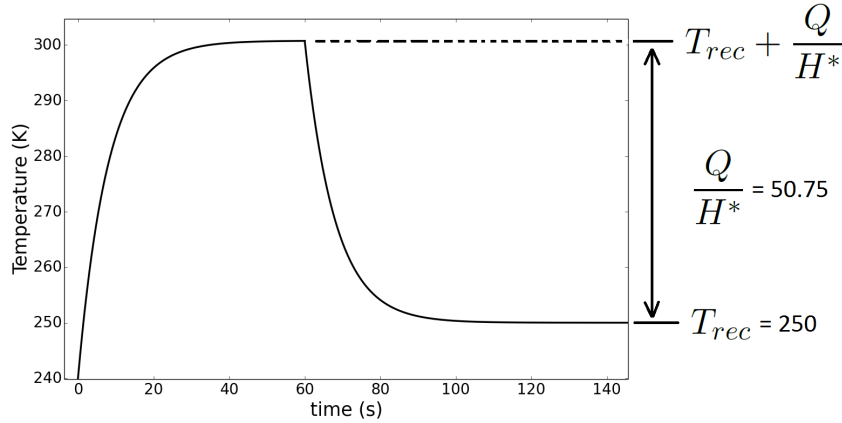
Figure 6.11: Transient solution to the simplified problem

In order to evaluate the variation introduced by an error on the input parameters, the partial derivatives of T with respect to every parameter are required. For T_{rec}, Q, htc and ρc_p and $0 \leq t \leq t_a$ they are given by:

$$\frac{\partial T}{\partial T_{rec}} = 1 - e^{-\frac{H^*}{\rho c_p L_x}t}$$

$$\frac{\partial T}{\partial Q} = \frac{1}{H^*}\left[1 - e^{-\frac{H^*}{\rho c_p L_x}t}\right]$$

$$\frac{\partial T}{\partial htc} = \frac{Q}{htc^2}\left[e^{-\frac{H^*}{\rho c_p L_x}t} - 1\right] - \left[T_0 - T_{rec} - \frac{Q}{H^*}\right]\frac{H^{*2}}{htc^2}\frac{t}{\rho c_p L_x}e^{-\frac{H^*}{\rho c_p L_x}t}$$

$$\frac{\partial T}{\partial \rho c_p} = \left[T_0 - T_{rec} - \frac{Q}{H^*}\right] \frac{H^*}{(\rho c_p)^2} \frac{t}{L_x} e^{-\frac{H^*}{\rho c_p L_x}t}$$

The parameters are set to the same value as in table 6.5 and the activation time is set to $t_a = 20s$. An error of 10% is set for Q and htc and 4% for T_{rec}. The error for ρc_p is set to 20% which roughly amounts to an error of 10% on ρ and c_p individually. The corresponding variations in temperature at t_a are gathered in table 6.6. The transient behaviour can be seen in figure 6.12. The recovery temperature is observed to have the most significant effect. Indeed, as could be expected, an error in T_{rec} induces an error of the same order in the predicted temperature T. The other parameters all induce errors of 3 to 4K. Moreover, note that some errors may compensate each other, as in the case of a higher htc and higher Q.

Parameter	$\Delta(\%)$	$\Delta(SI)$	$|\Delta T|$(K)
htc	10	30	3.6
T_{rec}	4	10	9.2
ρc_p	20	$5\,10^5$	2.6
Q	10	1500	4.6

Table 6.6: Error and induced variation

(a) Effect of T_{rec}

(b) Effect of htc

(c) Effect of Q

(d) Effect of ρc_p
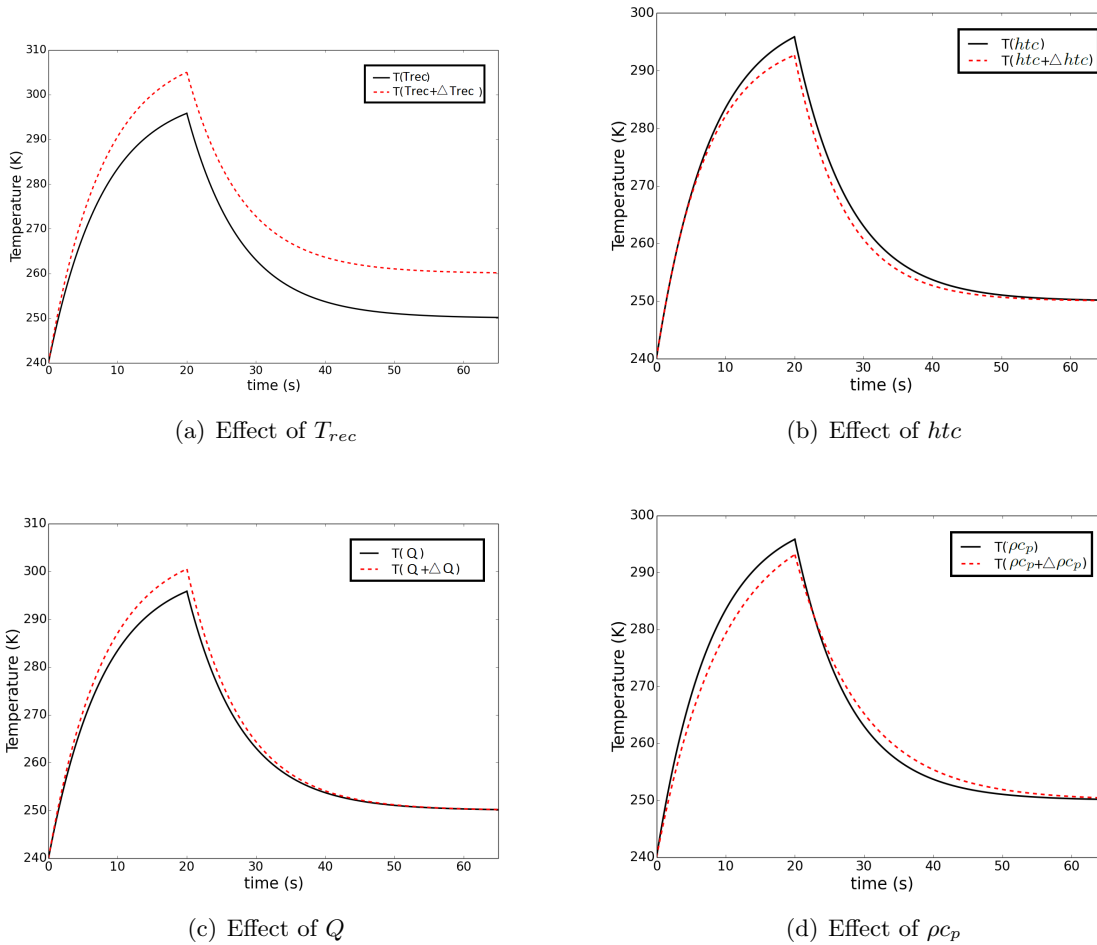
Figure 6.12: Variation of transient temperature due to errors in input parameters

An important source of error which has not been fully investigated in the previous analysis in laminar/turbulent transition. Indeed, laminar/turbulent transition is usually accompanied by a strong variation of htc. As can be seen in figure 6.7, at the end of the laminar region the htc has a value

in the order of $100SI$ as opposed to $300SI$ or more in the turbulent region following it. As shown in figure 6.13, such a variation has an important effect on the transient temperature.
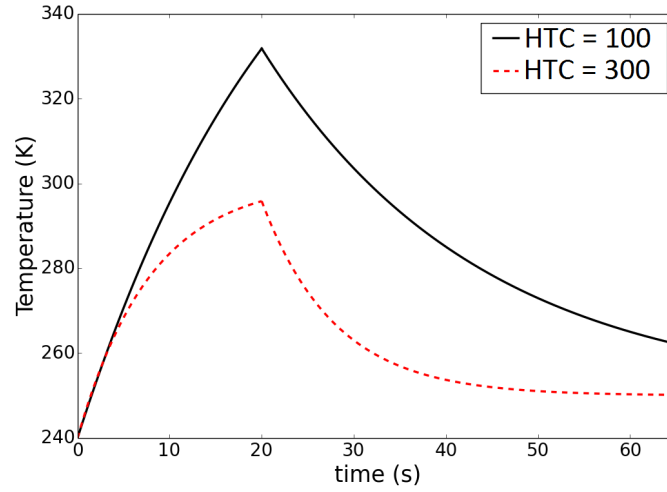
Figure 6.13: Difference between a laminar and turbulent *htc*

Another effect which has to be mentioned is that of conductivity. Indeed due to the small value of L_x (which is a typical value for an ice protection system) and given the value which was chosen for the analysis, its effect becomes negligible. Nevertheless, there is one case where conductivity can play a significant role: if it tends to small values. Indeed, figure 6.14 shows that for small values of λ, errors may induce significant variations in temperature.
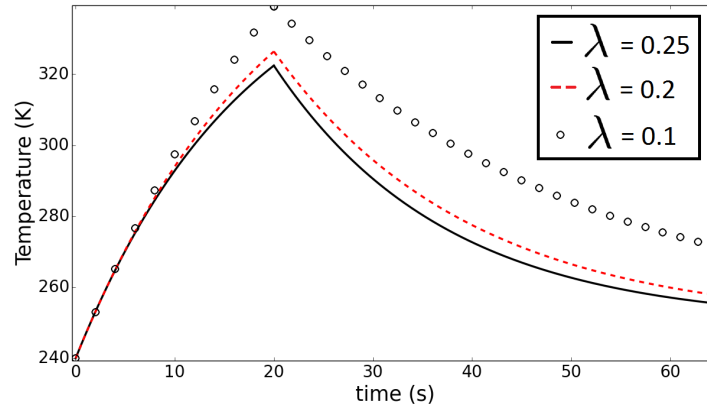
Figure 6.14: Difference in temperature for small values of λ

It should also be noted that, although not investigated here, imperfect contact between layers may also induce discrepancies when comparing experimental and simulation data. In effect, it may be taken into account via the concept of thermal contact resistance, which plays a role similar to a heat transfer coefficient when formulating thermal fluxes.

Finally, another source of discrepancy may be the temperature sensors themselves. Either due to uncertainty with respect to their position, which could create strong differences in probed temperatures due to the high temperature gradients present in ice protection systems. Or, due to the type of sensor, as will be shown in the following subsection.

6.2.5 Discussion

In the light of the previous analysis, several sources of error may be considered concerning the results obtained in subsection 6.2.3:

- **Convective boundary condition**: The convective boundary condition involving laminar/turbulent transition and turbulence is a difficult problem. It plays an important role. With the only goal of illustrating this aspect, the *htc* and T_{rec} distribution may be adapted and taken to be those of figure 6.15.
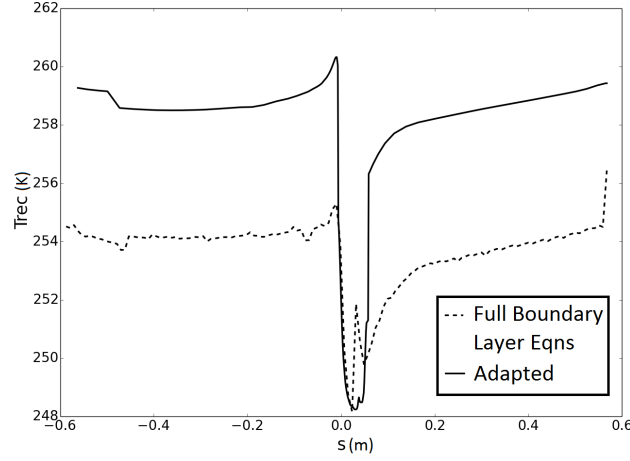
(a) Adapted T_{rec}
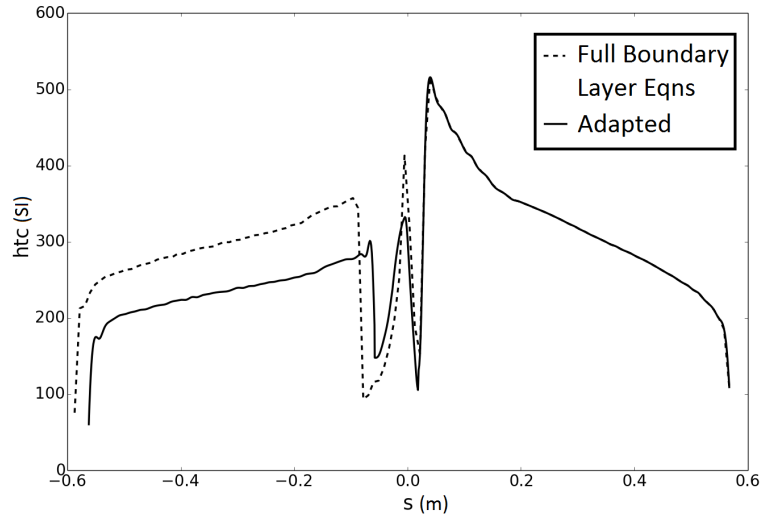
(b) Adapted *htc*

Figure 6.15: Adapted *htc* and T_{rec}

The results corresponding to such a disctribution are shown in figure 6.16. This distribution was manufactured to obtained improved results using the previous analysis as a guide. However it should be noted that only the sensor corresponding to heater B resides in the turbulent region. Although it appears natural to doubt the prediction of the transition zone, it seems questionable to adapt the *htc* and T_{rec} of the laminar region, where heaters C and D lie, for laminar flows do not exhibit the same difficulties as turbulent ones. Therefore, it would appear that in the laminar region, another source of error could be at play.
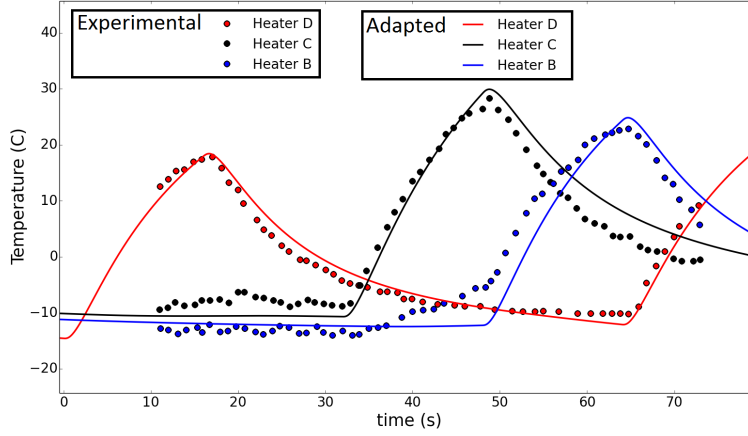
Figure 6.16: Comparison between experimental and numerical for manufactured htc and T_{rec}

It should also be noted that the surface of the airfoil was assumed to be perfectly smooth. Also, the heaters provide heat to the external flow and this effect is not taken into account. Finally, the inner boundary is assumed adiabatic. In fact, a small recirculation may be active inside the airfoil, meaning that a convective boundary condition should also be applied there. This would have the effect of extracting heat from the system.

- **Material properties**: as stated in the previous point, the convective boundary condition may not be the only parameter responsible for the observed discrepancies. By changing material properties of the first layer in the zone of heater D to $\rho = 800 kg.m^{-3}$, $c_p = 2000 J.kg^{-1}.K^{-1}$ and those of all the layers underneath to $\rho = 800 kg.m^{-3}$, $c_p = 1800 J.kg^{-1}.K^{-1}$, the result shown in figure 6.17. The results are improved when the heater is activated. However, as T_{rec} governs the asymptotic temperature when the heater is deactivated, the surface temperature still tends towards the wrong temperature.
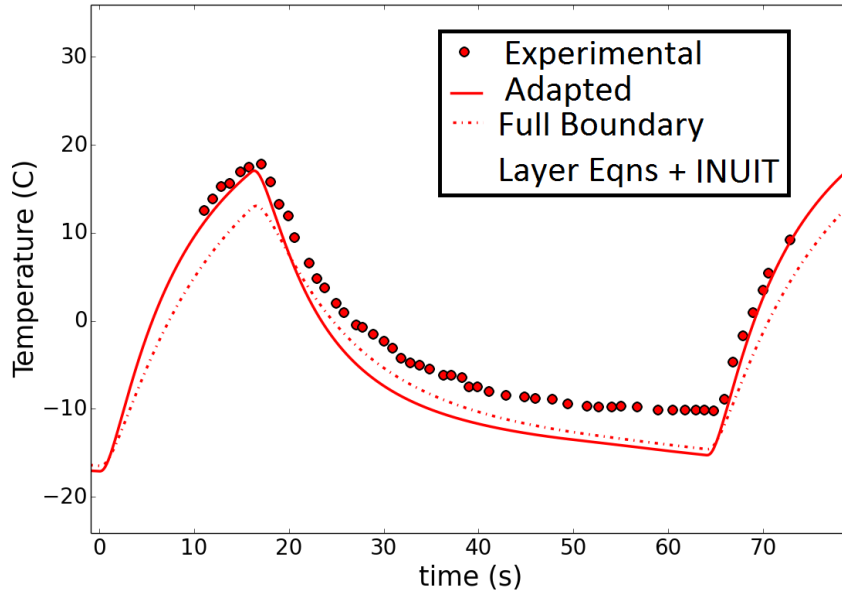
Figure 6.17: Improved surface temperature due to changes in material parameters

Other sources of error include possible air voids inside the multi-layered stack of materials due to the manufacturing process. One last aspect which is worth mentionning is the overall aerodynamics.

In the case of run 14, the pressure distribution on the airfoil is not available. Comparing such a distribution to that computed by the Euler solver would enable to assess the adequateness of the obtained aerodynamic field. Reasons for differences and need for pressure distribution rematching include three dimensional test section effects.

6.2.6   Dry Air Run: Conclusion

When combined with the rest of the IGLOO2D simulation tool, the ETIPS simulation module yields results which are in reasonable agreement with experimental temperature measurments. Improvement may be sought by considering the sources of error analysis. First, the convective heat transfer boundary condition has a significant effect on the predicted temperatures. Second, uncertainties in material parameters can also have a visible effect on the solution. A possible improvement could be to attempt to take into account imperfect contact between layers. However, this requires knowledge of the interface properties.

6.3   De-Icing with Delayed Activation: Preliminary Capability and Investigations

After having considered, in the previous section, a purely conductive dry air case, attention is now shifted to a de-icing application. Taking into account changes in ice shape due to accretion is not yet part of the presented simulation strategy. Hence, in the case that will be investigated, the ice shape will be defined at the beginning of the simulation and no further accretion will occur. An interesting and adapted setting within which such a hypothesis could fit in is that of delayed activation. In this case ice has already accreted to a certain extent before the ice protection system is activated, therefore demanding that it operates in non-nominal mode. This situation could arise from the fault of an automatic activation system or from a delay in the flight crew's identification of flight through icing conditions.

6.3.1   Ice Shape and Aerodynamics

The aerodynamic geometry chosen for this case is a NACA0012 airfoil. The ice shape (shown in figure 6.18) is defined so as to symmetrically cover a part of the protected area. It has a maximum thickness of $1mm$ at the leading edge. The aerodynamic conditions for this test case are given in table 6.7. The resulting flow field and pressure coefficient are shown in figures 6.19 and 6.20.

Mach	P_∞ (Pa)	T_∞ (K)	α (°)
0.4	61640.0	263.15	4.0

Table 6.7: Aerodynamic conditions for delayed activation de-icing case
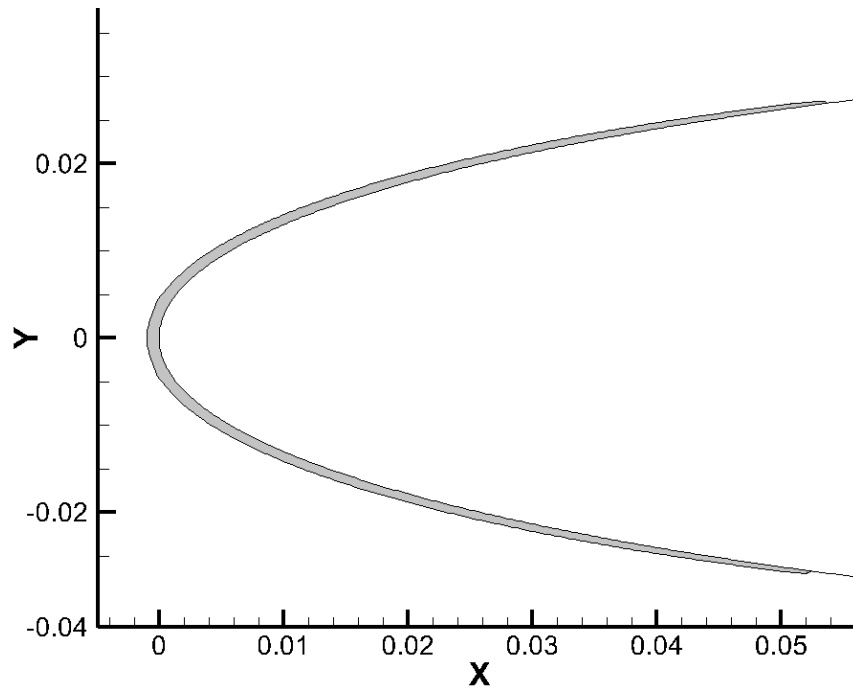
Figure 6.18: Ice shape for delayed activation case
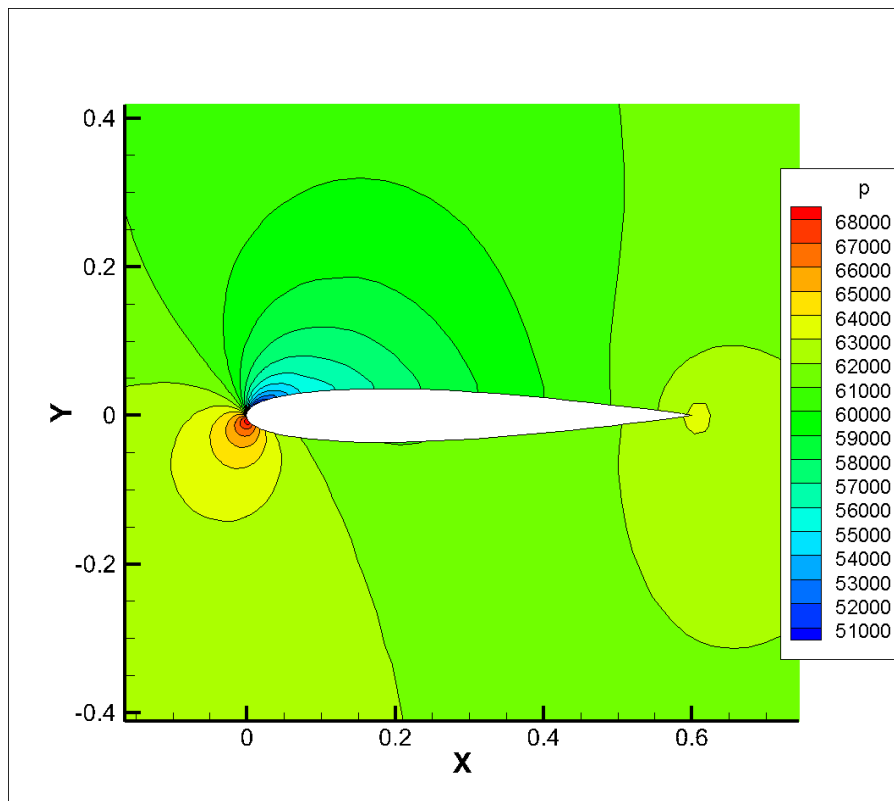
Figure 6.19: Initial pressure field for delayed activation case
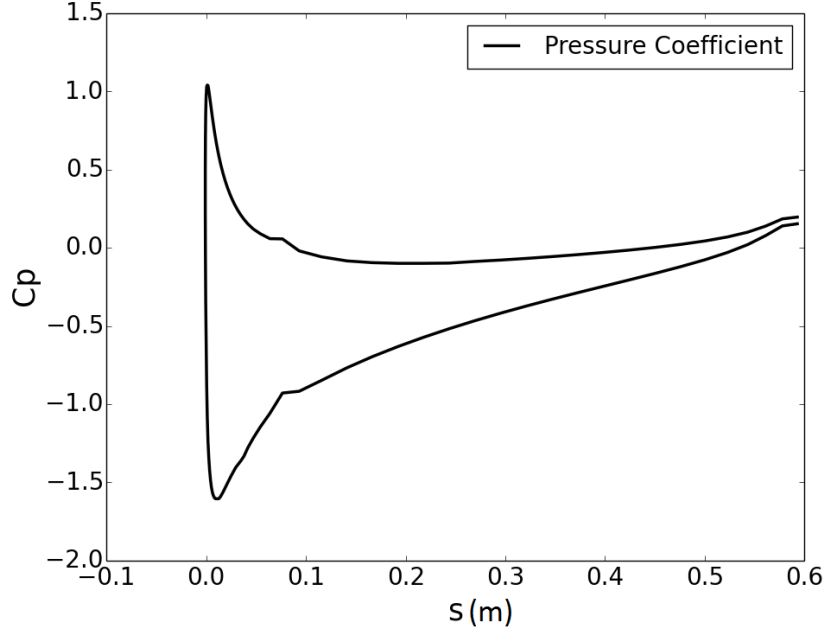
Figure 6.20: Initial pressure coefficient for delayed activation case as a function of curvilinear abscissa

The presence of ice was taken into account in the boundary layer computation by imposing a roughness of $1/1000th$ of the chord where ice was present (value commonly taken for icing problems). The rest of the airfoil was assumed smooth. Only the integral boundary layer module was used for this case and the results in terms of htc and T_{rec} are shown in figures 6.21 and 6.22.
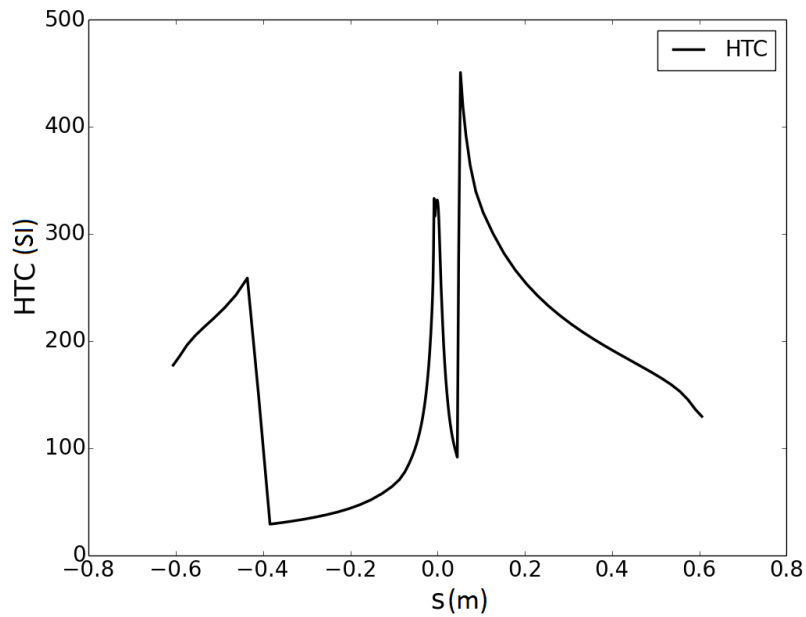
Figure 6.21: Heat transfer coefficient for delayed activation case
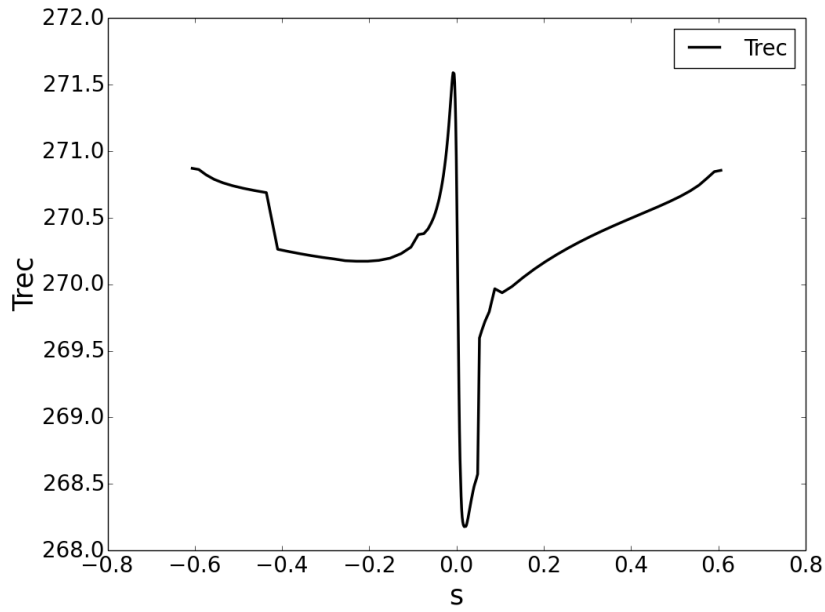
Figure 6.22: Recovery temperature for delayed activation case

6.3.2 System Setup

For this case, the system consists in 7 heater mats of length $2.2cm$, all seperated from each other by a distance of $2mm$. The heaters are labeled from A to E as shown in figure 6.23. Heater D is centered with respect to the leading edge.
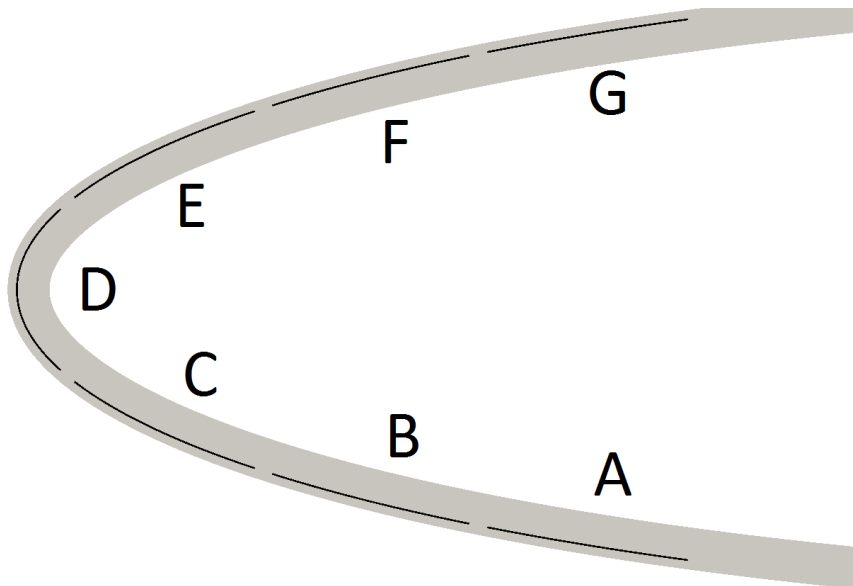
Figure 6.23: Illustration of the system

The materials constituting the muli-layered stack are defined by the characteristics given in the following table:

Layer No	$\rho(kg.m^{-3})$	$c_p(J.kg^{-1}.K^{-1})$	$\lambda_\xi(W.m^{-1}.K^{-1})$	$\lambda_\eta(W.m^{-1}.K^{-1})$	thickness (m)
1	1000	2350	17.03	17.03	$8.e-04$
2	1250	2009.	0.293	0.293	$2.e-04$
3	1250	2009.	0.293	0.293	$2.e-04$
4	1000	2381.	0.313	0.313	$3.e-04$
5	1250	2009.	0.293	0.293	$5.e-04$
6	1000	1717	0.25	0.25	$2.52e-03$

Table 6.8: Multi-layered stack characteristics for delayed activation case

The layers are numbered from the outer layer to the inner layer, that is to say layer no 1 is the layer in contact with the aerodynamic flow. The heaters are embedded between layers no 2 and 3. They have a density of $\rho = 1000.0 kg.m^{-3}$, a specific heat of $c_p = 3410.0 J.kg^{-1}.K^{-1}$ and a thickness of $1.e-04m$. The activation cycle and powers will be discussed later.

The mesh is defined using the curvilinear abscissa discretization (truncation abscissas set to $0.15m$ and $-0.15m$) defined in table 6.3 and layer discretization defined in table 6.4. The resulting mesh is shown in figure 6.5.

Zone No	$s_1(m)$	$s_2(m)$	nb of cells
1	-0.15	-0.083	100
2	-0.083	-0.061	80
3	-0.061	-0.059	8
4	-0.059	-0.037	80
5	-0.037	-0.015	8
6	-0.035	-0.013	80
7	-0.013	-0.011	8
8	-0.011	0.011	80
9	0.011	0.013	8
10	0.013	0.035	80
10	0.035	0.037	8
11	0.037	0.059	80
12	0.059	0.061	8
13	0.061	0.083	80
14	0.083	0.15	100

Table 6.9: Zone discretization

Layer No	thickness (m)	nb Cells
1	$8.e-04$	4
2	$2.e-04$	2
3	$2.e-04$	2
4	$3.e-04$	3
5	$5.e-04$	5
6	$2.52e-03$	20

Table 6.10: Layer discretization
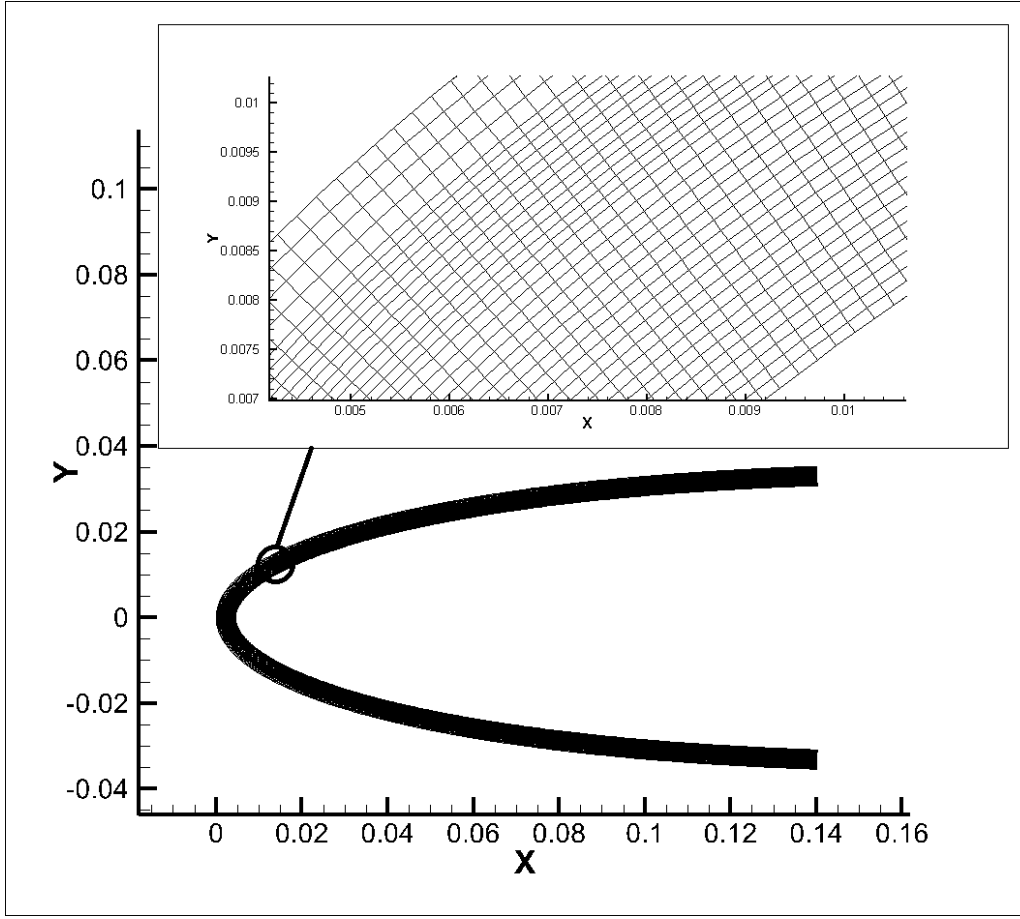
Figure 6.24: Mesh generated with data from tables 6.10 and 6.9

6.3.3   Case No1 : High Power Parting Strip

For the previously discussed ice shedding mechanisms to take place, it is necessary for the parting strip to be free of ice. Therefore, a possible strategy in the case of delayed activation would be to assign a high power to the parting strip so as to fully melt the ice accreted in that region. In doing so, the ice at the parting strip will turn into a liquid water film which will run back towards the trailing edge. The aerodynamic flow will then be able to create the expansion necessary to lift the remaining ice blocks.

Hence, the power cycle is chosen as follows. Heater D is the parting strip heater and is activated during the whole cycle. The other heaters are all activated for $20s$ according to the cycle $EC-FB-GA$ (that is to say E and C are activated at the same time, etc). The end of the cycle is followed by a pause of $60s$. The applied power for heater D is set to $60kW.m^{-2}$ and that for heaters $A-B-C-E-F-G$ is set to $30kW.m^{-2}$.

The mesh used for the ice consisted in 3000 triangular elements. It should be noted that refining the ice mesh becomes quickly limiting with respect to computational time due to the time step limit imposed by the explicit solver. The time step was set to $\Delta t = 0.002s$ according to the thermal ice module stability condition. The values of the thermal properties of ice that were used are given in table 6.11.

$\rho(kg.m^{-3})$	$c_s(J.kg^{-1}.K^{-1})$	$c_l(J.kg^{-1}.K^{-1})$	$k_s(W.m^{-1}.K^{-1})$	$k_l(W.m^{-1}.K^{-1})$	$L(J.kg^{-3})$	$T_m(K)$
1000.0	2110	4181	2	0.6	334000	273.15

Table 6.11: Thermal properties of ice

During the first $20s$ of the cycle, only heater D is activated. As shown in figure 6.25 a water film starts to form in the corresponding region. The film starts to become visible after $5s$. The

melting front then propagates principally in the normal direction as can be seen in figure 6.26. In this configuration, the aerodynamic load may only act to press the ice block against the airfoil.
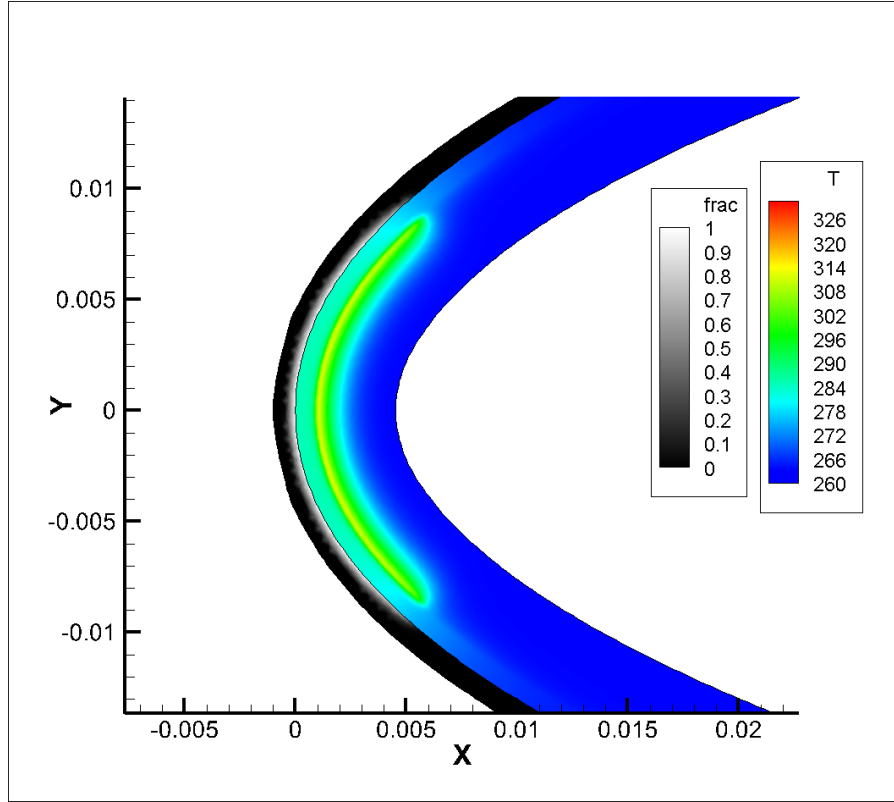
Figure 6.25: Temperature field and liquid fraction at 5*s*
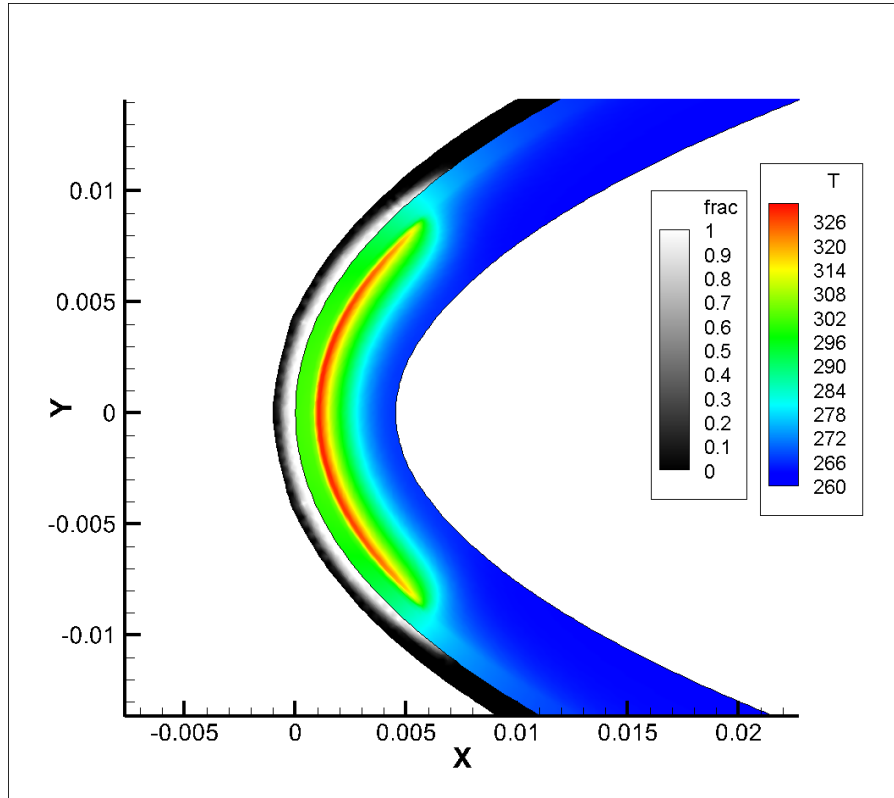
Figure 6.26: Temperature field and liquid fraction at 10*s*

At the end of the first 20s of the cycle the parting strip is free from ice (as shown in figure 6.27). As stated previously, the liquid water thus formed is assumed to runback under the effect of the aerodynamic forces.
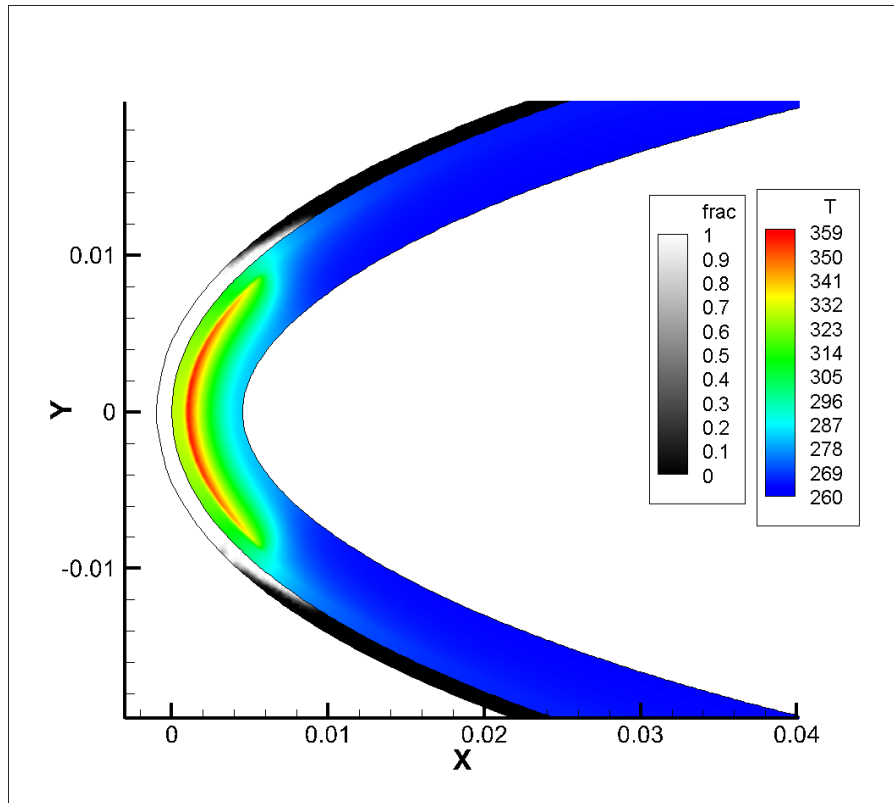
Figure 6.27: Temperature field and liquid fraction at 20s

The liquid water film would probably freeze downstream, leading to a change in ice shape. However, this effect can not be taken into account by the code in its present form. As a first approach, the ice shape will simply be replaced at this stage by the two remaining unmelted ice blocks as shown in figure 6.28.
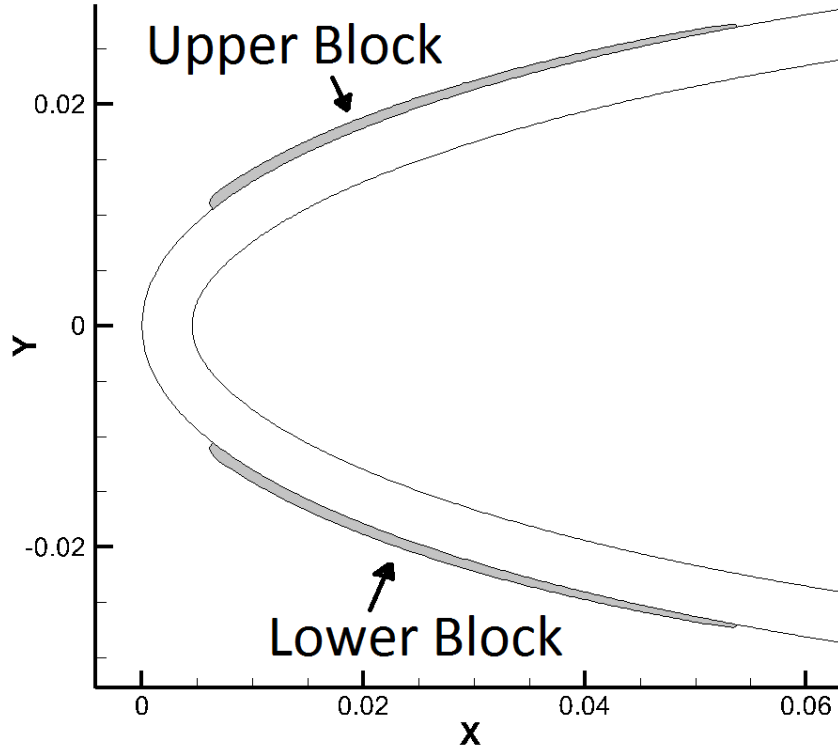
Figure 6.28: Ice blocks left after melting of parting strip

At a cycle time of $20s$, heaters C and E are activated and a melting front starts to propagate. Due to the fact that the parting strip region has a higher temperature, and under the effect of heaters C and E, the melting front also presents a strong transverse propagation component. For instance, the melted area between $t = 21s$ (figure 6.29) and $t = 23s$ (figure 6.30) shows significant transversal progress.
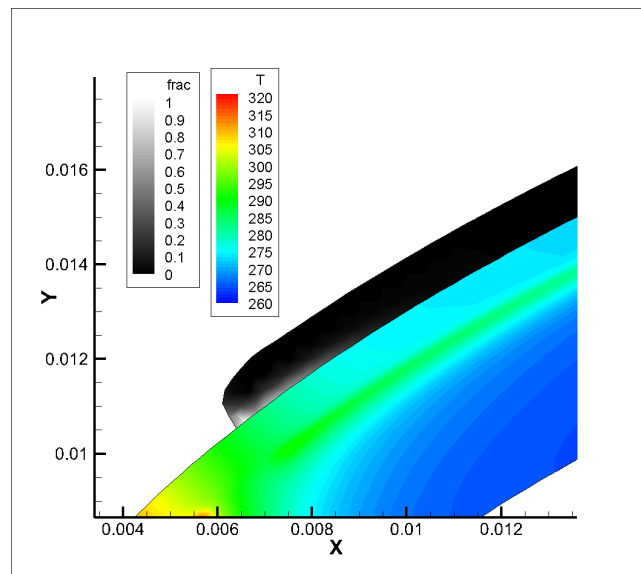
Figure 6.29: Ice blocks left after melting of parting strip
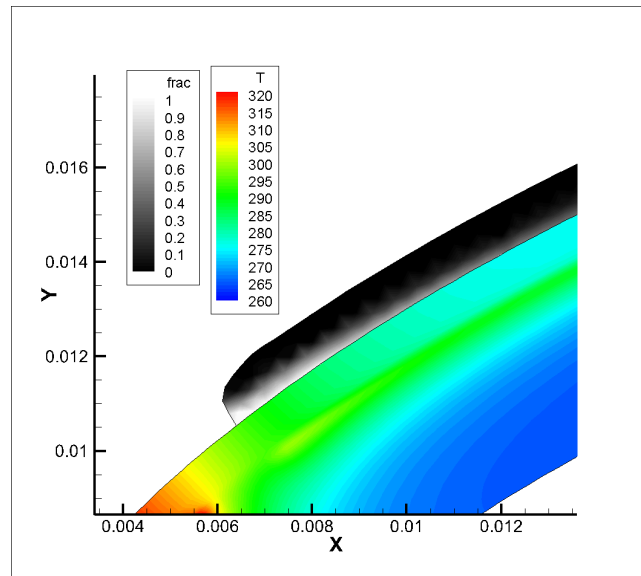
Figure 6.30: Ice blocks left after melting of parting strip

With the propagation of the melting front, the exterior pressure will start to be redistributed in the liquid film. However, if we assume that the aerodynamic field is not significantly impacted by the loss of the parting strip ice, the shedding mechanism will not be active on the upper ice block. Indeed, the pressure distribution on the upper and lower ice blocks are shown in figures 6.31 and 6.32. On the one hand, as the lower block is on the pressure side of the airfoil, pressure steadily increases downstream and eventually a shedding mechanism can be active there. On the other hand, the pressure distribution on the upper block will not be sufficient to produce a situation were an ice shedding mechanism will be possible. The redistributed pressure in the liquid film will be almost the minimum of the whole pressure distribution over the block.
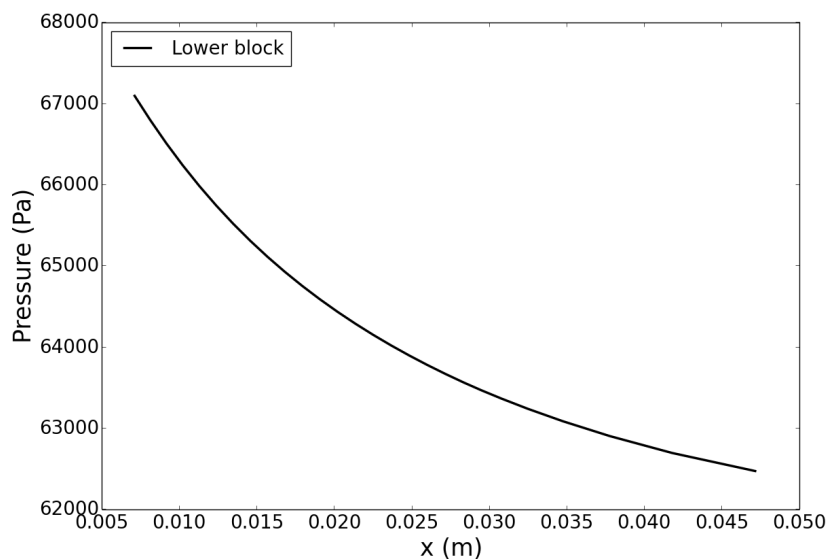
Figure 6.31: Pressure distribution on lower ice block
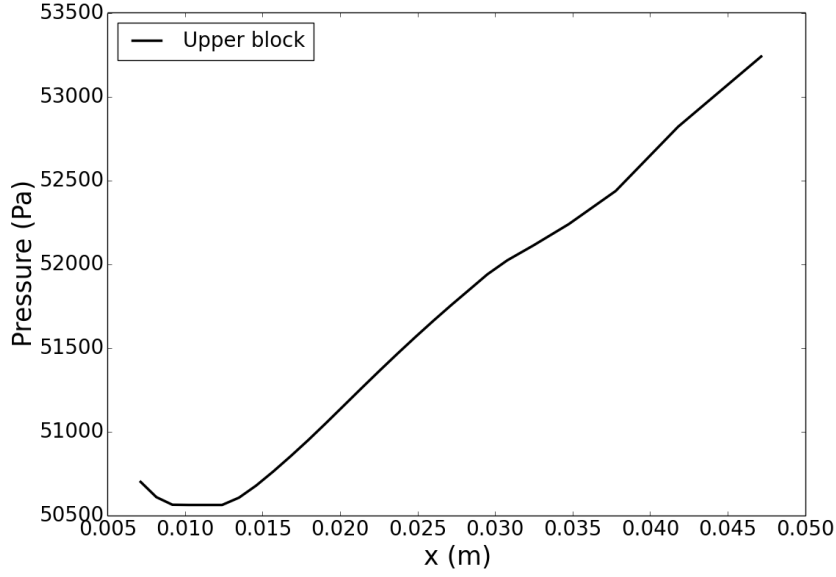
Figure 6.32: Pressure distribution on upper ice block

Therefore, it appears that if an ice shedding mechanism is to take place on the upper ice block, the aerodynamic flow field must be recomputed. Due to the nature of the geometry the choice is made to use an unstructured mesh and the commercial solver Fluent.Inc [35]. A compressible inviscid computation was performed using the second order upwind Roe scheme. The Courant number was set to 5 and residuals were converged to 10^{-4}. On figure 6.33 it can be observed that the global aerodynamic field has not been that much affected by the formation of lower and upper ice shapes.
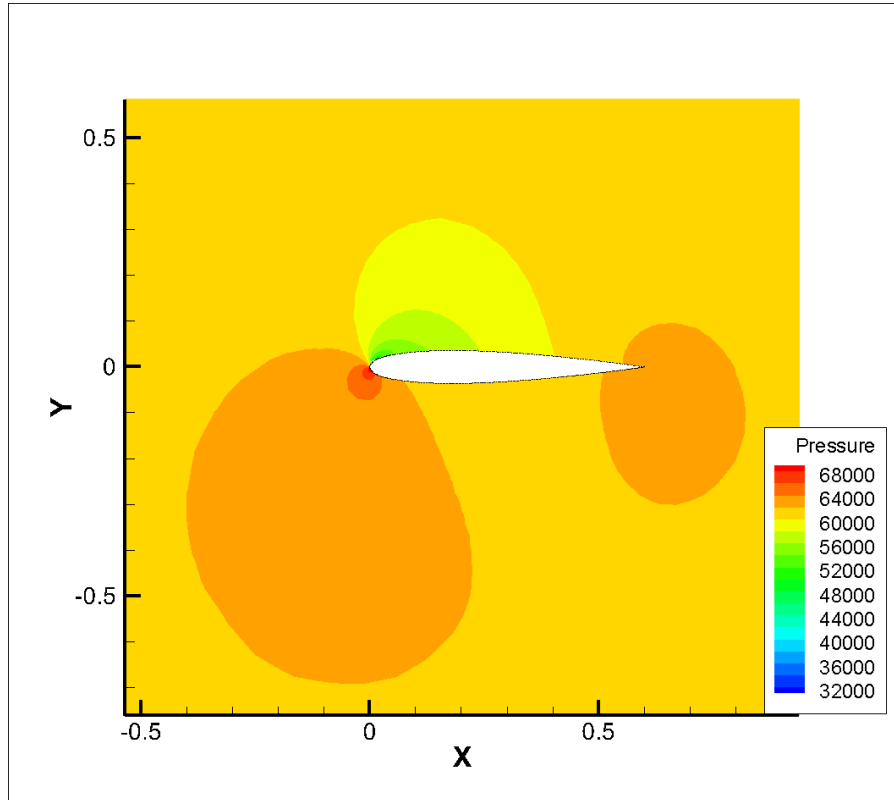
Figure 6.33: Pressure field around iced airfoil with freed parting strip

Nevertheless, figures 6.34 and 6.35 clearly show that a very localized effect takes place. On the upper block this effect is very strong. The sudden apparition of the ice block generates a strong and

very localized expansion. As for the lower block, the effect is weaker but still present. This type of pressure distribution is typically that which is required to activate ice shedding mechanisms. As the pressure drop is much higher on the upper block than on the lower one, the former will be shed much earlier than the latter.
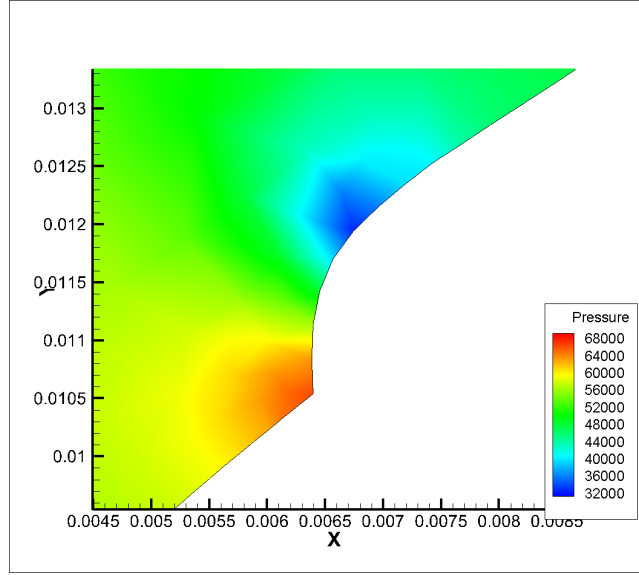
Figure 6.34: Pressure jump on upper block
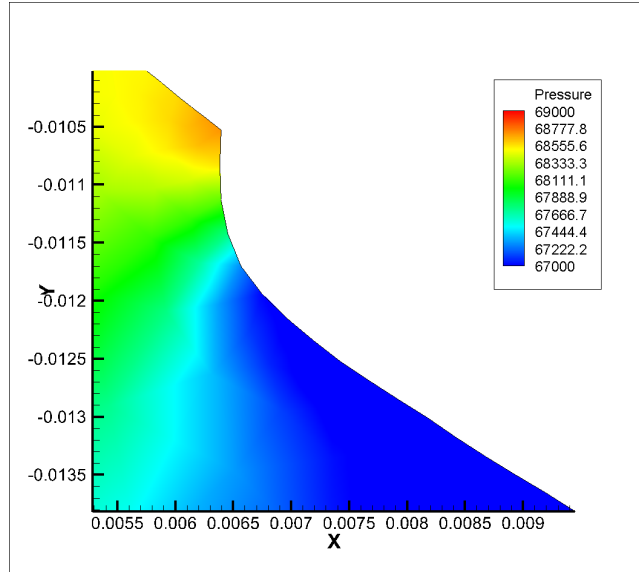
Figure 6.35: Pressure jump on lower block

Given this new fixed pressure distribution, every $0.1s$, a mechanical computation is performed. At the present state of developement, this case may be represented semi-quantitatively at best. Therefore, only a bulk failure shedding mechanism will be considered. To take into account the fact that the interface is melting a test is performed on the boundary cells. If the liquid fraction is greater than 0.9 then the corresponding boundary edge is set to a Neumann boundary condition where the aerodynamic pressure is applied.

The mesh used for the mechanical computation is the same as that used for the thermal one. The temperature inside the ice block was set to a mean value of $270K$ and the spreading length scale was set to $l = 7 \, 10^{-4}m$. As for porosity and grain size they were set to respectively 3% and $0.7mm$.

After $3s$ of activation for heaters E and C, the water film is sufficiently advanced to lead to a fully fractured state on the upper block. The fact that ice shedding occurs so soon on the upper block is

consistent with the high pressure drop to which it is subjected.
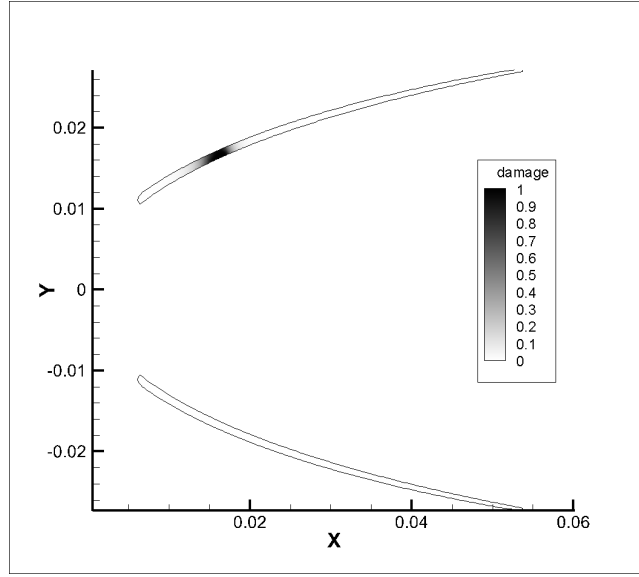
Figure 6.36: Broken state through upper ice block
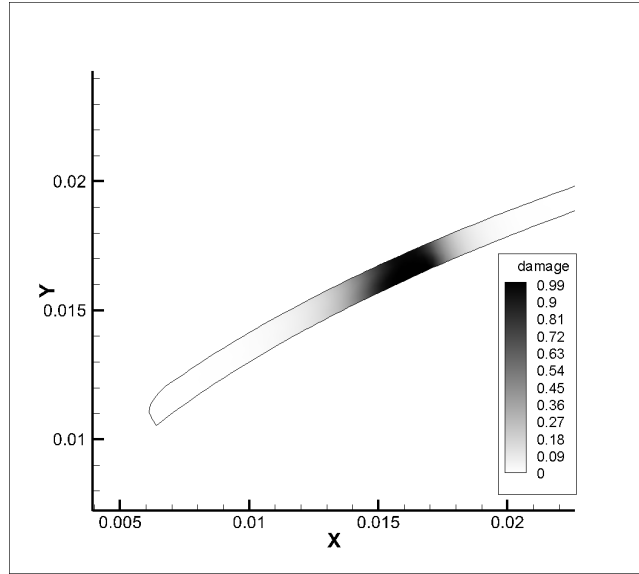
Figure 6.37: Broken state through upper ice block

As in this case, ice shedding is predicted after $3s$ of activation, there may be a possible gain by reducing the activation times. This is even more the case for the lower ice block. Indeed, leaving heater C activated for the full $20s$ would only lead to almost melting the whole thickness of the ice in that zone. This would not take advantage of a possible shedding mechanism which would activate if more of the interface was melted.

As shown in figure 6.38, a higher melted length is required to lead to detachement of a part of the lower block. The fully fractured state conducive to shedding on the lower part is predicted after for a melted length of about $0.025m$. This means that the critical position for which fracture occurs on the lower block is located beyond the area of heater C (at a curvilinear abscissa of about $0.038m$). Therefore, reducing activation times would allow heater B to activate and enable the critical fracture position to be reached.
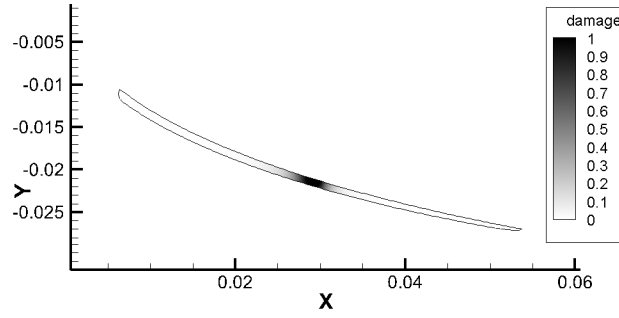
Figure 6.38: Broken state through lower ice block

6.3.4   Case No2 : Low Power Parting Strip

In nominal functionning mode, as the parting strip is designed to be activated all during the cycle, its assigned power is usually lower than that of the other heaters. To avoid wasting unnecessary amounts of energy to keep the parting strip clear from ice, its power typically varies in the order of 1/3 to 1/2 of the other heaters power.

Taking the same setup as in section 6.3.3, the power cycles are change according to the following table:

Heater	$t_0(s)$	Activation Time (s)	Power
D	0.0	80	10
$C - E$	20.0	20	30
$B - F$	40.0	20	30
$A - G$	60.0	20	30

Table 6.12:   Power cycle for lower parting strip case

In this configuration, as shown in figure 6.39, heater D is not able to free the parting strip from the accreted ice. However, when heaters C and E are activated, the applied power is sufficient to melt the wole thickness of the ice in their corresponding regions, as shown in figure 6.40. Once this configuration is achieved, exterior pressure will be redistributed leading to the possibility of ice shedding. The airfoil will nevertheless be cleaned from ice in a time much longer than that discussed in the previous section.
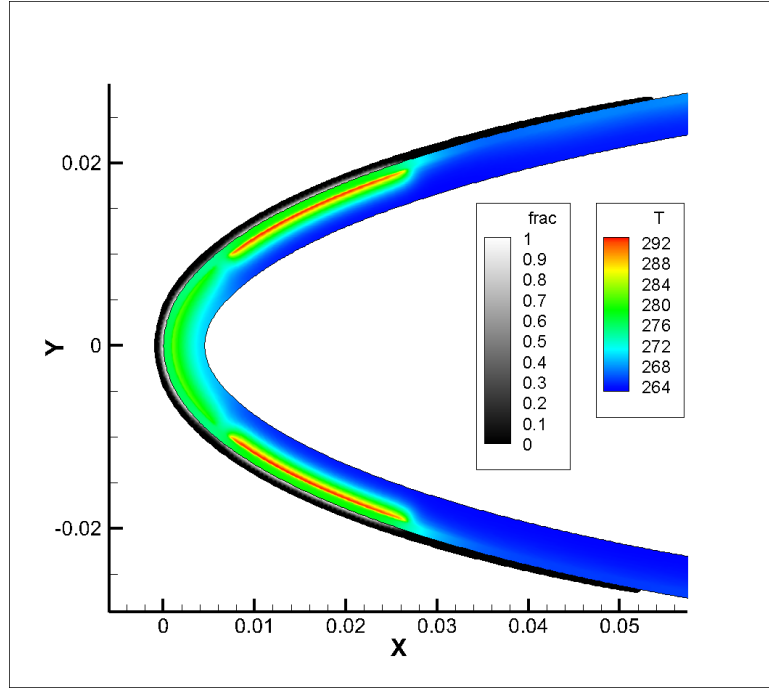
Figure 6.39: Temperature field in the system and liquid fraction in ice for low power parting strip case at $t = 27s$
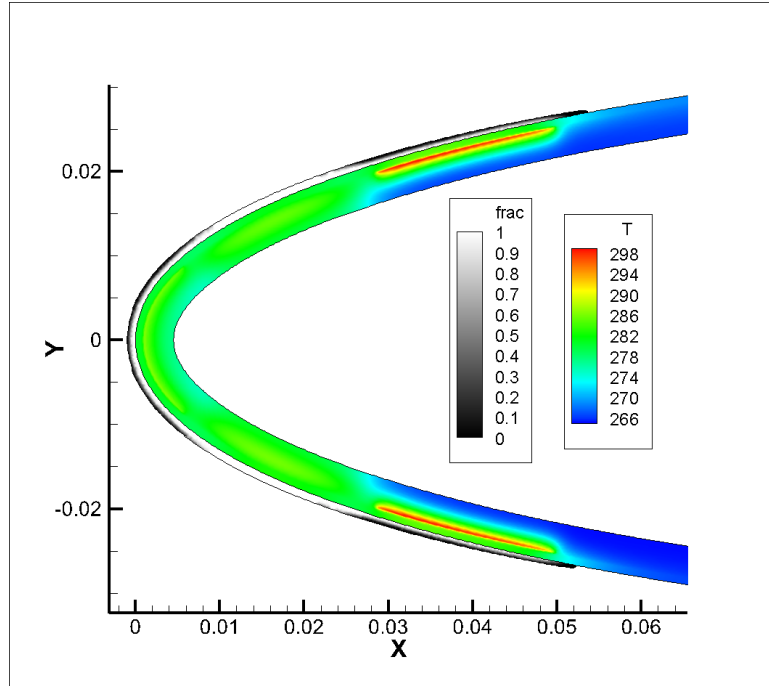
Figure 6.40: Temperature field in the system and liquid fraction in ice for low power parting strip case at $t = 50s$

6.3.5 Discussion

The previously described cases provide a first approach to the feasability of a fully coupled de-icing simulation for electro-thermal systems. It incorporates aerodynamics, thermal aspects including phase change and mechanical aspects with the fracture module. However, it should be beared in mind that this approach is more qualitative than quantitative at the present time, due to the many uncertainties concerning ice mechanical properties, ice shape prediction and change in time. Still, the results

given by the presented methodology are promising and have provided interesting insight on the possible mechanisms at play. The delayed activation case also showed the necessity to recompute the aerodynamic field each time the ice shape changes due to shedding.

The methodology presented in this section provides a first approach to a global computation strategy for electro-thermal ice protection systems with ice shedding prediction. However, aspects such as ice shape change in time, requiring remeshing, remain heavy. Hence, so as to improve this approach, an alternative solution strategy for the thermal treatment of the ice block is desirable. Such an alternative will be shortly discussed in the general conclusion.

The goal of this thesis was to setup a global methodology capable of simulating de-icing cycles of electro-thermal ice protection systems. After having set the industrial context and constraints, a litterature review of current state of the art icing simulation was given.

It was decided to develop a numerical tool built around the three main aspects of de-icing simulation: thermal conduction within the system, heat transfer with phase change in the ice and mechanical behaviour involved in ice shedding, such as fracture, in the ice.

The thermal models used as a starting point state of the art icing simulation methods. In some aspects the modelling remained quite similar. However, a strong effort was put to develop a tool which could be easily coupled with other modules. The finite volume method was chosen to discretize the governing equations. In the case of the de-icing system, care was taken to formulate the numerical scheme so as to take into account changes in material properties. The problem of phase change in the ice block was approached using the enthalpy method. Moreover, as the ice can have a rather arbitrary shape, unstructured meshes were used. Therefore the numerical fluxes had to be treated in a consistent way using a gradient reconstruction scheme. Both numerical modules were tested on several academic cases and compared very well to analytical solutions.

Concerning the crack propagation model it was based on a recent method which uses elements of the variational approach to fracture and operator splitting. It used a concept of energy transfer between elastic and crack energies. A history function is introduced to guarantee the "irreversible" aspect of crack propagation. The elastic energy also defined the constitutive stress-strain law. It was split into a tensile and compressive part. This introduced a non-linearity in the problem due to the introduction of projection operators which depend on the local strain state (its eigenvalues and eigenvectors to be more precise). An algorithm to linearize the problem was formulated. During the model assessment phase it was pointed out that the spreading parameter l had to be chosen in accordance with mesh size. The analysis joined other work in the literature considering that l should be taken at least equal to twice the mesh characteristic length. A double notched test case was finally performed and compared to experimental data. The crack topology was well represented by the model which recovered the two branches initiating at each notch tip.

After the literature review on the mechanical properties of atmospheric ice, it appeared that very few laws exist to characterise it. Using recent experimental data and the general form of some empirical laws it was possible to identify and formulate relations defining the behaviour of atmospheric ice. The mechanical properties were chosen to vary according to testing temperature, grain size and porosity. The effect of accumulation temperature may be taken into account through porosity and grain size as they are both direct translations of the conditions in which the ice was accumulated. It should be noted however that these laws only provide a first approach. Further research is necessary, as much from a numerical modelling than from an experimental point of view, so as to formulate more precise laws. Given the great amount of scatter and the difficulty of experimental procedures concerning atmospheric ice this point may be particularly challenging.

With the crack propagation and empirical laws at hand, ice shedding mechanisms were investigated. The idea was that due to the effect of the parting strip, which keeps the leading edge clear form ice, the

ice shapes present aft this region would present a lumped shape. This lump would induce a pressure drop in the flow field. At the same time, due to the heating action of the system, a liquid water film is able to form at the interface between the ice and the heated surface. If this film is in contact with the external air flow, then the exterior pressure will be redistributed in the melted area beneath the ice block. Considering there is a pressure drop over the ice lump, this has the effect of creating an uplifiting bending pressure differential. Starting with a flat plate test case and moving on to an airfoil case, it was shown that for a critical film length, the uplifiting force is able to create a crack and propagate it through the whole thickness of the ice. Aside from this bulk failure shedding mechanism, a purely adhesive, a purely cohesive and mixed shedding modes were proposed. The adhesive mode was investigated using a simple adhesion model based on an experimental yield stress. It provided a first approach and showed that ice may start to detach earlier than what was predicted in the bulk failure mode. A mixed adhesive/bulk failure mode was hence investigated, showing that ice may start to detach adhesively until the critical bulk failure stress is reached. A crack would then nucleate and propagate through the thickness of the ice, therefore leaving a residual ice shape.

Experimental and numerical modelling improvements are needed to confirm these shedding mechanisms. Several hypotheses were made when investigating ice shedding, such as neglecting surface tension effects. Therefore experimental tests could provide new information on the dominant effects. From a numerical modelling point of view, it would be interesting to study a fully combined shedding mechanisms involving adhesive/cohesive debonding and bulk failure. To do so a more precise adhesion model has to be used. To take into account cohesive debonding an interesting method would be to use cohseive zone models. However, using these more elaborate models will inevitably introduce new material parameters which will have to be identified experimentally.

The dry air test case represents a more industrial and realistic application. It however only uses the system thermal model and aerodynamic computations. Temperature was extracted at defined points at the surface of the system corresponding to infrared measurment locations. The numerical results were compared to the experimental data and provided the correct order of magnitude. However, in a search for more quantitative results on this type of case, a discussion on the sources of error was performed. Using a simplified model, the effect of uncertainties in material parameters, convective heat transfer variables and heat source were examined. It was shown that the convective boundary condition has an important effect. Given the fact this is a difficult information to obtain, it could explain the differences observed between experiment and numerical solution. However it was also shown that uncertainties in material parameters, in the case of manufacturing imperfections for example, could also have a significant effect.

Finally, the feasability of a complete simulation of de-icing was shown. The beginning of a delayed activation cycle was simulated. It showed the important role of the parting strip in initiating the ice shedding mechanisms. It also helped to point out some important points. The main one being that when the ice block geometry is changed due to departure of ice or melting, it is necessary to perform an additional aerodynamic computation. Whithout such an actualised flow field, it appears the pressure differential may not be correct to predict ice shedding.

So as to take this methodology to the next step, changes in ice shape due to ice accretion and/or film runback has to be taken into account. Using the ice heat transfer module developed in this work would imply frequent remeshing and interpolation procedures. Hence, to lighten such a process, another modelling strategy is being considered. Rémi Chauvin, a PhD student at ONERA, is working on running back freezing film modelling. This model, based on an integral formulation, is able to take into account ice build up, freezing runback shapes and melting at the ice/system interface at the same time. Therefore, combination of this method with the system thermal model and ice mechanical behaviour model developed in the present work would result in a computationally cheaper simulation strategy. The enthalpy method module developed in the present work may still be used if more precision is required, and will also serve to provide reference solutions and validation for the running back freezing film model.

[1] S. Zhang, O. El Kerdi, R. A. Khurram, W. G. Habashi . FEM analysis of in-flight ice break-up . *Finite elements in analysis and design* , 57 , 2012 .

[2] A. A. Griffith . The Phenomena of Rupture and Flow in Solids . *Philisophical Transactions of the Royal Society of London. Series A.* , 221 , 1921 .

[3] A. B. P. Cassie, S. Baxter . Wettability of Porous Surfaces . *Transactions of the Faraday Society* , 40 , 1944 .

[4] A. Bonnet, J. Luneau. Théories de la Dynamique des Fluides. *Cepadues editions.*

[5] A. J. Meuler, J. D. Smith, K. K. Varanasi,J. M. Mabry, G. H. McKinley, R. E. Cohen . Relationships Between Water Wettability and Ice Adhesion . *Applied materials and interfaces* , 2010 .

[6] A. P. Broeren, S. Lee, G. H. Shah, P. C. Murphy. Aerodynamic Effects of Simulated Ice Accretion on a Generic Transport Model. Technical Memorandum 2012-217246, NASA, 2012.

[7] A. R. Jones. An Investigation of a Thermal Ice Prevention System for a Twin Engine Transport Airplane. Report 862, NACA, 1946.

[8] A. Reehorst. NASA Icing Remote Sensing. Oral Presentation, 2013.

[9] A. Reich, R. Scavuzzo, M. Chu . Survey of the Mechanical Properties of Impact Ice . In *32nd Aerospace Sciences Meeting and Exhibit* , 1994 .

[10] A. Roche. Les theories de l'adhesion et mesure de l'adherence. *Le Vide, Les Couches Minces*, 257:197–230, 1992.

[11] A.M.A. Mohamed, M. Farzaneh . An experimental study on the tensile properties of atmospheric ice . *Cold regions science and technology* , 68 , 2011 .

[12] Anderson, D.N., Reich, A.D. . Tests of the Performance of Coatings for Low Ice Adhesion . Technical memorandum 107399 , NASA , 1997 .

[13] B. Aupoix. Couches Limites Bidimensionnelles Compressibles. Descriptif et mode d'emploi du code CLICET. Rapport Technique No 1/17015 SY, ONERA, 2010.

[14] B. Bourdin, G.A. Francfort, J.M. Marigo . The variational approach to fracture . *Journal of Elasticity* , 91 , 2008 .

[15] B. Diskin, J. L. Thomas, E. J. Nielsen, H. Nishikawa, J. A. White. Comparison of Node-Centered and Cell-Centered Unstructured Finite-Volume Discretizations: Viscous Fluxes. *AIAA Journal*, 48(7):1326–1338, 2010.

[16] B. G. Gulick. Effects of Simulated Ice Formation on the Aerodynamic Characteristics of an Airfoil. Advance Confidential Report N.A, NACA, 1938.

[17] B. L. Messinger . Equilibrium Temperature of an Unheated Icing Surface As A Function of Airspeed . *Journal of the Aeronautical Sciences* , 1953 .

[18] C. Antonini, M. Innocenti, T. Horn, M. Marengo, A. Amirfazli . Understanding the Effect of Superhydrophobic Coatings on Energy Reduction in Anti-Icing Systems . *Cold Regions Science and Technology* , 2011 .

[19] C. Geuzaine, J.-F. Remacle. Gmsh: a three-dimensional finite element mesh generator with built-in pre- and post-processing facilities. *International Journal for Numerical Methods in Engineering*, 79(11):1309–1331, 2009.

[20] C. Girardet, C. Toubin . Molecular Atmospheric Pollutant Adsorption on Ice: a Theoretical Survey .

[21] C. J. Johnston, D. J. Serke, D. R. Adriaansen, A. L. Reehorst, M. K. Poliotovich, C. A. Wolff, F. McDonough. Comparison of In-Situ, Model and Ground Based In-Flight Icing Severity. Technical Memorandum 2011-217141, NASA, 2011.

[22] C. Laforte, J.L. Laforte, and J.C. Carrier . How a Solid Coating Can Reduce the Adhesion of Ice on a Structure . In *IWAIS* , volume vol. 6 , 2002 .

[23] C. Miehe. Comparison of Two Algorithms for the Computation of Fourth-Order Isotropic Tensor Functions. *Computers and Structures*, 66(1):37–43, 1998.

[24] C. Miehe, M. Hofacker, F. Welschinger . A phase field model for rate-independant crack propagation Robust algorithmic implementation based on operator splits . *Computer Methods in Applied Mechanics and Engineering* , 2010 .

[25] Comité d'Etude du Givrage. Rapport du 19 Mai 1938. Bulletin des Services Techniques 85, Publication Scientifiques et Techniques du Ministère de l'Air, 1939.

[26] D. Gross, T. Seelig. *Fracture Mechanics with and Introduction to Micromechanics.* Springer, Second edition edition, 2011.

[27] D. Jackson, J. Goldberg. Ice Detection Systems: A Historical Perspective. Technical Paper 2007-01-3325, SAE, 2007.

[28] D. S. Dugdale. Yielding of steel sheets containing slits. *Journal of the Mechanics and Physics of Solids*, 8(2):100–104, 1960.

[29] D. W. A. Rees . *Basic Engineering Plasticity* . Elsevier , 2006 .

[30] E. Gürses, Ercan, C. Miehe. A computational framework of three-dimensional configurational-force-driven brittle crack propagation. *Computer Methods in Applied Mechanics and Engineering*, 198(15):1413–1428, 2009.

[31] E. M. Schulson . The Structure and Mechanical Behavior of Ice . *JOM* , 51 (2), 1999 .

[32] E. M. Schulson . Brittle Failure of Ice . *Engineering Fracture Mechanics* , 68 , 2001 .

[33] E. M. Schulson, P. Duval . *Creep and Fracture of Ice* . Cambridge University Press , 2009 .

[34] F. Saeed. State-of-the-Art Aircraft Icing and Anti-Icing Simulation. *ARA Journal*, 2000(25-27), 2002.

[35] Fluent, ANSYS. Fluent 6.3 Documentation. *Fluent Inc., Lebanon, NH*, 2006.

[36] G. A. Francfort, J. J. Marigo. Revisiting brittle fracture as an energy minimization problem. *Journal of the Mechanics and Physics of Solids*, 46(8):1319–1342, 1998.

[37] G. Dantl . Die elastischen Moduln von Eis-Einkristallen . *Zeitschrift fur Physik B Condensed Matter* , 1968 .

[38] G. E. Schneider, M. Zedan . A modified strongly implicit procedure for the numerical solution of field problems . *Numerical Heat Transfer* , 4 (1), 1981 .

[39] G. Fortin, J. Perron . Ice Adhesion Models to Predict Shear Stress at Shedding . *Journal of adhesion science and technology* , 26 :523–553, 2012 .

[40] G. Fortin, M. Adomou, J. Perron . Experimental Study of Hybrid Anti-Icing Systems Combining Thermoelectric and Hydrophobic Coatings . In *SAE 2011 International Conference on Aircraft and Engine Icing and Ground Deicing, June 2011* .

[41] G. H. Holdaway. Corrosion Tests of a Heated Wing Utilizing an Exhaust-Gas-Air Mixture for Ice Prevention. Technical Note 1791, NACA, 1949.

[42] G. I. Barenblatt. The mathematical theory of equilibrium cracks in brittle fracture. *Advances in Applied Mechanics*, 7:55–129, 1962.

[43] Gent, R.W., Guffond, D., and Reinmann, J. DRA/NASA/ONERA Collaboration on Icing Research: Part I - Prediction of Water Droplet Trajectories. Technical Report TR93085, DRA/NASA/ONERA, 1993.

[44] Guffond, D., Reinmann, J. Gent, R.W. DRA/NASA/ONERA Collaboration on Icing Research: Part III - Prediction of Thermal Deicer Simulations. Technical Report T.R. 2/7766 PN, DRA/NASA/ONERA, 1993.

[45] G.W. Zumwalt, R.L Schrag, W.D. Bernhart, R.A. Friedberg. Analysis and Tests for Design of an Electro-Impulse De-Icing System. Contractor Report 174919, NASA, 1985.

[46] H. Belghazi . *Modélisation Analytique du Transfert Instationnaire de la Chaleur dans un Matériau Bicouche en Contact Imparfait et Soumis à une Source de Chaleur en Mouvement* . PhD thesis, Université de Limoges , 2008 .

[47] H. Brezis. *Functional Analysis, Sobolev Spaces and Partial Differential Equations*. Springer, 2010.

[48] H. H. G. Jellinek . Adhesive Properties of Ice . *Journal of Colloid Science* , 1959 .

[49] H. H. G. Jellinek . Liquid-like Layers on Ice . *Journal of Applied Physics* , 1961 .

[50] H. H. G. Jellinek . Ice Adhesion . *Canadian Journal of Physics* , 1962 .

[51] H. H. G. Jellinek . Liquid-like (Transition) Layer on Ice . *Journal of Colloid and Interface Science* , 1967 .

[52] H. J. Frost. Mechanisms of crack nucleation in ice. *Engineering Fracture Mechanics*, 68(17):1823–1837, 2001.

[53] M. Bragg H. Kim. Effects of leading-edge ice accretion geometry on airfoil performance. In American Institute of Aeronautics and Astronautics, editors, *17th Applied Aerodynamics Conference*, number AIAA-99-3150, 1999.

[54] H. Li, I. Roisman, C. Tropea. Physics of supercooled large drops (SLD): Literature Review. EXTrime ICing Environment (EXTICE), WP2, Intermediate Report, TU Darmstadt, 2009.

[55] H. W. Liu and K. J. Miller . Fracture Toughness of Fresh-Water Ice . *Journal of Glaciology* , 22 (86), 1979 .

[56] I. A. Ryzhkin, V. F. Petrenko . Physical Mechanisms Responsible for Ice Adhesion . *J. Phys. Chem. B* , 101 , 1997 .

[57] J. Cousteix. *Couche Limite Laminaire.* Cepadues-éditions, 1989.

[58] J. Cousteix. *Turbulence et Couche Limite.* Cepadues-éditions, 1989.

[59] J. Druez, C. L. Phan, J. L. Laforte, D. D. Nguyen . The Adhesion of Glaze and Rime on Aluminium Electrical Conductors . *Transactions of the CSME* , 5 (4), 1978-79 .

[60] J. H. VanSant . *Conduction heat transfer solutions* . Lawrence Livermore National Laboratory , 1980 .

[61] J. J. Petrovic . Review: Mechanical Properties of Ice and Snow . *Journal of Material Science* , 38 , 2003 .

[62] J. L. Orr. Interim Report on Flight Tests of Thermal-Electric Propeller De-Icing. Report MD-25, National Research Council of Canada, 1942.

[63] J. Lemaitre, J.L. Chaboche, A. Benallal, R. Desmorat . *Mecanique des materiaux solides* .

[64] J. M. Melenk and I. Babuska. The Partition of Unity Finite Element Method: Basic Theory and Applications. *Computer Methods in Applied Mechanics and Engineering*, 139(1-4):289–314, 1996.

[65] J. P. Lewis, D. T. Bowden. Preliminary Investigation of Cyclic De-Icing of an Airfoil Using an External Electric Heater. Research Memorandum E51J30, NACA, 1952.

[66] J. R. Rice. Mathematical analysis in the mechanics of fracture. *Fracture: an advanced treatise*, 2:191–311, 1968.

[67] J. R. Shewchuk . Triangle: Engineering a 2D Quality Mesh Generator and Delaunay Triangulator . In M. C. Lin, D. Manocha , editor, *Applied Computational Geometry: Towards Geometric Engineering* , volume 1148 of *Lecture notes in computer science* . Springer-Verlag , 1996 .

[68] J. Rasler, H. Harders, M. Baker . *Mechanical Behaviour of Engineering Materials* . Springer , 2007 .

[69] J. Tynall, J. F. Huxley . On the Structure of Glaciers . *Philosophical Transactions of the Royal Society of London* , 1857 .

[70] J. W. Glen . The Mechanics of Ice . Technical report, U.S. Army Cold Regions Research and Engineering Laboratory , 1975 .

[71] J.D. Bernal, R.H. Fowler . A Theory of Water and Ionic Solution, with Particular Reference to Hydrogen and Hydroxyl ions . *Journal of Chemical Physics* .

[72] K. K. Varanasi, T. Deng, J. D. Smith, M. Hsu, N. Bhate . Frost Formation and Ice Adhesion on Superhydrophobic Surfaces . *Applied Physics Letters* , 97 , 2010 .

[73] K. M. Al-Khalil, T. F. W. Ferguson. Hybrid Ice Protection System for Use on Roughness-Sensitive Airfoils, 2001. US Patent 6,196,500.

[74] K. Pham . *Construction et analyse de modeles d'endommagement a gradient* . PhD thesis, Universite Pierre et Marie Curie , 2010 .

[75] L. A. Rodert. A Preliminary Study of the Prevention of Ice on Aircraft by the Use of Engine Exhaust Heat. Technical Note 712, NACA, 1939.

[76] L. A. Rodert. An Investigation of the Prevention of Ice on the Airplane Windshield. Technical Note 754, NACA, 1940.

[77] L. A. Rodert, R. Jackson. A Description of the Ju-88 Airplane Anti-Icing Equipment. Wartime Report, NACA, 1942.

[78] L. Pauling . The Structure and Entropy of Ice and of Other Crystals with Some Randomness of Atomic Arrangement . *J. Am. Chem. Soc.* , 57 (12):pp 2680–2684 , 1935 .

[79] Loughborough, D.L., Haas E.G. . Reduction of the Adhesion of Ice to De-icer Surfaces . *Journal of the Aeronautical Sciences* , 1946 .

[80] M. Alfano, F. Furgiuele, A. Leonardi, C. Maletta and G. H. Paulino. Cohesive Zone Modeling of Mode I Fracture in Adhesive Bonded Joints. *Key Engineering Materials*, 348-349:13–16, 2007.

[81] M. E. Gurtin, P. Podio-Guidugli. Configurational forces and the basic laws for crack propagation. *Journal of the Mechanics and Physics of Solids*, 44(6):905–927, 1996.

[82] M. E. R. Shanahan . Adhesion and Wetting: Similarities and Differences . *Rubber world* , 205 , 1991 .

[83] M. Eskandarian . *Ice Shedding from Overhead Electrical Lines by Mechanical Breaking* . PhD thesis, Universite du Quebec a Chicoutimi , 2005 .

[84] M. Faraday . Lecture Given at the Royal Institution, London , June 1850 .

[85] M. Faraday . Note on Regelation . *Proc. Roy. Soc; (London)* , 1860 .

[86] M. Fremond . Adhérence des Solides . *J. Mécanique Theorique et Ap- pliquée* , 6 (3), 1987 .

[87] M. J. Raw ; G. E. Schneider . A New Implicit Solution Procedure for Multidimensional Finite-Difference Modeling of the Stefan Problem . *Numerical Heat Transfer* , 1985 .

[88] M. K. Koosheh . *Ice Shedding from Cables and Conductors - a Cracking Model of Atmospheric Ice* . PhD thesis, Universite du Quebec a Chicoutimi , 2007 .

[89] M. Kermani. *Ice Shedding from Cables and Conductors - A Cracking Model of Atmospheric Ice.* PhD thesis, Universite du Quebec a Chicoutimi , 2007.

[90] M. Kermani, M. Farzaneh, R. Gagnon . Bending strength and effective modulus of atmospheric ice . *Cold regions science and technology* , 53 , 2008 .

[91] M. Kermani, M. Farzaneh, R. Gagnon. Compressive strength of atmospheric ice. *Cold Regions science and technology*, 49(3):195–205, 2007.

[92] M. Knight, W. C. Clay. Refrigirated Wind Tunnel Tests on Surface Coatings for Preventing Ice Formation. Technical Note 339, NACA, 1930.

[93] M. Landy, A. Freiberger . Studies of Ice Adhesion . *Journal of Colloid and Interface Science* , 1967 .

[94] M. Ma, R. M. Hill . Superhydrophobic Surfaces . *Current Opinion in Colloid and Interface Science* , 11 , 2006 .

[95] M. Mellor . Mechanical Properties of Polycrystalline Ice . In P. Tryde , editor, *Physics and Mechanics of Ice* . Springer-Verlag , 1980 .

[96] M. Montagnat, P. Duval . The Viscoplastic Behaviour of Ice in Polar Ice Sheets: Experimental Results and Modelling . *C. R. Physique* , 5 , 2004 .

[97] M. Vargas, J. A. Giriunas, T. P. Ratvasky. Ice Accretion Formations on a NACA 0012 Swept Wing Tip in Natural Icing Conditions. Technical Memorandum 2012-211357, NASA, 2002.

[98] M. Zou, S. Beckford, R. Wei, C. Ellis, G. Hatton, M.A. Miller . Effects of Surface Roughness and Energy on Ice Adhesion Strength . *Applied Surface Science* , 257 , 2011 .

[99] N. Azuma . A Flow Law for Anisotropic Polycrystalline Ice Under Uniaxial Compressive Deformation . *Cold Regions Science and Technology* , 23 , 1995 .

[100] N. H. Fletcher . *The Chemical Physics of Ice* . Cambridge University Press , 1970 .

[101] N. Sonwalkar . *Molecular Dynamics of Ice-solid Bi-material Interfaces* . PhD thesis, M.I.T. , 1992 .

[102] Nooru-Mohamed, M.B. . *Mixed-mode fracture of concrete: an experimental approach* . PhD thesis, Technische Univ., Delft , 1992 .

[103] NTSB . In-Flight Icing Encounter and Loss of Control Simmons Airlines, d.b.a. American Eagle Flight 4184 Avions de Transport Regional (ATR) Model 72-212, N401AM Roselawn, Indiana October 31, 1994 . Number AAR-96/01 .

[104] O. Chau, J. Fernandez, M. Shillor, M. Sofonea. Variational and numerical analysis of a quasistatic viscoelastic contact problem with adhesion. *J. Comput. Appl. Math.*, 2003.

[105] Overmeyer, Austin and Palacios, Jose and Smith, Edward. Ultrasonic De-Icing Bondline Design and Rotor Ice Testing. *AIAA Journal*, 51(12):2965–2976, 2013.

[106] P. Gribelin. *Structure Cristalline et Organisation des Canaux d'Inclusions d'Air dans le Givre Atmospherique: Analyse Experimentale et Modelisation.* PhD thesis, Université Blaise Pascal, 1988.

[107] P. H. Gammon, H. Kiefte, M. J. Clouter, W. W. Denner . Elastic Constants of Artificial and Natural Ice Samples by Brillouin Spectroscopy . *Journal of Glaciology* , 29 ((103)):433–460, 1983 .

[108] P. J. Perkins, S. McCullough, R. D. Lewis. A Simplified Instrument for Recording and Indicating Frequency and Intensity of Icing Conditions Encountered in Flight. Research Memorandum E51E16, NACA, 1951.

[109] P. Laborde, J. Pommier, Y Renard, M. Salaun. High-Order Extended Finite Element Method for Cracked Domains. *International Journal for Numerical Methods in Engineering*, 64:354–381, 2005.

[110] R. Henry . Development of an Electrothermal De-icing/Anti-icing Model . In *AIAA 30th meeting, Reno, NV (USA)* .

[111] R. Henry. Modélisation Bidimensionelle du Degivrage/Antigivrage d'une Pale d'Helicoptère. Rapport Technique 67/5146 SY, ONERA, 1991.

[112] R. J. Brun, W. Lewis, P. J. Perkins, J. S. Serafini. Impingement of Cloud Droplets on a Cylinder and Procedure for Measuring Liquid Water Content and Droplet Sizes in Supercooled Clouds by Rotating Multicylinder Method. Technical Report 1215, NACA, 1952.

[113] R. J. Shaw, G. P. Richter. The UH-1H Helicopter Icing Flight Test Program: An Overview. Technical Memorandum 86925, NASA, 1985.

[114] R. Jafari, R. Menini, M. Farzaneh . Superhydrophobic and Icephobic Surfaces Prepared by RF-sputtered Polytetrafluoroethylene Coatings . *Applied Surface Science* , 257 , 2010 .

[115] R. Menini, Z. Ghalmi, M. Farzaneh . Highly Resistant Icephobic Coatings on Aluminum Alloys . *Cold Regions Science and Technology* , 65 , 2011 .

[116] R. N. Wenzel . Resistance of Solid Surfaces to Wetting by Water . *Ind. Eng. Chem.* , 28 , 1936 .

[117] R. Rosenberg . Why is Ice Slippery? . *Physics Today* , 2005 .

[118] R. Scavuzzo, M. Chu, V. Ananthaswamy . Influence of aerodynamic forces in ice shedding . In *29th aerospace sciences meeting and exhibit* , 1991 .

[119] R. Scherrer. An Analytical Investigation of Thermal-Electric Means of Preventing Ice Formations on a Propeller Blade. Advance Confidential Report 4H31, NACA, 1944.

[120] R. Scherrer, L. A. Rodert. Tests of Thermal-Electric De-Icing Equipment for Propellers. Advance Restricted Report 4A20, NACA, 1944.

[121] J. T. Cansdale R. W. Gent, N. P. Dart. Aircraft icing. *Phil. Trans. R. Soc. Lond. A*, 358:2873–2911, 2000.

[122] R.J. Scavuzzo, M.L. Chu . Structural Properties of Impact Ices Accreted on Aircraft Structures . Technical Report NASA Contractor Report 179580 , The University of Akron , 1987 .

[123] S. Jung, M. Dorrestijn, D. Raps, A. Das, C. M. Megaridis, and D. Poulikakos . Are Superhydrophobic Surfaces Best for Icephobicity? . *Langmuir* , 2011 .

[124] S. Kumar and S.V. Barai . Size-effect of fracture parameters for crack propagation in concrete: a comparative study . *Computers and Concrete.* , 9 (1), 2012 .

[125] S. Yang, Q. Xia, L. Zhu, J. Xue, Q. Wang, Q. Chen . Research on the Icephobic Properties of Fluoropolymer-based Materials . *Applied Surface Science* , 257 , 2011 .

[126] S.A. Kulinich, M. Farzaneh . On Ice-releasing Properties of Rough Hydrophobic Coatings . *Cold Regions Science and Technology* , 65 , 2011 .

[127] SAE AS 5147 . Thermal and fluid anti-icing systems and equipment, aircraft external surfaces . SAE subcommittee AC-9 Aircraft Environmental Systems , July 1996 .

[128] M. Salaun. Résolution numérique des equations au dérivées partielles. Cours ISAE ENSICA.

[129] Solomon A. D. Alexiades V. . *Mathematical Modelling of Melting and Freezing Processes* . Hemisphere , 1993 .

[130] T. Belytschko and T. Black. Elastic Crack Growth in Finite Elements with Minimal Remeshing. *International Journal for Numerical Methods in Engineering*, 45(5):601–620, 1999.

[131] T. Belytschko, R. Gracie, G. Ventura. A review of extended/generalized finite element methods for material modeling. *Modelling and Simulation in Materials Science and Engineering*, 17(4), 2009.

[132] T. Carroll, W. H. MacAvoy. The Formation of Ice Upon Exposed Parts of an Airplane in Flight. Technical Note 293, NACA, 1928.

[133] T. Carroll, W. H. MacAvoy. The Formation of Ice Upon Airplanes in Flight. Technical Note 313, NACA, 1929.

[134] T. F. Gelder, J. P. Lewis, S. L. Koutz. Ice Protection for a Turbojet Transport Airplane: Heating Requirements, Methods of Protection and Performance Penalties. Technical Note 2866, NACA, 1953.

[135] T. H. Bond, J. Shin. Results of Low Power Deicer Tests on a Swept Inlet Component in the NASA Lewis Icing Research Tunnel. Technical Memorandum 105968, NASA, 1993.

[136] T. P. Ratvasky, B. P. Barnhart, S. Lee, J. Cooper . Flight Testing an Iced Business Jet for Flight Simulation Model Validation. Technical Memorandum 2007-214936, NASA, 2007.

[137] T. Rabczuk. Computational Methods for Fracture in Brittle and Quasi-Brittle Solids: State-of-the-Art Review and Future Perspectives. *ISRN Applied Mathematics*, 2013, 2013.

[138] T. Theodorsen, W. C. Clay. Ice Prevention on Aircraft by Means of Engine Exhaust Heat and a Technical Study of Heat Transmission From a Clark Y Airfoil. Report 403, NACA, 1931.

[139] T.W. Harper. An Introduction to Aircraft Ice Protection Systems: A Series of Articles Dealing with the Protection of Aircraft from Ice Accretion. *Aircraft Engineering and Aerospace Technology*, 40(7), 1968.

[140] U. von Glahn, R. E. Blatz. Investigation of Power Requirements for Ice Prevention and Cyclical De-Icing of Inlet Guide Vanes with Internal Electric Heaters. Research Memorandum E50H29, NACA, 1950.

[141] U.S. Department of Transportation. Characteristics of Runback Ice Accretions and Their Aerodynamic Effects. Final Report DOT/FAA/AR-07/16, Federal Aviation Administration, 2007.

[142] V. F. Petrenko . The Surface of Ice . Technical report, US Army Corp of Engineers: Cold Regions Research and Engineering Laboratory , 1994 .

[143] V. F. Petrenko, I. A. Ryzhkin . Surface States of Charge Carriers and Electrical Properties of the Surface Layer of Ice . *J. Phys. Chem. B* , 101 , 1997 .

[144] V. F. Petrenko, R. W. Whltworth . Structure of Ordinary Ice Ih Part II: Defects in Ice. Volume 1: Point Defects . Technical report, US Army corp of engineers: Cold regions research and engineering laboratory , 1994 .

[145] V. H. Gray, D. T. Bowden, U. von Glahn. preliminary results of cyclical de-icing of a gas heated airfoil. Research Memorandum E51J29, NACA, 1952.

[146] W. A. Fleming, M. J. Saari. Inlet Icing and Effectiveness of Hot-Gas Bleedback for Ice Protection of Turbojet Engines. Research Memorandum E8J25c, NACA, 1948.

[147] W. B. Wright. *User Manual for the NASA Glenn Ice Accretion Code LEWICE.* National Aeronautics and Space Administration, Glenn Research Center, 2002.

[148] W. B. Wright, R. W. Gent, D. Guffond. DRA/NASA/ONERA Collaboration on Icing Research: Part II - Prediction of Airfoil Ice Accretion. Contractor Report 202349, DRA/NASA/ONERA, 1997.

[149] W. B. Wright, T.G. Keith, K.J. De Witt . Numerical Simulation of Icing, Deicing and Shedding . In *29th Aerospace Sciences Meeting, Reno, Nevada, AIAA-91-0665* , 1991 .

[150] W. C. Geer. An Analysis of the Problem of Ice on Airplanes. *Journal of the Aeronautical Sciences*, 6(11):451–459, 1939.

[151] W. C. Geer, M. Scott. The Prevention of the Ice Hazard on Airplanes. Technical Note 345, NACA, 1930.

[152] W. D. King, N. H. Fletcher . Thermal Shock as an Ice multiplication Mechanism. Part I. Theory . *Journal of the atmospheric sciences* , 33 , 1976 .

[153] W. D. King, N. H. Fletcher . Thermal Shock as an Ice Multiplication Mechanism. Part II. Experimental . *Journal of the atmospheric sciences* , 33 , 1976 .

[154] W. H. Gowan Jr., D. R. Mulholland. Effectiveness of Thermal Pneumatic Airfoil Ice Protection System. Research Memorandum E50K10a, NACA, 1951.

[155] W. L. Smith. Weather Problems Peculiar to the New York-Chicago Airway. *Monthly Weather Review*, 57:503–506, December 1929.

[156] W. Lewis. A Flight Investigation of the Meteorological Conditions Conducive to the Formation of Ice on Airplanes. Technical Note 1393, NACA, 1947.

[157] W. M. Kays, M. E. Crawford. Convective heat and mass transfer, 1980.

[158] W. M. Leary. We Freeze to Please: A History of NASA's Icing Research Tunnel and the Quest for Flight Safety. The NASA History Series, 2002.

[159] Y. Coudiere, J.P. Vila, P. Villedieu. Convergence of a finite volume scheme for a diffusion problem. *Finite volumes for complex applications, Problems and Perspectives (Hermes, Paris)*, pages 161–168, 1996.

[160] Y. Wei, R. M. Adamson, J. P. Dempsey . Ice/metal Interfaces: Fracture Energy and Fractography . *Journal of materials science* , 31 , 1996 .

[161] Y.Y. Yan, N. Gao, W. Barthlott . Mimicking Natural Superhydrophobic Surfaces and Grasping the Wetting Process: A Review on Recent Progress in Preparing Superhydrophobic Surfaces . *Advances in Colloid and Interface Science* , 169 , 2011 .

Appendix

In section 3.3, it is shown that the stress tensor is deduced from the elastic energy through the relation: $\sigma = \frac{\partial \psi}{\partial \epsilon}$. As the elastic energy is split into positive and negative parts, terms such as $\frac{\partial \epsilon_+}{\partial \epsilon}$ (which may be identified with a projection operator) need to be evaluated. The algorithm by which this task is performed is presented in this appendix. It follows, in a more detailed way, the presentation given in [23].

Let B be a second order symmetric tensor and let G be a tensor valued tensor function (such as $G : \epsilon \longrightarrow \epsilon_+$). The main idea is to express the tensor B in its eigenbasis and use this representation to evaluate $G(B)$, $\dot{B}$ and $\dot{G}$ (time differentiation will be used for convenience of notation). The final step then consists in identifying $\frac{\partial G}{\partial B}$ thanks to the relation: $\dot{G} = \frac{\partial G}{\partial B} : \dot{B}$.

Consider the following representation of B on its eigen basis (λ_a stands is the a-th eigenvalue and n_a is the associated eigenvector):

$$B = \sum_a \lambda_a n_a \otimes n_a \tag{A.1}$$

In order to differentiate, consider a fixed cartesian basis $e_{a\,a=1,2}$ and a time dependant rotation R such that:

$$n_a = R.e_a \tag{A.2}$$

Time differentiating the previous relation yields:

$$\dot{n}_a = \dot{R}.e_a$$

Moreover, inverting relation (A.2):

$$e_a = R^{-1}.n_a$$

Thus $\dot{n}_a$ may be written as:

$$\dot{n}_a = \dot{R}R^{-1}.n_a = \Omega.n_a$$

where $\Omega = \dot{R}R^{-1}$ is the spin of the principal axes due to rotation R. Ω has the property of being skew-symmetric. Indeed, as R is a rotation matrix, $R^{-1} = R^T$, and therefore:

$$(R\dot{R}^T) = \dot{I} = 0$$

$$(\dot{R\dot{R}^T}) = \dot{R}R^T + R\dot{R}^T$$

which yields the result:

$$\dot{R}R^T = -R\dot{R}^T \Rightarrow \Omega = -\Omega^T$$

Ω may be recast into the eigen basis of B:

$$\Omega = \sum_a \sum_b \Omega_{ab} n_a \otimes n_b$$

The components Ω_{ab} may be expressed thanks to the following steps:

$$\Omega.n_b = \sum_c \sum_d \Omega_{cd} n_c \otimes n_d.n_b$$

$$n_c \otimes n_d.n_b = \delta_{db} n_c \Rightarrow \Omega.n_b = \sum_c \Omega_{cb} n_c = \dot{n}_b$$

$$\sum_c \Omega_{cb} n_c.n_a = \Omega_{ab} = \dot{n}_b.n_a$$

Therefore the components of Ω can be expressed in terms of the eigenvectors of B as $\Omega_{ab} = \dot{n}_b.n_a$. Time differentiation of B may now be addressed and splits into two parts:

$$\dot{B} = \sum_a \dot{\lambda}_a n_a \otimes n_a + \sum_a \lambda_a (n_a \dot{\otimes} n_a)$$

Using the previous results, the summand of the second term may be obtained:

$$
\begin{aligned}
\lambda_a (n_a \dot{\otimes} n_a) &= \lambda_a \dot{n}_a \otimes n_a + \lambda_a n_a \otimes \dot{n}_a \\
&= \lambda_a \left[(\Omega.n_a) \otimes n_a + n_a \otimes (\Omega n_a) \right] \\
&= \lambda_a \left[\left(\sum_b \Omega_{ba} n_b \right) \otimes n_a + n_a \otimes \left(\sum_b \Omega_{ba} n_b \right) \right] \\
&= \lambda_a \sum_b \Omega_{ba} n_b \otimes n_a + \lambda_a \sum_b \Omega_{ba} n_a \otimes n_b
\end{aligned}
$$

Taking the sum over a and using the previous result yields:

$$
\begin{aligned}
\sum_a \lambda_a (n_a \dot{\otimes} n_a) &= \sum_a \sum_b \lambda_a \Omega_{ba} n_b \otimes n_a + \sum_a \sum_b \lambda_a \Omega_{ba} n_a \otimes n_b \\
&= \sum_a \sum_b \lambda_b \Omega_{ab} n_a \otimes n_b - \sum_a \sum_b \lambda_a \Omega_{ab} n_a \otimes n_b \\
&= \sum_a \sum_b (\lambda_b - \lambda_a) \Omega_{ab} n_a \otimes n_b
\end{aligned}
$$

Therefore the time derivative of B is expressed as:

$$\dot{B} = \sum_a \dot{\lambda}_a n_a \otimes n_a + \sum_a \sum_b (\lambda_b - \lambda_a) \Omega_{ab} n_a \otimes n_b \tag{A.3}$$

The tensor valued tensor function G may also be expressed using the eigenbasis of B:

$$G(B) = \sum_a g_a n_a \otimes n_a$$

where g_a are diagonal functions associated with G. For example, if G is the positive part, then $g_a = <\lambda_a>_+$. Using this representation, time differentiation works in the same way as for B and yields:

$$\dot{G} = \sum_a \sum_b \frac{\partial g_a}{\partial \lambda_b} \dot{\lambda}_b n_a \otimes n_a + \sum_a \sum_b (\lambda_b - \lambda_a) \Omega_{ab} n_a \otimes n_b \tag{A.4}$$

The final part is to identify $\dot{G}$ using the previous results and the general formula:

$$\dot{G} = \frac{\partial G(B)}{\partial B} : \dot{B}$$

$\frac{\partial G(B)}{\partial B}$ being a fourth order tensor, we may express it in terms of the eigenbasis of B as:

$$\frac{\partial G(B)}{\partial B} = \sum_i \sum_j \sum_k \sum_l A_{ijkl} n_i \otimes n_j \otimes n_k \otimes n_l$$

Contracting this expression with the first term of $\dot{B}$:

$$\sum_i \sum_j \sum_k \sum_l A_{ijkl} \sum_m \dot{\lambda}_m n_i \otimes n_j \otimes \underbrace{n_k \otimes n_l : n_m \otimes n_m}_{=\delta_{km}\delta_{lm}} = \sum_i \sum_j \sum_m A_{ijmm} \dot{\lambda}_m n_i \otimes n_j$$

and therefore:

$$\sum_i \sum_j \sum_m A_{ijmm} \dot{\lambda}_m n_i \otimes n_j = \sum_a \sum_b \frac{\partial g_a}{\partial \lambda_b} \dot{\lambda}_b n_a \otimes n_a$$

Identifying using the previous relation gives:

$$A_{ijmm} = \begin{cases} 0 & \text{if } i \neq j \\ \frac{\partial g_i}{\partial \lambda_m} & \text{if } i = j \end{cases}$$

Contracting of the general expression of $\frac{\partial G(B)}{\partial B}$ with the second term of $\dot{B}$:

$$
\begin{aligned}
\sum_i \sum_j \sum_k \sum_l A_{ijkl} \sum_m \sum_n \Omega_{nm}(\lambda_n - \lambda_m) n_i \otimes n_j \otimes n_k \otimes n_l : n_m \otimes n_m &= \sum_i \sum_j \sum_k \sum_l A_{ijkl} \Omega_{lk}(\lambda_k - \lambda_l) n_i \otimes n_j \\
&= \sum_i \sum_j \Omega_{ij}(g_j - g_i) n_i \otimes n_j
\end{aligned}
$$

Identification of summands implies:

$$\sum_k \sum_l A_{ijkl} \Omega_{lk}(\lambda_k - \lambda_l) = \Omega_{ij}(g_j - g_i)$$

Given the skew-symmetry of Ω the only two possibilities are $k = i, l = j$ and $k = j, l = i$:

$$\left(A_{ijij} + A_{ijji} \right) \Omega_{ij}(\lambda_j - \lambda_i) = \Omega_{ij}(g_j - g_i)$$

Moreover, as $\Omega_{ii} = 0$:

$$A_{ijij} = A_{ijji} = \frac{1}{2} \frac{g_j - g_i}{\lambda_j - \lambda_i} \qquad \text{if } i \neq j$$

which completes the identification, yielding the final result:

$$\frac{\partial G(B)}{\partial B} = \sum_a \sum_b \frac{\partial g_a}{\partial \lambda_b} n_a \otimes n_a \otimes n_b \otimes n_b + \sum_a \sum_{b \neq a} \frac{1}{2} \frac{g_a - g_b}{\lambda_a - \lambda_b} n_a \otimes n_b \otimes (n_a \otimes n_b + n_b \otimes n_a) \qquad \text{(A.5)}$$

Thanks to this expression positive and negative projection operators required for constitutive modelling purposes may be computed.

MAXIMUM PRINCIPLE WITH NEUMANN BOUNDARY CONDITIONS

The maximum principle constitues an important results of PDE and functional analysis. Roughly speaking, it states that under certain conditions the solution to an elliptic PDE is bounded between the minimum and maximum value of the right hand side. Only the proof of boundedness below of the solution will be reproduced here. It follows closely the proof given in [47].

Consider the following weak formulation:

$$\int_\Omega au\phi\, dV + \int_\Omega b\nabla u\nabla\phi\, dV = \int_\Omega f\phi\, dV$$

where a, b and f are positive and ϕ is a test function.

The following proposition is needed for the proof:

Proposition 1. *Let $G \in C^1(\mathbb{R})$ be such that $G(0) = 0$ and $|G'(s)| \leq M$ $\forall s \in \mathbb{R}$ for some constant M. Let $u \in W^{1,p}(\Omega)$ with $1 \leq p \leq \infty$. Then*

$$G \circ u \in W^{1,p}(\Omega) \quad and \quad \frac{\partial}{\partial x_i}(G \circ u) = (G' \circ u)\frac{\partial u}{\partial x_i} \;\; i = 1, ..., N$$

Hence, let $u^\star = -u$, $K = \inf_\Omega f$ and $G \in C^1(\mathbb{R})$ defined as follows:

1. $|G'(s)| \leq M \; \forall s \in \mathbb{R}$

2. G is strictly increasing on $[0, +\infty[$

3. $G(s) = 0 \; \forall s \leq 0$

Thanks to proposition 1, the maximum principle may be proved as follows. Let $v = G(u^\star - K)$. As $u^\star \in H^1$ then $v \in H^1$. Therefore v may be chosen as the test function ϕ:

$$\int_\Omega au^\star v\, dV + \int_\Omega b\nabla u^\star \nabla v\, dV = -\int_\Omega fv\, dV$$

Replacing v by its definition yields:

$$\int_\Omega a(u^\star - K)G(u^\star - K)\, dV + \int_\Omega b\nabla u^\star \nabla G(u^\star - K)\, dV = -\int_\Omega (f - K)G(u^\star - K)\, dV$$

Applying the second result of proposition (1) and due to the properties of G:

$$\nabla u^\star \nabla G(u^\star - K) = G'(u^\star - K)\nabla u^\star \nabla u^\star \geq 0$$

$K = \inf_\Omega f$ therefore $f - K \geq 0$. Hence:

$$\int_\Omega (f - K)G(u^\star - K)\, dV \geq 0$$

which means that:

$$\int_\Omega a(u^\star - K)G(u^\star - K)\, dV \leq 0$$

But $tG(t) \geq 0$ hence $(u^\star - K)G(u^\star - K) = 0$ a.e. $\Rightarrow u^\star \leq K$. Therefore $u \geq \inf_\Omega f$.

In this appendix, a brief overview of some phenomena relative to ice at the microscopic level are given. Its goal is not to be exhaustive but only to provide a quick view at some specific aspects which can be linked to macroscopical behaviour such as plasticity (due to defects) and adhesion.

C.1   The Crystalline Structure of Ice

Although some of the results concerning ice structural and adhesive properties may be understood through the eye of continuum mechanics, its crystalline nature remains a core element in the analysis of some phenomena specific to ice. As shown in the phase diagram of ice (fig C.1) water may crystallise in many ways depending on the pressure and temperature conditions.
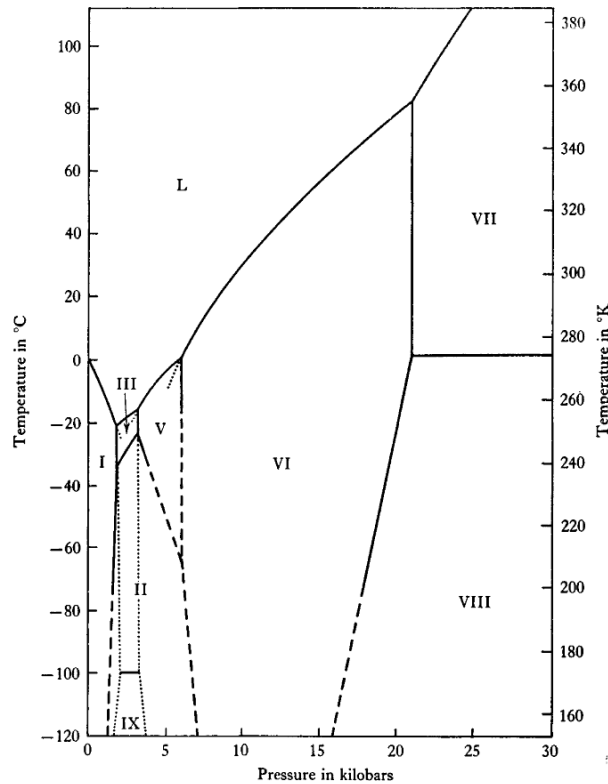
Figure C.1: Phase diagram of ice [100]. Dotted lines: metastable continuation of a phase in neighbouring regions. Broken lines: extrapolation of phase boundaries

In standard pressure conditions, ice (noted ice I, also called "ordinary" ice) may crystallise in two ways [33]:

- Ice with hexagonal symmetry, noted Ih. It is the most commonly encountered form of ice.

- Ice with cubic symmetry, noted Ic. This form crystallises from water vapour deposits at temperatures less then $-130°C$ and is hence less frequently encountered.

The position of a hydrogen atom in the Ih structure is governed by what are called the Bernal-Fowler rules [71, 33, 100] :

- Two hydrogen atoms must be located near each oxygen atom.

- Only one hydrogen atom must lie on each O–O bond.

However as stated by Bernal and Fowler [71] and later confirmed by Pauling [78, 100] there is a degree of randomness in the position of the hydrogen atoms. Bernal and Fowler suggested that even below the melting point, the molecular arrangement may very well remain irregular. Ice would thus be crystalline in the position of its molecules but glass-like in their orientation. The following figure (C.2) shows a possible arrangement of hydrogen atoms (protons) in an ice Ih crystal structure :
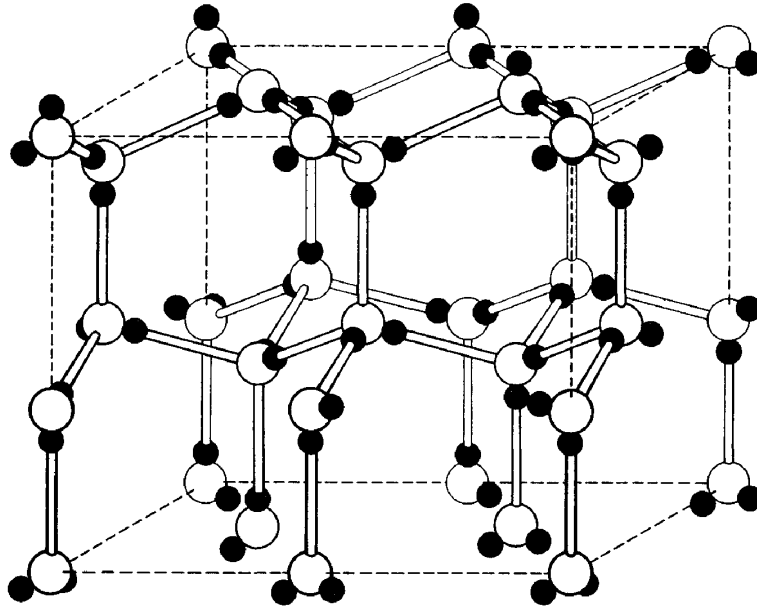
Figure C.2: Oxygen and hydrogen atom arrangement in an ice Ih structure [100]

Ice can take the form of a perfect crystal provided its structure obeys the following rules (similar to the Bernal-Fowler rules) [100]

- A water molecule must occupy each lattice position and be tetrahedrally bonded to its four nearest neighbours.

- For each water molecule there are only two protons near the oxygen atom.

- There is only one proton on each bond.

Breaking these rules (or the Bernal-Fowler rules) leads to the creation of point defects. A point defect is located at a specific point in the crystal lattice structure and within one or two unit cells [144]. A vacancy (empty molecular site), an interstitial (a molecule inserted in an open space of the crystal lattice) or an impurity atom will arise from breaking the first rule while breaking the second or third rule will generate defects specific to ice (protonic defects).

- Ion states: these states are made when a proton moves on the O-O bond. This leads to the creation of OH^- and H_3O^+ ion states. These states are however unstable and further proton jumps are necessary to stabilise both defects. This may lead to either a recombination or diffusive separation. A schematic view of this process is shown figure C.3.

(a) Formation   (b) Separation
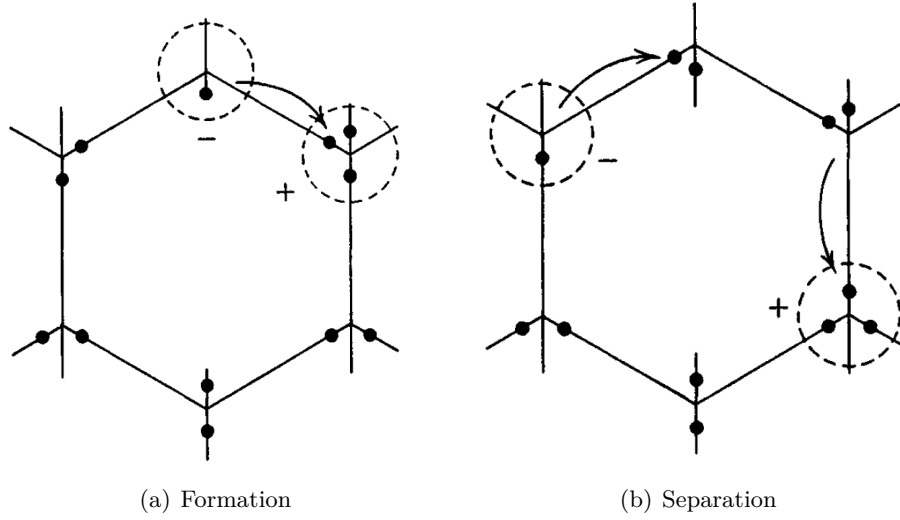
Figure C.3: formation of ion states and separation by proton jumps [100]

- Orientational defects: these states, originally introduced by Bjerrum, are made by rotation of a water molecule about one of its bonding axes. Thus one of the bonds will be occupied by two protons (D-defect) leaving the other bond empty (L-defect). These defects can migrate and diffuse by successive rotations of water molecules. This protonic motion redistributes the electronic density and contributes to the electrical conductivity of ice [144] and plays a role in ice adhesion models[56]. Moreover protonic defects also have an effect on dislocation mobility and therefore will affect creep [33].

(a) Formation   (b) Migration
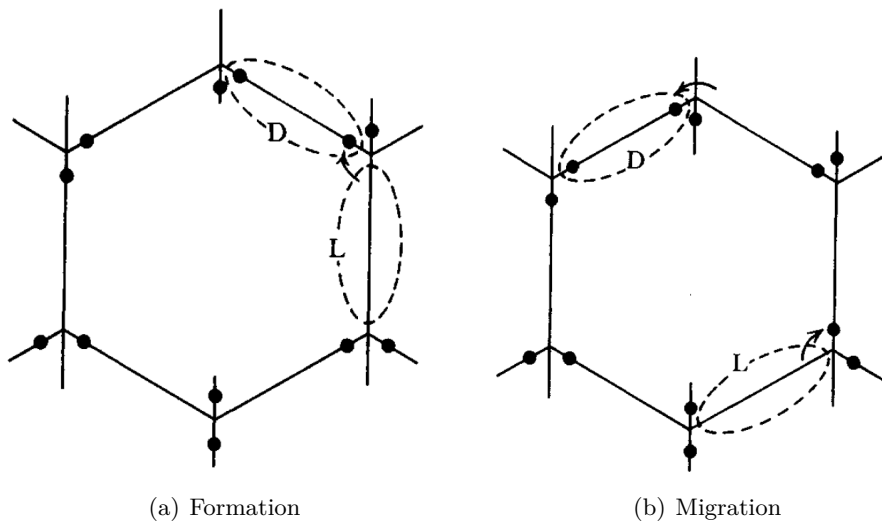
Figure C.4: formation of L and D defects and migration by molecular rotation[100]

C.2 Ice Adhesion

There are several general theories of adhesion that describe the various mechanisms by which adhesion may occur [93, 82, 10] such as electrostatic charge transfer, mechanical interlocking, molecular diffusion or chemical bonding.

- Electrostatic : adhesion is the result of a transfer of electrical charge between materials. Electrical discharges and high adhesion energies were observed during peel tests of polyvinyl chloride to glass. This led to the theory according to which the high peel energies were related to the dissipation of electrical charges by analogy with a capacitor. The adhesion energy would thus be equivalent to that needed to separate two charged plates. Currently the dominant theory is that the energy dissipation observed during peel tests is a result of rheological phenomena taking place in the bulk of the material. The electrical discharge would in fact be a consequence of the de-bonding.

- Diffusion : This theory was originally proposed to describe the adhesion between two polymers, also referred to as auto-adhesion. At the interface, molecular movement (due to thermal processes for example) leads to molecular interdiffusion. This has the effect of creating an interphase where chemical bonds link the two materials.

- Mechanical : Adhesion is due to the adhesive flowing into the microscopic pores and asperities of the substrate and solidifying, therefore creating an interlocking system. This theory applies only to rough surfaces such as wood.

- Chemical : Adhesion is due to the formation of chemical bonds between the materials. These bonds can be of different nature and can be classified into two kinds : Inter-atomic (ionic, covalent, metalic) and inter-molecular (Van Der Waals type bonds such as hydrogen bonds).

- Thermodynamic theory − adsorption or wetting : In this theory, the Young, Laplace and Dupré equations are combined so as to define the reversible work of adhesion : $W_a = \gamma_1 + \gamma_2 - \gamma_{12}$ Where γ_i are the surface or interfacial free energies resulting from intermolecular forces (Van Der Waals). This reversible work of adhesion is the minimum energy required to separate the two phases/materials. If it is negative then spontaneous separation is favoured.

- Weak boundary layer : this theory suggests that the debonding process does not strictly restrain itself to the interface between the two materials and could deviate into the bulk of one of them. This means that cohesive failure occurs in a region of reduced mechanical strength : the weak boundary layer. Bikerman, the original author of this theory, proposes 7 types of weak boundary layers. The first type would correspond to an interface in which pockets of air would be trapped. The second and third type are based on the fact that some interfaces have unusual properties thus enabling the possibility of migration of impurities from the bulk of one material to another. This would lead to reduced mechanical strength and therefore would be favourable to failure. The fourth to seventh types correspond to the presence of an aggressive environment resulting in chemical or physical attack at the interface.

- Rheological theory : When proceeding to peel tests, the measured value of the adhesion work W is often much greater than the reversible work of adhesion W_a (by several factors of ten). Nevertheless it has been observed that there is a proportionality between W and W_a over certain ranges of peel rate R and temperature T. This leads to the following formula : $W = f(R, T)W_a$.

It is also interesting to note that adhesion has also been formulated in a mathematical framework, initiated with the work of Frémond [86], which is still under study [104].

One of the first ice adhesion mechanisms which comes to mind is mechanical interlocking. However, other theories have also been developed based on the observation of a special layer at the surface of ice and point defects (see section C.1) inducing surface charge accumulation.

C.2.1   Liquid like layer

We can trace back the story of ice adhesion theories to the 1850's [51, 84]. At that time Faraday described the phenomenon that would later be named "regelation": if two blocks of ice are brought into contact at a temperature equal or above the freezing point they start to freeze together and adhere to one another. To explain this observation Faraday pointed out the fact that water can exist

in supercooled state. Thus he hypothesised the existence of a thin film of supercooled liquid particles at the surfaces of both ice blocks, that would flow and freeze when the blocks would be brought into contact[85]. J. Tyndall accepted Faraday's theory and used it to give an explanation for glacier flow [69]. However, before the discovery of regelation, J. Thomson had studied the effects of pressure on lowering the melting point of water. He therefore tried to explain regelation by pressure melting, and opposed Faraday's view. As a response to this criticism Faraday performed experiments to prove his ideas without managing to convince Thomson (also supported by Helmholtz). At the time, regelation could not be explained properly and Thomson's view eventually prevailed [51].

It will take until 1951 for Faraday's original idea to be revived by Weyl on theoretical grounds[51, 50]. His idea was that water being a dipolar molecule, a water surface as well as an ice surface will lower its surface energy by changin the way the electronegative part of the dipoles (the oxygen atom) are distributed at the outer surface. This would have the effect of inducing an electrical double layer at the surface of water or ice, creating disturbances in the surface layers. The surface layers and the bulk would therefore have different properties. According to Weyl a transition layer of several Angstroms is required to go from the outer surface layer to the actual crystal structure of the ice block [51]. These considerations lead him to assume the existence of a liquid-like transition layer. This layer would exist at and below the freezing point, eventually disappearing at very low temperatures. It would have properties between that of ice and liquid water (but being neither one). The final idea is that this transition layer not only exists at the ice/air interface, but also at ice/solid interfaces.

Based on this theory, Jellinek estimated the tensile and shear stress needed to separate an ice block from a solid surface [48]. However, quantitative estimates yield values well above the tensile strength of ice, thus predicting a cohesive break. He also formulated an estimation of the shear strength needed for separation, assuming the solid surface has velocity v_t and the liquid to be Newtonian. Jellinek pointed out the fact that discussions assuming a liquid-like layer should be semi-quantitative at best due to the lack of knowledge on such a layer. Nevertheless he considers the assumption of a liquid-like layer essential to understanding experimental results on the adhesive properties of ice[48].

Since then, further progress has been made. In the light of X-Ray diffraction, proton channelling, optical ellipsometry and nuclear magnetic resonance experiments it becomes evident that a special layer exists at the surface of ice. Petrenko [142] reports and describes these experiments, giving further insight on the nature, structure and thickness of the liquid-like layer. As predicted before, the thickness of the layer decreases with temperature. Atomic force microscopy experiments provided upper limit values of $12nm$ at $-24°C$ and $70nm$ at $-0.7°C$ [117].

Molecular dynamics simulations where also run by Girardet and Toubin [20]. Figure C.5 clearly shows the apparition of a disordered layer at the surface of ice with increasing temperature, thus confirming the possibility of the existence of a liquid-like layer at the surface of ice.

T = 190 K   T = 235 K   T = 270 K

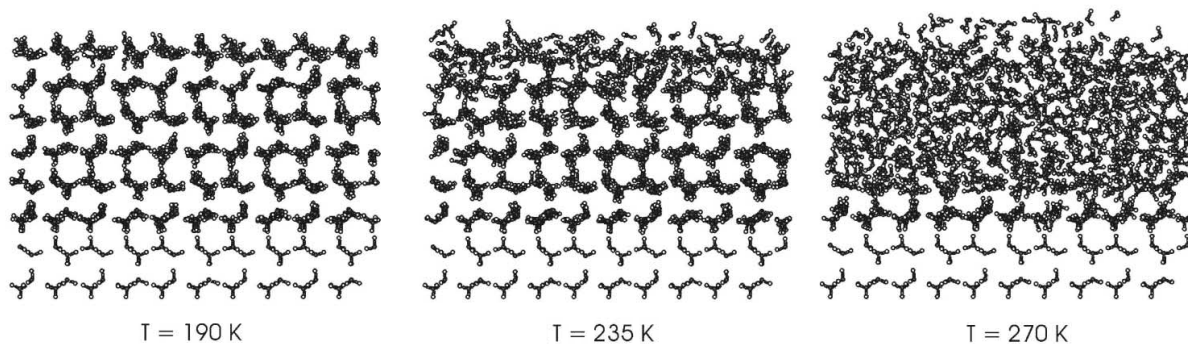Figure C.5: Molecular dynamics simulation showing the apparition of a liquid-like layer with increasing temperature [20]

Without going into further detail, suffice it to say that there is now clear evidence of the existence of the liquid-like layer and that the subject is still actively studied. However, the role this layer could play in ice adhesion (especially atmospheric impact ice) is still not very clear.

C.2.2 electrostatic theory

In the previous section we saw that electrical arguments were used in order to assume the existence of a liquid-like layer. However research has also been conducted on the actual electrical properties of the surface of ice. From a theoretical point of view, the main argument is the same as in the liquid-layer theory. Petrenko and Ryzhkin [56] assumed high density surface charges at the ice/solid and ice/vapour interfaces based on experimental and theoretical evidence. This surface charge is induced by protonic point defects (H_30^+, OH^-, L and D). These defects may be captured at the ice surface resulting in a buildup of surface charge. Moreover when considering an ice/substrate interface, mobile ions and Bjerrum deffects are attracted to the interface by an electrostatic attraction known as image force.

Petrenko and Ryzhkin evaluate the adhesion energy per unit area by numerically solving the problem of minimization of potential electrostatic energy. The results of the numerical resolution of these equations are shown figure C.6 for different surface state occupancies. The adhesion energies range from $0.08 J.m^{-2}$ to $1.3 J.m^{-2}$. These results are comparable, at least in the proximity of the lower bound, to those obtained experimentally by Sonwalkar [101] using Raman spectroscopy (bearing in mind that they were obtained at different temperatures). Thus, as concluded by Petrenko and Ryzhkin, electrostatic interaction may play an essential role in ice adhesion.

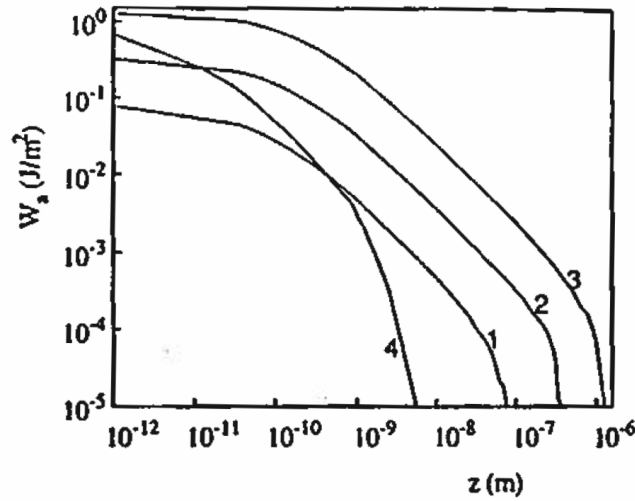

Figure C.6: Adhesion energy as a function of distance z separating the metal surface from the ice. 1,2 and 3 correspond to perfect occupancy of surface states by D, H_3O^+ and protons. 4 corresponds to protonic equilibrium occupancy at $-10°C$

CONVECTIVE HEAT TRANSFER IN A BOUNDARY LAYER OVER A SMOOTH SURFACE

This aim of this appendix is to briefly give more details relative to the boundary layer computations which where used in chapter 6. In aerodynamics, the boundary layer designates the region, for example near the surface of the body, where viscous effects are no longer negligible. In boundary layer theory the flow is separated into two parts. An exterior flow which may be treated with inviscid flow theory and a flow inside the boundary layer. A boundary layer has a local thickness δ. Inside the boundary layer, the velocity is zero at the wall and increases until it matches the exterior flow velocity as illustrated in figure D.1. This very brief presentation of boundary layer theory follows closely references [58, 57, 157].

It should be noted that the methods used in the ONERA icing tool box are in fact more complicated than those presented here (which assume a smooth surface). Indeed, ice presents a rough surface which has an effect on boundary layer properties.

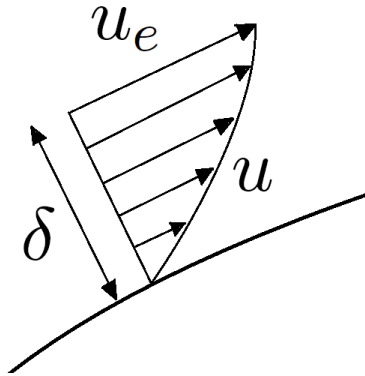Figure D.1: Illustration of a boundary layer

D.1 Two Dimensional Compressible Boundary Layer Equations

In the case of a two dimensional plane steady flow it can be shown, for example by using matched asymptotic expansion or an order of magnitude analysis, that the boundary layer equations are:

- Continuity equation:

$$\frac{\partial \rho u}{\partial x} + \frac{\partial \rho v}{\partial y} = 0$$

- Longitudinal momentum equation:

$$\rho u \frac{\partial u}{\partial x} + \rho v \frac{\partial u}{\partial y} = -\frac{\partial p}{\partial x} + \frac{\partial \tau}{\partial y}$$

- Transversal momentum equation:

$$\frac{\partial p}{\partial y} = 0$$

- Energy equation:

$$\rho u \frac{\partial h_i}{\partial x} + \rho v \frac{\partial h_i}{\partial y} = \frac{\partial}{\partial y} (u\tau - \phi)$$

- Equation of state:

$$p = \rho r T$$

where h_i is the total enthalpy, u and v are respectively the longitudinal and transversal mean components of the velocity, p is the mean value of pressure, ρ is the density and r is the ideal gas constant. τ is the stress tensor and is given by:

$$\tau = \mu \frac{\partial u}{\partial y} - \rho < u'v' >$$

where the superscript $'$ denotes a fluctuating variable (Reynolds decomposition) and $< . >$ is the averaging operator. Finally, ϕ is the heat flux, given by:

$$\phi = -\lambda \frac{\partial T}{\partial y} + \rho c_p < v'T' >$$

Associated to these equations are the boundary conditions relative to the surface of the body on the one hand, and the matching to the exterior 'free stream' field on the other hand.

Note that a quantity of great interest is the skin friction coefficient. Skin friction is linked to the drag force and is therefore important when studying the motion of a body through a fluid. Moreover, as will be seen later, it may also be linked to the heat transfer coefficient. It is defined as:

$$C_f = \frac{\tau_w}{\frac{1}{2}\rho_e u_e^2}$$

where τ_w is the shear stress at the surface of the flat plate, defined by:

$$\tau_w = \mu \frac{\partial u}{\partial y}\bigg|_{y=0}$$

D.2   Simple Integral Method

In order to obtain a simpler form to the boundary layer equations, one can integrate them along y, which yields their global form. The integration along y leads to the definition of global variables such as the displacement thickness δ_1 and the momentum thickness θ:

$$\delta_1 = \int_0^\delta \left(1 - \frac{\rho u}{\rho_e u_e}\right) dy$$

$$\theta = \int_0^\delta \frac{\rho u}{\rho_e u_e} \left(1 - \frac{u}{u_e}\right) dy$$

One of the most important of the integral equations is the global momentum equation, also known as the von Karman equation. For a plane two dimensional flow it is written as:

$$\frac{d\theta}{dx} + \theta \left(\frac{H+2}{u_e} \frac{du_e}{dx} + \frac{1}{\rho_e} \frac{d\rho_e}{dx}\right) = \frac{C_f}{2}$$

with $H = \delta_1/\theta$. In this equation, there a three unknown variables: θ, C_f and H. A possible approximate closure model is to use the flat plate results to set C_f and H (shown in section D.3.1). Then, by integrating the von Karman equation between two positions x_0 and x_1, one can compute θ step by step. The value of θ has to be given at an initial point in order to proceed with this method. The initial point is usually chosen to be the stagnation point. The momentum thickness can be evaluated at that point by using the Falkner-Skan solutions (shown in section D.3.2). The last remaining point is to predict the laminar-turbulent transition point. Criterions based on experimental data may be used as well as more elaborate techniques based on stability analysis and the Orr-Sommerfeld equation [58]. As an illustration, a simple criterion based on experimental data, states that the transition point is defined by [58]:

$$Re_{\theta,t} = 1.535 Re_{x,t}^{0.444}$$

where Re_θ is the Reynolds number based on the momentum thickness and Re_x is the one based on the position abscissa. Hence, during the step by step process described previously, at each new point Re_θ can be compared to Re_x and when the criterion is met the boundary layer becomes turbulent.

D.3 Self Similar Falkner-Skan Solutions for a Laminar Incompressible Boundary Layer

Consider the flow over a wedge as illustrated in figure D.2.
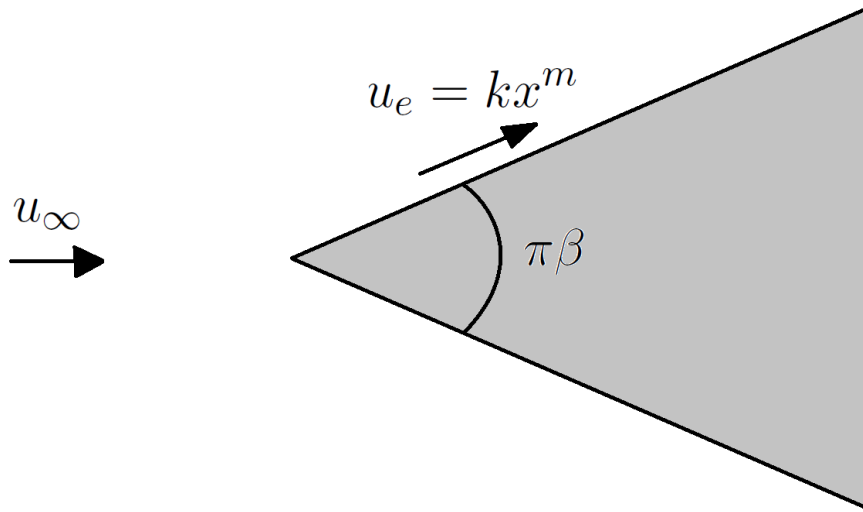
Figure D.2: Illustration of the flow over a wedge

For this kind of flow, potential theory yields the following expression for the external velocity [4]:

$$u_e = kx^m$$

where k is a constant linked to the free-stream velocity u_∞ and m is linked to the wedge angle $\pi\beta$ through the relation $\beta = \frac{2m}{m+1}$.

By using the change of variables:

$$\zeta = y\sqrt{\frac{m+1}{2}\frac{u_e}{\nu x}}$$

it can be shown that the boundary layer equations reduce to the following ordinary differential equation:

$$f''' + ff'' + \beta\left(1 - f'^2\right) = 0$$

with boundary conditions:
$$f(0) = 0 \; ; \; f'(0) = 0 \; ; \; f'(\infty) = 1$$

This equation needs to be solved numerically and yields the velocity in the boundary layer through the formula:

$$\frac{u}{u_e} = f'$$

and also the friction coefficient:

$$C_f = 2f''(0) \left(\frac{m+1}{2}\right)^{1/2} Re_x^{-1/2}$$

where $Re_x = \frac{\rho_e u_e x}{\mu_e}$ is the Reynolds number based on the external flow variables and length x.

D.3.1   Flat Plate Boundary Layer

The external flow over a flat plate corresponds to the case $m = 0$ and $\beta = 0$, meaning that u_e is constant and equal to its free-stream value. In this case, the Falkner-Skan method retrieves the classical Blasius solution, which yields the following expression for the friction coefficient:

$$C_{f,lam} = \frac{0.664}{\sqrt{Re_x}}$$

In the case of a turbulent flow, the friction coefficient is obtained thanks to experimental data and is written as [58]:

$$C_{f,turb} = \frac{0.0368}{Re_x^{1/6}}$$

In order to study the convective heat transfer due to the flow over the flat plate, the Stanton number is introduced. In the case where the heat flux at the surface of the flat plate can be written $\phi_w = htc\,(T_w - T_{rec})$, the Stanton number reads:

$$St = \frac{htc}{\rho_e u_e c_p}$$

where T_{rec} is the recovery temperature given by:

$$T_{rec} = T_e \left(1 + r\frac{\gamma - 1}{2}M_e^2\right)$$

where r is the recovery coefficient. For air, the following values are often used: $r = 0.85$ for laminar flow and $r = 0.9$ for turbulent flow. These values can be deduced from the Crocco-Van Driest method.

The convective heat transfer coefficient is then obtained by assuming an analogy between the momentum transfer and heat transfer. If the viscous energy dissipation term is neglected, then for an incompressible flow the energy equation is:

$$u\frac{\partial T}{\partial x} + v\frac{\partial T}{\partial y} = \alpha\frac{\partial^2 T}{\partial x^2}$$

On the other hand, as there is no pressure gradient in this case, the longitudinal momentum equation for an incompressible flow is:

$$u\frac{\partial u}{\partial x} + v\frac{\partial u}{\partial y} = \nu\frac{\partial^2 u}{\partial x^2}$$

The similarity between the two previous equations is the main motivation for the momentum and heat transfer analogy assumption: the solutions to the momentum and energy equations are assumed to be similar. Hence, a parameter s, called the Reynolds analogy factor, is introduced. Assuming similar velocity and temperature profiles, it links the Stanton number to the friction coefficient through the following formula:

$$St = s\frac{C_f}{2}$$

In this case where the Prandtl number is equal to 1, s also takes the value of 1. Assuming flow conditions summed up in table D.1, the resulting heat transfer coefficient is shown in figure D.3

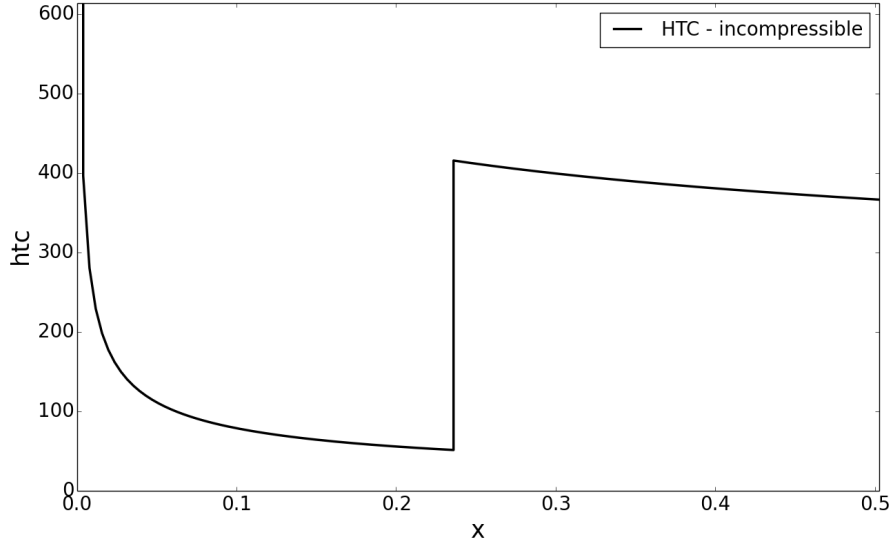| Mach	P_∞ (Pa)	T_∞ (K)
0.5	101325.0	260.0

Table D.1:   Aerodynamic conditions

Figure D.3: Heat transfer coefficient for an incompressible boundary layer over a flat plate

The shape of the curve may be interpreted by taking a look at the approximate boundary layer thickness given by:

$$\delta_{0.99} = 5\frac{\sqrt{x}}{\sqrt{u_e/\nu}}$$

Therefore the boundary layer thickness grows as the square root of x. Inuitively, this means that in order to match the exterior constant velocity u_e, the velocity profile will need a greater slope near the leading edge than further downstream. This leads to predicting a greater friction at the leading edge. Given the analogy assumption between friction and heat transfer, the heat transfer coefficient decreases with increasing boundary layer thickness. The discontinuity in the curve is due to laminar-turbulent transition (predicted using the simple criterion discussed earlier). Indeed, a feature of turbulent flows is that they have better mixing properties than laminar ones and hence enhance heat transfer.

D.3.2   Boundary Layer in the Neighbourhood of a Stagnation Point

The external flow in the neighbourhood of a stagnation point corresponds to the case $m = 1$ and $\beta = 1$, meaning that $u_e = kx$. In this case the wall shear stress is given by the expression:

$$\tau_p = 1.2326\rho_e kx\sqrt{k\nu}$$

and therefore the friction coefficient is given by:

$$C_f \stackrel{\text{def}}{=} \frac{\tau_w}{\frac{1}{2}\rho_e u_e^2} = \frac{2.4652\sqrt{k\nu}}{kx}$$

By using the Reynolds analogy, the Stanton number is then given by:

$$St \stackrel{\text{def}}{=} \frac{htc}{\rho_e u_e c_p} = s \frac{1.2326\sqrt{k\nu}}{kx}$$

Hence, the Falkner-Skan solution can be used to obtain the heat transfer coefficient in the neighbourhood of the stagnation point.

D.4 Heat Transfer for a Compressible Boundary Layer Over a Flat Plate

In the case of a compressible flow, the skin friction over a flat plate can be obtained by assuming it has a form analogous to that of the incompressible case:

$$C_f = f \frac{2a}{Re_x^p}$$

where f is a function that represents the effects of compressibility, and is defined as:

$$f = \left(\frac{\mu^*}{\mu_e}\right)^p \left(\frac{\rho^*}{\rho_e}\right)^{1-p}$$

To compute the function f, Monaghan proposes the use of a reference temperature given by (in both laminar and turbulent cases):

$$T^* = T_e + 0.54(T_w - T_e) + 0.16(T_{rec} - T_e)$$

which enables the computation of ρ^* and μ^*:

$$\frac{\rho^*}{\rho_e} = \frac{T_e}{T^*}$$

$$\frac{\mu^*}{\mu_e} = \left(\frac{T^*}{T_e}\right)^{1/2} \frac{1 + S/T_e}{1 + S/T^*}$$

where $S = 110.4K$.

The Reynolds analogy can once again be used to compute the heat transfer coefficient. However, in the compressible case, s can be computed by using the Crocco-Van Driest method, which provides: $s = Pr^{-2/3}$. Setting the wall temperature to $300K$, the heat transfer coefficient is computed and compared to that obtained for an incompressible flow in figure D.4.
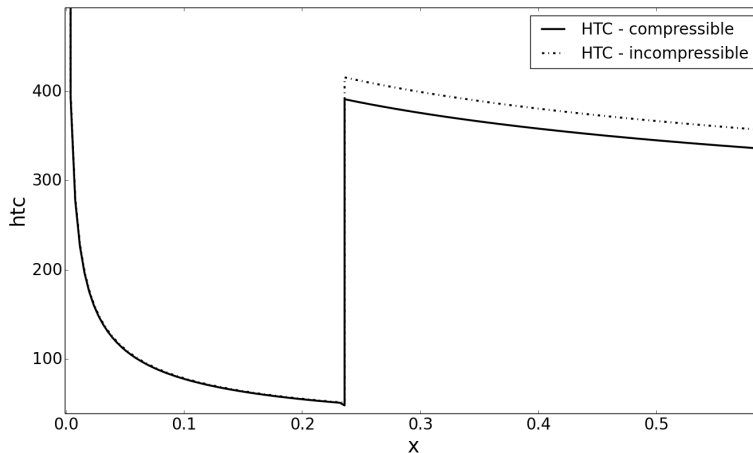

Figure D.4: Heat transfer coefficient for an incompressible boundary layer over a flat plate

D.5 Heat Transfer Coefficient in an Incompressible Laminary Layer using the Eckert-Smith-Spalding Method

As shown previously, the simple integral method can be employed using, for example, flat plate closure models in order to obtain the heat transfer coefficient. However, another way of dealing with this problem is to use the Eckert-Smith-Spalding method in the laminar region [157]. Eckert proposed to introduce the conduction thickness $\Delta_4 = \lambda/htc$ and considered the following set of equations, which are based on the wedge external flow $u_e = kx^m$:

$$\frac{u_e}{\nu} \frac{d\Delta_4^2}{dx} = \frac{1 - m}{c^2}$$

$$\frac{\Delta_4^2}{\nu} \frac{du_e}{dx} = \frac{m}{c^2}$$

where $c = Nu_x Re_x^{-1/2}$ and $Nu_x = htc\, x/k$ is the Nusselt number based on the length x. Combining the two previous equations leads to:

$$\frac{u_e}{\nu} \frac{d\Delta_4^2}{dx} = \frac{1}{c^2} - \frac{\Delta_4^2}{\nu} \frac{du_e}{dx}$$

which can be solved numerically. Based on this approach, Smith and Spalding propose, for $Pr = 0.7$, a simpler integration procedure given by:

$$\Delta_4^2 = \frac{11.68\nu \int_0^x u_e^{1.87} dx}{u_e^{2.87}}$$

from which the heat transfer coefficient can be deduced. The integral boundary layer module of IGLOO2D uses this kind of approach in the laminar region.

Modélisation bidimensionnelle de systèmes électrothermiques de protection contre le givre

Le givrage a depuis longtemps été identifié comme une problématique sérieuse dans le monde aéronautique. L'accrétion de givre, due à la présence de gouttelettes d'eau surfondue dans les nuages, dégrade les performances aérodynamiques et le rendement des entrées d'air parmi d'autres conséquences néfastes. Ainsi, les avionneurs sont sujets à des règles de certifications concernant la capacité à voler en conditions givrantes. Pour se faire, des systèmes de protection contre le givre sont utilisés. En raison de la complexité des phénomènes physiques mis en jeux, la simulation numérique constitue un atout lors de la phase de conception.

Ce travail de thèse porte sur la modélisation et la simulation numérique des systèmes électrothermiques de protection contre le givre. Il s'articule autour de trois approches de modélisation, qui ont donné lieu au développement de trois modules. Deux d'entre eux sont dédiés à la simulation du transfert de chaleur dans le système et dans la glace (changement de phase). Le troisième est lié à la modélisation du comportement mécanique du givre atmosphérique avec fissuration.

Ainsi, les propriétés mécaniques du givre atmosphérique sont revues de façon à pouvoir identifier les paramètres intervenant dans le modèle de fissuration. Ce modèle est ensuite utilisé pour étudier les mécanismes possibles de détachement du givre, qui ne sont à l'heure actuelle pas encore bien compris.

Le but final de ce travail est de proposer une méthodologie de simulation couplée pour les systèmes électrothermiques de protection contre le givre. Ainsi, la faisabilité d'un calcul couplé thermique-fissuration avec prédiction de détachement de givre est présentée.

Mots-clés : GIVRAGE ; PROTECTION CONTRE LE GIVRE ; ELECTROTHERMIQUE ; DEGIVRAGE ; THERMIQUE ; CHANGEMENT DE PHASE ; FISSURATION ; ENDOMMAGEMENT ; MODELISATION NUMERIQUE

Two Dimensional modelling of electrothermal ice protection systems

Icing has since long been identified as a serious issue in the aeronautical world. Ice build up, due to the presence of supercooled water droplets in clouds, leads to degradation of aerodynamic and/or air intake performances, among other undesirable consequences. Hence aircraft manufacturers must comply with certifications and regulations regarding flight safety in icing conditions. In order to do so, ice protection systems are used. Due to the multi-physical context within which these systems operate, numerical simulation can be a valuable asset.

The present work deals with the numerical modelling of electro-thermal ice protection systems.

It is built around the development of three modules. Two of them are dedicated to modelling heat transfer in the system and in the ice block. The other one models the mechanical behaviour of ice and fracture.

Hence, the mechanical properties of atmospheric ice are reviewed in order to identify some mechanical parameters relevant to the fracture model. The fracture mechanics numerical method is used to investigate possible ice shedding mechanisms, that is to say the mechanisms leading to the detachment of ice, which are not yet well understood.

The final goal of this work is to propose a completely coupled 2nd generation simulation methodology for electro-thermal ice protection systems. Hence the feasibility of a coupled thermal computation with ice shedding prediction based on the developed modules is shown.

Keywords : ICING ; ICE SHEDDING ; ICE PROTECTION ; ELECTRO-THERMAL ; DE-ICING ; HEAT TRANSFER ; PHASE CHANGE ; FRACTURE MECHANICS ; DAMAGE MECHANICS ; NUMERICAL MODELLING